UNIVERSITY OF SOUTHAMPTON
FACULTY OF ENGINEERING, SCIENCE AND MATHEMATICS
SCHOOL OF ELECTRONICS AND COMPUTER SCIENCE
COMMUNICATIONS RESEARCH GROUP

Minimum Error Rate Beamforming Transceivers

by

Shuang Tan
BEng, MSc

A thesis submitted for the degree of Doctor of Philosophy

June 2008

SUPERVISORS:
Professor Lajos Hanzo
Dipl. Ing., MSc, PhD, FIEEE, FIEE, DSc, FREng
and
Professor Sheng Chen
BEng, PhD, SMIEEE, DSc

To my family

UNIVERSITY OF SOUTHAMPTON

ABSTRACT

FACULTY OF ENGINEERING, SCIENCE AND MATHEMATICS
SCHOOL OF ELECTRONICS AND COMPUTER SCIENCE
COMMUNICATIONS RESEARCH GROUP

A thesis submitted for the degree of Doctor of Philosophy

Minimum Error Rate Beamforming Transceivers

by Shuang Tan

Iterative multiuser receivers constitute an effective solution for transmission over Multiple Access Interference (MAI) infested channels, when invoking a combined Multiuser Detector (MUD) and channel decoder. Most reduced-complexity methods in this area use the Minimum Mean Squared Error (MMSE) MUD. Since the desired output of Binary Phase Shift Keying (BPSK) modulated systems is real-valued, minimising the Mean Squared Error (MSE) between the beamformer's desired output and the real part of the beamformer output has the potential of significantly improving the attainable Bit Error Rate (BER) performance. We refer to this MMSE design as the Real-valued Minimum Mean Squared Error (RMMSE) receiver. In this thesis, we explore a new Soft-Input Soft-Output (SISO) Interference Cancellation (IC) aided multiuser detection algorithm based on the novel Minimum Bit Error Rate (MBER) criterion. We demonstrate that the MBER turbo receiver outperforms both the MMSE and the RMMSE algorithms, particularly in so-called rank-deficient beamforming systems, where the number of receiver antennas is lower than the number of users supported. A novel iterative Soft Interference Cancellation (SIC) aided beamforming receiver is also developed for high-throughput Quadrature Amplitude Modulation (QAM) assisted systems. The proposed SIC based Minimum Symbol Error Rate (MSER) multiuser detection scheme guarantees the direct and explicit minimisation of the Symbol Error Rate (SER) at the output of the detector.

This thesis also studies the Mutual Information (MI) transfer characteristics of the proposed iterative SIC aided beamforming receiver communicating over both Additive White Gaussian Noise (AWGN) and slow-fading channels. Based on the Extrinsic Information Transfer (EXIT) chart technique, we investigate

the convergence behaviour of the iterative MBER multiuser detection scheme as a function of the system parameters and channel conditions. We also compare the performance and the convergence behaviour of different MUDs and channel decoders. Our simulation results show that the EXIT chart analysis is sufficiently accurate for the MBER MUD and the MSER MUD, despite its non-Gaussian output distribution. As expected, the proposed SIC-MBER MUD and the SIC-MSER MUD outperform the SIC-MMSE MUD.

Based on EXIT charts, the convergence behaviour of a three-stage serially concatenated multiuser beamforming receiver is also presented. This system uses an MBER MUD as the inner detection module. Due to the non-recursive nature of this inner module, the system has a finite-duration Impulse Response (IR) and hence a modest-efficiency extrinsic information exchange. Therefore an Infinite Impulse Response (IIR) unity-rate memory-1 recursive precoder is placed in front of the channel in order to create an IIR system, which benefits from an efficient extrinsic information exchange and hence improves the iterative detection scheme's performance. Novel Irregular Convolutional Codes (IRCCs) are constructed, which are used as the outer code for the sake of achieving a near-capacity performance. Our simulations show that this system outperforms traditional two-component iterative detection aided structures and is capable of significantly reducing the error floor encountered.

The problem of designing an optimal linear transmit preprocessing transformation for the downlink of Multi-Input Multi-Output (MIMO) aided communication systems is also addressed. The BER is minimised under a maximum total transmit power constraint. The transmitter of the Base Station (BS) requires explicit knowledge of the channel transfer function coefficients and of the receiver processing matrix. It is shown that the proposed Linear Minimum Bit Error Rate (LMBER) Multiuser Transmitter (MUT) outperforms the Wiener precoding method in terms of the achievable BER versus channel quality performance.

Acknowledgements

First and foremost, I would like to take this opportunity to extend my sincere gratitude to both my supervisors, Professor Lajos Hanzo and Professor Sheng Chen for their patience, guidance and motivation throughout my study. Professor Hanzo has been an invaluable guide and dedicated his time to helping me with every aspect of this work. Professor Chen's ideas and insightful thoughts have always inspired me.

I would also like to thank staff members and colleagues in the communications research group, namely Dr. Lie Liang Yang, Dr. Soon X (Michael) Ng, Dr. Robert Maunder, Dr. Yosef (Jos) Akhtman, the group secretary Denise Harvey and many others. My special thanks also go to Dr. Mohamad Yusoff Alias, Dr. Nurul Nadia Ahmad, Lei Xu, Nan Wu and Du Yang for the fruitful discussions as well as for their friendship.

I would also like to thank Overseas Research Students Awards Scheme (ORSAS) and School of Electronics and Computer Science (ECS) of University of Southampton for their financial support.

Finally, very special thanks go to my dear parents and my sister in China for their love, understanding and financial support. Especially to my lovely wife Fan Zhang, who first encouraged me to come to England and always supports me.

List of Publications

Journal Papers and Letters

1. S. Chen, L. Hanzo and **S. Tan**, "Symmetric complex-valued RBF receiver for multiple-antenna aided wireless systems," Accepted for publication in *IEEE Transactions on Neural Networks*

2. S. Chen, **S. Tan**, L. Xu and L. Hanzo, "Adaptive minimum error-rate filtering design: A review," *Signal Processing*, vol.88, no.7, pp.1671–1697, July 2008

3. **S. Tan**, J. Wang, S. X. Ng, S. Chen and L. Hanzo, "Three-stage turbo MBER multiuser beamforming receiver using irregular convolutional codes," *IEEE Transactions on Vehicular Technology*, vol.57, no.3, pp.1657–1663, May 2008

4. **S. Tan**, S. Chen and L. Hanzo, "Iterative multiuser minimum symbol error rate beamforming aided QAM receiver," *IEEE Signal Processing Letters*, vol.15, pp.301–304, February 2008

5. **S. Tan**, S. Chen and L. Hanzo, "On multi-user EXIT chart analysis aided turbo-detected MBER beamforming designs," *IEEE Transactions on Wireless Communications*, vol.7, no.1, pp.314–323, January 2008

6. S. Chen, **S. Tan** and L. Hanzo, "Adaptive beamforming for binary phase shift keying communication systems," *Signal Processing*, vol.87, no.1, pp.68–78, January 2007

Conference Papers

1. S. Sugiura, **S. Tan**, S. Chen and L. Hanzo, "Turbo MBER space-time equalization for the cooperative STBC aided SDMA uplink," Submitted to *IEEE Global Communications Conference*, 2008

2. S. Chen, L. Hanzo and **S. Tan**, "Nonlinear beamforming for multiple-antenna assisted QPSK wireless systems," In *Proceeding of IEEE International Conference on Communications*, Beijing, China, May 2008

3. **S. Tan**, S. Chen and L. Hanzo, "Minimum symbol error rate turbo multiuser beamforming aided QAM receiver," In *Proceeding of IEEE Wireless Communications & Networking Conference*, pp.912–916, Las Vegas, USA, April 2008

4. **S. Tan**, S. Chen and L. Hanzo, "MBER turbo multiuser beamforming aided QPSK receiver design using EXIT chart analysis," In *Proceeding of IEEE Vehicular Technology Conference*, vol.1, pp.561–565, Baltimore, USA, October 2007

5. **S. Tan**, L. Xu, S. Chen and L. Hanzo, "Iterative soft interference cancellation aided minimum bit error rate uplink receiver beamforming," In *Proceeding of IEEE Vehicular Technology Conference*, vol.1, pp.17–21, Melbourne, Australia, May 2006

6. L. Xu, **S. Tan**, S. Chen and L. Hanzo, "Iterative minimum bit error rate multiuser detection in multiple antenna aided OFDM," In *Proceeding of IEEE Wireless Communications & Networking Conference*, vol.3, pp.1603–1607, Las Vegas, USA, April 2006

7. S. Chen, **S. Tan** and L. Hanzo, "Linear beamforming assisted receiver for binary phase shift keying modulation systems," In *Proceeding of IEEE Wireless Communications & Networking Conference*, vol.3, pp.1741–1746, Las Vegas, USA, April 2006

Contents

Abbreviations

3GPP	3rd Generation Partnership Project
AE	Antenna Element
AOA	Angle of Arrival
APP	*A Posteriori* Probability
AWGN	Additive White Gaussian Noise
BER	Bit Error Rate
BLAST	Bell Laboratories Layered Space-Time
BPSK	Binary Phase Shift Keying
BS	Base Station
CDMA	Code Division Multiple Access
CIR	Channel Impulse Response
CSI	Channel State Information
DOA	Direction of Arrival
DS-CDMA	Direct Sequence Code Division Multiple Access
D-BLAST	Diagonal BLAST
EXIT	Extrinsic Information Transfer
FDD	Frequency Division Duplex
FEC	Forward Error Correction
FIR	Finite Impulse Response
HSPA	High-Speed Packet Access
H-BLAST	Horizontal BLAST
IC	Interference Cancellation
IIR	Infinite Impulse Response
IR	Impulse Response
IRCC	Irregular Convolutional Code
ISI	Intersymbol Interference

LMBER	Linear Minimum Bit Error Rate
LMSER	Linear Minimum Symbol Error Rate
LLR	Log-Likelihood Ratio
LOS	Line of Sight
LTE	Long-Term Evolution
MAI	Multiple Access Interference
MAP	Maximum *A Posteriori* Probability
MBER	Minimum Bit Error Rate
MF	Matched Filter
MI	Mutual Information
MIMO	Multi-Input Multi-Output
ML	Maximum Likelihood
MMSE	Minimum Mean Squared Error
MS	Mobile Station
MSE	Mean Squared Error
MSER	Minimum Symbol Error Rate
MUD	Multiuser Detector
MUI	Multiuser Interference
MUT	Multiuser Transmitter
NSC	Non-Systematic Convolutional
NSR	Noise-to-Signal Ratio
OFDM	Orthogonal Frequency Division Multiplexing
PDF	Probability Density Function
QAM	Quadrature Amplitude Modulation
QPSK	Quadrature Phase Shift Keying
RMMSE	Real-valued Minimum Mean Squared Error
RSC	Recursive Systematic Convolutional
SCG	Simplified Conjugate Gradient
SDM	Space Division Multiplexing
SDMA	Spatial Division Multiple Access
SER	Symbol Error Rate
SIC	Soft Interference Cancellation
SIMO	Single-Input Multi-Output
SINR	Signal-to-Interference-plus-Noise Ratio
SIR	Signal-to-Interference Ratio
SISO	Soft-Input Soft-Output

SNR	Signal-to-Noise Ratio
SQP	Sequential Quadratic Programming
STBC	Space-Time Block Code
STC	Space-Time Code
STTC	Space-Time Trellis Code
SVD	Singular Value Decomposition
TDD	Time Division Duplex
TMF	Transmit Matched Filter
TMinBer	Minimum Bit Error Rate Transmission
TMMSE	Transmit Minimum Mean Squared Error
TWF	Transmit Wiener Filter
TZF	Transmit Zero Forcing
VAA	Virtual Antenna Array
VQ	Vector Quantization
V-BLAST	Vertical BLAST
WiMAX	Worldwide Interoperability for Microwave Access
WL	Widely Linear

Notations and Symbols

Notations

x	Variable
$\mathbf{x}$	Column vector
x_i	ith element of the vector $\mathbf{x}$
$\mathbf{x}_c$, $\mathbf{x}_{c'}$	Real-valued vertically concatenated vector
$\mathbf{X}$	Matrix
$\mathbf{x}_i$	ith column vector of the matrix $\mathbf{X}$
x_{ij}	(i,j)th element of the matrix $\mathbf{X}$
$\mathbf{X}_c$, $\mathbf{X}_{c'}$	Real-valued vertically concatenated matrix
$x^{(i)}$	ith possible variable of a constellation
$\hat{x}$	Estimated variable
$\bar{x}$	Mean of a variable
$\check{x}$	Hard decision of a variable
$f(\cdot)$	Function
$I(\cdot)$	Mutual information
$L(\cdot)$	Information in terms of LLR
$\mathcal{O}(\cdot)$	Complexity order
$p(x)$	PDF of a random variable
$P(x)$	Probability of a random variable

Operators

$\lvert\cdot\rvert$	Absolute value
$\lVert\cdot\rVert$	Norm of a vector
$(\cdot)^*$	Complex conjugate
$(\cdot)^T$	Transpose
$(\cdot)^H$	Hermitian (conjugate transpose)

$(\cdot)^{-1}$	Matrix inversion
$\Re[\cdot]$	Real part of a variable
$\Im[\cdot]$	Imaginary part of a variable
$E[\cdot]$	Expectation
$\nabla(\cdot)$	Gradient
diag[·]	Diagonal matrix
blockdiag[·]	Block Diagonal matrix
$\exp(\cdot)$	Exponential function
$\ln(\cdot)$	Hyperbolic logarithm function
$Q(\cdot)$	Area under the tail of the standardized Gaussian distribution
sgn(·)	Signum Function
$\tanh(\cdot)$	Hyperbolic tangent function
tr(·)	Trace of a matrix

Symbols

α	Weighting coefficient of IRCC subcode
β	Optimization termination scalar
δ	Optimization step size
θ	LOS angle
λ	Lagrange multiplier
$\Delta\lambda$	Optimization correction of λ
μ	Mean of estimated signal
ξ	Cost function criterion
σ^2	Variance of estimated signal
σ_n^2	Noise variance
ω	Carrier angular frequency
A	Area under EXIT curve
$b(i)$	ith bit of symbol s
$\mathbb{C}$	Set of all complex numbers
$\mathbf{D}$	Receive filter
E_b	Average bit energy
E_s	Average symbol energy
E_t	Transmit power
$\mathbf{G}_2$	STBC coding matrix for two-transmit antenna system
$\mathbf{H}$	Channel matrix

i	Number of iterations
$\mathbf{I}_D$	$(D \times D)$-dimensional identity matrix
j	Imaginary unit
K	Number of users
k	User number
L	Number of antenna elements
l	Antenna element number
M	Number of symbols in modulation constellation
n	Symbol index
$\mathbf{n}$	AWGN
N_0	Noise power spectral density
N_b	Block length of block-fading channel
N_{cg}	Iteration number of the SCG algorithm
P	Number of IRCC subcodes
p	IRCC subcode number
$\mathbf{P}$	MUT preprocessing matrix
$\mathbf{p}$	Real-valued vertically concatenated vector of $\mathbf{P}$
$\Delta\mathbf{p}$	Optimization correction of $\mathbf{p}$
Pe_b	Bit error rate
Pe_s	Symbol error rate
R	Code rate
$\mathbf{R}$	Covariance matrix
$\mathbb{R}$	Set of all real numbers
r	Code rate of IRCC subcode
$\mathbf{r}$	Received signal
$\mathfrak{R}_s$	Real-valued block diagonal matrix of $\mathbf{R}_s$
$\mathbf{s}$	Transmitted source symbols
$\mathbf{t}$	Transmitted signal
v	Variance of source symbol
$\mathbf{v}$	Real-valued vertically concatenated vector
$\mathbf{W}$	MUD weight matrix
x	Decision variable

Chapter 1

Introduction

1.1 Wireless Communication Systems

There are two fundamental aspects of wireless communication that make it challenging and interesting. Firstly, the phenomenon of fading: results in the time-variation of the channel's magnitude and phase due to the small-scale effects of multipath fading, as well as owing to the larger scale effects, such as the path loss proportional to distance and shadowing due to obstacles. Secondly, wireless users communicate over the air and there is significant interference between them in wireless communication. The interference can be between transmitters communicating with a common receiver as in the uplink of a cellular system, or between signals emerging from a single transmitter to multiple receivers, as in the downlink of a cellular system, as well as between different transmitter-receiver pairs (e.g. interference between users in different cells). How to deal with fading and with interference is central to the design of wireless communication systems.

The increasing demand for the higher data rates to be supported by future wireless systems inevitably comes at the cost of an increased bandwith occupied by the transmitted signal, since the bandwidth is proportional to the symbol rate of the transmitted signal. In order to efficiently exploit the limited bandwidth available, the most recently introduced communication systems consider the employment of multiple transmit and receive antennas for the transmission of independent bit-streams. This trend towards the employment of Multi-Input Multi-Output (MIMO) systems introduced for the sake of achieving spatial multiplexing has largely been motivated by the work of Foschini and Gans, who showed

in [1] that under idealized assumptions the capacity of the wireless channel increases linearly with the minimum of the number of transmit and receive antennas. Their work is a logical evolution of the channel capacity analysis provided by Shannon in [2] 1948. In order to exploit this potential increase in channel capacity and therefore the increase of the theoretically achievable data throughput, MIMO transceivers are expected to be an integral part of most future wireless communication systems. Further work on the capacity of MIMO channels has for example been provided by Goldsmith *et al.* in [3] and by Shamai in [4] who also contributed an extensive tutorial overview with Biglieri in [5].

However, even with the advent of MIMO transceivers and higher order modulation schemes, the bandwidth occupied by the transmitted signal is generally significantly higher than the coherence bandwidth of the wireless channel and will therefore result in multi-path propagation of the transmitted signal. Often the multi-path channels exhibiting frequency selective fading are also referred to as wideband channels. Orthogonal Frequency Division Multiplexing (OFDM) [6] is proposed in the 3rd Generation Partnership Project (3GPP) and in its Long-Term Evolution (LTE) [7] drafts, as well as in a range of other communication systems, such as WiFi [8] and Worldwide Interoperability for Microwave Access (WiMAX) [9]. The OFDM scheme, which belongs to the family of multi-carrier [6] transmission schemes is capable of supporting high data-rates, while the detection of the signal at the Mobile Station (MS) can be achieved at a relatively low computational cost. The problem of a high peak-to-average power ratio [6] for the modulated signal can be solved by employing a linear or linearized and hence less power efficient amplifier at the Base Station (BS) transmitter's radio frequency front-end.

However, since mobile operators want to keep the cost and the power consumption of MSs low, OFDM is less attractive for the uplink of the communication system. For this reason and because typically a lower data rate is required for the uplink, it was proposed in [10] to consider single-carrier transmission for the reverse link as part of the 3GPP LTE. Single-carrier transmission imposes a low computational complexity and hence imposes modest hardware demands on the transmitter in exchange for an increased equalization complexity at the receiver. Generally, an increased complexity at the BS poses less of a problem than at the MS. The increased complexity of the BS is mainly imposed by the space-time equalizer required for detecting the signal.

1.2 Motivation and Novel Contributions

The increasing demand for mobile communication services supported within a limited radio-frequency bandwidth motivates the design of antenna array assisted beamforming techniques [11] as well as Spatial Division Multiple Access (SDMA) arrangements [6]. By appropriately combining the signals received by the different elements of an antenna array, beamforming becomes capable of creating an angularly selective transmitter/receiver beam, hence potentially separating signals transmitted on the same carrier frequency but arriving from sufficiently different angles.

Since the discovery of turbo codes in 1993 [12], iterative detection [13] has been applied in the context of joint channel estimation and equalization [14], in turbo equalization [15, 16], in multiuser detection [17, 18, 19] and numerous other coded communication systems [15, 20]. In iterative multiuser receivers [13], the Multiuser Detector (MUD) and the channel decoder exchange extrinsic information in a number of consecutive iterations. During each iteration, the extrinsic information alternately extracted either from the MUD or the channel decoder is used as the *a priori* input by the other detection stage in the next iteration. The information exchanged is exploited for the sake of improving the receiver's attainable performance. In [18], a suboptimal linear MUD was introduced, which benefitted from both Soft Interference Cancellation (SIC) and instantaneous linear Minimum Mean Squared Error (MMSE) filtering.

Against this background, in this thesis we propose a novel family of iterative beamforming receivers. To elaborate a little further, the conventional beamformer combines the signals received with the aid of each Antenna Element (AE) for the sake of minimising the Mean Squared Error (MSE) between the complex-valued locally stored and received reference signal. For Binary Phase Shift Keying (BPSK) systems, however, the beamformer's desired output is real-valued. By minimising the MSE between the beamformer's desired output and the real part of the beamformer output, the system's achievable Bit Error Rate (BER) performance can be significantly enhanced. We will refer to this alternative MMSE design as the Real-valued Minimum Mean Squared Error (RMMSE) arrangement in order to contrast it with the standard MMSE. However, the MMSE and RMMSE algorithms do not guarantee the direct and explicit minimisation of the system's BER. Hence in references [21, 22, 23, 24, 25, 26, 27, 28, 29, 30, 31, 32] the

BER rather than the MSE was minimised at the MUD's output. The Minimum Bit Error Rate (MBER) beamforming design is the true optimal solution and hence it generally outperforms the MMSE and the RMMSE solutions, particularly in the context of the so-called rank-deficient systems, where the degree of freedom for the antenna array is lower than the number of users. The achievable BER difference of the MMSE and MBER receivers becomes particularly substantial in this scenario. The MBER detectors are challenging to derive for higher-order Quadrature Amplitude Modulation (QAM), but nonetheless, Yeh and Barry have succeeded in directly minimising the detector's output Symbol Error Rate (SER) [33] for a QAM equalizer. Motivated by their work, a novel Minimum Symbol Error Rate (MSER) beamforming assisted receiver has been developed for high-throughput QAM schemes [34]. In this thesis, an iterative SIC aided MSER beamformer is proposed for QAM signals. Note that the shifting properties and the symmetrical distribution of the output signal's Probability Density Function (PDF), which were exploited in the derivation of the original MSER beamforming solution of [34], are no longer valid in our iterative system. Therefore, we derive a new *a priori* information assisted MSER MUD suitable for employment in the proposed iterative SIC aided receiver. Motivated by the idea of RMMSE algorithm and the Widely Linear (WL) method of [35], we also introduce the WL-MMSE, the WL-MBER and the WL-MSER SIC MUDs, which employ two separate weight vectors for individually detecting the in-phase and quadrature-phase component of the transmitted symbol. These WL algorithms are capable of achieving a better performance at a similar complexity.

In order to investigate the iterative detection process and its convergence, the powerful concept of semi-analytical Extrinsic Information Transfer (EXIT) charts was introduced in [36] and [37]. This semi-analytic technique uses the Mutual Information (MI) between the inputs and outputs of the concatenated receiver components in order to analyse the achievable system performance. For example, EXIT charts were employed in turbo equalization in [16, 38, 39], while in [19] and [40] they were used to examine the convergence properties of a turbo MUD. Until recently EXIT chart analysis was only capable of predicting the achievable decoding performance, when the extrinsic information was Gaussian distributed, but Li and Wang [40] succeeded in adopting this technique also in the context encountering a non-Gaussian distribution at the output of a turbo MUD.

It is widely recognized that in a serially concatenated receiver employing iterative decoding the inner code should be recursive in order to maximize the at-

tainable interleaver gain [41]. This benefit may be generalized to diverse serially concatenated schemes. However, not all inner modules of serially concatenated schemes can be readily rendered recursive, which hence limits the achievable decoding performance. In our system, a Soft-Input Soft-Output (SISO) MBER MUD [29, 30] is invoked, which directly minimises the BER at the MUD's output, rather than minimising the MSE, as in the classic MMSE detector. The non-recursive nature of the MBER MUD may be ameliorated with the aid of a simple unity-rate memory-1 recursive precoder incorporated at the transmitter, and hence the attainable performance may be further improved [42]. Then, the inner component of the receiver constituted by the MBER MUD, the intermediate channel decoder and the outer channel decoder constitute a three-stage serially concatenated scheme. In this thesis we design this three-stage concatenated multiuser receiver for the sake of achieving near-capacity performance [39]. By combining and projecting a series of three-dimensional EXIT functions onto a single two-dimensional EXIT chart [43], the convergence behaviour of the system is visualized. Specifically, Irregular Convolutional Codes (IRCCs) [38] are constructed, which are used as the outer code for the sake of solving the EXIT curve fitting problem of [44], i.e. that of minimising the area of the EXIT chart's open tunnel, implying that the system becomes capable of approaching the achievable capacity.

In particular, downlink transmission is of interest. The BS is assumed to know the linear processing performed by the MS. The BS is capable of acquiring the required MIMO channel coefficients with the aid of the side-information feedback channel transmitted from the MS or by estimating the uplink channel and assuming that the downlink channel is similar, as in Time Division Duplex (TDD) systems [45]. An important advantage of transmit preprocessing is that the affordable computational complexity of the BS is higher than that of the MS, and as a benefit, the processing in the MS can be simpler. Consequently, it is cheaper to produce the MS. A specific transmit preprocessing scheme maximizing the output Signal-to-Noise Ratio (SNR) at the receiver was derived in [46], which is the Transmit Matched Filter (TMF) based preprocessor. The most intuitive approach designed for transmit preprocessing is Transmit Zero Forcing (TZF), which removes all interference at the receivers [47, 48]. A modified MSE transmit preprocessing defined under a specific power constraint was considered in [49, 50, 51], which is referred to as the Transmit Wiener Filter (TWF). In a practical communication system, however, the goal is to directly minimise the BER. Hence in this

thesis, a linear preprocessing method that directly minimises the BER is derived. The proposed method leads to an improved BER versus channel SNR performance. The related problem of designing a minimum BER transmit preprocessor for a known channel has been considered in [52, 53, 54, 55].

The thesis is based on the publications [56, 57, 58, 59, 60, 61, 62]. In summary, the novel contributions of this thesis are:

- **A soft MBER MUD aided iterative beamforming receiver was investigated, which directly minimises the BER at the MUD's output. The proposed MBER scheme significantly outperforms the conventional MMSE method at the cost of a higher computational complexity [56, 57].**

- **We derived a new *a priori* information assisted MSER MUD suitable for employment in the proposed iterative SIC aided receiver designed for high-throughput QAM schemes. The proposed linear SIC aided MSER multiuser detection scheme guarantees the direct and explicit minimisation of the SER at the output of the detector [60, 61].**

- **The WL-MMSE, WL-MBER and WL-MSER SIC MUDs, which employ two separate weight vectors for individually detecting the in-phase and quadrature-phase component of the transmitted symbol, were introduced. These WL algorithms are capable of achieving a better performance than the corresponding non-WL MUDs operating at a similar detection complexity.**

- **We studied the mutual information transfer characteristics of the proposed novel iterative SIC aided beamforming receiver communicating over both Additive White Gaussian Noise (AWGN) and flat-fading channels. Based on the EXIT chart technique, we investigated the convergence behaviour of the iterative MBER MUD scheme as a function of both the system parameters and channel conditions in comparison to the SIC aided MMSE MUD [58, 59, 60, 61].**

- **Based on EXIT charts, the convergence behaviour of a three-stage serially concatenated multiuser beamforming receiver was pre-**

sented. This system used a linear MBER MUD as the inner detection module. Due to the non-recursive nature of this inner module, the system has a finite-duration Impulse Response (IR) and hence a modest-efficiency extrinsic information exchange. Therefore an Infinite Impulse Response (IIR) unity-rate memory-1 recursive precoder is placed in front of the channel in order to create an IIR system, which benefits from an efficient extrinsic information exchange and hence improves the iterative detection scheme's performance. Novel IRCCs were constructed to be used as the outer code for the sake of achieving a near-capacity performance [62].

- **A linear Multiuser Transmitter (MUT) that minimises the BER subject to a power constraint was proposed. The proposed Linear Minimum Bit Error Rate (LMBER) transmission scheme is capable of achieving a better performance than the Wiener MUT, and its complexity can be significantly reduced in the presence of slow-fading channels compared to its non-linear Minimum Bit Error Rate Transmission (TMinBer) aided counterpart.**

1.3 Organization of the Thesis

An overview of MIMO systems is presented in **Chapter 2**, where the various categories of multiple antenna aided communication systems are introduced. A range of multiuser detection techniques are reviewed for the sake of providing the necessary background to this exciting research field. We will mainly concentrate our attention on linear multiuser detection schemes.

In **Chapter 3**, we explore the SISO Interference Cancellation (IC) multiuser detection algorithm based on the novel MBER criterion. We demonstrate that the MBER turbo receiver outperforms both the MMSE and the RMMSE algorithms. We also study the MI transfer characteristics of a novel iterative SIC aided beamforming receiver communicating over both AWGN and slow-fading channels. Based on the EXIT chart technique, we investigate the convergence behaviour of an iterative MBER multiuser detection scheme as a function of the system parameters and channel conditions. We also compare the attainable per-

formance and the convergence behaviour of different MUDs and channel decoders. Our simulation results show that the EXIT chart analysis is sufficiently accurate for the MBER MUD, despite its non-Gaussian output distribution. As expected, the proposed SIC-MBER MUD outperforms the SIC-MMSE MUD. We also investigate the iterative MSER receiver design in the context of a high-order QAM system. This proposed MSER system outperforms the well-known MMSE aided system. The performance of the WL-MMSE MUD, the WL-MBER MUD and the WL-MSER MUD are also studied.

In **Chapter 4**, we extend the two-stage iterative receiver to three SISO modules, namely the inner MUD, the intermediate unity-rate channel decoder and the outer channel decoder. The convergence behaviour of our design example was analysed using 3D EXIT charts and their 2D projections. The three-stage system is capable of eliminating the residual BER encountered in the conventional two-stage system. With the advent of 2D EXIT-chart projection, an IRCC was constructed for employment as the outer code, whose EXIT function was matched to the joint EXIT function, and as a result, the channel capacity was closely approached.

In **Chapter 5**, a LMBER MUT was explored. The LMBER optimization process was detailed. The simulation results show that the proposed algorithm outperforms the previously proposed Wiener multiuser transmission method [49]. The BER performance of the MUT systems using imperfect and outdated channel information was also studied.

Finally, in **Chapter 6**, we offered our conclusions and provided suggestions for future research.

Chapter 2

Multi-Input Multi-Output Detection

2.1 Multi-Input Multi-Output Communications

Multi-Input Multi-Output (MIMO) wireless systems may be conveniently described by an abstract mathematical model. Another commonly used term for MIMOs is 'smart antennas', which perform spatio-temporal information processing with the aid of multiple antennas. In MIMO wireless communication systems, significant throughput and/or integrity improvements can be achieved within a given bandwidth and at a given total transmit power, as detailed below.

Smart antennas provide us with a wide variety of design options, ranging from Single-Input Multi-Output (SIMO) architectures that harvest more energy using multiple receiver antennas to improve the SNR at the receiver, to MIMO architectures that create multiple parallel data links. The number of inputs and outputs here refers to the number of AEs used at the transmitter and receiver, respectively. To elaborate a little further, in smart antenna assisted systems multiple AEs may be invoked at the transmitter and/or the receiver, where again, the AEs may be arranged for achieving spatial diversity gains, directional beamforming or multiplexing gains, as well as for attaining both diversity and beamforming. In these smart antenna aided systems the achievable performance improvements are usually a function of the antenna spacing and that of the baseband algorithms invoked for processing the signals received by the AEs [17]. Terms commonly used today that embrace various aspects of smart antenna systems include in-

telligent antennas, adaptive antennas, phased arrays, Spatial Division Multiple Access (SDMA), spatial processing, spatial multiplexing, digital beamforming and others [11, 45]. Different smart antenna architectures provide different benefits, which can be broadly classified as achieving array gain, diversity gain, multiplexing gain and interference reduction [63]. The signaling strategy at the transmitter and the corresponding processing at the receiver are designed based on the specific system specifications. Table 2.1 summarizes the evolution of the state-of-the-art in MIMO designs.

Table 2.1: Selection of MIMO papers

Author(s)	Contribution
[64] Foschini	Proposed the Bell Laboratories Layered Space-Time (BLAST) architecture capable of capturing much of the MIMO capacity promised by information theory.
[1] Foschini and Gans	Examined the benifits of multiple AEs representing the spatial dimension to improve the achievable wireless capacity in certain applications. Fixing the overall transmitted power, the authors expressed the capacity offered by multiple AEs and quantified how the capacity scales upon increasing the SNR for a large but practical number of AEs at both the transmitter and receiver.
[65] Tarokh *et al.*	Considered the design of Space-Time Trellis Codes (STTCs) for improving the data rate and/or the reliability of communications over fading channels using multiple transmit antennas.
[66] Wolniansky *et al.*	Described a wireless communication architecture known as Vertical BLAST (V-BLAST).
[67] Alamouti	Presented a low-complexity two-branch Space-Time Block Code (STBC). Using two transmit and a single receive antenna the scheme achieves the same diversity order as a maximal-ratio combining receiver employing a single transmit ántenna and two receive antennas.

Author(s)	Contribution
[68] Tarokh *et al.*	Documented the attainable performance of a novel class of STBCs, which provide a new design paradigm for transmission over Rayleigh fading channels using multiple transmit antennas.
[69] Tarokh *et al.*	Introduced the combination of array processing at the receiver and coding techniques for multiple transmit antennas at the transmitter, which can provide reliable high data rate communication over narrowband wireless channels, while providing both diversity and coding gains.
[70] Tarokh *et al.*	Introduced STBC for communication over Rayleigh fading channels using multiple transmit antennas.
[71] Foschini *et al.*	Investigated robust wireless communication in rich-scattering propagation environments using multiple AEs at both the transmit and receive sites in the context of V-BLAST, which is a simplified, but spectrally efficient space-time processing method.
[72] Jafarkhani	Designed unity rate codes, which are quasi-orthogonal and provide partial rather than 'full' diversity. The decoder of the proposed codes processes pairs of transmitted symbols instead of single symbols.
[4] Shamai and Marzetta	Investigated the channel capacity of a multiuser system employing multiple receive AEs communicating over Rayleigh block-fading channels without requiring Channel State Information (CSI).
[73] Sellathurai and Haykin	Presented the concept of turbo-BLAST, which is a novel MIMO scheme designed for high-throughput wireless communications. It amalgamated the following ideas: the BLAST architecture, random layered space-time coding using independent block codes and random space-time interleaving, a sub-optimal turbo-like iterative detection aided receiver and estimated channel matrix in a simple iterative fashion.

Author(s)	Contribution
[74] Foschini *et al.*	Discussed three architectural superstructures designed for wireless links employing multiple antennas, including Diagonal BLAST (D-BLAST), Horizontal BLAST (H-BLAST) and the single outer code architecture.
[3] Goldsmith *et al.*	Provided an overview of the capacity of single-user and multi-user MIMO channels. The results indicated that the capacity gain achieved for single-user MIMO channels heavily depends on the available channel information at both the receiver and transmitter, as well as on the channel SNR and the correlation between the channel gains of each antenna element. The capacity region of the MIMO multiple access and the highest achievable rate region (also referred to as the dirty-paper coding region) of the MIMO broadcast channel are intimately inter-related by a duality transformation, which facilitates finding the transmission strategies that achieve a point on the boundary of the MIMO multiple-access channel's capacity region.
[75] Diggavi *et al.*	The effect of spatial diversity on the attainable throughput and reliability of wireless networks was examined. The authors illustrated the benefits of spatial diversity across the entire physical (signal transmission/coding and receiver signal processing) as well as networking (resource allocation, routing, and applications) layers, discussed the associated engineering intuitions and tradeoffs, emphasizing the strong interactions between the various network functionalities.
[76] Tao and Cheng	Presented the architecture of generalized layered space-time codes as a combination of the BLAST architecture and Space-Time Codes (STCs) in multiple-antenna aided wireless communication systems. This approach provides both spectral and power efficiency gains at a moderate complexity.

Author(s)	Contribution
[77] Pabst *et al.*	Presented an overview of important applications in the context of relaying and covered different approaches to exploiting the benefits of multihop communications via relays. Relaying was presented as a means of reducing the infrastructure deployment costs. It was also shown that through the exploitation of spatial diversity, multihop relaying is capable of enhancing the achievable capacity of cellular networks.
[78] Nosratinia *et al.*	Presented an overview of the developments in cooperative communication proposed for enabling single-antenna aided mobiles in a multi-user environment to share their antennas and hence to generate a virtual multiple-antenna aided transmitter that allows them to achieve a substantial transmit diversity.

2.1.1 Space-Time Codes

Space-Time Codes (STCs) [13] are capable of improving the reliability of data transmission in wireless communication systems using multiple transmit antennas with the aid of their transmit diversity gain. More explicitly, STCs rely on transmitting multiple, redundant copies of a data stream to the receiver in the hope that at least some of them may arrive over the physical path between the transmitter and receiver unimpaired to allow reliable decoding. The fact that the transmitted data must traverse a potentially hostile propagation environment contaminated by scattering, reflection, refraction and by the thermal noise in the receiver implies that some of the received copies of the data will be more corrupted than others. More explicitly, space-time coding combines all the copies of the received signal in order to extract as much information from each of them as possible. Space time codes may be classified into two main types. Space-Time Trellis Codes (STTCs) [65] employ a trellis code for mapping the information to multiple antennas and multiple time-slots and hence to provide both coding gain and diversity gain. Space-Time Block Codes (STBCs) [67, 68, 70] act by encoding a short block of data at a time and provide only diversity gain. However, STBCs are less complex in implementation terms than STTCs. The aim of using spatial diversity is to provide both transmit as well as receive diversity and hence to enhance the system's integrity/robustness. This typically results in a

better physical-layer performance and hence a better network-layer performance. Therefore, STCs are capable of indirectly increasing not only the transmission integrity, but also the achievable spectral efficiency.

While STCs require multiple transmit antennas, it is not necessary to have multiple receive antennas, although they substantially improve the achievable performance. An STBC's action is usually represented by an encoding matrix, where each row of the matrix represents a time slot and each column corresponds to a specific antenna's transmissions over time. The code rate of an STBC quantifies how many symbols per time slot it transmits on average over the course of an STBC block. STBCs as originally proposed [67] were designed to be orthogonal, ensuring that the vectors representing any pair of columns taken from the coding matrix are orthogonal. The benefit of this is that simple linear decoding can be used at the receiver. Its most serious disadvantage is that all but one of the STBCs that satisfy this criterion must make a sacrifice in terms of their coding rate.

Alamouti invented the first STBC in 1998 [67]. It was designed for a two-transmit antenna system and has the coding matrix of

$$\mathbf{G}_2 = \begin{bmatrix} s_1 & s_2 \\ -s_2^* & s_1^* \end{bmatrix}, \tag{2.1}$$

where the superscript * denotes the complex conjugate of the variables. It is the only complex modulated orthogonal STBC that achieves a coding rate of unity. That is to say that it is the only STBC that can achieve its full diversity gain without having to make a sacrifice in terms of its coding rate. This property lends Alamouti's code a potential throughput advantage over the higher-order STBCs, even though they achieve a better error-rate performance. Stimulated by Alamouti's work, Tarokh *et al.* discovered a set of STBCs [68, 70] that are particularly beneficial and yet straightforward. The authors also showed that no STBC using more than two transmit antennas may achieve 'full-rate'. A quasi-orthogonal STBC was then proposed by Jafarkhani [72]. Although these codes exhibit partial orthogonality and hence provide only part of the maximum achievable diversity gain, their benefit is that they exhibit a unity rate. As a further advantage, they only require linear processing at the receiver, although their decoding is slightly more complex than that of Alamouti's [67] and Tarokh's [68, 70] orthogonal STBCs.

2.1.2 Space Division Multiplexing

The basic concept of Space Division Multiplexing (SDM) or spatial multiplexing is that several different data bits are transmitted via several independent spatial channels. It may be viewed as an improved-throughput point-to-point communication system requiring no frequency band expansion. The data streams can be separated by the space-time equalizer of the receiver.

Bell Laboratories Layered Space-Time (BLAST) scheme was developed by Foschini in 1996 [64]. It is an extraordinarily bandwidth-efficient approach to wireless communication, which takes advantage of the spatial dimension by transmitting and detecting a number of independent co-channel data streams using multiple, essentially co-located, antennas. The central philosophy of BLAST is the exploitation of the different Channel Impulse Responses (CIRs) encountered by the AEs imposed by their different multipath effects in order to achieve a high spectral efficiency (bits/sec/Hz), significantly higher than that, when multipath propagation is viewed as an adversary rather than an ally. Under the widely used theoretical assumption of having independent Rayleigh scattering, the theoretical capacity of the BLAST architecture grows roughly linearly with the number of antennas, even when the total transmitted power is fixed.

BLAST uses multi-element antennas at both the transmitter and receiver to support transmission rates far in excess of those possible using conventional approaches by treating the multiplicity of scattering paths as separate parallel diversity subchannels. BLAST accomplishes this by splitting a single user's data stream into multiple substreams and using an array of transmitter antennas to simultaneously launch the parallel substreams. Again, all the substreams are transmitted in the same frequency band, hence the spectrum is used very efficiently. Since the user's data is transmitted in parallel over multiple antennas, the effective transmission rate is increased roughly in proportion to the number of transmitter antennas used. At the receiver, again an array of antennas is used to pick up the multiple transmitted substreams and their scattered images. Each receive antenna 'sees' all of the transmitted substreams superimposed, not separately. However, if the multipath scattering is sufficiently rich, then the parallel substreams are all scattered slightly differently, since they originate from different transmit antennas that are located at different points in space. Using sophisticated signal processing, these slight differences in scattering allow the substreams to be identified and recovered. In effect, the unavoidable multipath is exploited to

support parallel streams and hence to improve the achievable data transmission rates. Thus, when using the BLAST technique, the more multipath, components can be resolved the better.

The diagonally-layered space-time architecture proposed in [64], now known as Diagonal BLAST or D-BLAST, utilizes an elegant diagonally layered coding structure in which the code blocks are dispersed diagonally across the space-time dimensions. A space-time layering scheme using four transmit antennas may be represented by a matrix, where each column represents a time slot and each row represents a specific antenna's transmissions over time, as seen below:

$$\begin{bmatrix} a_1 & b_1 & c_1 & d_1 & a_5 & b_5 & c_5 & d_5 & \cdots \\ 0 & a_2 & b_2 & c_2 & d_2 & a_6 & b_6 & c_6 & \cdots \\ 0 & 0 & a_3 & b_3 & c_3 & d_3 & a_7 & b_7 & \cdots \\ 0 & 0 & 0 & a_4 & b_4 & c_4 & d_4 & a_8 & \cdots \end{bmatrix},$$

where a_i is the ith symbol arriving from layer a. However, the diagonal approach suffers from certain implementation complexities, which make it inappropriate for low-complexity implementation. In [66, 71], a simplified version of BLAST known as Vertical BLAST or V-BLAST was described. The essential difference between D-BLAST and V-BLAST lies in their encoding process. In D-BLAST, redundancy is introduced between the substreams using a specific inter-substream block coding. The D-BLAST code blocks are organized by delaying each antenna's signal by one additional signalling interval for the sake of achieving diversity gains in both space and time. It is this particular space-time coding arrangement that equips D-BLAST with a higher spectral efficiency for a given number of transmitters and receivers than V-BLAST. In V-BLAST, however, the vector encoding process is simply a demultiplexing operation, followed by independent bit-to-symbol mapping of each substream. No inter-substream coding is required, although conventional channel coding may certainly be applied before the serial-to-parallel conversion block. Another BLAST structure which employs a serial-to-parallel block for generating multiple independent substreams and has a separate encoder for each layer is known as Horizontal BLAST (H-BLAST) [74]. The H-BLAST structure was not designed for achieving transmit diversity gain, because the symbols of different layers are uncorrelated. In [73], a BLAST architecture referred to as turbo-BLAST was devised. Similar to the D-BLAST, the turbo-BLAST scheme also has a space-time interleaver after the inter-substream channel encoders. However, the turbo-BLAST arrangement does not delay each

antenna's signal by one signalling interval, but transmits them simultaneously. This simplification decreases the achievable BER performance compared to that of the D-BLAST scheme, but it benefits from achieving a higher data throughput. The turbo-BLAST scheme employs both channel coding and space-time interleaving, hence it is capable of achieving both spatial diversity as well as a multiplexing gain.

2.1.3 Spatial Division Multiple Access

Another application of smart antennas is often referred to as Spatial Division Multiple Access (SDMA), in which different users transmit independent data through different multipath channels. The SDMA technique exploits these unique, user-specific 'spatial signatures' of the individual users for differentiating amongst them. In simple conceptual terms one could argue that both a conventional Code Division Multiple Access (CDMA) spreading code and the CIR affect the transmitted signal similarly - namely they are convolved with it. Hence, provided that the CIR is accurately estimated, it becomes known and certainly unique, although not orthogonal to the other CIRs. Nonetheless, it may be used for uniquely identifying users after channel estimation and hence for supporting several users within the same bandwidth. Provided that a powerful MUD is available, one can support even more users than the number of antennas. Hence this method directly enhances the achievable spectral efficiency.

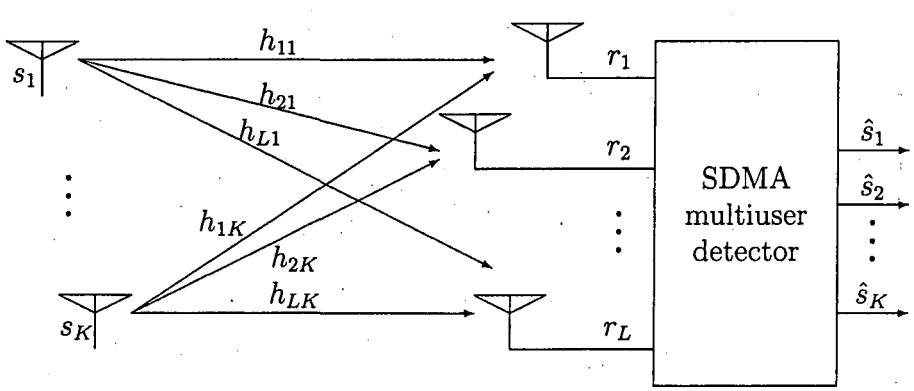

Figure 2.1: Signal flow graph for uplink SDMA system equipped with L receive AEs and supporting K users.

Figure 2.1 shows an uplink SDMA system equipped with L receive AEs and supporting K users. These K users are transmitting symbols $[s_1 \cdots s_K]^T$ at the same frequency, where the superscript ^{T} denotes the transpose. The original signals travel through the wireless channels and arrive at the receive antennas. When the signals pass through the channel, they will vary in both amplitude and phase depending on the multipath environment. The CIR h_{lk} in the diagram is a complex quantity or a complex vector representing the channel spanning from user k to the lth receive AE. Since the users and receive AEs are located at different positions, each of the complex-valued CIR coefficients should be uncorrelated with each other. The received signals $[r_1 \cdots r_L]^T$, then contain all components of the transmitted signals. To express the received signals in matrix form, we use the following equation

$$\begin{bmatrix} r_1 \\ r_2 \\ \vdots \\ r_L \end{bmatrix} = \begin{bmatrix} h_{11} & h_{12} & \cdots & h_{1K} \\ h_{21} & h_{22} & \cdots & h_{2K} \\ \vdots & \vdots & \ddots & \vdots \\ h_{L1} & h_{L2} & \cdots & h_{LK} \end{bmatrix} \times \begin{bmatrix} s_1 \\ s_2 \\ \vdots \\ s_K \end{bmatrix} + \begin{bmatrix} n_1 \\ n_2 \\ \vdots \\ n_L \end{bmatrix}, \tag{2.2}$$

where n_l is the additive noise at AE l. Then the received noisy signals are processed by the SDMA MUD, which exploits the unique CIR of each user to estimate the original symbols. Various linear and non-linear MUD algorithms can be used [6].

2.1.4 Beamforming

Beamforming is a signal processing technique designed for $\lambda/2$-spaced AEs either at the transmitters or at the receivers that controls the directionality of a radiation or reception pattern. When receiving a signal, beamforming can increase the gain in the direction of wanted signals and decrease the gain in the direction of interfering sources. When transmitting a signal, beamforming has the potential of increasing the gain in the direction of the desired user. This is achieved by creating beams and nulls in the radiation pattern. Beamforming can also be viewed as angular filtering, which is achieved by feeding the $\lambda/2$-spaced AEs with appropriately phased signals and hence creating their constructively or destructively phased superposition. In other words, when transmitting, a beamformer appropriately controls the amplitude and phase of the signal at each transmitter AE, in order to create a pattern of constructively and destructively phased inter-

ference in the wavefront. When receiving, the signal impinging on the different AEs is combined in such a way that the expected angular selectivity is observed.

Again, unlike in other smart antenna systems spacing the AEs as far as possible, in beamforming arrangements typically $\lambda/2$-spaced AEs are used for the sake of creating a spatially selective transmitter/receiver beam, where λ is the wavelength. Smart antennas using beamforming have widely been employed for mitigating the effects of interfering received signals and for providing a transmit beamforming gain. Furthermore, beamforming arrangement is capable of suppressing the effects of co-channel interference, which allows the system to support multiple users within the same bandwidth and/or same time-slot by separating them angularly. This angular separation, however, becomes only feasible, if the corresponding users are separable in terms of the Direction of Arrival (DOA) of their beams. These beamforming schemes, which employ appropriately phased antenna array elements that are spaced at distances of $\lambda/2$ typically result in an improved Signal-to-Interference-plus-Noise Ratio (SINR) distribution and hence in an enhanced network capacity [11].

The physical and mathematical description is essentially the same for both the transmitter and receiver beamformings, hence we will concentrate on receiver beamforming to explain the concept further. An example consisting of four signal sources and a three-element linear antenna array is shown in Figure 2.2. The DOAs of the sources are $\theta_1 = 45°$, $\theta_2 = 15°$, $\theta_3 = -30°$ and $\theta_4 = -70°$, respectively. Since the elements of the antenna array are quite close, we can assume that the CIR coefficients between the kth source and each of the receiver AEs is

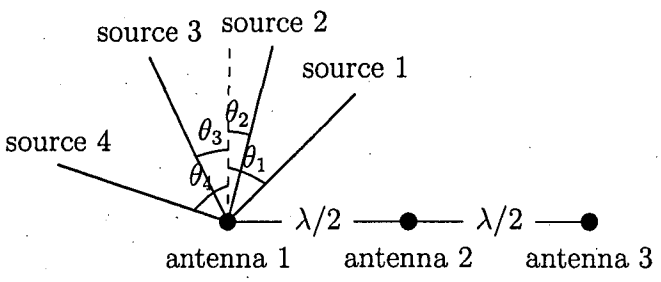

Figure 2.2: Geometric structure of beamforming consisting of four signal sources and a three-element linear antenna array. The DOAs of the sources are $\theta_1 = 45°$, $\theta_2 = 15°$, $\theta_3 = -30°$ and $\theta_4 = -70°$.

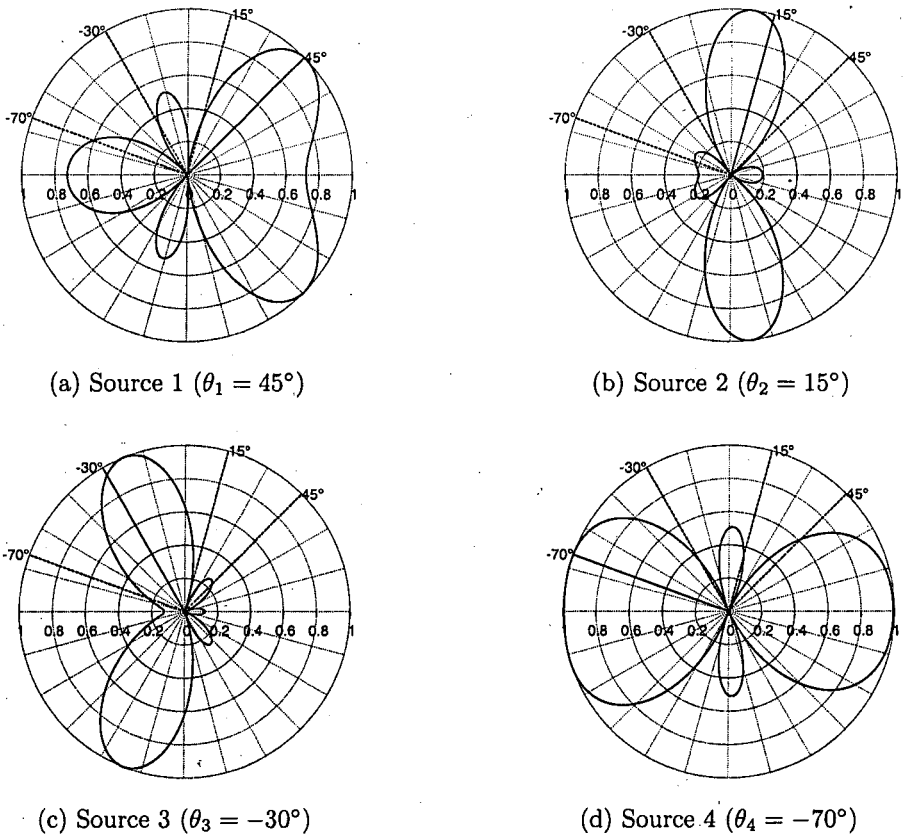

(a) Source 1 ($\theta_1 = 45°$)

(b) Source 2 ($\theta_2 = 15°$)

(c) Source 3 ($\theta_3 = -30°$)

(d) Source 4 ($\theta_4 = -70°$)

Figure 2.3: Beam patterns, when employing three AEs to support the four sources seen in Figure 2.2. The solid radial line indicates the direction of the desired source, and the dashed radial lines denote the interfering sources.

the same, which is denoted as h_k. Then the received signal can be expressed as

$$\begin{bmatrix} r_1 \\ r_2 \\ r_3 \end{bmatrix} = \begin{bmatrix} h_1 & h_2 & h_3 & h_4 \\ h_1 e^{j\pi \sin\theta_1} & h_2 e^{j\pi \sin\theta_2} & h_3 e^{j\pi \sin\theta_3} & h_4 e^{j\pi \sin\theta_4} \\ h_1 e^{j2\pi \sin\theta_1} & h_2 e^{j2\pi \sin\theta_2} & h_3 e^{j2\pi \sin\theta_3} & h_4 e^{j2\pi \sin\theta_4} \end{bmatrix} \times \begin{bmatrix} s_1 \\ s_2 \\ s_3 \\ s_4 \end{bmatrix} + \begin{bmatrix} n_1 \\ n_2 \\ n_3 \end{bmatrix}, \quad (2.3)$$

where n_l is the additive noise at AE l. Figure 2.3 shows the resultant beam patterns for all four sources after beamforming aided detection. The solid radial line indicates the direction of the desired source, and the dashed radial lines denote the interfering sources. It is clear that the beamformer creates its 'main beam' in the desired source's direction. At the same time, the beamformer creates a null in the other three directions, namely in those of the interfering sources. Hence the Signal-to-Interference Ratio (SIR) is increased at the output of the beamformer.

2.1.5 Multi-functional MIMOs

As we have seen in Sections 2.1.1–2.1.4, the benefits of multiple antenna aided systems are manifold, since they are capable of achieving increased bit rates with the aid of spatial multiplexing, or reduced error rates using spatial diversity, and of improving the SNR with the aid of adaptive antenna arrays. The basic smart antenna structures introduced above are summarized in Table 2.2. Each

Table 2.2: Benefits of different smart antenna structures

	Array gain	Diversity gain	Multiplexing gain	Interference reduction	Coding gain
STTC		✓			✓
STBC		✓			
D-BLAST		✓	✓		
V-BLAST			✓		
H-BLAST			✓		
SDMA				✓	
Beamforming	✓			✓	

structure exhibits different key advantages compared to the single-input single-output system. These differences inspire the combination of two or more smart antenna schemes, in order to create so called 'multi-functional MIMOs'. It was proposed in [69] to combine the benefits of STBCs and of V-BLAST techniques for the sake of providing both antenna diversity as well as spectral efficiency gains. This hybrid scheme was improved in [76] by optimizing the specific decoding order of the different antenna layers.

2.1.6 Distributed MIMOs

In space-time coding and spatial multiplexing techniques, it is typically assumed that the individual AEs are co-located, i.e. they belong to the same antenna array, and that their antenna spacing is sufficiently high in order to justify the assumption of having statistically independent links. In many practical scenarios, having a sufficiently high antenna spacing cannot be guaranteed, which results in correlation between the individual transmission links. Mobile terminals, for example, are typically characterized by a small size, where ensuring a sufficiently high separation of the AEs is difficult. However, even if no correlation is experienced between the transmission links, experiencing shadow fading may result in a

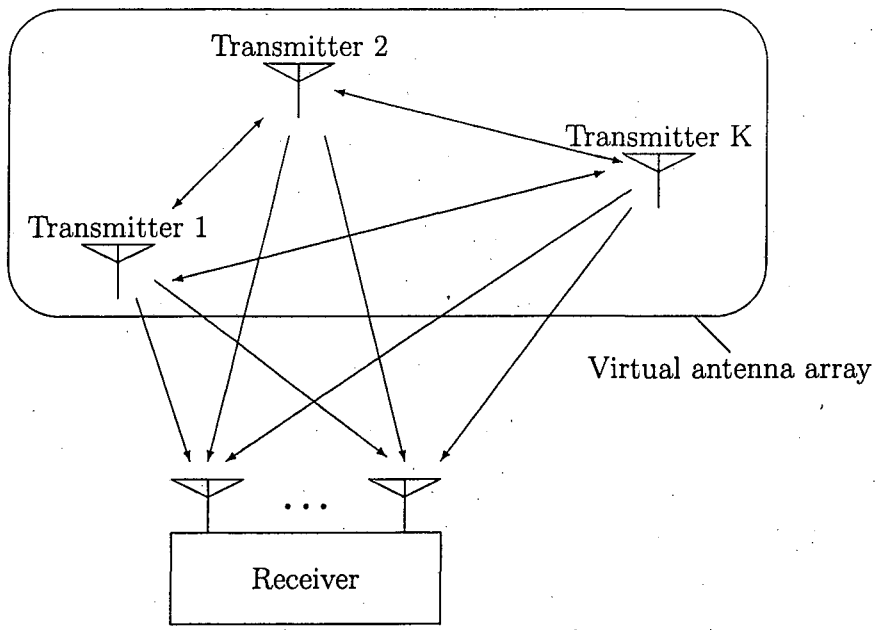

Figure 2.4: Distributed MIMO system with K-node VAA at the transmitter side.

poor SNR for all channel links. In this scenario, spatial diversity remains unable to improve the achievable BER performance.

In order to circumvent the limitations of wireless communications, new and unconventional concepts are required. An attractive idea that has recently gained considerable interest is the concept of cooperative wireless networks [78]. In such networks, multiple network nodes cooperate and share their antennas, for example by using a distributed space-time coding scheme (or a distributed diversity reception scheme). By this means, a Virtual Antenna Array (VAA) may be established, as seen in Figure 2.4. The cooperating nodes, possibly equipped with only a single antenna, can thus enjoy the benefits offered by conventional MIMO systems having co-located antennas. Cooperative wireless networks can be viewed as a mixture of hierarchical and ad-hoc networks [75]. Current wireless networks are typically characterized by an inflexible hierarchical structure, where communication is mainly controlled by a central network node, namely a BS. By allowing some cooperation between the individual network nodes, elements of an ad-hoc network may be introduced. Cooperation can, for example, be performed between multiple BSs having intersecting coverage areas. Another

example of cooperation between fixed network nodes are constituted by wireless sensors, where data measured by wireless sensors are collected by multiple distributed receiving nodes and are then processed in a joint fashion. Cooperation can also be performed between mobile terminals. An example of the latter is given by relay-assisted networks [77], where the mobile terminals mutually relay their transmitted or received signals.

2.2 Multiuser Detection

The philosophy of multiuser detection is based upon treating the signals generated by all simultaneous users as 'wanted' signals, which must be jointly detected at the receiver. Verdú's optimum MUD [79,80] uses a bank of matched filters followed by Viterbi's Maximum Likelihood (ML) sequence estimator [81] invoked for detecting the most likely data sequence. Although the optimum MUD exhibits a significant performance improvement over conventional single-user detectors, this is achieved at an enormous complexity. The sub-optimum MUDs can generally be divided into two main classes, namely adaptive and non-adaptive MUDs [6]. The latter class would normally require knowledge of some *a priori* information about the channel and the system itself. By contrast, adaptive MUDs would relax either all or some of the *a priori* information requirements of the non-adaptive MUDs. The non-adaptive MUD class can be further divided into linear and non-linear MUDs. In linear multiuser detection a linear mapping is applied to the soft outputs of the conventional matched filter detector in order to produce a new set of outputs. By contrast, in non-linear detection some form of Interference Cancellation (IC) is carried out, in order to cancel the Multiple Access Interference (MAI) imposed on each other. This typically achieves a better performance in comparison to linear MUDs.

The most well-known linear MIMO detector is the MMSE detector [6], which is discussed in detail in numerous text-books, such as [82,6]. It is well known that the MMSE detection approach is optimum in terms of minimising the MSE of a linear detector. However, a linear detector directly designed for achieving the lowest BER is optimum in terms of minimising the BER. Hence, the set of linear detectors, which achieve the minimum BER are referred to as MBER detectors. They have been studied for example in [29] by Chen *et al.* A simplified MBER detector has for example been proposed by Gesbert in [83] on the basis of a closed-

form expression for certain channel conditions. At the time of writing MBER detectors have mainly been proposed for BPSK signals as well as 4-level QAM signals. MBER detectors are challenging to derive for higher-order QAM, and this open problem was solved in [33] by Yeh and Barry, who have proposed a Minimum Symbol Error Rate (MSER) detector for high-order QAM. A generic framework for adaptive minimum error-probability filter design was reviewed in [84] by Chen *et al.*

In systems, where the number of transmit AEs is higher than the number of receive AEs, the linear detectors are often incapable of correctly detecting the desired signal and hence the family of non-linear detectors has to be employed. The optimum non-linear detector is the ML or Maximum *A Posteriori* Probability (MAP) detector, which is also often referred to as the Bayesian detector [85]. It was shown in [85] that the Bayesian detector achieves the lowest possible BER of all non-linear detectors. Another attractive non-linear MUD is the IC based MUD, classified into successive IC [86] and parallel IC [87]. In general, the signals transmitted by the various users in a communication system are channel coded. Instead of separating the signal processing operations of the demodulator from those of the decoder as in the IC algorithms, a better strategy is to use the soft-information metrics output by the channel decoder to enhance the suppression of the MAI at the demodulator with the aid of a turbo-style iterative detection algorithm [88,18]. It is widely recognized that the optimum MUD has a non-linear decision boundary [80] and that the employment of non-linear MUDs typically provides a better performance in comparison to linear MUDs. However, this performance improvement is achieved at an increased complexity.

Table 2.3 summarizes the history of MUD design.

Table 2.3: Selection of MUD papers

Author(s)	Contribution
[79] Verdú	Investigated the uncoded probability of error achievable by optimum ML MUDs for transmission over asynchronous Gaussian multiple-access channels.
[87] Varanasi and Aazhang	Proposed and analysed a multistage MAI mitigation scheme for coherent demodulation in an asynchronous CDMA system.

Author(s)	Contribution
[86] Patel and Holtzman	Analysed a simple SIC scheme for coherent and noncoherent modulation of Direct Sequence Code Division Multiple Access (DS-CDMA) systems, where the channel parameter estimation was carried out using the output of a linear correlator.
[88] Reed *et al.*	Introduced an iterative multiuser receiver for DS-CDMA employing forward error control coding. The receiver employed the MAP criterion for the multiuser received signal, but employed only single-user decoders.
[18] Wang and Poor	An iterative receiver structure was proposed for detecting multiuser information in a convolutionally coded asynchronous multipath DS-CDMA system. The receiver performs two successive soft-output decisions carried out by a SISO MUD and a bank of single-user SISO channel decoders with the aid of an iterative process.
[83] Gesbert	It was stated that minimum error-rate linear receivers have the potential of significantly outperforming MMSE receivers, but no simple direct method of designing minimum error-rate receivers exists. The author derived a closed-form approximate solution for this problem.
[40] Li and Wang	Based on the Extrinsic Information Transfer (EXIT) chart technique, the authors studied the mutual information transfer characteristics of SIC aided MUDs designed for coded CDMA systems operating in synchronous AWGN and asynchronous multipath fading channels.
[29] Chen *et al.*	An adaptive beamforming technique was proposed based on directly minimising the BER. This MBER approach adjusts the antenna array elements more intelligently than the standard MMSE approach.
[19] Tarable *et al.*	A structure based on a linear user separation technique was introduced and analysed, where the matched filter outputs were generated according to the MMSE criterion for the first few iterations, and then the MMSE filter was by-passed, when the interferers' bits became known with a sufficiently high probability.

Author(s)	Contribution
[89] Schober *et al.*	It was showed that for DS-CDMA using BPSK modulation transmission over complex baseband channels the real part of the Matched Filter (MF) output and not the MF output itself should be used as sufficient statistics for further processing. Based on this observation, the authors derived novel linear and decision-feedback aided MMSE receivers.
[30] Alias *et al.*	Invoked genetic algorithms for finding the optimum weight vectors of the MBER MUD in the context of multiple-antenna-aided multiuser OFDM.
[34] Chen *et al.*	A novel MSER design was proposed for a beamforming assisted receiver, where the system's SER was directly optimized for a QAM system.
[84] Chen *et al.*	Provided a genenic framework for adaptive minimum error-probability filter design suitable for the employment in a variety of communication systems. The advantages and disadvantages of the adaptive minimum error-probability filter design were analysed in comparison to the classic Wiener filter aided design.

2.2.1 System Model

The system considered consists of K uplink MSs employing a single-element transmit antenna and a BS receiver, which has L number of AEs. The symbol s_k of the kth MS is transmitted to the BS's lth AE over a narrowband channel characterized by the channel coefficients h_{lk}. The channel coefficient h_{lk} represents the complex-valued gain of the channel between MS k and the lth BS receiver AE. The output signal of the lth AE of the BS receiver can be written as

$$r_l = \sum_{k=1}^{K} h_{lk} s_k + n_l, \tag{2.4}$$

where n_l is the complex-valued AWGN having a variance of $\mathrm{E}\left[|n_l|^2\right] = 2\sigma_n^2$. Under the assumption of perfect synchronization, the channel's output is described by a $(L \times K)$-dimensional matrix $\mathbf{H} = [\mathbf{h}_1\ \mathbf{h}_2 \cdots \mathbf{h}_K]$, where the (l,k)th element of the

matrix is given by h_{lk}. The channel's output vector $\mathbf{r}$ can now be expressed as

$$\mathbf{r} = \mathbf{H}\mathbf{s} + \mathbf{n}, \tag{2.5}$$

where the column vector $\mathbf{s} = [s_1\ s_2 \cdots s_K]^T$ contains the symbols transmitted by the MSs and the associated AWGN is given by $\mathbf{n} = [n_1\ n_2 \cdots n_L]^T$.

In this thesis, we only discuss BPSK modulation, Quadrature Phase Shift Keying (QPSK) modulation and 16QAM modulation using Gray mapping. The constellation diagrams are shown in Figure 2.5, in which E_s denotes the average symbol energy.

The soft output estimated symbol vector $\hat{\mathbf{s}}$ of a linear MUD can be written as

$$\hat{\mathbf{s}} = \mathbf{W}^H\mathbf{r}, \tag{2.6}$$

where $\mathbf{W}$ represents a $(L\times K)$-element complex-valued MUD weight matrix and the superscript ^{H} denotes the Hermitian transpose. The different columns of $\mathbf{W}$ denoted as $\mathbf{w}_k$ are associated with the different transmitters' symbols. The hard detected bits are given by

BPSK:

$$\check{b}_k(1) = \mathrm{sgn}(\Re[\hat{s}_k]), \tag{2.7}$$

QPSK:

$$\check{b}_k(1) = \mathrm{sgn}(\Re[\hat{s}_k]), \tag{2.8a}$$
$$\check{b}_k(2) = \mathrm{sgn}(\Im[\hat{s}_k]), \tag{2.8b}$$

16QAM:

$$\check{b}_k(1) = \mathrm{sgn}(\Re[\hat{s}_k]), \tag{2.9a}$$
$$\check{b}_k(2) = \mathrm{sgn}\Big(\big|\Re[\hat{s}_k]\big| - \tfrac{2}{\sqrt{10}}E_s\Big), \tag{2.9b}$$
$$\check{b}_k(3) = \mathrm{sgn}(\Im[\hat{s}_k]), \tag{2.9c}$$
$$\check{b}_k(4) = \mathrm{sgn}\Big(\big|\Im[\hat{s}_k]\big| - \tfrac{2}{\sqrt{10}}E_s\Big), \tag{2.9d}$$

where $\check{b}_k(i)$ is the ith bit of the kth user's hard decision based symbol $\check{s}_k$, $\mathrm{sgn}(\cdot)$ is signum function, $|\cdot|$ represents the absolute value of a real number, $\Re[\cdot]$ denotes

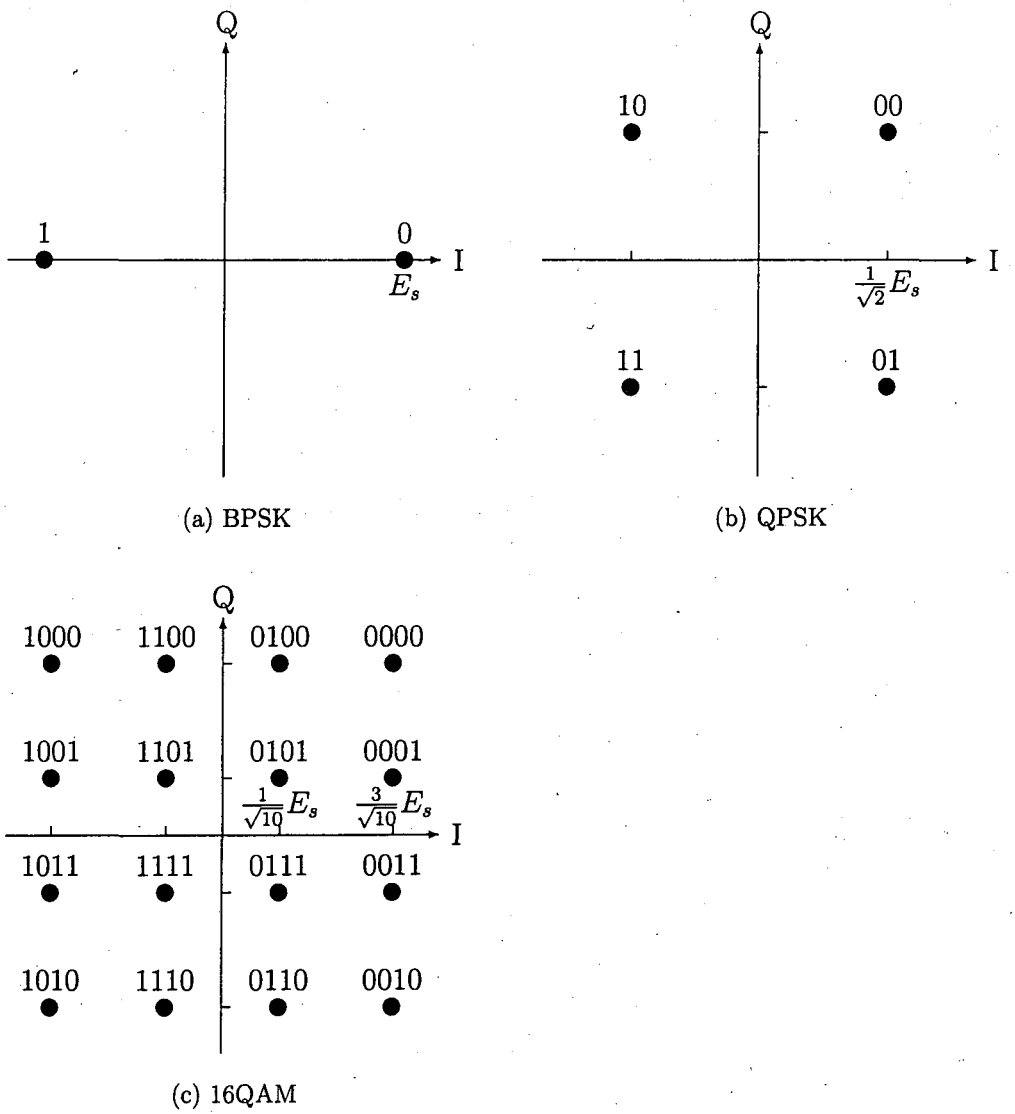

(a) BPSK

(b) QPSK

(c) 16QAM

Figure 2.5: Constellation diagrams of BPSK, QPSK and rectangular 16-QAM using Gray mapping. E_s denotes the average symbol energy.

the real part and $\Im[\cdot]$ denotes the imaginary part.

Let us now consider a two-user, single receive antenna aided system as an example for plotting the cost function surface of various multiuser detection algorithms. BPSK signals are transmitted over a narrowband non-dispersive channel and the CIR matrix of the two uplink users is given by $\mathbf{H} = [0.708 - j0.707,\ 0.997 - j0.083]$.

2.2.2 Bayesian Detection

We wish to design a signal detector that makes a decision concerning the kth user's transmitted signal s_k based on the observation of the vector $\mathbf{r}$, in order that the probability of a correct decision is maximized. With this goal in mind, we consider a decision rule based on the computation of the *a posteriori* probabilities defined as $P\big(s_k{=}s^{(m)}|\mathbf{r}\big)$, where $s^{(m)}$ is the mth symbol of the modulation constellation, $m \in \{1, 2, \cdots, M\}$, and M denotes the number of possible symbols in the modulation constellation. The decision criterion is based on selecting the signal corresponding to the maximum of the set of *a posteriori* probabilities:

$$\begin{aligned}\hat{s}_k &= \arg\max_{s^{(m)}} P\big(s_k{=}s^{(m)}|\mathbf{r}\big) \\ &= \arg\max_{s^{(m)}} \sum_{\substack{\forall \mathbf{s}^{(q)} \\ s_k^{(q)}=s^{(m)}}} P\big(\mathbf{s}^{(q)}|\mathbf{r}\big),\end{aligned} \tag{2.10}$$

where $\mathbf{s}^{(q)}$ is the qth possible transmitted signal combination of the K users, $q \in \{1, 2, \cdots, M^K\}$, and $s_k^{(q)}$ is the kth user's signal in this combination. This decision criterion is referred to as the Maximum *A Posteriori* Probability (MAP) criterion, which minimises the probability of error. Using Bayes' rule, the criterion may be expressed as

$$\begin{aligned}\hat{s}_k &= \arg\max_{s^{(m)}} \sum_{\substack{\forall \mathbf{s}^{(q)} \\ s_k^{(q)}=s^{(m)}}} \frac{P\big(\mathbf{r}|\mathbf{s}^{(q)}\big)P\big(\mathbf{s}^{(q)}\big)}{P(\mathbf{r})} \\ &= \arg\max_{s^{(m)}} \sum_{\substack{\forall \mathbf{s}^{(q)} \\ s_k^{(q)}=s^{(m)}}} P\big(\mathbf{r}|\mathbf{s}^{(q)}\big)P\big(\mathbf{s}^{(q)}\big),\end{aligned} \tag{2.11}$$

where $P\big(\mathbf{s}^{(q)}\big) = \prod_{k=1}^{K} P\big(\mathbf{s}_k^{(q)}\big)$ is the *a priori* probability of the qth possible signal combination being transmitted, and $P\big(\mathbf{r}|\mathbf{s}^{(q)}\big)$ is the conditional probability of the observed vector given $\mathbf{s}^{(q)}$, which can be expressed as

$$P\big(\mathbf{r}|\mathbf{s}^{(q)}\big) = \frac{1}{2\pi\sigma_n^2} \exp\left(-\frac{\big\|\mathbf{r} - \mathbf{H}\mathbf{s}^{(q)}\big\|^2}{2\sigma_n^2}\right). \tag{2.12}$$

Simplification of the MAP criterion becomes possible, when the transmitted signals are equally probable. Consequently, the decision rule based on find-

ing the signal that maximizes $P(\mathbf{s}^{(q)}|\mathbf{r})$ is equivalent to finding the signal that maximizes $P(\mathbf{r}|\mathbf{s}^{(q)})$. The conditional probability $P(\mathbf{r}|\mathbf{s}^{(q)})$ is usually referred to as the likelihood function, and the decision criterion based on the maximum of $P(\mathbf{r}|\mathbf{s}^{(q)})$ over all the possible transmitted signal combinations is called the Maximum Likelihood (ML) criterion, which now may be written as

$$\hat{s}_k = \arg\max_{s^{(m)}} \sum_{\substack{\forall \mathbf{s}^{(q)} \\ s_k^{(q)}=s^{(m)}}} P(\mathbf{r}|\mathbf{s}^{(q)}). \tag{2.13}$$

Let us now consider a BPSK system and define the signed ML decision function as

$$f_k(\mathbf{r}) = \sum_{\substack{\forall \mathbf{s}^{(q)} \\ s_k^{(q)}=+1}} P(\mathbf{r}|\mathbf{s}^{(q)}) - \sum_{\substack{\forall \mathbf{s}^{(q)} \\ s_k^{(q)}=-1}} P(\mathbf{r}|\mathbf{s}^{(q)}). \tag{2.14}$$

Then the corresponding decision rule can be written as

$$\hat{s}_k = \mathrm{sgn}\big(f_k(\mathbf{r})\big). \tag{2.15}$$

The bold line shown in Figure 2.6 indicates, how the ML detector formulates an optimum non-linear decision boundary. The surface illustrates the first user's channel-output for the specific channel setup defined in the last paragraph of Section 2.2.1 at E_b/N_0=10dB.

2.2.3 Minimum Mean Squared Error Detection

The Minimum Mean Squared Error (MMSE) MUD optimizes the kth user's weight vector $\mathbf{w}_k$ based on minimising the MSE between the actual transmitted symbol s_k and the soft output $\hat{s}_k$ of the MUD. The MSE criterion can be expressed as follows

$$\begin{aligned}
\xi_{MSE} &= \mathrm{E}\big[|s_k - \hat{s}_k|^2\big] \\
&= \mathrm{E}\Big[\big|s_k - \mathbf{w}_k^H\mathbf{r}\big|^2\Big] \\
&= \mathrm{E}[s_k s_k^*] - \mathbf{w}_k^H\mathrm{E}[s_k^*\mathbf{r}] - \mathbf{w}_k^T\mathrm{E}[s_k\mathbf{r}^*] + \mathbf{w}_k^H\mathrm{E}\big[\mathbf{r}\mathbf{r}^H\big]\mathbf{w}_k \\
&= E_s - \mathbf{w}_k^H\mathbf{H}\mathrm{E}[s_k^*\mathbf{s}] - \mathbf{w}_k^T\mathbf{H}^*\mathrm{E}[s_k\mathbf{s}^*] + \mathbf{w}_k^H\Big(\mathbf{H}\mathrm{E}\big[\mathbf{s}\mathbf{s}^H\big]\mathbf{H}^H + \mathrm{E}\big[\mathbf{n}\mathbf{n}^H\big]\Big)\mathbf{w}_k \\
&= E_s - E_s\mathbf{w}_k^H\mathbf{h}_k - E_s\mathbf{w}_k^T\mathbf{h}_k^* + \mathbf{w}_k^H\big(E_s\mathbf{H}\mathbf{H}^H + 2\sigma_n^2\mathbf{I}_L\big)\mathbf{w}_k,
\end{aligned} \tag{2.16}$$

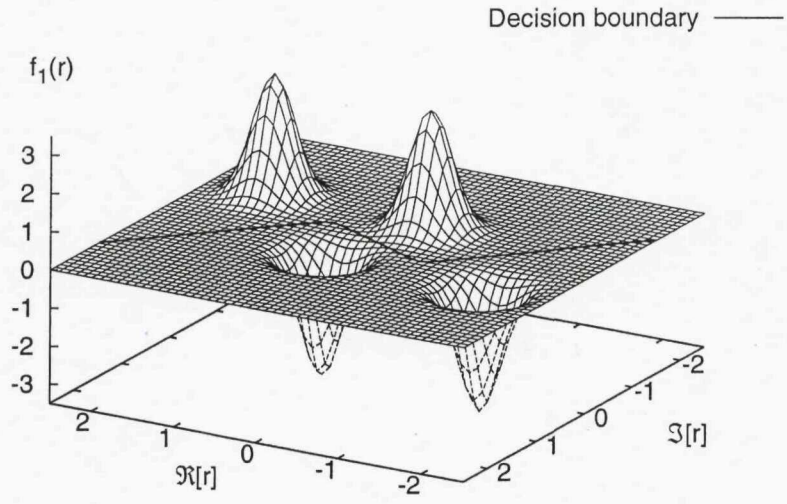

Figure 2.6: ML decision boundary (bold line) and the first user's channel-output (surface) for the specific channel setup defined in Section 2.2.1 at E_b/N_0=10dB.

where E[·] denotes the expected value, and $\mathbf{I}_L$ denotes the $(L\times L)$-element identity matrix.

The MMSE solution is now defined as

$$\mathbf{w}_k = \arg\min_{\mathbf{w}_k} \xi_{MSE}. \tag{2.17}$$

Figure 2.7 shows the MSE surface for the first user of our example introduced in the last paragraph of Section 2.2.1 at E_b/N_0=10dB as a function of the weight's real part $\Re[\mathbf{w}_1]$ and imaginary part $\Im[\mathbf{w}_1]$. The contours of the MSE surface are plotted on the base plate of Figure 2.7. We can see the typical quadratic shape of the cost function, which may be minimised by taking the derivate of Equation (2.16) and setting it to zero. The gradient of the MSE cost function is given by

$$\begin{aligned}\nabla\xi_{MSE} &= 2\frac{\partial\xi_{MSE}}{\partial\mathbf{w}_k^*} \\ &= -2E_s\mathbf{h}_k + 2\big(E_s\mathbf{H}\mathbf{H}^H + 2\sigma_n^2\mathbf{I}_L\big)\mathbf{w}_k.\end{aligned} \tag{2.18}$$

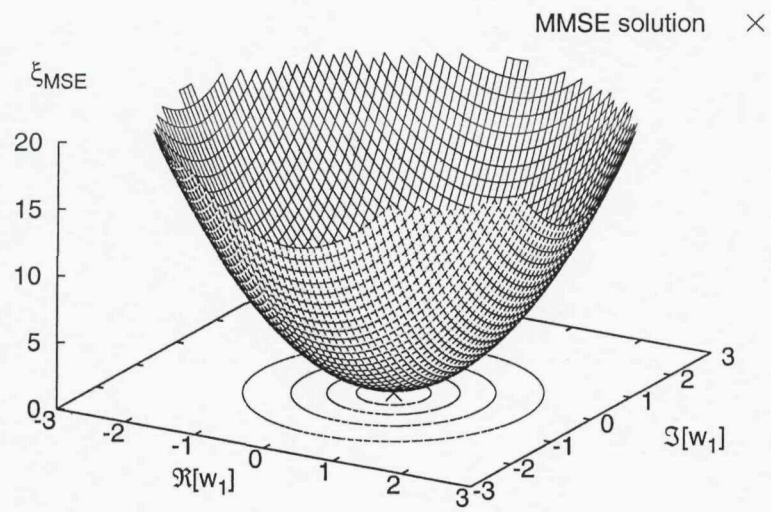

Figure 2.7: MSE cost function surface for the first user of our example introduced in Section 2.2.1 at E_b/N_0=10dB as a function of the weight's real part $\Re[\mathbf{w}_1]$ and imaginary part $\Im[\mathbf{w}_1]$.

By setting $\nabla\xi_{MSE} = 0$, the MMSE weight vector can be shown to be [6]

$$\mathbf{w}_k = \left(\mathbf{H}\mathbf{H}^H + \frac{2\sigma_n^2}{E_s}\mathbf{I}_L\right)^{-1}\mathbf{h}_k. \tag{2.19}$$

It is apparent that the MMSE weight vector attempts to reduce the effects of noise enhancement. Therefore the MMSE solution can be viewed as a striking compromise that takes into account the relative importance of each interfering user as well as of the background noise.

2.2.4 Real-valued Minimum Mean Squared Error Detection

For BPSK systems, the optimal MMSE receiver would only minimise the MSE between the transmitted signal and the real part of the MUD's output signal. Accordingly, the Real-valued Minimum Mean Squared Error (RMMSE) solution is introduced to avoid considering the imaginary part's minimisation. Let us

define the complex matrices' vertical stacking by the subscript $_c$. Then we have

$$\mathbf{M}_c = \begin{bmatrix} \Re[\mathbf{M}] \\ \Im[\mathbf{M}] \end{bmatrix}, \tag{2.20}$$

where $\mathbf{M}_c$ can be any matrix, which is vertically stacked. The real-valued MSE criterion may be expressed as

$$\begin{aligned} \xi_{RMSE} &= \mathrm{E}\big[(s_k - \Re[\hat{s}_k])^2\big] \\ &= \mathrm{E}\Big[\big(s_k - \mathbf{w}_{k,c}^T \mathbf{r}_c\big)^2\Big] \\ &= E_s - 2E_s \mathbf{w}_{k,c}^T \mathbf{h}_{k,c} + \mathbf{w}_{k,c}^T \big(E_s \mathbf{H}_c \mathbf{H}_c^T + \sigma_n^2 \mathbf{I}_{2L}\big)\mathbf{w}_{k,c}. \end{aligned} \tag{2.21}$$

Similarly to the MMSE solution, the RMMSE optimization problem can now be defined as

$$\mathbf{w}_{k,c} = \arg\min_{\mathbf{w}_{k,c}} \xi_{RMSE}. \tag{2.22}$$

Figure 2.8 shows the real-valued MSE surface for the first user of the example introduced in the last paragraph of Section 2.2.1 at E_b/N_0=10dB as a function of the weight's real part $\Re[\mathbf{w}_1]$ and imaginary part $\Im[\mathbf{w}_1]$. The contours of the real-valued MSE surface are plotted on the base plate of Figure 2.8. The minimum point on this surface can be found by setting the gradient of Equation (2.21) to zero. The gradient of ξ_{RMSE} is given by

$$\begin{aligned} \nabla \xi_{RMSE} &= \frac{\partial \xi_{RMSE}}{\partial \mathbf{w}_{k,c}} \\ &= -2E_s \mathbf{h}_{k,c} + 2\big(E_s \mathbf{H}_c \mathbf{H}_c^T + \sigma_n^2 \mathbf{I}_{2L}\big)\mathbf{w}_{k,c}. \end{aligned} \tag{2.23}$$

Setting the gradient to zero leads to the closed-form solution [89]

$$\mathbf{w}_{k,c} = \left(\mathbf{H}_c \mathbf{H}_c^T + \frac{\sigma_n^2}{E_s}\mathbf{I}_{2L}\right)^{-1} \mathbf{h}_{k,c}. \tag{2.24}$$

The first half of the elements in $\mathbf{w}_{k,c}$ are the real part of the RMMSE solution $\mathbf{w}_k$, while the second half of the elements form the imaginary part.

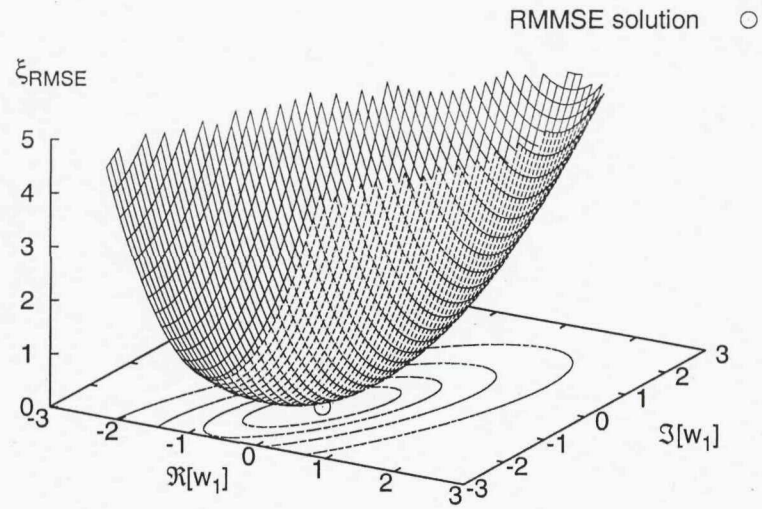

Figure 2.8: Real-valued MSE cost function surface for the first user of the example introduced in Section 2.2.1 at E_b/N_0=10dB as a function of the weight's real part $\Re[\mathbf{w}_1]$ and imaginary part $\Im[\mathbf{w}_1]$.

2.2.5 Minimum Bit Error Rate Detection

The MMSE algorithm is the most popular design strategy in the context of linear MUDs. However, a better strategy is to choose the linear MUD's coefficients so as to directly minimise the bit error probability or the BER, rather than the MSE. This is because minimising the MSE does not necessarily guarantee that the BER of the system is also minimised. The family of detectors that directly minimises the BER is referred to as the class of Minimum Bit Error Rate (MBER) detectors.

For BPSK systems, the BER encountered at the output of the MUD characterized by the combiner weight vector $\mathbf{w}_k$ of user k may be expressed as

$$Pe_b = P\big(\text{sgn}(\Re[s_k]) \cdot \Re[\hat{s}_k(\mathbf{w}_k)] < 0\big). \tag{2.25}$$

Define $x = \text{sgn}(\Re[s_k]) \cdot \Re[\hat{s}_k(\mathbf{w}_k)]$ as a signed decision variable. The PDF of x is constituted by a mixture of the Gaussian distribution associated with each possible combination of the transmitted data symbols of all users. Under the assumption that all the noise-free signal states are equiprobable, the PDF of x is

given by [29]

$$p(x) = \frac{1}{M^K\sqrt{2\pi}\sigma_n\sqrt{\mathbf{w}_k^H\mathbf{w}_k}}\sum_{q=1}^{M^K}\exp\left(-\frac{\left(x-\mathrm{sgn}\left(\Re\left[s_k^{(q)}\right]\right)\cdot\Re\left[\bar{s}_k^{(q)}\right]\right)^2}{2\sigma_n^2\mathbf{w}_k^H\mathbf{w}_k}\right), \quad (2.26)$$

where M^K is the number of equiprobable combinations of the binary vectors of the K users for M-*ary* PSK systems. Furthermore, $\bar{s}_k^{(q)} = \mathbf{w}_k^H\mathbf{H}\mathbf{s}^{(q)}$ denotes the noiseless signal at the output of the MUD related to the kth user, when the qth possible combination of the K users $\mathbf{s}^{(q)}$ is transmitted. The erroneous decision events are associated with the area under the PDF curve in the interval $(-\infty, 0)$, which is quantified as

$$\begin{aligned} Pe_b &= \int_{-\infty}^{0} p(x)dx \\ &= \frac{1}{M^K}\sum_{q=1}^{M^K}\mathrm{Q}\left(\frac{\mathrm{sgn}\left(\Re\left[s_k^{(q)}\right]\right)\cdot\Re\left[\bar{s}_k^{(q)}\right]}{\sigma_n\sqrt{\mathbf{w}_k^H\mathbf{w}_k}}\right). \end{aligned} \quad (2.27)$$

The MBER solution is defined as

$$\mathbf{w}_k = \arg\min_{\mathbf{w}_k} Pe_b. \quad (2.28)$$

In Figure 2.9 the BER surface is plotted as a function of the array weight coefficients for the example introduced in the last paragraph of Section 2.2.1 at E_b/N_0=10dB. The contours of the BER surface are plotted on the base plate of Figure 2.9. The different array weights of the MMSE, the RMMSE and the MBER solutions are also indicated. The corresponding BERs are distinctly different at a specific array weight value. Even when the optimum weight value is used for all three MUDs, the MBER solution has the lowest BER. As already mentioned above, the solution to this problem can be found by taking the derivate of Equation (2.27) and setting it to zero. From the expression of Equation (2.27), we know that the BER is independent of the magnitude of the MUD's weight vector, as also seen in Figure 2.9 indicated by the straight-line BER contours and the narrow trough near $\Re[w_1] = 0$, which has an infinite number of solutions along its spine. The gradient of Equation (2.27) may be expressed as [29]

$$\nabla Pe_b = 2\frac{\partial Pe_b}{\partial \mathbf{w}_k^*}$$

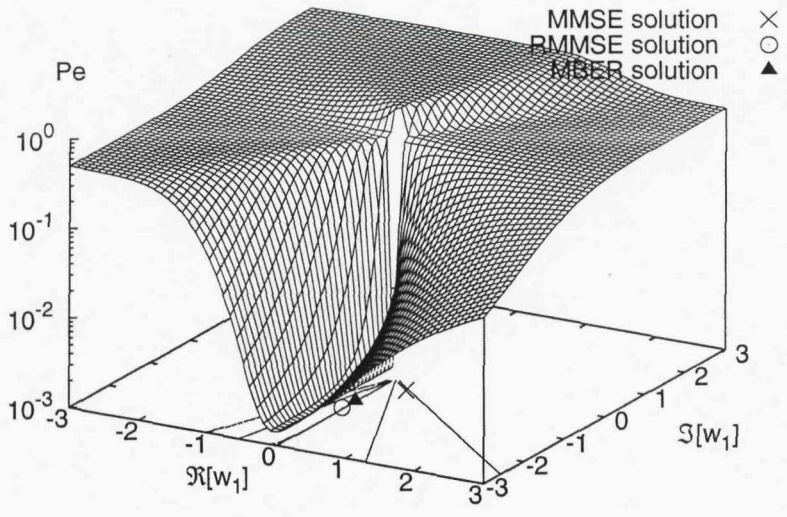

Figure 2.9: BER cost function surface for the first user of the example introduced in Section 2.2.1 at E_b/N_0=10dB as a function of the weight's real part $\Re[\mathbf{w}_1]$ and imaginary part $\Im[\mathbf{w}_1]$.

$$= \frac{1}{M^K\sqrt{2\pi}\sigma_n\sqrt{\mathbf{w}_k^H\mathbf{w}_k}} \sum_{q=1}^{M^K} \exp\left(-\frac{\left(\Re\left[\bar{s}_k^{(q)}\right]\right)^2}{2\sigma_n^2\mathbf{w}_k^H\mathbf{w}_k}\right) \cdot \operatorname{sgn}\left(\Re\left[s_k^{(q)}\right]\right)\left(\frac{\Re\left[\bar{s}_k^{(q)}\right]\mathbf{w}_k}{\mathbf{w}_k^H\mathbf{w}_k} - \mathbf{H}\mathbf{s}^{(q)}\right), \tag{2.29}$$

which is derived in Appendix A.1, when considering the absence of *a priori* information.

Equation (2.29) does not provide us with a closed-form solution for the MBER MUD weights. Therefore, an iterative strategy based on the steepest-descent gradient method can be used for finding the MBER solution. The steepest-descent gradient algorithm is summarized as follows

$$\begin{aligned}\mathbf{w}_k(i+1) &= \mathbf{w}_k(i) + \delta\mathbf{d}_k(i) \\ &= \mathbf{w}_k(i) - \delta\nabla Pe_b[\mathbf{w}_k(i)],\end{aligned} \tag{2.30}$$

where i is the iteration index, δ represents the step size and $\nabla Pe_b[\mathbf{w}_k(i)]$ is the gradient of the bit error probability during the ith iteration. According to this method the weight vector $\mathbf{w}_k$ of the linear MUD is updated iteratively, until the

specific weight vector that exhibits the lowest BER is arrived at. Unfortunately, the steepest-descent gradient algorithm may converge relatively slowly. In order to circumvent this convergence problem, we invoke the Simplified Conjugate Gradient (SCG) method [29], which uses a constant step size for all iterations comparing with the original conjugate gradient algorithm. This strategy chooses the vectorial direction of the current MUD weight vector update to be orthogonal to that of the previous update and improves the achievable convergence speed. The SCG algorithm operates as follows [90]:

Initialization: Set the iteration index i=1. Choose a step size δ>0 and a termination scalar β>0. Given $\mathbf{w}(1)$ and $\mathbf{d}(1) = -\nabla Pe_b[\mathbf{w}(1)]$, carry out:

Loop: If $\|\nabla Pe_b[\mathbf{w}(i)]\| < \beta$, goto **End**. Else

$$\mathbf{w}(i+1) = \mathbf{w}(i) + \delta\mathbf{d}(i), \tag{2.31}$$

$$\phi_i = \frac{\left\|\nabla Pe_b[\mathbf{w}(i+1)]\right\|^2}{\left\|\nabla Pe_b[\mathbf{w}(i)]\right\|^2}, \tag{2.32}$$

$$\mathbf{d}(i+1) = \phi_i\mathbf{d}(i) - \nabla Pe_b[\mathbf{w}(i+1)], \tag{2.33}$$

and $i = i + 1$. Goto **Loop**.

End: Weight vector $\mathbf{w}(i)$ is the chosen solution.

Figure 2.10 shows the iterative weight-update convergence process of the SCG algorithm, emerging from the MMSE solution and approaching the MBER solution.

For QPSK systems, we have in effect two binary phase-modulated signals in phase quadrature. Since there is no crosstalk or interference between the signals modulating the two quadrature carriers, the bit error probability can be expressed as

$$Pe_b = \tfrac{1}{2}(Pe_I + Pe_Q). \tag{2.34}$$

The gradient of the probability is

$$\nabla Pe_b = \tfrac{1}{2}(\nabla Pe_I + \nabla Pe_Q). \tag{2.35}$$

The in-phase error probability Pe_I and its gradient ∇Pe_I are the same as in Equations (2.27) and (2.29). The quadrature-phase error probability Pe_Q is sim-

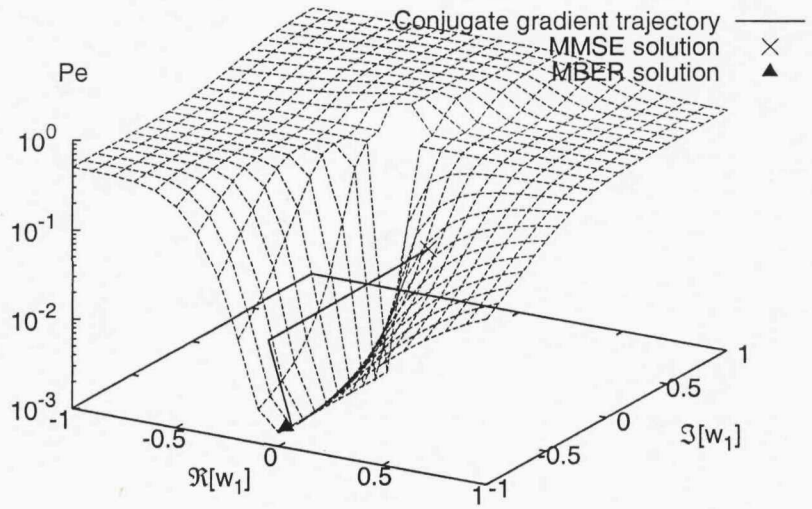

Figure 2.10: BER surface and the iterative weight-update trajectory of the SCG algorithm (polygonal line), emerging from the MMSE solution and approaching the MBER solution.

ilar to that in Equation (2.27), except for considering the imaginary-part of the desired symbol, which can be expressed as

$$Pe_Q = \frac{1}{M^K} \sum_{q=1}^{M^K} \mathrm{Q}\left(\frac{\mathrm{sgn}\left(\Im\left[s_k^{(q)}\right]\right) \cdot \Im\left[\bar{s}_k^{(q)}\right]}{\sigma_n \sqrt{\mathbf{w}_k^H \mathbf{w}_k}} \right). \tag{2.36}$$

Based on Appendix A.1, when considering the absence of *a priori* information, the gradient of Pe_Q can be expressed as

$$\begin{aligned} \nabla Pe_Q &= 2\frac{\partial Pe_Q}{\partial \mathbf{w}_k^*} \\ &= \frac{1}{M^K \sqrt{2\pi}\sigma_n \sqrt{\mathbf{w}_k^H \mathbf{w}_k}} \sum_{q=1}^{M^K} \exp\left(-\frac{\left(\Im\left[\bar{s}_k^{(q)}\right]\right)^2}{2\sigma_n^2 \mathbf{w}_k^H \mathbf{w}_k} \right) \\ &\quad \cdot \mathrm{sgn}\left(\Im\left[s_k^{(q)}\right]\right) \left(\frac{\Im\left[\bar{s}_k^{(q)}\right]\mathbf{w}_k}{\mathbf{w}_k^H \mathbf{w}_k} + j\mathbf{H}\mathbf{s}^{(q)} \right). \end{aligned} \tag{2.37}$$

2.2.6 Minimum Symbol Error Rate Detection

Since the MBER algorithm cannot be directly applied in high-order QAM systems, a Minimum Symbol Error Rate (MSER) algorithm has to be designed. Let us now consider an M-QAM system, and define the constellation symbol as $s^{(m,n)} = \frac{\sqrt{3E_s}}{\sqrt{2(M-1)}}\big(2m - \sqrt{M} - 1\big) + j\frac{\sqrt{3E_s}}{\sqrt{2(M-1)}}\big(2n - \sqrt{M} - 1\big)$, where we have $m \in \{1, 2, \cdots, \sqrt{M}\}$ and $n \in \{1, 2, \cdots, \sqrt{M}\}$. When the desired user k transmits symbol $s_k = s^{(m,n)}$, the conditional PDF of $\hat{s}_k$ is a mixture of Gaussian distributions, each of which is centered at the legitimate symbol position $\bar{s}_k^{(q)} = \mathbf{w}_k^H \mathbf{H}\mathbf{s}^{(q)} = \mathbf{w}_k^H\big(\mathbf{h}_k s^{(m,n)} + \sum_{k' \neq k} \mathbf{h}_{k'} s_{k'}^{(q)}\big)$. Then the conditional PDF is expressed as [34]

$$p(\hat{s}_k | s_k = s^{(m,n)}) = \frac{1}{M^{K-1} \cdot 2\pi\sigma_n^2 \mathbf{w}_k^H \mathbf{w}_k} \sum_{\substack{\forall \mathbf{s}^{(q)} \\ s_k^{(q)} = s^{(m,n)}}} \exp\left(- \frac{\big|\hat{s}_k - \bar{s}_k^{(q)}\big|^2}{2\sigma_n^2 \mathbf{w}_k^H \mathbf{w}_k} \right). \quad (2.38)$$

In general, $\mathbf{w}_k^H \mathbf{h}_k$ is complex-valued and the vector rotation operation of $\mathbf{w}_k^{new} = \frac{\mathbf{w}_k^H \mathbf{h}_k}{|\mathbf{w}_k^H \mathbf{h}_k|}\mathbf{w}_k$ can be used to ensure that $\mathbf{w}_k^H \mathbf{h}_k$ positive and real-valued. This vector rotation is a linear transformation and does not affect the system's SER [34]. By defining $b_i = \frac{\sqrt{3E_s}}{\sqrt{2(M-1)}}\big(2i - \sqrt{M}\big)$, $i \in \{1, 2, \cdots, \sqrt{M}-1\}$, the decision boundaries of $\hat{s}_k$ are determined by $b_i \mathbf{w}_k^H \mathbf{h}_k$ for the in-phase component and by $j b_i \mathbf{w}_k^H \mathbf{h}_k$ for the quadrature-phase component. Assuming that the kth user transmits symbol $s^{(m,n)}$, it may be readily seen that the points $\bar{s}_k^{(q)}$ conditioned on $s_k^{(q)} = s^{(m,n)}$ are distributed symmetrically around the symbol point $\mathbf{w}_k^H \mathbf{h}_k s^{(m,n)}$ [34]. Furthermore, when user k transmits an arbitrary legitimate symbol $s^{(m,n)}$, the conditional PDF of $p\big(\hat{s}_k | s_k = s^{(m,n)}\big)$ retains the same shape and remains in the same position with respect to the corresponding decision boundaries, which is referred to as the shifting property [34]. Then the conditional in-phase component error probability of the hard detected symbol $\Re[\check{s}_k] \neq \Re\big[s^{(m,n)}\big]$ can be shown to be

$$\begin{aligned} Pe_I = \frac{1}{M} \sum_{n=1}^{\sqrt{M}} \Bigg(& \int_{b_1 \mathbf{w}_k^H \mathbf{h}_k}^{+\infty} p\big(\hat{s}_k | s_k = s^{(1,n)}\big) d\Re[\hat{s}_k] \\ & + \sum_{m=2}^{\sqrt{M}-1} \Bigg(\int_{-\infty}^{b_{m-1} \mathbf{w}_k^H \mathbf{h}_k} p\big(\hat{s}_k | s_k = s^{(m,n)}\big) d\Re[\hat{s}_k] \\ & + \int_{b_m \mathbf{w}_k^H \mathbf{h}_k}^{+\infty} p\big(\hat{s}_k | s_k = s^{(m,n)}\big) d\Re[\hat{s}_k] \Bigg) \end{aligned}$$

$$+\int_{-\infty}^{b_{\sqrt{M}-1}\mathbf{w}_k^H\mathbf{h}_k} p\big(\hat{s}_k|s_k{=}s^{(\sqrt{M},n)}\big)\,d\Re[\hat{s}_k]\Bigg)$$
$$=\frac{2M-2\sqrt{M}}{M}\int_{b_1\mathbf{w}_k^H\mathbf{h}_k}^{+\infty} p\big(\hat{s}_k|s_k{=}s^{(1,n)}\big)\,d\Re[\hat{s}_k]$$
$$=\frac{2M-2\sqrt{M}}{M^K}\sum_{\substack{\forall\mathbf{s}^{(q)}\\ s_k^{(q)}=s^{(1,n)}}} \mathrm{Q}\left(\frac{b_1\mathbf{w}_k^H\mathbf{h}_k-\Re\big[\bar{s}_k^{(q)}\big]}{\sigma_n\sqrt{\mathbf{w}_k^H\mathbf{w}_k}}\right). \tag{2.39a}$$

Similarly, the conditional quadrature-phase component error probability of the hard detected symbol $\Im[\check{s}_k]\neq\Im\big[s^{(m,n)}\big]$ can be shown to be

$$Pe_Q=\frac{2M-2\sqrt{M}}{M^K}\sum_{\substack{\forall\mathbf{s}^{(q)}\\ s_k^{(q)}=s^{(m,1)}}} \mathrm{Q}\left(\frac{b_1\mathbf{w}_k^H\mathbf{h}_k-\Im\big[\bar{s}_k^{(q)}\big]}{\sigma_n\sqrt{\mathbf{w}_k^H\mathbf{w}_k}}\right). \tag{2.39b}$$

Then the resultant symbol error rate is given by

$$Pe_s=Pe_I+Pe_Q-Pe_I\cdot Pe_Q. \tag{2.40}$$

The resultant MSER solution is defined as the one that minimises the upper bound of the SER given by

$$\begin{aligned}\mathbf{w}_k&=\arg\min_{\mathbf{w}_k} Pe_{sB}\\ &=\arg\min_{\mathbf{w}_k}(Pe_I+Pe_Q).\end{aligned} \tag{2.41}$$

The upper bound Pe_{sB} is very tight, i.e. very close to the true SER Pe_s since $Pe_I\cdot Pe_Q$ is typically small [34].

In order to arrive at the optimum weights for the MSER solution by using the SCG method, we need the gradient of Pe_{sB}

$$\nabla Pe_{sB}=\nabla Pe_I+\nabla Pe_Q, \tag{2.42}$$

where based on Appendix A.2 and in the absence of *a priori* information, ∇Pe_I and ∇Pe_Q can be expressed as

$$\nabla Pe_I=2\frac{\partial Pe_I}{\partial\mathbf{w}_k^*}$$

$$= \frac{2M - 2\sqrt{M}}{M^K \sqrt{2\pi}\sigma_n \sqrt{\mathbf{w}_k^H \mathbf{w}_k}} \sum_{\substack{\forall \mathbf{s}^{(q)} \\ s_k^{(q)} = s^{(1,n)}}} \exp\left(- \frac{\left(b_1 \mathbf{w}_k^H \mathbf{h}_k - \Re\left[\bar{s}_k^{(q)}\right]\right)^2}{2\sigma_n^2 \mathbf{w}_k^H \mathbf{w}_k} \right)$$
$$\cdot \left(\frac{\left(b_1 \mathbf{w}_k^H \mathbf{h}_k - \Re\left[\bar{s}_k^{(q)}\right]\right)\mathbf{w}_k}{\mathbf{w}_k^H \mathbf{w}_k} + \mathbf{H}\mathbf{s}^{(q)} - b_1 \mathbf{h}_k \right) \quad (2.43a)$$

and

$$\nabla Pe_Q = 2\frac{\partial Pe_Q}{\partial \mathbf{w}_k^*}$$
$$= \frac{2M - 2\sqrt{M}}{M^K \sqrt{2\pi}\sigma_n \sqrt{\mathbf{w}_k^H \mathbf{w}_k}} \sum_{\substack{\forall \mathbf{s}^{(q)} \\ s_k^{(q)} = s^{(m,1)}}} \exp\left(- \frac{\left(b_1 \mathbf{w}_k^H \mathbf{h}_k - \Im\left[\bar{s}_k^{(q)}\right]\right)^2}{2\sigma_n^2 \mathbf{w}_k^H \mathbf{w}_k} \right)$$
$$\cdot \left(\frac{\left(b_1 \mathbf{w}_k^H \mathbf{h}_k - \Im\left[\bar{s}_k^{(q)}\right]\right)\mathbf{w}_k}{\mathbf{w}_k^H \mathbf{w}_k} - j\mathbf{H}\mathbf{s}^{(q)} - b_1 \mathbf{h}_k \right). \quad (2.43b)$$

2.2.7 Interference Cancellation Aided Detection

In addition to linear detection schemes, researchers have also proposed nonlinear detectors that cancel the interferers' signals from the composite multiuser signal to detect that of the desired user. More explicitly, the Interference Cancellation (IC) based MUDs attempt to remove the MAI by reconstructing the original transmitted signals of one or several users and cancel the interference imposed by these reconstructed signals on the composite received signal. The resultant signal is then processed iteratively for removing the effects of all users, invoking the same procedure, in order to obtain the data estimates for the remaining users, until all the users' signals are detected. The IC aided detectors include two classes: the family of successive IC [86] and the parallel IC techniques [87].

The successive IC assisted MUDs [86] adopt a serial approach to canceling the effects of interference. Each stage of the successive IC MUD makes a decision, regenerates and cancels the effects of the modulated signal of one user from the composite received signal. Intuitively, the process commences by removing the effects of the strongest signal, since it has the most detrimental effect on the remaining users and can be most reliably demodulated. More explicitly, the successive IC MUD is susceptible to the initial estimation error and the strongest signal can provide the most reliable data estimates for initiating the process.

Thus, the successive IC aided MUD requires sorting all the users in descending order according to their received signal powers and then successively eliminates the effect of the strongest signals, until all users' data are detected. Paradoxically, successive IC detectors perform most reliably, when the interference is strong relative to the desired signal, i.e. when there is a significant power difference between the users' signals. By contrast, the successive IC MUD's performance is poor, when the power levels are similar. Naturally, the received signals have to be sorted according to their power correctly, and further signal reordering is required, whenever the power profile changes. This will be a particular risk in a high capacity system having widely varying power levels. Finally, serial cancellation of the users' signals one by one will lead to a relatively high complexity.

As opposed to the above-mentioned successive IC technique, the parallel IC based MUD [87] estimates and subtracts all the MAI for each user simultaneously. It usually consists of multiple stages of IC, so the parallel IC MUD is also often referred to as multistage IC. In each cancellation stage, the signal of each user is reconstructed using the data estimates generated during the previous cancellation stage. Then, for each user, the reconstructed signals of all other users are subtracted from the composite received signal and the resultant signal is processed by a MF, in order to obtain a new set of data estimates for this user. The number of parallel IC stages is determined by the tolerable detection complexity that the system can afford. The iterative parallel IC can be repeated the affordable number of times, in order to achieve the best possible performance. Hence parallel IC detection has been regarded as one of the most promising MUD techniques. In an accurately power-controlled, equal-power scenario the classic parallel IC scheme tends to perform better than the successive IC scheme. A straightforward enhancement of the parallel IC detection is to use soft decisions rather than hard decisions in each iteration, except for the last one.

2.2.8 Computational Complexity of MUD Schemes

For the sake of fair comparisons of the MUD algorithms, the number of real-valued operations is used as the unit of complexity, and the complexities imposed by a real-valued multiplication and a real-valued addition might be considered equivalent. A single complex-valued addition's complexity is equivalent to that of two real-valued operations, and a complex-valued multiplication's complexity is equivalent to that of six real-valued operations. The computational complexity

of a $(N \times N)$-element complex-valued matrix inversion is on the order of $8N^3$ real-valued operations, denoted by $\mathcal{O}(8N^3)$.

The comparison of the different MUD schemes' computational complexity is summarized in Table 2.4 when considering the detection of single transmitted symbol. The optimum Bayesian detector has the computational complexity of $\mathcal{O}(LM^K)$, which increases exponentially with the number of users K. The MBER and MSER detectors have similar complexities of $\mathcal{O}(N_{cg}LM^K)$, where N_{cg} denotes the number of iterations in the SCG algorithm. It is clear that the computational complexity of the MBER and MSER MUDs is about N_{cg} times higher than that of the Bayesian MUD. The high computationally complexity associated with determining the MBER or MSER weights is owing to the fact that the number of legitimate channel output states is proportional to $\mathcal{O}(M^K)$ and thus grows exponentially with the number of transmit AEs. However, the complexities seen in Table 2.4 were obtained under an assumption of rapid fading environments. For a slowly fading channel scenario, the complexity of all linear MUD algorithms will be significantly lower than the corresponding complexity in the table, because the weights calculated already can be reused, when the channels are considered time-invariant.

Table 2.4: Comparison of computational complexity per symbol of different MUD schemes

MUD	Computational complexity	Equation(s)
Bayesian	$\left(8L+3+\frac{7L+2}{K}\right)M^K - M$	(2.12), (2.14)
MMSE	$\mathcal{O}\left(\frac{8L^3}{K}\right) + 16L^2 - \frac{2L^2}{K} + 6L + \frac{L}{K} - 2$	(2.19)
RMMSE	$\mathcal{O}\left(\frac{8L^3}{K}\right) + 16L^2 - \frac{4L^2}{K} + 2L + \frac{2L}{K} - 1$	(2.24)
MBER	$\left(\left((4L+2)\log_2 M + 8L - 2\right)N_{cg} + 8L - \frac{2L}{K}\right)M^K +$ $(18L+5)N_{cg} + 8L - 2$	(2.28), (2.29), (2.37)
MSER	$\left(\left(\frac{20L+10}{\sqrt{M}} + 8L - 2\right)N_{cg} + 8L - \frac{2L}{K}\right)M^K + (24L +$ $11)N_{cg} + 8L - 2$	(2.41), (2.43)

2.2.9 Performance of MUD Schemes

Let us now consider a receiver beamforming scheme employing a three-element antenna array. All users have the same transmit power as well as channel coef-

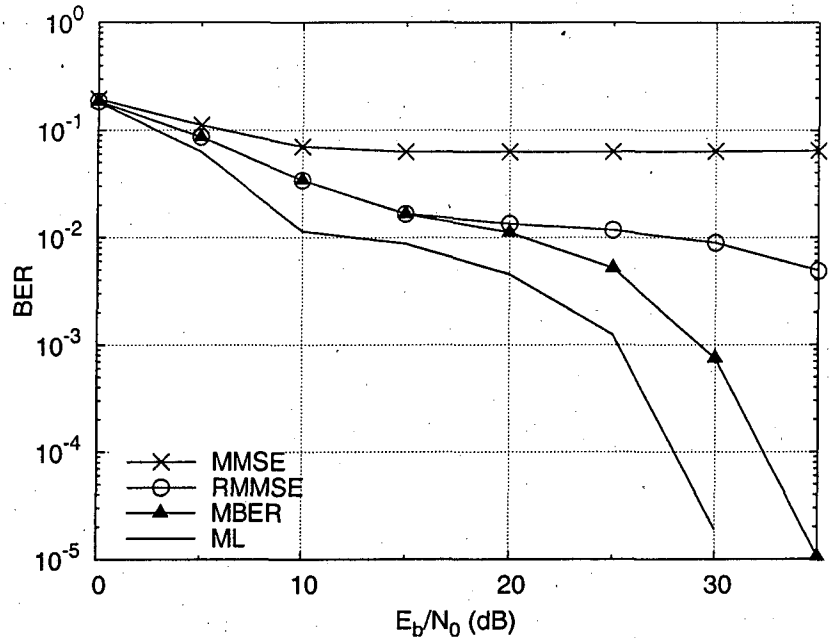

Figure 2.11: BER versus E_b/N_0 performance of the ML, MMSE, RMMSE and MBER beamformers employing L=3 receive AEs for supporting K=6 BPSK users communicating over AWGN channels. The DOAs of the desired user and the other interference users are seen in Figure 2.12.

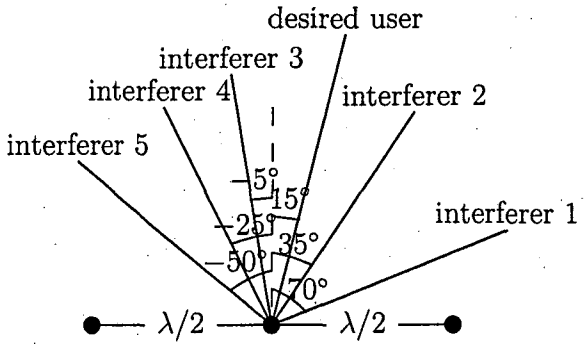

Figure 2.12: Three AEs, where the signal of the desired user arrives from 15°, while the interfering signals from 70°, 35°, −5°, −25° and −50°.

ficients of $h_k = 1.0+j0.0$ ($k \in \{1, \cdots, K\}$). Figure 2.11 shows the BER versus E_b/N_0 performance of our BPSK system supporting K=6 users. The DOA of the desired user is 15°, and the DOAs of the other interference users are 70°, 35°, −5°, −25° and −50°, respectively, as seen in Figure 2.12. It can be observed that the ML receiver exhibits a significantly better performance than the linear detectors. For BPSK modulated signals, the MBER detector clearly outperforms

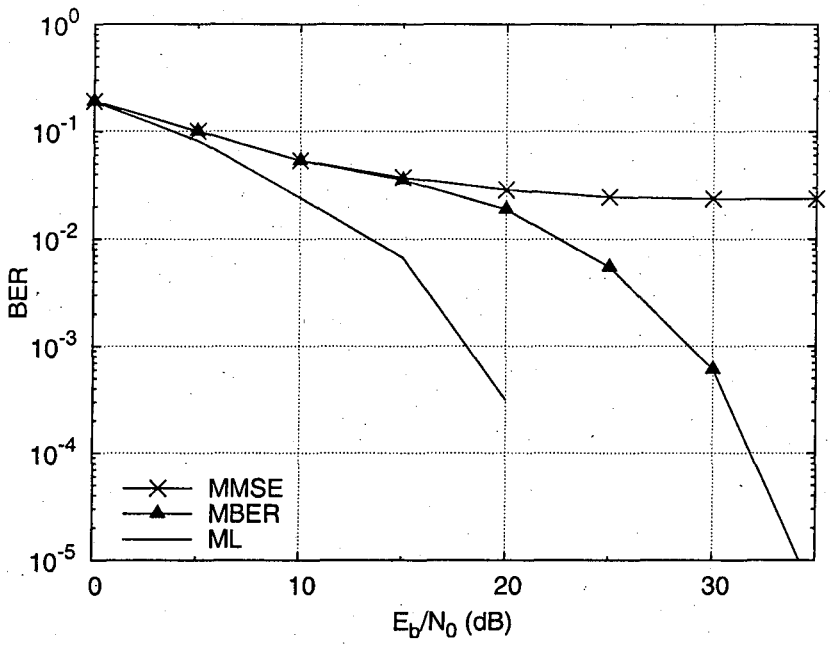

Figure 2.13: BER versus E_b/N_0 performance of the ML, MMSE and MBER beamformers employing L=3 receive AEs for supporting K=4 QPSK users communicating over AWGN channels. The DOAs of the desired user and the other interference users are seen in Figure 2.14.

the MMSE detector. This is mainly due-to the fact that the MBER detector only optimizes the real-part of the filter's output, whereas the MMSE algorithm minimises the MSE composed of both the real and the imaginary part of the filter output. The RMMSE detector performs similarly to the MBER detector, when the E_b/N_0 value is lower than 20dB. However, in the high-SNR region the RMMSE detector cannot match the performance of the MBER detector, since the residual interference plus noise is non-Gaussian distributed [83].

The BER versus E_b/N_0 performance of the QPSK system supporting K=4 users is shown in Figure 2.13. The DOA of the desired user is also 15°, and the DOAs of the other interference users are 45°, $-20°$ and $-50°$, respectively, as seen in Figure 2.14. In this QPSK case, the ML detector still has the best performance. The MBER detector outperforms the MMSE algorithm at high SNRs. This performance difference indicates that the MMSE algorithm is incapable of optimally separating the linearly separable data sets owing to its MSE-based optimization function, whereas the MBER algorithm achieves this goal.

Figure 2.15 shows the SER versus E_b/N_0 performance of a 16QAM modulated system supporting K=4 users. The DOA of the desired user is 15°, and the

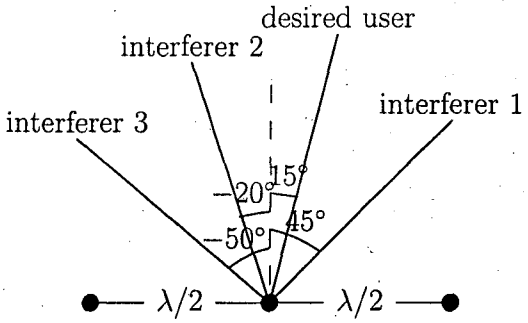

Figure 2.14: Three AEs, where the signal of the desired user arrives from 15°, while the interfering signals from 45°, −20° and −50°.

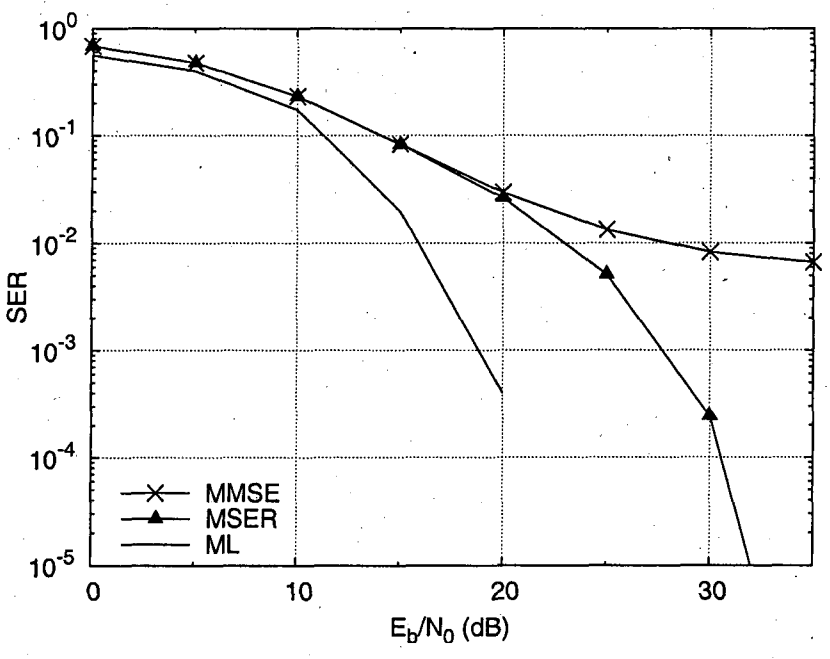

Figure 2.15: SER versus E_b/N_0 performance of the ML, MMSE and MSER beamformers employing L=3 receive AEs for supporting K=4 16QAM users communicating over AWGN channels. The DOAs of the desired user and the other interference users are seen in Figure 2.16.

DOAs of the interfering users are −12°, −43° and −57°, respectively, as seen in Figure 2.16. For this example, the MSER beamformer achieved a significantly better performance than the MMSE beamformer at high SNRs. We should be aware that if the data sets conditioned on the desired user's transmitted symbol are not linearly separable, both the MMSE and the MBER algorithms will have a similarly poor performance.

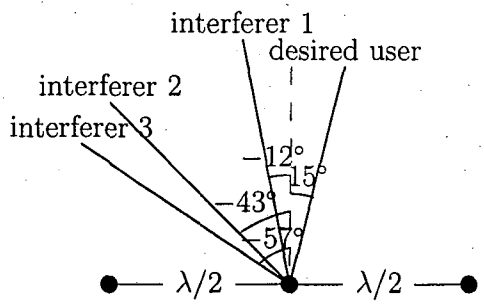

Figure 2.16: Three AEs, where the signal of the desired user arrives from 15°, while the interfering signals from −12°, −43° and −57°.

2.3 Conclusions

In this chapter different MIMO structures, namely the STCs of Section 2.1.1, the spatial multiplexing of Section 2.1.2, the SDMA of Section 2.1.3, the beamforming of Section 2.1.4 as well as the multi-functional MIMOs of Section 2.1.5 and the distributed MIMOs of Section 2.1.6 have been introduced. Different smart antenna architectures provide different benefits, such as array gain, diversity gain, multiplexing gain, interference reduction and coding gain. The advantages of the basic smart antenna structures compared to single-input single-output systems were summarized in Table 2.2.

In Section 2.2, we introduced various MIMO multiuser detection algorithms. The non-linear Bayesian detector of Section 2.2.2 constitutes the optimum non-linear receiver, which significantly outperforms all linear MUDs. The RMMSE MUD of Section 2.2.4 designed for BPSK systems considers only the real-part of the signal, hence it is capable of achieving a better performance than the conventional MMSE MUD of Section 2.2.3. The MBER MUD of Section 2.2.5 and the MSER MUD of Section 2.2.6 both constitute the optimum linear multiuser detection algorithms, where the former was designed for BPSK and QPSK schemes, while the latter for higher-order QAM schemes. The MBER and MSER algorithms minimise the BER or SER directly at the output of the MUDs and hence are capable of outperforming the MMSE and RMMSE MUDs at the cost of a higher complexity. Furthermore, we also introduced IC based MUDs in Section 2.2.7.

The detailed performance and computational complexity of the methods men-

tioned above are summarized in Table 2.5. The system uses the parameters of Section 2.2.9, depending on the modulation scheme used. It can be seen in Table 2.5 that the Bayesian detector outperforms other MUDs as a benefit of its non-linear decision characteristic. The MMSE MUD has the lowest computational complexity. The RMMSE algorithm designed for BPSK systems is capable of achieving a better performance than that of the MMSE MUD at the cost of a similar complexity. Furthermore, the optimum linear MBER and MSER detectors significantly outperform the MMSE and RMMSE methods. Although the MBER and MSER MUDs cannot achieve a performance similar to that of the Bayesian MUD, they impose a lower computational complexity, when communicating over block-fading channels.

Table 2.5: Performance and complexity summary of MUD schemes

MUD	Section	Complexity	Modulation	SNR at a BER of 10^{-3}
Bayesian	2.2.2	$\mathcal{O}\left(LM^K\right)$	BPSK	25.5dB
			QPSK	18dB
			16QAM	18.5dB
MMSE	2.2.3	$\mathcal{O}\left(\frac{L^3}{K}\right)$	BPSK	unachievable
			QPSK	unachievable
			16QAM	unachievable
RMMSE	2.2.4	$\mathcal{O}\left(\frac{L^3}{K}\right)$	BPSK	40dB
MBER	2.2.5	$\mathcal{O}\left(LN_{cg}M^K\right)$	BPSK	29dB
			QPSK	29dB
MSER	2.2.6	$\mathcal{O}\left(LN_{cg}M^K\right)$	16QAM	27.5dB

Chapter 3

Iterative Beamforming Receiver

In this chapter, multiuser detection and channel decoding are combined in order to improve the achievable multiuser beamforming receiver's performance, following the 'turbo detection principle'. The soft output of the channel decoder is fed back to the beamformer's input to improve the achievable multiuser detection performance. In return this improvement then benefits the decoder. The resultant iterative multiuser receiver is designed based on the soft parallel IC algorithm and the MBER algorithm, not the conventional MMSE algorithm. Based on the EXIT chart technique [36], we analyse the achievable performance and the convergence behaviour of different joint detection schemes, both of which are highly dependent upon the different system parameters and channel conditions. The EXIT chart analysis is shown to be valid for the MBER MUD[1], despite the non-Gaussian distribution of its output.

Iterative processing was introduced by Berrou in [12] in the context of iteratively decoding two parallel concatenated convolutional codes referred to as a turbo-code. His work has later been extended to serially concatenated codes [91] and then found its way gradually into iterative detector designs, such as for example iterative equalizers [92, 15, 16] or iterative multi-user detectors [18, 19]. In this section we propose a novel iterative beamforming receiver. The MBER beamforming design is optimal in terms of the BER and hence it generally outperforms the MMSE and the RMMSE solutions at the cost of a higher complexity. EXIT charts [36] can be used to analyse the convergence behaviour of an iterative MBER

[1]This treatise deals with the design of beamformers, where typically only the desired user's signal is detected. However, the same detection procedure may be applied for all the users and hence we will employ the more general terminology of MUD.

multiuser detection scheme as a function of the system parameters and channel conditions.

3.1 System Description

3.1.1 Signal Model

The system supports K users and each user transmits his/her signal on the same carrier angular frequency of $\omega = 2\pi f$. The receiver is equipped with a linear antenna array consisting of L elements, which have a uniform element spacing of $\lambda/2$, as shown in Figure 3.1, where λ is the wavelength.

Assume that the channel is non-dispersive in both the angular domain as well as in the time domain and hence does not induce Intersymbol Interference (ISI). Then the symbol-rate received signal samples can be expressed as

$$r_l(n) = \sum_{k=1}^{K} h_k s_k(n) e^{j\omega t_l(\theta_k)} + n_l(n) \tag{3.1}$$

where $l \in \{1, 2, \cdots, L\}$, h_k is the non-dispersive complex-valued channel coefficient of user k, $s_k(n)$ is the nth symbol of the kth user, $n_l(n)$ is a complex-valued Gaussian white noise process associated with $E\left[|n_l(n)|^2\right] = 2\sigma_n^2$, and

$$t_l(\theta_k) = \frac{\lambda}{2c}(l-1)\sin(\theta_k)$$

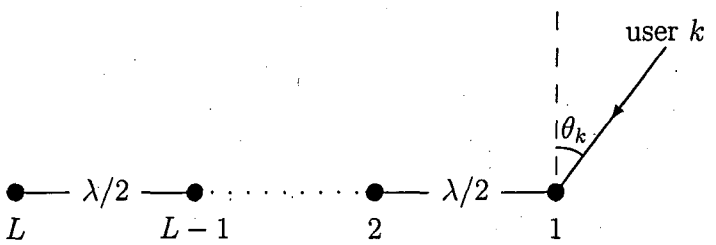

Figure 3.1: Geometric structure of the antenna array consisting of L elements showing the received signal of user k, where θ_k is the LOS component's angle of arrival.

$$= \frac{\pi}{\omega}(l-1)\sin(\theta_k) \tag{3.2}$$

is the relative time delay at array element l for the source signal of user k, with θ_k being the Line of Sight (LOS) angle of arrival for source k, and c is the speed of light.

If source k is the desired user and the rest of the sources are the interfering users, then the desired-user's Signal-to-Noise Ratio becomes $\text{SNR}_k = \frac{|h_k|^2 E_s}{2\sigma_n^2}$ and the desired Signal-to-Interference Ratio of user k' is $\text{SIR}_{k,k'} = \frac{|h_k|^2}{|h_{k'}|^2}$, where E_s is the symbol energy. The received signal vector $\mathbf{r}(n) = [r_1(n)\ r_2(n)\cdots r_L(n)]^T$ is given by

$$\mathbf{r}(n) = \mathbf{H}\mathbf{s}(n) + \mathbf{n}(n), \tag{3.3}$$

where we have $\mathbf{n}(n) = [n_1(n)\ n_2(n)\cdots n_L(n)]^T$, the transmitted symbol vector of the K users is $\mathbf{s}(n) = [s_1(n)\ s_2(n)\cdots s_K(n)]^T$ and the system matrix is denoted by $\mathbf{H} = [\mathbf{h}_1\ \mathbf{h}_2\cdots\mathbf{h}_K]$, which is associated with the steering vector

$$\mathbf{h}_k = \left[h_k e^{-j\omega t_1(\theta_k)}\ \ h_k e^{-j\omega t_2(\theta_k)}\ \ \ldots\ \ h_k e^{-j\omega t_L(\theta_k)}\right]^T \tag{3.4}$$

for source k, $k \in \{1, 2, \cdots, K\}$. The system vector $\mathbf{h}_k$ is the unique, user-specific signature of user k. In this chapter, we assume that the relative time delay of all users with respect to the angularly closest neighbours is the same. All the angular locations of the users were selected under this constraint.

3.1.2 Iterative Multiuser Beamforming Receiver Structure

The iterative multiuser beamforming receiver's structure is shown in Figure 3.2, which consists of two stages, namely the Soft-Input Soft-Output Interference Cancellation aided beamforming MUD, followed by K parallel single-user SISO channel decoders. The two stages are separated by the usual deinterleavers and interleavers.

The proposed SISO beamforming MUD first computes the estimated symbol $\hat{s}_k(n)$ corresponding to the transmitted symbol $s_k(n)$ using a linear filter, which determines the coefficients of the beamformer weight $\mathbf{w}_k(n)$ according to the specific design criterion employed and uses this weight to estimate $\hat{s}_k(n)$ from the received signal $\mathbf{r}(n)$ with the aid of a linear transformation [17]. Let us now

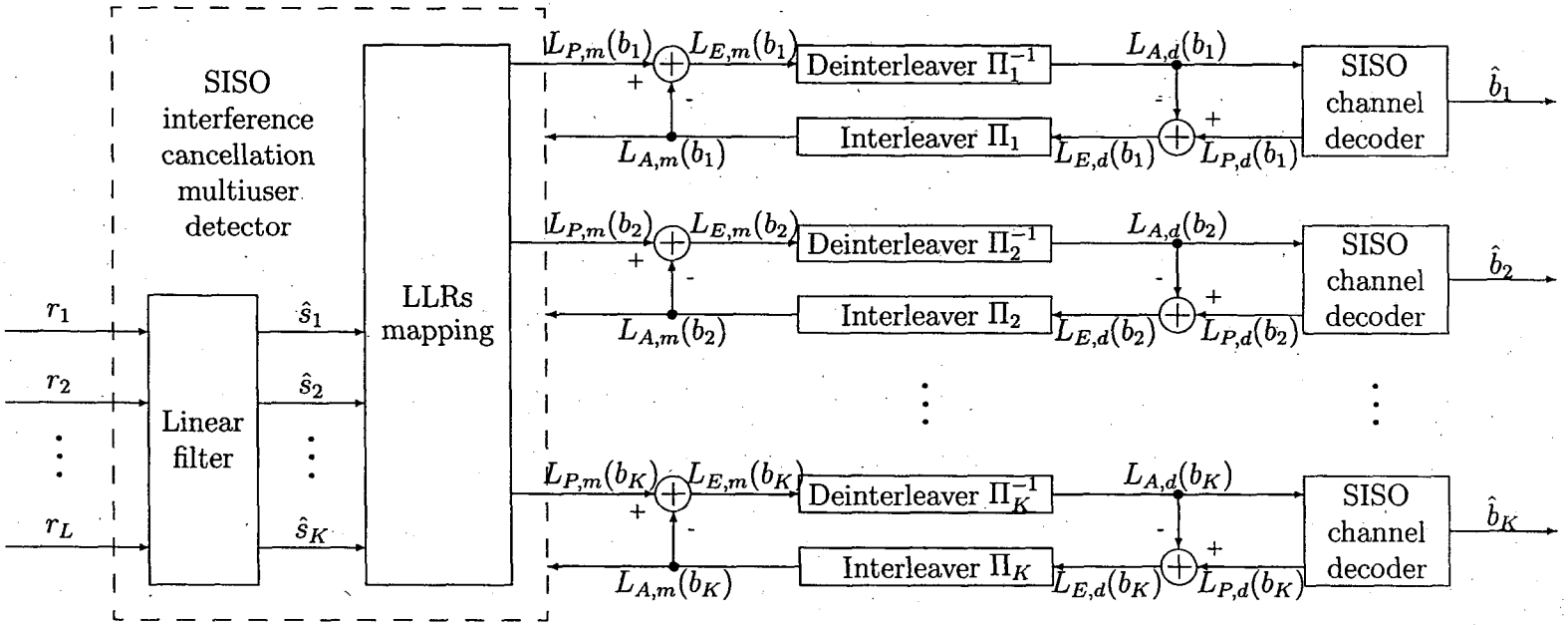

Figure 3.2: Iterative multiuser beamforming receiver structure, which consists of two stages, namely the SISO Interference Cancellation aided beamforming MUD, followed by K parallel single-user SISO channel decoders. The two stages are separated by the usual deinterleavers and interleavers.

define $b_k(n,i)$ as the ith bit of symbol $s_k(n)$, whereas $b_k(j)$ is the same bit but in a different position of the bit-based interleaving block after the deinterleaver. $L_A(\cdot)$, $L_P(\cdot)$ and $L_E(\cdot)$ denote the *a priori*, *a posteriori* and extrinsic information in terms of Log-Likelihood Ratio (LLR), and the indices $_m$ and $_d$ are associated with the MUD and channel decoder, respectively. Then the SISO beamforming MUD delivers the *a posteriori* information of bit $b_k(n,i)$ expressed in terms of its LLR as [13]

$$\begin{aligned} L_{P,m}\big(b_k(n,i)\big) &= \ln \frac{P\big(b_k(n,i)=+1|\hat{s}_k(n)\big)}{P\big(b_k(n,i)=-1|\hat{s}_k(n)\big)} \\ &= \ln \frac{P\big(\hat{s}_k(n)|b_k(n,i)=+1\big)}{P\big(\hat{s}_k(n)|b_k(n,i)=-1\big)} + \ln \frac{P\big(b_k(n,i)=+1\big)}{P\big(b_k(n,i)=-1\big)} \\ &= L_{E,m}\big(b_k(n,i)\big) + L_{A,m}\big(b_k(n,i)\big), \end{aligned} \tag{3.5}$$

where the second term, denoted by $L_{A,m}\big(b_k(n,i)\big)$, represents the *a priori* LLR of the interleaved and encoded bit $b_k(n,i)$. For the first iteration, assuming equiprobable encoded bits, i.e. that no *a priori* information is available, all bits have a probability of 0.5. Hence in the LLR domain we have $L_{A,m}\big(b_k(n,i)\big) = 0$. The first term in Equation (3.5), which is denoted by $L_{E,m}\big(b_k(n,i)\big)$, represents the extrinsic information delivered by the SISO MUD, based on the received signal $\mathbf{r}(n)$ and on the *a priori* information about the encoded bits of all users, except the ith bit of the desired user k. The extrinsic information, which is not influenced by the *a priori* information of the desired bit i provided by the kth channel decoder, is then deinterleaved and fed into the kth user's channel decoder, which will be used as the *a priori* information in the next iteration.

As seen in Figure 3.2, between the banks of channel decoders and interleavers, based on the *a priori* information $L_{A,d}\big(b_k(j)\big)$ provided by the SISO beamforming MUD for the SISO decoder, we compute the extrinsic LLR as [13]

$$L_{E,d}\big(b_k(j)\big) = L_{P,d}\big(b_k(j)\big) - L_{A,d}\big(b_k(j)\big), \tag{3.6}$$

where the extrinsic information is gleaned from the surrounding encoded bits, excluding the specific bit considered [14]. We note that as usual in joint iterative detection and decoding schemes [14], we exchange the extrinsic information concerning both the original information bits and parity bits, rather than only that of the information bits, although only the LLRs of the latter are needed in the classic turbo decoder of Berrou *et al.* [12]. After interleaving, the extrin-

sic information delivered by the channel decoders is then fed back to the SISO MUD, as the *a priori* information concerning the encoded bits of all the users for exploitation during the next iteration.

At the first iteration, the extrinsic information contributions $L_{E,m}(b_k)$ and $L_{E,d}(b_k)$ are statistically independent. However, during the subsequent iterations they will become more and more correlated and hence the incremental iteration gains become more modest.

3.2 SISO Interference Cancellation

As described in the previous section, the task of SISO IC is to choose the beamformer weight $\mathbf{w}_k$ of the linear filter seen in Figure 3.2 according to an appropriate design criterion and compute the corresponding output LLRs.

Given the *a priori* LLRs

$$L_A\big(b_k(i)\big) = \ln \frac{P\big(b_k(i)=+1\big)}{P\big(b_k(i)=-1\big)}, \tag{3.7}$$

where the symbol-index n was dropped for notational convenience, the *a priori* probabilities of the bit $b_k(i)$ can be expressed as

$$\begin{aligned} P_A\big(b_k(i)=+1\big) &= \frac{e^{L_A(b_k(i))}}{e^{L_A(b_k(i))}+1} \\ &= \tfrac{1}{2}\left(1+\tanh\left(\tfrac{L_A(b_k(i))}{2}\right)\right), \qquad (3.8a) \\ P_A\big(b_k(i)=-1\big) &= \frac{1}{e^{L_A(b_k(i))}+1} \\ &= \tfrac{1}{2}\left(1-\tanh\left(\tfrac{L_A(b_k(i))}{2}\right)\right), \qquad (3.8b) \end{aligned}$$

where $\tanh(x) = \frac{e^x-e^{-x}}{e^x+e^{-x}}$ is the hyperbolic tangent function. Then the *a priori* probability of the pth legitimate value of the symbol s_k is given by

$$P_A\big(s_k=s^{(p)}\big) = \prod_{i=1}^{\log_2 M} P_A\big(b_k(i)=b^{(p)}(i)\big), \tag{3.9}$$

where $s^{(p)}$ is the pth symbol in the modulation constellation, $p \in \{1, 2, \cdots, M\}$,

M is the number of symbols in modulation constellation and $b^{(p)}(i)$ is the value of $s^{(p)}$'s ith bit. Using the Gray-labeled constellations in seen Figure 2.5, all transmitted bits can be decided independently. Then we can define the mean and variance of the kth user's symbols as in [18]:

$$\begin{aligned}
\bar{s}_k &= \mathrm{E}[s_k] \\
&= \sum_{p=1}^{M} s^{(p)} \cdot P_A\big(s_k{=}s^{(p)}\big) \\
&= \begin{cases}
\sqrt{E_s}\tanh\left(\frac{L_A(b_k(1))}{2}\right) & \text{(BPSK)} \\
\sqrt{\frac{E_s}{2}}\left(\tanh\left(\frac{L_A(b_k(1))}{2}\right)+j\tanh\left(\frac{L_A(b_k(2))}{2}\right)\right) & \text{(QPSK)} \\
\sqrt{\frac{E_s}{10}}\left(\tanh\left(\frac{L_A(b_k(1))}{2}\right)\left(\tanh\left(\frac{L_A(b_k(2))}{2}\right)+2\right)\right. & \\
\quad \left. +j\tanh\left(\frac{L_A(b_k(3))}{2}\right)\left(\tanh\left(\frac{L_A(b_k(4))}{2}\right)+2\right)\right) & \text{(16QAM)}
\end{cases}
\end{aligned} \tag{3.10}$$

and

$$\begin{aligned}
v_k &= \mathrm{E}\big[|s_k|^2\big] - \big|\mathrm{E}[s_k]\big|^2 \\
&= \sum_{p=1}^{M} \big|s^{(p)}\big|^2 \cdot P_A\big(s_k{=}s^{(p)}\big) - |\bar{s}_k|^2 \\
&= \begin{cases}
E_s - |\bar{s}_k|^2 & \text{(BPSK)} \\
E_s - |\bar{s}_k|^2 & \text{(QPSK)} \\
E_s\left(1+\frac{2}{5}\tanh\left(\frac{L_A(b_k(2))}{2}\right)+\frac{2}{5}\tanh\left(\frac{L_A(b_k(4))}{2}\right)\right) - |\bar{s}_k|^2 & \text{(16QAM)}
\end{cases}
\end{aligned} \tag{3.11}$$

When using the SIC principle, the estimated symbol of user k can be expressed as [18]

$$\hat{s}_k = \mathbf{w}_k^H(\mathbf{r} - \mathbf{H}\underline{\bar{\mathbf{s}}}_k), \tag{3.12}$$

where we have $\underline{\bar{\mathbf{s}}}_k = [\bar{s}_1 \cdots \bar{s}_{k-1}\ 0\ \bar{s}_{k+1} \cdots \bar{s}_K]^T$.

3.2.1 SISO Interference Cancellation Using the MMSE MUD

3.2.1.1 Weights of the Soft MMSE MUD

Classically, the beamformer's weight vector $\mathbf{w}_k$ is determined by minimising the complex-valued MSE metric of [11]

$$\xi_{MSE} = \mathrm{E}\big[|s_k - \hat{s}_k|^2\big]. \tag{3.13}$$

Using Equation (3.12) and (3.3), the MSE cost function can be expressed as

$$\begin{aligned}
\xi_{MSE} &= \mathrm{E}\Big[\big|s_k - \mathbf{w}_k^H(\mathbf{Hs} - \mathbf{H}\underline{\bar{\mathbf{s}}}_k + \mathbf{n})\big|^2\Big] \\
&= \mathrm{E}[s_k s_k^*] - \mathbf{w}_k^H\mathbf{H}\cdot\mathrm{E}[s_k^*(\mathbf{s} - \underline{\bar{\mathbf{s}}}_k)] - \mathrm{E}\big[s_k\big(\mathbf{s}^H - \underline{\bar{\mathbf{s}}}_k^H\big)\big]\cdot\mathbf{H}^H\mathbf{w}_k \\
&\quad + \mathbf{w}_k^H\Big(\mathbf{H}\cdot\mathrm{E}\big[(\mathbf{s} - \underline{\bar{\mathbf{s}}}_k)\big(\mathbf{s}^H - \underline{\bar{\mathbf{s}}}_k^H\big)\big]\cdot\mathbf{H}^H + \mathrm{E}\big[\mathbf{n}\mathbf{n}^H\big]\Big)\mathbf{w}_k \\
&= E_s - E_s\mathbf{w}_k^H\mathbf{h}_k - E_s\mathbf{h}_k^H\mathbf{w}_k + \mathbf{w}_k^H\big(\mathbf{H}\underline{\mathbf{V}}_k\mathbf{H}^H + E_s\mathbf{h}_k\mathbf{h}_k^H + 2\sigma_n^2\mathbf{I}_L\big)\mathbf{w}_k,
\end{aligned} \tag{3.14}$$

where $\mathbf{I}_L$ denotes the $(L\times L)$-dimensional identity matrix and we have $\underline{\mathbf{V}}_k = \mathrm{diag}[v_1 \cdots v_{k-1}\ 0\ v_{k+1} \cdots v_K]$, in which $\mathrm{diag}[\cdot]$ denotes a diagonal matrix. The gradient of Equation (3.14) can be derived as

$$\begin{aligned}
\nabla\xi_{MSE} &= 2\frac{\partial\xi_{MSE}}{\partial\mathbf{w}_k^*} \\
&= -2E_s\mathbf{h}_k + 2\big(\mathbf{H}\underline{\mathbf{V}}_k\mathbf{H}^H + E_s\mathbf{h}_k\mathbf{h}_k^H + 2\sigma_n^2\mathbf{I}_L\big)\mathbf{w}_k.
\end{aligned} \tag{3.15}$$

Setting this gradient to zero leads to the closed-form MMSE solution of [18]

$$\mathbf{w}_k = \big(\mathbf{H}\underline{\mathbf{V}}_k\mathbf{H}^H + E_s\mathbf{h}_k\mathbf{h}_k^H + 2\sigma_n^2\mathbf{I}_L\big)^{-1}\cdot E_s\mathbf{h}_k. \tag{3.16}$$

3.2.1.2 Output LLRs of the Soft MMSE MUD

The exact expression of the bit $b_k(i)$'s output LLR is [18]

$$L_E\big(b_k(i)\big)$$

$$= \ln \frac{\sum_{\substack{\forall \mathbf{s}^{(q)} \\ b_k^{(q)}(i)=+1}} \exp\left(-\frac{\left|\hat{s}_k - \mathbf{w}_k^H \mathbf{H}\left(\mathbf{s}^{(q)} - \bar{\mathbf{s}}_k\right)\right|^2}{2\sigma_n^2}\right) \prod_{\forall (k',i') \neq (k,i)} P\left(b_{k'}(i') = b_{k'}^{(q)}(i')\right)}{\sum_{\substack{\forall \mathbf{s}^{(q)} \\ b_k^{(q)}(i)=-1}} \exp\left(-\frac{\left|\hat{s}_k - \mathbf{w}_k^H \mathbf{H}\left(\mathbf{s}^{(q)} - \bar{\mathbf{s}}_k\right)\right|^2}{2\sigma_n^2}\right) \prod_{\forall (k',i') \neq (k,i)} P\left(b_{k'}(i') = b_{k'}^{(q)}(i')\right)}, \tag{3.17}$$

where $\mathbf{s}^{(q)}$ is the qth possible symbol combination, $q \in \{1, 2, \cdots, M^K\}$ and $b_k^{(q)}(i)$ is the value of the kth user's ith bit in this combination. It is clear from Equation (3.17) that the computational complexity of the MUD's output LLRs is exponentially increases with the number of users K. Fortunately, we can use an approximate method to simplify this calculation [18].

The conditional PDF $p\left(\hat{s}_k | s_k = s^{(p)}\right)$ is a mixture of all M^{K-1} legitimate transmitted signals' Gaussian distributions, in which the kth user transmits symbol $s^{(p)}$ and all other interfering users transmit an arbitrary symbol. Figure 3.3 shows some examples of the conditional PDF of the MMSE MUD's output signal supporting K=4 users in the presence of AWGN but in the absence of fading at E_b/N_0=5dB, both with and without *a priori* information. The arrival angles of the users' signal are 15°, 49°, −14° and −48°, respectively, as seen in Figure 3.4. We consider the first user as the desired user and assume that the transmitted symbol is $s_1 = +1$ for BPSK, $s_1 = +\frac{1}{\sqrt{2}} + j\frac{1}{\sqrt{2}}$ for QPSK and $s_1 = +\frac{3}{\sqrt{10}} + j\frac{3}{\sqrt{10}}$ for 16QAM. In the scenarios associated with *a priori* information, all the interfering users' *a priori* LLRs are randomly generated, exemplified in Table 3.1. In

Table 3.1: *A priori* LLRs of the interfering users

	BPSK	QPSK	16QAM
User 2	-0.582	-0.582, 0.597	-0.582, 0.597, 0.187, 1.511
User 3	-1.969	-1.969, -0.423	-1.969, -0.423, -0.268, 0.909
User 4	-0.499	-0.499, 0.574	-0.499, 0.574, 0.592, 0.292

every sub-figure, the conditional 3-dimensional PDF $p(\hat{s}_1)$ (surface), the marginal conditional PDF of the real part $p(\Re[\hat{s}_1])$ and the marginal conditional PDF of the imaginary part $p(\Im[\hat{s}_1])$ (solid curves) of the MUDs' output are shown. As stated in [18], the conditional PDF $p\left(\hat{s}_k | s_k = s^{(p)}\right)$ can be assumed to be Gaussian distributed. Since the Gaussian distribution can be defined by two parameters, namely the mean and the variance, we can generate the approximate PDF by calculating these two values. Using Equation (3.12), the mean and the variance

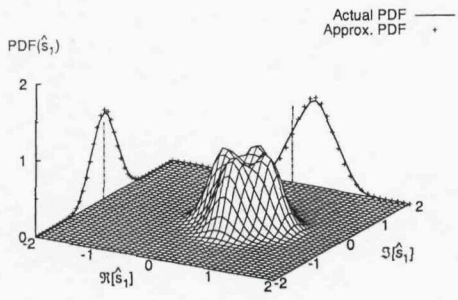

(a) BPSK without *a priori* information

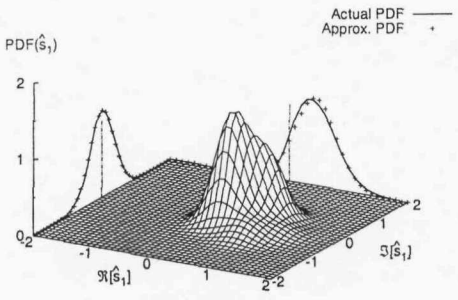

(b) BPSK with *a priori* information

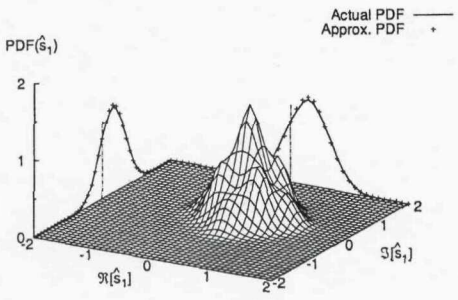

(c) QPSK without *a priori* information

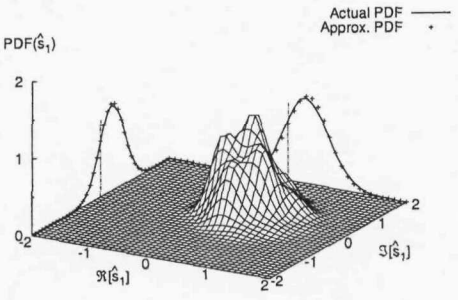

(d) QPSK with *a priori* information

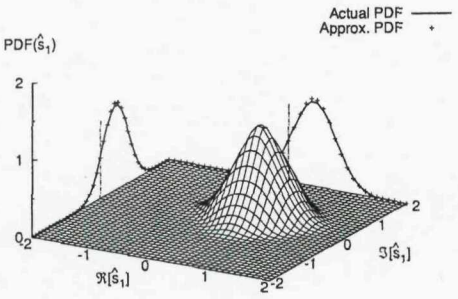

(e) 16QAM without *a priori* information

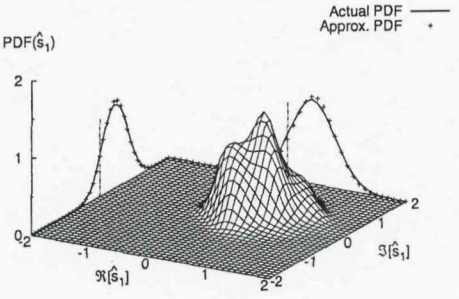

(f) 16QAM with *a priori* information

Figure 3.3: Conditional PDF $p(\hat{s}_1)$ (surface), marginal conditional PDFs $p(\Re[\hat{s}_1])$ and $p(\Im[\hat{s}_1])$ (solid curves) of the MMSE MUD's output signal, and approximate Gaussian marginal conditional PDFs (+).

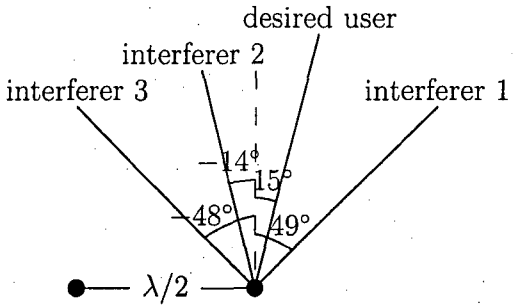

Figure 3.4: Two AEs, where the signal of desired user arrives from 15°, while the interfering signal from 49°, −14° and −48°.

are given by

$$\begin{aligned}\mu_k^{(p)} &= \mathrm{E}\big[\hat{s}_k | s_k{=}s^{(p)}\big] \\ &= \mathbf{w}_k^H \mathbf{H} \cdot \mathrm{E}\big[\mathbf{s} - \underline{\bar{\mathbf{s}}}_k | s_k{=}s^{(p)}\big] \\ &= s^{(p)} \mathbf{w}_k^H \mathbf{h}_k \end{aligned} \tag{3.18}$$

and

$$\begin{aligned}\sigma_k^2 &= \mathrm{E}\big[|\hat{s}_k|^2 | s_k{=}s^{(p)}\big] - \big|\mu_k^{(p)}\big|^2 \\ &= \mathbf{w}_k^H \mathbf{H} \cdot \mathrm{E}\big[(\mathbf{s} - \underline{\bar{\mathbf{s}}}_k)(\mathbf{s}^H - \underline{\bar{\mathbf{s}}}_k^H) | s_k{=}s^{(p)}\big] \cdot \mathbf{H}^H \mathbf{w}_k + \mathbf{w}_k^H \cdot \mathrm{E}\big[\mathbf{n}\mathbf{n}^H\big] \cdot \mathbf{w}_k \\ &\quad - \big|s^{(p)}\big|^2 \mathbf{w}_k^H \mathbf{h}_k \mathbf{h}_k^H \mathbf{w}_k \\ &= \mathbf{w}_k^H \big(\mathbf{H} \underline{\mathbf{V}}_k \mathbf{H}^H + 2\sigma_n^2 \mathbf{I}_L\big) \mathbf{w}_k. \end{aligned} \tag{3.19}$$

Using Equation (3.16) and $\mathbf{w}_k^H \mathbf{h}_k = \mathbf{h}_k^H \mathbf{w}_k$, the variance can be simplified to

$$\begin{aligned}\sigma_k^2 &= \mathbf{w}_k^H \big(\mathbf{H} \underline{\mathbf{V}}_k \mathbf{H}^H + E_s \mathbf{h}_k \mathbf{h}_k^H + 2\sigma_n^2 \mathbf{I}_L\big) \mathbf{w}_k - E_s \mathbf{w}_k^H \mathbf{h}_k \mathbf{h}_k^H \mathbf{w}_k \\ &= E_s \mathbf{w}_k^H \mathbf{h}_k - E_s \mathbf{w}_k^H \mathbf{h}_k \mathbf{h}_k^H \mathbf{w}_k \\ &= E_s \mathbf{w}_k^H \mathbf{h}_k \big(1 - \mathbf{w}_k^H \mathbf{h}_k\big). \end{aligned} \tag{3.20}$$

Then the approximate Gaussian PDF can be expressed as

$$\begin{aligned}\tilde{p}\big(\hat{s}_k | s_k{=}s^{(p)}\big) &= \frac{1}{\pi \sigma_k^2} \exp\left(- \frac{\big|\hat{s}_k - \mu_k^{(p)}\big|^2}{\sigma_k^2} \right) \\ &= \frac{1}{\pi E_s \mathbf{w}_k^H \mathbf{h}_k \big(1 - \mathbf{w}_k^H \mathbf{h}_k\big)} \exp\left(- \frac{\big|\hat{s}_k - s^{(p)} \mathbf{w}_k^H \mathbf{h}_k\big|^2}{E_s \mathbf{w}_k^H \mathbf{h}_k \big(1 - \mathbf{w}_k^H \mathbf{h}_k\big)} \right). \end{aligned} \tag{3.21}$$

In Figure 3.3, we can see that the one-dimensional Gaussian distribution indicated by the '+' points constitutes an adequate practical assumption in all the scenarios.

Based on the Gaussian distribution, the extrinsic output LLRs of the MMSE MUD can be expressed as [18]

$$L_E\big(b_k(i)\big) = \ln \frac{\sum_{\substack{\forall s^{(p)} \\ b^{(p)}(i)=+1}} \exp\left(- \frac{\left|\hat{s}_k - s^{(p)} \mathbf{w}_k^H \mathbf{h}_k\right|^2}{E_s \mathbf{w}_k^H \mathbf{h}_k \big(1 - \mathbf{w}_k^H \mathbf{h}_k\big)} \right) \prod_{\forall i' \neq i} P\big(b_k(i') = b^{(p)}(i')\big)}{\sum_{\substack{\forall s^{(p)} \\ b^{(p)}(i)=-1}} \exp\left(- \frac{\left|\hat{s}_k - s^{(p)} \mathbf{w}_k^H \mathbf{h}_k\right|^2}{E_s \mathbf{w}_k^H \mathbf{h}_k \big(1 - \mathbf{w}_k^H \mathbf{h}_k\big)} \right) \prod_{\forall i' \neq i} P\big(b_k(i') = b^{(p)}(i')\big)}. \tag{3.22}$$

For BPSK and QPSK systems, this expression can be further simplified to [15]

BPSK:

$$\begin{aligned} L_E\big(b_k(1)\big) &= \ln \frac{\exp\left(- \frac{\left|\hat{s}_k - \sqrt{E_s} \mathbf{w}_k^H \mathbf{h}_k\right|^2}{E_s \mathbf{w}_k^H \mathbf{h}_k \big(1 - \mathbf{w}_k^H \mathbf{h}_k\big)} \right)}{\exp\left(- \frac{\left|\hat{s}_k + \sqrt{E_s} \mathbf{w}_k^H \mathbf{h}_k\right|^2}{E_s \mathbf{w}_k^H \mathbf{h}_k \big(1 - \mathbf{w}_k^H \mathbf{h}_k\big)} \right)} \\ &= \frac{\left|\hat{s}_k + \sqrt{E_s} \mathbf{w}_k^H \mathbf{h}_k\right|^2 - \left|\hat{s}_k - \sqrt{E_s} \mathbf{w}_k^H \mathbf{h}_k\right|^2}{E_s \mathbf{w}_k^H \mathbf{h}_k \big(1 - \mathbf{w}_k^H \mathbf{h}_k\big)} \\ &= \frac{4\sqrt{E_s} \Re[\hat{s}_k] \mathbf{w}_k^H \mathbf{h}_k}{E_s \mathbf{w}_k^H \mathbf{h}_k \big(1 - \mathbf{w}_k^H \mathbf{h}_k\big)} \\ &= \frac{4\Re[\hat{s}_k]}{\sqrt{E_s}\big(1 - \mathbf{w}_k^H \mathbf{h}_k\big)}, \end{aligned} \tag{3.23}$$

QPSK:

$$\begin{aligned} L_E\big(b_k(1)\big) = \ln \frac{\begin{array}{r} \exp\left(- \frac{\left|\hat{s}_k - \left(\sqrt{\frac{E_s}{2}} + j\sqrt{\frac{E_s}{2}}\right) \mathbf{w}_k^H \mathbf{h}_k\right|^2}{E_s \mathbf{w}_k^H \mathbf{h}_k \big(1 - \mathbf{w}_k^H \mathbf{h}_k\big)} \right) \cdot P\big(b_k(2) = +1\big) + \\ + \exp\left(- \frac{\left|\hat{s}_k - \left(\sqrt{\frac{E_s}{2}} - j\sqrt{\frac{E_s}{2}}\right) \mathbf{w}_k^H \mathbf{h}_k\right|^2}{E_s \mathbf{w}_k^H \mathbf{h}_k \big(1 - \mathbf{w}_k^H \mathbf{h}_k\big)} \right) \cdot P\big(b_k(2) = -1\big) \end{array}}{\begin{array}{r} \exp\left(- \frac{\left|\hat{s}_k - \left(-\sqrt{\frac{E_s}{2}} + j\sqrt{\frac{E_s}{2}}\right) \mathbf{w}_k^H \mathbf{h}_k\right|^2}{E_s \mathbf{w}_k^H \mathbf{h}_k \big(1 - \mathbf{w}_k^H \mathbf{h}_k\big)} \right) \cdot P\big(b_k(2) = +1\big) + \\ + \exp\left(- \frac{\left|\hat{s}_k - \left(-\sqrt{\frac{E_s}{2}} - j\sqrt{\frac{E_s}{2}}\right) \mathbf{w}_k^H \mathbf{h}_k\right|^2}{E_s \mathbf{w}_k^H \mathbf{h}_k \big(1 - \mathbf{w}_k^H \mathbf{h}_k\big)} \right) \cdot P\big(b_k(2) = -1\big) \end{array}} \\ = \ln \frac{\exp\left(- \frac{\left(\Re[\hat{s}_k] - \sqrt{\frac{E_s}{2}} \mathbf{w}_k^H \mathbf{h}_k\right)^2}{E_s \mathbf{w}_k^H \mathbf{h}_k \big(1 - \mathbf{w}_k^H \mathbf{h}_k\big)} \right)}{\exp\left(- \frac{\left(\Re[\hat{s}_k] + \sqrt{\frac{E_s}{2}} \mathbf{w}_k^H \mathbf{h}_k\right)^2}{E_s \mathbf{w}_k^H \mathbf{h}_k \big(1 - \mathbf{w}_k^H \mathbf{h}_k\big)} \right)} \end{aligned}$$

$$= \frac{\left(\Re[\hat{s}_k] + \sqrt{\frac{E_s}{2}}\mathbf{w}_k^H\mathbf{h}_k\right)^2 - \left(\Re[\hat{s}_k] - \sqrt{\frac{E_s}{2}}\mathbf{h}_k\right)^2}{E_s\mathbf{w}_k^H\mathbf{h}_k\left(1 - \mathbf{w}_k^H\mathbf{w}_k^H\mathbf{h}_k\right)}$$
$$= \frac{4\sqrt{\frac{E_s}{2}}\Re[\hat{s}_k]\mathbf{w}_k^H\mathbf{h}_k}{E_s\mathbf{w}_k^H\mathbf{h}_k\left(1 - \mathbf{w}_k^H\mathbf{h}_k\right)}$$
$$= \frac{2\sqrt{2}\Re[\hat{s}_k]}{\sqrt{E_s}\left(1 - \mathbf{w}_k^H\mathbf{h}_k\right)}, \tag{3.24a}$$

and similarly

$$L_E\left(b_k(2)\right) = \frac{2\sqrt{2}\Im[\hat{s}_k]}{\sqrt{E_s}\left(1 - \mathbf{w}_k^H\mathbf{h}_k\right)}. \tag{3.24b}$$

3.2.1.3 · Computational Complexity of the Soft MMSE MUD

The complexity of a linear MUD might be divided into three parts, namely the calculation of the *a priori* mean and variance values, the calculation of the weight vector and the calculation of the output extrinsic LLR values. Real-valued operations are used as the basis of our calculations and the complexity imposed by a real-valued multiplication and a real-valued addition might be considered equivalent. The soft MMSE MUD's complexity per symbol per user is summarized in Table 3.2. The related equations are also given in this table. It is shown that the complexity of the soft MMSE MUD mainly depends on the calculation of the weight vector.

Table 3.2: Computational complexity of the soft MMSE MUD

		Computational complexity	Equation(s)
Means & variances	BPSK	6	(3.10), (3.11)
	QPSK	12	
	16QAM	25	
Weight vector		$\mathcal{O}(8L^3) + 4KL^2 + 12L^2 + L$	(3.16)
LLRs	BPSK	$8KL + 8L + 1$	(3.23)
	QPSK	$8KL + 8L + 3$	(3.24)
	M-QAM	$8KL+8L+(M\log_2 M+M+9)\log_2 M+13M-4$	(3.22)

3.2.2 SISO Interference Cancellation Using the RMMSE MUD

For BPSK systems, the beamformer's desired output $\hat{s}_k$ is real-valued. It is clear that the MMSE solution of Section 3.2.1 attempts to simultaneously minimise the MSE between the desired signal and both the real part and imaginary part of the beamformer's output. However, in case of BPSK modulation the beamformer's decision depends only on the real part of the multiuser signal at the beamformer's output. Hence minimising the MSE associated with the imaginary part does not contribute to improving the beamformer's performance. Rather it imposes an unnecessary constraint on the beamforming weight [89]. Hence we introduce the soft RMMSE solution.

3.2.2.1 Weights of the Soft RMMSE MUD

The real-valued MSE cost function minimising the MSE between the desired signal and the real part of the beamformer's output can be written as

$$\begin{aligned}\xi_{RMSE} &= \mathrm{E}\left[(s_k - \Re[\hat{s}_k])^2\right] \\ &= \mathrm{E}\left[\left(s_k - \Re\left[\mathbf{w}_k^H(\mathbf{Hs} - \mathbf{H}\underline{\bar{\mathbf{s}}}_k + \mathbf{n})\right]\right)^2\right].\end{aligned} \tag{3.25}$$

The RMMSE solution is defined by

$$\mathbf{w}_k = \arg\min_{\mathbf{w}_k} \xi_{RMSE}. \tag{3.26}$$

In order to derive a closed-form solution for this RMMSE design, the real-valued vertical concatenation matrix method of [89] is applied. Let us define the index c as the subscript to indicate the matrices' vertical concatenation, then we have

$$\mathbf{M}_c = \begin{bmatrix}\Re[\mathbf{M}] \\ \Im[\mathbf{M}]\end{bmatrix}, \tag{3.27}$$

where $\mathbf{M}_c$ can be any matrix which is vertically concatenated. Hence, Equation (3.25) becomes

$$\begin{aligned}\xi_{RMSE} &= \mathrm{E}\left[\left(s_k - \mathbf{w}_{k,c}^T(\mathbf{H}_c\mathbf{s} - \mathbf{H}_c\underline{\bar{\mathbf{s}}}_k + \mathbf{n}_c)\right)^2\right] \\ &= \mathrm{E}\left[s_k^2\right] - 2\mathbf{w}_{k,c}^T\mathbf{H}_c \cdot \mathrm{E}[s_k(\mathbf{s} - \underline{\bar{\mathbf{s}}}_k)]\end{aligned}$$

$$+ \mathbf{w}_{k,c}^T \Big(\mathbf{H}_c \cdot \mathrm{E}\big[(\mathbf{s} - \underline{\bar{\mathbf{s}}}_k)(\mathbf{s}^T - \underline{\bar{\mathbf{s}}}_k^T)\big] \cdot \mathbf{H}_c^T + \mathrm{E}\big[\mathbf{n}_c \mathbf{n}_c^T\big] \Big) \mathbf{w}_{k,c}$$
$$= E_s - 2E_s \mathbf{w}_{k,c}^T \mathbf{h}_{k,c} + \mathbf{w}_{k,c}^T \big(\mathbf{H}_c \underline{\mathbf{V}}_k \mathbf{H}_c^T + E_s \mathbf{h}_{k,c} \mathbf{h}_{k,c}^T + \sigma_n^2 \mathbf{I}_{2L} \big) \mathbf{w}_{k,c}. \quad (3.28)$$

The gradient of the real-valued MSE cost function can be expressed as

$$\nabla \xi_{RMSE} = \frac{\partial \xi_{RMSE}}{\partial \mathbf{w}_{k,c}}$$
$$= -2E_s \mathbf{h}_{k,c} + 2\big(\mathbf{H}_c \underline{\mathbf{V}}_k \mathbf{H}_c^T + E_s \mathbf{h}_{k,c} \mathbf{h}_{k,c}^T + \sigma_n^2 \mathbf{I}_{2L} \big) \mathbf{w}_{k,c}. \quad (3.29)$$

Then in contrast to the closed-form MMSE solution of Equation (3.16), the closed-form solution of the concatenated weight matrix $\mathbf{w}_{k,rmmse,c}$ is derived from Equation (3.29), yielding

$$\mathbf{w}_{k,c} = \big(\mathbf{H}_c \underline{\mathbf{V}}_k \mathbf{H}_c^T + E_s \mathbf{h}_{k,c} \mathbf{h}_{k,c}^T + \sigma_n^2 \mathbf{I}_{2L} \big)^{-1} \cdot E_s \mathbf{h}_{k,c}. \quad (3.30)$$

The first L elements of $\mathbf{w}_{k,c}$ are the real part of the RMMSE solution $\mathbf{w}_k$, and the last L elements of $\mathbf{w}_{k,c}$ form the imaginary part of $\mathbf{w}_k$.

3.2.2.2 Output LLRs of the Soft RMMSE MUD

When computing the MMSE solution, the conditional PDF $p\big(\hat{s}_k | s_k = s^{(p)}\big)$ of Figure 3.3 is assumed to be Gaussian distributed. By contrast, the RMMSE solution considers only the in-phase component and the corresponding marginal conditional PDF becomes $p\big(\Re[\hat{s}_k] | s_k = s^{(p)}\big)$. Figure 3.5 shows the conditional PDFs of the RMMSE MUD's output signal supporting K=4 BPSK users at E_b/N_0=5dB both with and without *a priori* information. As seen in Figure 3.4, the arrival angles of the users' signal are 15°, 49°, −14° and −48°, respectively. We consider the first user as the desired user and assume that the transmitted symbol is $s_1 = +1$. In the scenario associated with *a priori* information, all the interfering users' *a priori* LLRs are listed in Table 3.1. Recall that the MMSE solution's output constellation seen in Figure 3.3 had a symmetric distribution. Observe by contrasting Equation (3.16) and Equation (3.30) that the beamformer weights of the RMMSE design are different and hence the weighted beamformer output phasors are positioned differently in Figure 3.5, which results in a non-Gaussian distribution for the ignored quadrature-phase component. However, the in-phase component of Figure 3.5 appears to be near-Gaussian. Explicitly, $p(\hat{s}_1)$ is spread more widely along the $\Im[\hat{s}_1]$ axis, resulting in a distribution for $p(\Re[\hat{s}_1])$ which

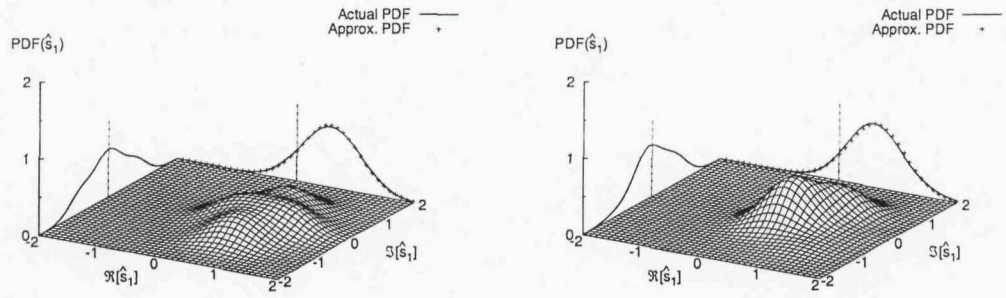

(a) Without *a priori* information (b) With *a priori* information

Figure 3.5: Conditional PDF $p(\hat{s}_1)$ (surface), marginal conditional PDFs $p(\Re[\hat{s}_1])$ and $p(\Im[\hat{s}_1])$ (solid curves) of the RMMSE MUD's output signal, and approximate Gaussian marginal conditional PDFs (+).

has its center of gravity further away from the decision boundary of $\Re[\hat{s}_1] = 0$ than that in Figure 3.3.

Then the conditional mean and variance of $\Re[\hat{s}_k]$ can be formulated as:

$$\begin{aligned}\mu_k^{(p)} &= \mathrm{E}\big[\Re[\hat{s}_k]|s_k{=}s^{(p)}\big] \\ &= \Re\big[\mathbf{w}_k^H\mathbf{H}\big]\cdot\mathrm{E}\big[\mathbf{s}-\underline{\bar{\mathbf{s}}}_k|s_k{=}s^{(p)}\big] \\ &= s^{(p)}\Re\big[\mathbf{w}_k^H\mathbf{h}_k\big] \\ &= s^{(p)}\mathbf{w}_{k,c}^T\mathbf{h}_{k,c}\end{aligned} \tag{3.31}$$

and

$$\begin{aligned}\sigma_k^2 &= \mathrm{E}\big[\Re^2[\hat{s}_k]|s_k{=}s^{(p)}\big] - \big(\mu_k^{(p)}\big)^2 \\ &= \mathbf{w}_{k,c}^T\mathbf{H}_c\cdot\mathrm{E}\big[(\mathbf{s}-\underline{\bar{\mathbf{s}}}_k)\big(\mathbf{s}^T-\underline{\bar{\mathbf{s}}}_k^T\big)|s_k{=}s^{(p)}\big]\cdot\mathbf{H}_c^T\mathbf{w}_{k,c} + \mathbf{w}_{k,c}^T\cdot\mathrm{E}\big[\mathbf{n}_c\mathbf{n}_c^T\big]\cdot\mathbf{w}_{k,c} \\ &\quad - \big(s^{(p)}\big)^2\mathbf{w}_{k,c}^T\mathbf{h}_{k,c}\mathbf{h}_{k,c}^T\mathbf{w}_{k,c} \\ &= \mathbf{w}_{k,c}^T\big(\mathbf{H}_c\underline{\mathbf{V}}_k\mathbf{H}_c^T+\sigma_n^2\mathbf{I}_{2L}\big)\mathbf{w}_{k,c}.\end{aligned} \tag{3.32}$$

Using Equation (3.30), the variance can be simplified to

$$\begin{aligned}\sigma_k^2 &= \mathbf{w}_{k,c}^T\big(\mathbf{H}_c\underline{\mathbf{V}}_k\mathbf{H}_c^T + E_s\mathbf{h}_{k,c}\mathbf{h}_{k,c}^T+\sigma_n^2\mathbf{I}_{2L}\big)\mathbf{w}_{k,c} - E_s\mathbf{w}_{k,c}^T\mathbf{h}_{k,c}\mathbf{h}_{k,c}^T\mathbf{w}_{k,c} \\ &= E_s\mathbf{w}_{k,c}^T\mathbf{h}_{k,c} - E_s\mathbf{w}_{k,c}^T\mathbf{h}_{k,c}\mathbf{h}_{k,c}^T\mathbf{w}_{k,c} \\ &= E_s\mathbf{w}_{k,c}^T\mathbf{h}_{k,c}\big(1-\mathbf{w}_{k,c}^T\mathbf{h}_{k,c}\big).\end{aligned} \tag{3.33}$$

Given the approximate Gaussian distribution

$$\tilde{p}\big(\Re[\hat{s}_k]|s_k{=}s^{(p)}\big) = \frac{1}{\sqrt{2\pi}\sigma_k}\exp\left(-\frac{\big(\Re[\hat{s}_k]-\mu_k^{(p)}\big)^2}{2\sigma_k^2}\right)$$
$$= \frac{1}{\sqrt{2\pi}\sigma_k}\exp\left(-\frac{\big(\Re[\hat{s}_k]-s^{(p)}\mathbf{w}_{k,c}^T\mathbf{h}_{k,c}\big)^2}{2E_s\mathbf{w}_{k,c}^T\mathbf{h}_{k,c}\big(1-\mathbf{w}_{k,c}^T\mathbf{h}_{k,c}\big)}\right), \tag{3.34}$$

the extrinsic output LLR can be expressed as

$$L_E\big(b_k(1)\big) = \ln\frac{\exp\left(-\frac{\left(\Re[\hat{s}_k]-\sqrt{E_s}\mathbf{w}_{k,c}^T\mathbf{h}_{k,c}\right)^2}{2E_s\mathbf{w}_{k,c}^T\mathbf{h}_{k,c}\left(1-\mathbf{w}_{k,c}^T\mathbf{h}_{k,c}\right)}\right)}{\exp\left(-\frac{\left(\Re[\hat{s}_k]+\sqrt{E_s}\mathbf{w}_{k,c}^T\mathbf{h}_{k,c}\right)^2}{2E_s\mathbf{w}_{k,c}^T\mathbf{h}_{k,c}\left(1-\mathbf{w}_{k,c}^T\mathbf{h}_{k,c}\right)}\right)}$$
$$= \frac{\big(\Re[\hat{s}_k]+\sqrt{E_s}\mathbf{w}_{k,c}^T\mathbf{h}_{k,c}\big)^2-\big(\Re[\hat{s}_k]-\sqrt{E_s}\mathbf{w}_{k,c}^T\mathbf{h}_{k,c}\big)^2}{2E_s\mathbf{w}_{k,c}^T\mathbf{h}_{k,c}\big(1-\mathbf{w}_{k,c}^T\mathbf{h}_{k,c}\big)}$$
$$= \frac{4\sqrt{E_s}\Re[\hat{s}_k]\mathbf{w}_{k,c}^T\mathbf{h}_{k,c}}{2E_s\mathbf{w}_{k,c}^T\mathbf{h}_{k,c}\big(1-\mathbf{w}_{k,c}^T\mathbf{h}_{k,c}\big)}$$
$$= \frac{2\mathbf{w}_{k,c}^T(\mathbf{r}_c-\mathbf{H}_c\bar{\mathbf{s}}_k)}{\sqrt{E_s}\big(1-\mathbf{w}_{k,c}^T\mathbf{h}_{k,c}\big)}. \tag{3.35}$$

3.2.2.3 Computational Complexity of the Soft RMMSE MUD

The soft RMMSE MUD's complexity per symbol per user is summarized in Table 3.3 which was valuated by counting the number of real-valued additions and multiplications. The related equations are also given in Table 3.3. It can be seen that the computational complexity of the soft RMMSE is almost the same as that of the soft MMSE beamformer portrayed in Table 3.2. However, the soft RMMSE system may be expected to have a better performance as we will show in Section 3.4.

Table 3.3: Computational complexity of the soft RMMSE MUD

	Computational complexity	Equation(s)
Means & variances	6	(3.10), (3.11)
Weight vector	$\mathcal{O}(8L^3)+8KL^2+8L^2+2L$	(3.30)
LLR	$4KL+4L+3$	(3.35)

3.2.3 SISO Interference Cancellation Using Widely Linear MMSE MUD

The WL algorithm [35] may be defined as that employing two separate weight vectors for separately detecting the in-phase and quadrature-phase component of the transmitted symbol. In contrast to Equation (3.12), the estimated symbol of the kth user is given by

$$\hat{s}_k = \Re\big[\mathbf{w}_{k,I}^H(\mathbf{r} - \mathbf{H}\underline{\bar{\mathbf{s}}}_k)\big] + j\Im\big[\mathbf{w}_{k,Q}^H(\mathbf{r} - \mathbf{H}\underline{\bar{\mathbf{s}}}_k)\big], \tag{3.36}$$

where $\mathbf{w}_{k,I}$ and $\mathbf{w}_{k,Q}$ are the kth user's weight vectors for the in-phase and quadrature-phase component, respectively.

3.2.3.1 Array Weights of the Soft WL-MMSE MUD

The soft WL-MMSE solution using separate in-phase/quadrature-phase array weights is defined as

$$\begin{aligned}\mathbf{w}_{k,I} &= \arg\min_{\mathbf{w}_k} \xi_{IMSE} \\ &= \arg\min_{\mathbf{w}_k} \mathrm{E}\big[(\Re[s_k] - \Re[\hat{s}_k])^2\big], \qquad (3.37a)\\ \mathbf{w}_{k,Q} &= \arg\min_{\mathbf{w}_k} \xi_{QMSE} \\ &= \arg\min_{\mathbf{w}_k} \mathrm{E}\big[(\Im[s_k] - \Im[\hat{s}_k])^2\big], \qquad (3.37b)\end{aligned}$$

which minimise the MSE between the in-phase component and the quadrature-phase component of the beamformer's output and that of the desired symbol, respectively. Defining the vertically stacked matrix

$$\mathbf{M}_{c'} = \begin{bmatrix} -\Im[\mathbf{M}] \\ \Re[\mathbf{M}] \end{bmatrix}, \tag{3.38}$$

where $\mathbf{M}$ can be any arbitrary matrix and when using Equation (3.27), the cost functions of the WL-MMSE solution can be expressed as

$$\begin{aligned}\xi_{IMSE} &= \mathrm{E}\Big[\big(\Re[s_k] - \Re\big[\mathbf{w}_k^H(\mathbf{H}\mathbf{s} - \mathbf{H}\underline{\bar{\mathbf{s}}}_k + \mathbf{n})\big]\big)^2\Big] \\ &= \mathrm{E}\Big[\Big(\Re[s_k] - \mathbf{w}_{k,c}^T\big(\mathbf{H}_c(\Re[\mathbf{s}] - \Re[\underline{\bar{\mathbf{s}}}_k]) + \mathbf{H}_{c'}(\Im[\mathbf{s}] - \Im[\underline{\bar{\mathbf{s}}}_k]) + \mathbf{n}_c\big)\Big)^2\Big]\end{aligned}$$

$$
\begin{aligned}
&= \mathrm{E}\big[\Re^2[s_k]\big] - 2\mathbf{w}_{k,c}^T\mathbf{H}_c \cdot \mathrm{E}\big[\Re[s_k](\Re[\mathbf{s}] - \Re[\underline{\bar{\mathbf{s}}}_k])\big] \\
&\quad + \mathbf{w}_{k,c}^T\mathbf{H}_c \cdot \mathrm{E}\big[(\Re[\mathbf{s}] - \Re[\underline{\bar{\mathbf{s}}}_k])\big(\Re[\mathbf{s}^T] - \Re[\underline{\bar{\mathbf{s}}}_k]^T\big)\big] \cdot \mathbf{H}_c^T\mathbf{w}_{k,c} \\
&\quad + \mathbf{w}_{k,c}^T\mathbf{H}_{c'} \cdot \mathrm{E}\big[(\Im[\mathbf{s}] - \Im[\underline{\bar{\mathbf{s}}}_k])\big(\Im[\mathbf{s}^T] - \Im[\underline{\bar{\mathbf{s}}}_k]^T\big)\big] \cdot \mathbf{H}_{c'}^T\mathbf{w}_{k,c} \\
&\quad + \mathbf{w}_{k,c}^T \cdot \mathrm{E}\big[\mathbf{n}_c\mathbf{n}_c^T\big] \cdot \mathbf{w}_{k,c} \\
&= E_{sI} - 2E_{sI}\mathbf{w}_{k,c}^T\mathbf{h}_{k,c} + \mathbf{w}_{k,c}^T\big(\mathbf{H}_c\underline{\mathbf{V}}_{k,I}\mathbf{H}_c^T + E_{sI}\mathbf{h}_{k,c}\mathbf{h}_{k,c}^T + \mathbf{H}_{c'}\underline{\mathbf{V}}_{k,Q}\mathbf{H}_{c'}^T \\
&\quad + E_{sQ}\mathbf{h}_{k,c'}\mathbf{h}_{k,c'}^T + \sigma_n^2\mathbf{I}_{2L}\big)\mathbf{w}_{k,c}, \qquad (3.39a)
\end{aligned}
$$

$$
\begin{aligned}
\xi_{QMSE} &= \mathrm{E}\Big[\big(\Im[s_k] - \Im\big[\mathbf{w}_k^H(\mathbf{H}\mathbf{s} - \mathbf{H}\underline{\bar{\mathbf{s}}}_k + \mathbf{n})\big]\big)^2\Big] \\
&= \mathrm{E}\Big[\Big(\Im[s_k] - \mathbf{w}_{k,c}^T\big(\mathbf{H}_c(\Im[\mathbf{s}] - \Im[\underline{\bar{\mathbf{s}}}_k]) - \mathbf{H}_{c'}(\Re[\mathbf{s}] - \Re[\underline{\bar{\mathbf{s}}}_k]) - \mathbf{n}_{c'}\big)\Big)^2\Big] \\
&= \mathrm{E}\big[\Im^2[s_k]\big] - 2\mathbf{w}_{k,c}^T\mathbf{H}_c \cdot \mathrm{E}\big[\Im[s_k](\Im[\mathbf{s}] - \Im[\underline{\bar{\mathbf{s}}}_k])\big] \\
&\quad + \mathbf{w}_{k,c}^T\mathbf{H}_c \cdot \mathrm{E}\big[(\Im[\mathbf{s}] - \Im[\underline{\bar{\mathbf{s}}}_k])\big(\Im[\mathbf{s}^T] - \Im[\underline{\bar{\mathbf{s}}}_k]^T\big)\big] \cdot \mathbf{H}_c^T\mathbf{w}_{k,c} \\
&\quad + \mathbf{w}_{k,c}^T\mathbf{H}_{c'} \cdot \mathrm{E}\big[(\Re[\mathbf{s}] - \Re[\underline{\bar{\mathbf{s}}}_k])\big(\Re[\mathbf{s}^T] - \Re[\underline{\bar{\mathbf{s}}}_k]^T\big)\big] \cdot \mathbf{H}_{c'}^T\mathbf{w}_{k,c} \\
&\quad + \mathbf{w}_{k,c}^T \cdot \mathrm{E}\big[\mathbf{n}_{c'}\mathbf{n}_{c'}^T\big] \cdot \mathbf{w}_{k,c} \\
&= E_{sQ} - 2E_{sQ}\mathbf{w}_{k,c}^T\mathbf{h}_{k,c} + \mathbf{w}_{k,c}^T\big(\mathbf{H}_c\underline{\mathbf{V}}_{k,Q}\mathbf{H}_c^T + E_{sQ}\mathbf{h}_{k,c}\mathbf{h}_{k,c}^T + \mathbf{H}_{c'}\underline{\mathbf{V}}_{k,I}\mathbf{H}_{c'}^T \\
&\quad + E_{sI}\mathbf{h}_{k,c'}\mathbf{h}_{k,c'}^T + \sigma_n^2\mathbf{I}_{2L}\big)\mathbf{w}_{k,c}, \qquad (3.39b)
\end{aligned}
$$

where E_{sI} and E_{sQ} are the in-phase component and the quadrature-phase component of the total symbol energy. Furthermore, we have $\underline{\mathbf{V}}_{k,I} = \mathrm{diag}[v_{1,I} \cdots v_{k-1,I}\ 0\ v_{k+1,I} \cdots v_{K,I}]$, $v_{k',I} = \mathrm{E}\big[\Re^2[s_{k'}]\big] - \Re^2[\bar{s}_{k'}]$, and $\underline{\mathbf{V}}_{k,Q} = \mathrm{diag}[v_{1,Q} \cdots v_{k-1,Q}\ 0\ v_{k+1,Q} \cdots v_{K,Q}]$, $v_{k',Q} = \mathrm{E}\big[\Im^2[s_{k'}]\big] - \Im^2[\bar{s}_{k'}]$. Setting the gradient of the WL-MMSE cost functions to zero, we have the WL-MMSE solution as

$$
\begin{aligned}
\mathbf{w}_{k,I,c} &= \big(\mathbf{H}_c\underline{\mathbf{V}}_{k,I}\mathbf{H}_c^T + E_{sI}\mathbf{h}_{k,c}\mathbf{h}_{k,c}^T + \mathbf{H}_{c'}\underline{\mathbf{V}}_{k,Q}\mathbf{H}_{c'}^T + E_{sQ}\mathbf{h}_{k,c'}\mathbf{h}_{k,c'}^T + \sigma_n^2\mathbf{I}_{2L}\big)^{-1} \\
&\quad \cdot E_{sI}\mathbf{h}_{k,c}, \qquad (3.40a) \\
\mathbf{w}_{k,Q,c} &= \big(\mathbf{H}_c\underline{\mathbf{V}}_{k,Q}\mathbf{H}_c^T + E_{sQ}\mathbf{h}_{k,c}\mathbf{h}_{k,c}^T + \mathbf{H}_{c'}\underline{\mathbf{V}}_{k,I}\mathbf{H}_{c'}^T + E_{sI}\mathbf{h}_{k,c'}\mathbf{h}_{k,c'}^T + \sigma_n^2\mathbf{I}_{2L}\big)^{-1} \\
&\quad \cdot E_{sQ}\mathbf{h}_{k,c}. \qquad (3.40b)
\end{aligned}
$$

For BPSK systems, we have $E_{sI} = E_s$, $E_{sQ} = 0$, $\underline{\mathbf{V}}_{k,I} = \underline{\mathbf{V}}_k$ and $\underline{\mathbf{V}}_{k,Q}$ is a null matrix. Then the expression of the weight vector $\mathbf{w}_{k,I,c}$ in Equation (3.40a) can be simplified to

$$
\mathbf{w}_{k,I,c} = \big(\mathbf{H}_c\underline{\mathbf{V}}_k\mathbf{H}_c^T + E_s\mathbf{h}_{k,c}\mathbf{h}_{k,c}^T + \sigma_n^2\mathbf{I}_{2L}\big)^{-1} \cdot E_s\mathbf{h}_{k,c}, \qquad (3.41)
$$

which is the same as the RMMSE solution of Equation (3.30). Hence the RMMSE

technique constitutes a particular manifestation of the WL-MMSE algorithm in the context of BPSK systems. For non-BPSK systems, assuming $E_{sI} = E_{sQ} = \frac{1}{2}E_s$ and $\underline{\mathbf{V}}_{k,I} = \underline{\mathbf{V}}_{k,Q} = \frac{1}{2}\underline{\mathbf{V}}_k$, the weight vector expression of Equations (3.40) may be simplified to

$$\mathbf{w}_{k,I,c} = \mathbf{w}_{k,Q,c} = \left(\mathbf{H}_c\underline{\mathbf{V}}_k\mathbf{H}_c^T + \mathbf{H}_{c'}\underline{\mathbf{V}}_k\mathbf{H}_{c'}^T + E_s\mathbf{h}_c\mathbf{h}_c^T + E_s\mathbf{h}_{c'}\mathbf{h}_{c'}^T + 2\sigma_n^2\mathbf{I}_{2L}\right)^{-1} \cdot E_s\mathbf{h}_{k,c}. \tag{3.42}$$

This equation is equivalent to

$$\mathbf{w}_{k,I} = \mathbf{w}_{k,Q} = \left(\mathbf{H}\underline{\mathbf{V}}_k\mathbf{H}^H + E_s\mathbf{h}_k\mathbf{h}_k^H + 2\sigma_n^2\mathbf{I}_L\right)^{-1} \cdot E_s\mathbf{h}_k, \tag{3.43}$$

which is the same as the soft MMSE solution of Equation (3.16). This observation indicates that the soft WL-MMSE solution may have some potential gain over the soft MMSE solution, but only when the *a priori* information's variance recorded for the in-phase and quadrature-phase signal is different.

3.2.3.2 Output LLRs of the soft WL-MMSE MUD

Figure 3.6 shows the conditional PDFs of the WL-MMSE MUD's output signal using different weight vectors, when supporting K=4 users at E_b/N_0=5dB with the aid of *a priori* information. The arrival angles of the users' signal are 15°, 49°, −14° and −48°, respectively, as shown in Figure 3.4. We consider the first user as the desired user and assume that the transmitted symbol is $s_1 = +\frac{1}{\sqrt{2}}+j\frac{1}{\sqrt{2}}$ for QPSK and $s_1 = +\frac{3}{\sqrt{10}}+j\frac{3}{\sqrt{10}}$ for 16QAM. All the interfering users' *a priori* LLRs are listed in Table 3.1. Since different weight vectors $\mathbf{w}_{1,I}$ and $\mathbf{w}_{1,Q}$ are selected for detecting the in-phase and quadrature-phase components of signal s_1, the conditional PDFs $p(\hat{s}_1|\mathbf{w}_{1,I})$ and $p(\hat{s}_1|\mathbf{w}_{1,Q})$ may be different, which can be seen from Figure 3.6.

Similar to the distribution of the RMMSE beamformer's in-phase output, we can assume that the marginal conditional PDFs $p\left(\Re[\hat{s}_k]|s_k{=}s^{(p)}, \mathbf{w}_{k,I}\right)$ and $p\left(\Im[\hat{s}_k]|s_k{=}s^{(p)}, \mathbf{w}_{k,Q}\right)$ of the detector's output are both one-dimensional Gaussian distributed, which are indicated by the '+' points in Figure 3.6. Then, the means and variances of the marginal conditional PDFs are given by

$$\begin{aligned}\mu_{k,I}^{(p)} &= \mathrm{E}\left[\Re[\hat{s}_k]|s_k{=}s^{(p)}, \mathbf{w}_{k,I}\right] \\ &= \mathbf{w}_{k,I,c}^T\mathbf{H}_c \cdot \mathrm{E}\left[\Re[\mathbf{s}] - \Re[\underline{\mathbf{s}}_k]|s_k{=}s^{(p)}\right] + \mathbf{w}_{k,I,c}^T\mathbf{H}_{c'} \cdot \mathrm{E}\left[\Im[\mathbf{s}] - \Im[\underline{\mathbf{s}}_k]|s_k{=}s^{(p)}\right]\end{aligned}$$

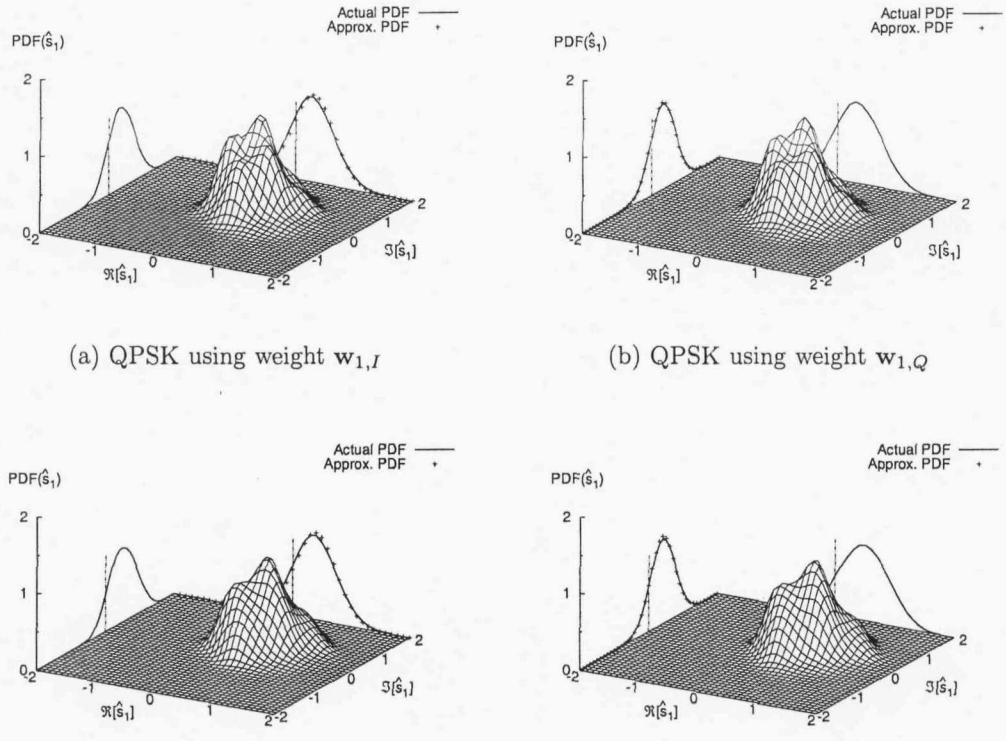

(a) QPSK using weight $\mathbf{w}_{1,I}$

(b) QPSK using weight $\mathbf{w}_{1,Q}$

(c) 16QAM using weight $\mathbf{w}_{1,I}$

(d) 16QAM using weight $\mathbf{w}_{1,Q}$

Figure 3.6: Conditional PDF $p(\hat{s}_1)$ (surface), marginal conditional PDFs $p(\Re[\hat{s}_1])$ and $p(\Im[\hat{s}_1])$ (solid curves) of the WL-MMSE MUD's output signal, and approximate Gaussian marginal conditional PDFs (+).

$$= \Re\big[s^{(p)}\big]\mathbf{w}_{k,I,c}^T\mathbf{h}_{k,c} + \Im\big[s^{(p)}\big]\mathbf{w}_{k,I,c}^T\mathbf{h}_{k,c'}, \tag{3.44a}$$

$$\begin{aligned}\mu_{k,Q}^{(p)} &= \mathrm{E}\big[\Im[\hat{s}_k]|s_k{=}s^{(p)}, \mathbf{w}_{k,Q}\big] \\ &= \mathbf{w}_{k,I,c}^T\mathbf{H}_c \cdot \mathrm{E}\big[\Im[\mathbf{s}] - \Im[\underline{\bar{\mathbf{s}}}_k]|s_k{=}s^{(p)}\big] - \mathbf{w}_{k,I,c}^T\mathbf{H}_{c'} \cdot \mathrm{E}\big[\Re[\mathbf{s}] - \Re[\underline{\bar{\mathbf{s}}}_k]|s_k{=}s^{(p)}\big] \\ &= \Im\big[s^{(p)}\big]\mathbf{w}_{k,Q,c}^T\mathbf{h}_{k,c} - \Re\big[s^{(p)}\big]\mathbf{w}_{k,Q,c}^T\mathbf{h}_{k,c'}\end{aligned} \tag{3.44b}$$

and

$$\begin{aligned}\sigma_{k,I}^2 &= \mathrm{E}\big[\Re^2[\hat{s}_k]|s_k{=}s^{(p)}, \mathbf{w}_{k,I}\big] - \big(\mu_{k,I}^{(p)}\big)^2 \\ &= \mathbf{w}_{k,I,c}^T\mathbf{H}_c \cdot \mathrm{E}\big[\big(\Re[\mathbf{s}] - \Re[\underline{\bar{\mathbf{s}}}_k]\big)\big(\Re^T[\mathbf{s}] - \Re^T[\underline{\bar{\mathbf{s}}}_k]\big)|s_k{=}s^{(p)}\big] \cdot \mathbf{H}_c^T\mathbf{w}_{k,I,c} \\ &\quad + \mathbf{w}_{k,I,c}^T\mathbf{H}_{c'} \cdot \mathrm{E}\big[\big(\Im[\mathbf{s}] - \Im[\underline{\bar{\mathbf{s}}}_k]\big)\big(\Im^T[\mathbf{s}] - \Im^T[\underline{\bar{\mathbf{s}}}_k]\big)|s_k{=}s^{(p)}\big] \cdot \mathbf{H}_{c'}^T\mathbf{w}_{k,I,c} \\ &\quad + 2\mathbf{w}_{k,I,c}^T\mathbf{H}_c \cdot \mathrm{E}\big[\big(\Re[\mathbf{s}] - \Re[\underline{\bar{\mathbf{s}}}_k]\big)\big(\Im^T[\mathbf{s}] - \Im^T[\underline{\bar{\mathbf{s}}}_k]\big)|s_k{=}s^{(p)}\big] \cdot \mathbf{H}_{c'}^T\mathbf{w}_{k,I,c} \\ &\quad + \mathbf{w}_{k,I,c}^T \cdot \mathrm{E}\big[\mathbf{n}_c\mathbf{n}_c^T\big] \cdot \mathbf{w}_{k,I,c} - \big(\Re\big[s^{(p)}\big]\mathbf{w}_{k,I,c}^T\mathbf{h}_{k,c} + \Im\big[s^{(p)}\big]\mathbf{w}_{k,I,c}^T\mathbf{h}_{k,c'}\big)^2 \\ &= \mathbf{w}_{k,I,c}^T\big(\mathbf{H}_c\underline{\mathbf{V}}_{k,I}\mathbf{H}_c^T + \mathbf{H}_{c'}\underline{\mathbf{V}}_{k,Q}\mathbf{H}_{c'}^T + \sigma_n^2\mathbf{I}_{2L}\big)\mathbf{w}_{k,I,c},\end{aligned} \tag{3.45a}$$

$$\begin{aligned}\sigma_{k,Q}^2 &= \mathrm{E}\big[\Im^2[\hat{s}_k]|s_k{=}s^{(p)}, \mathbf{w}_{k,Q}\big] - \big(\mu_{k,Q}^{(p)}\big)^2 \\ &= \mathbf{w}_{k,Q,c}^T\mathbf{H}_c \cdot \mathrm{E}\big[(\Im[\mathbf{s}] - \Im[\underline{\bar{\mathbf{s}}}_k])\big(\Im^T[\mathbf{s}] - \Im^T[\underline{\bar{\mathbf{s}}}_k]\big)|s_k{=}s^{(p)}\big] \cdot \mathbf{H}_c^T\mathbf{w}_{k,Q,c} \\ &\quad + \mathbf{w}_{k,Q,c}^T\mathbf{H}_{c'} \cdot \mathrm{E}\big[(\Re[\mathbf{s}] - \Re[\underline{\bar{\mathbf{s}}}_k])\big(\Re^T[\mathbf{s}] - \Re^T[\underline{\bar{\mathbf{s}}}_k]\big)|s_k{=}s^{(p)}\big] \cdot \mathbf{H}_{c'}^T\mathbf{w}_{k,Q,c} \\ &\quad - 2\mathbf{w}_{k,Q,c}^T\mathbf{H}_c \cdot \mathrm{E}\big[(\Im[\mathbf{s}] - \Im[\underline{\bar{\mathbf{s}}}_k])\big(\Re^T[\mathbf{s}] - \Re^T[\underline{\bar{\mathbf{s}}}_k]\big)|s_k{=}s^{(p)}\big] \cdot \mathbf{H}_{c'}^T\mathbf{w}_{k,Q,c} \\ &\quad + \mathbf{w}_{k,Q,c}^T \cdot \mathrm{E}\big[\mathbf{n}_{c'}\mathbf{n}_{c'}^T\big] \cdot \mathbf{w}_{k,Q,c} - \big(\Im\big[s^{(p)}\big]\mathbf{w}_{k,Q,c}^T\mathbf{h}_{k,c} - \Re\big[s^{(p)}\big]\mathbf{w}_{k,Q,c}^T\mathbf{h}_{k,c'}\big)^2 \\ &= \mathbf{w}_{k,Q,c}^T\big(\mathbf{H}_c\underline{\mathbf{V}}_{k,Q}\mathbf{H}_c^T + \mathbf{H}_{c'}\underline{\mathbf{V}}_{k,I}\mathbf{H}_{c'}^T + \sigma_n^2\mathbf{I}_{2L}\big)\mathbf{w}_{k,Q,c}. \end{aligned} \tag{3.45b}$$

Using Equations (3.40), the variances are simplified to

$$\begin{aligned}\sigma_{k,I}^2 &= \mathbf{w}_{k,I,c}^T\big(\mathbf{H}_c\underline{\mathbf{V}}_{k,I}\mathbf{H}_c^T + E_{sI}\mathbf{h}_{k,c}\mathbf{h}_{k,c}^T + \mathbf{H}_{c'}\underline{\mathbf{V}}_{k,Q}\mathbf{H}_{c'}^T + E_{sQ}\mathbf{h}_{k,c'}\mathbf{h}_{k,c'}^T + \sigma_n^2\mathbf{I}_{2L}\big)\mathbf{w}_{k,I,c} \\ &\quad - E_{sI}\mathbf{w}_{k,I,c}^T\mathbf{h}_{k,c}\mathbf{h}_{k,c}^T\mathbf{w}_{k,I,c} - E_{sQ}\mathbf{w}_{k,I,c}^T\mathbf{h}_{k,c'}\mathbf{h}_{k,c'}^T\mathbf{w}_{k,I,c} \\ &= E_{sI}\mathbf{w}_{k,I,c}^T\mathbf{h}_{k,c} - E_{sI}\mathbf{w}_{k,I,c}^T\mathbf{h}_{k,c}\mathbf{h}_{k,c}^T\mathbf{w}_{k,I,c} - E_{sQ}\mathbf{w}_{k,I,c}^T\mathbf{h}_{k,c'}\mathbf{h}_{k,c'}^T\mathbf{w}_{k,I,c} \\ &= E_{sI}\mathbf{w}_{k,I,c}^T\mathbf{h}_{k,c}\big(1 - \mathbf{w}_{k,I,c}^T\mathbf{h}_{k,c}\big) - E_{sQ}\big(\mathbf{w}_{k,I,c}^T\mathbf{h}_{k,c'}\big)^2, \end{aligned} \tag{3.46a}$$

$$\begin{aligned}\sigma_{k,Q}^2 &= \mathbf{w}_{k,Q,c}^T\big(\mathbf{H}_c\underline{\mathbf{V}}_{k,Q}\mathbf{H}_c^T + E_{sQ}\mathbf{h}_{k,c}\mathbf{h}_{k,c}^T + \mathbf{H}_{c'}\underline{\mathbf{V}}_{k,I}\mathbf{H}_{c'}^T + E_{sI}\mathbf{h}_{k,c'}\mathbf{h}_{k,c'}^T + \sigma_n^2\mathbf{I}_{2L}\big)\mathbf{w}_{k,Q,c} \\ &\quad - E_{sQ}\mathbf{w}_{k,Q,c}^T\mathbf{h}_{k,c}\mathbf{h}_{k,c}^T\mathbf{w}_{k,Q,c} - E_{sI}\mathbf{w}_{k,Q,c}^T\mathbf{h}_{k,c'}\mathbf{h}_{k,c'}^T\mathbf{w}_{k,Q,c} \\ &= E_{sQ}\mathbf{w}_{k,Q,c}^T\mathbf{h}_{k,c} - E_{sQ}\mathbf{w}_{k,Q,c}^T\mathbf{h}_{k,c}\mathbf{h}_{k,c}^T\mathbf{w}_{k,Q,c} - E_{sI}\mathbf{w}_{k,Q,c}^T\mathbf{h}_{k,c'}\mathbf{h}_{k,c'}^T\mathbf{w}_{k,Q,c} \\ &= E_{sQ}\mathbf{w}_{k,Q,c}^T\mathbf{h}_{k,c}\big(1 - \mathbf{w}_{k,Q,c}^T\mathbf{h}_{k,c}\big) - E_{sI}\big(\mathbf{w}_{k,Q,c}^T\mathbf{h}_{k,c'}\big)^2. \end{aligned} \tag{3.46b}$$

For BPSK system, the expression of the output LLRs is the same as that of the RMMSE solution shown in Equation (3.35). For higher-order QAM schemes the output LLRs of the WL-MMSE MUD are

$$L_E\big(b_k(i)\big) = \ln \frac{\sum_{\substack{\forall s^{(p)} \\ b^{(p)}(i)=+1}} \exp\left(-\frac{\left(\Re[\hat{s}_k]-\mu_{k,I}^{(p)}\right)^2}{2\sigma_{k,I}^2}\right)\prod_{\forall i'\neq i} P\big(b_k(i')=b^{(p)}(i')\big)}{\sum_{\substack{\forall s^{(p)} \\ b^{(p)}(i)=-1}} \exp\left(-\frac{\left(\Re[\hat{s}_k]-\mu_{k,I}^{(p)}\right)^2}{2\sigma_{k,I}^2}\right)\prod_{\forall i'\neq i} P\big(b_k(i')=b^{(p)}(i')\big)} \tag{3.47a}$$

when $b_k(i)$ is mapped to the real part of s_k, and

$$L_E\big(b_k(i)\big) = \ln \frac{\sum_{\substack{\forall s^{(p)} \\ b^{(p)}(i)=+1}} \exp\left(-\frac{\left(\Im[\hat{s}_k]-\mu_{k,Q}^{(p)}\right)^2}{2\sigma_{k,Q}^2}\right)\prod_{\forall i'\neq i} P\big(b_k(i')=b^{(p)}(i')\big)}{\sum_{\substack{\forall s^{(p)} \\ b^{(p)}(i)=-1}} \exp\left(-\frac{\left(\Im[\hat{s}_k]-\mu_{k,Q}^{(p)}\right)^2}{2\sigma_{k,Q}^2}\right)\prod_{\forall i'\neq i} P\big(b_k(i')=b^{(p)}(i')\big)} \tag{3.47b}$$

when $b_k(i)$ is mapped to the imaginary part of s_k. Compared to the MMSE solution's output LLRs seen in Equation (3.22), the WL-MMSE MUD's output LLRs have the same expression, but exhibit different means and variances for the in-phase and quadrature-phase components of the signal.

3.2.3.3 Computational Complexity of the Soft WL-MMSE MUD

The soft WL-MMSE MUD's computational complexity per symbol per user is summarized in Table 3.4. The related equations are also given in Table 3.4. For BPSK systems, the complexity is the same as that of the RMMSE solution listed in Table 3.3. For higher-order QAM constellations, the complexity of the soft WL-MMSE is about twice of that of the soft MMSE. This doubled complexity is attributable to that of the weight vector calculation.

Table 3.4: Computational complexity of the soft WL-MMSE MUD

		Computational complexity	Equations
Mean & variance	QPSK	16	(3.10), (3.11)
	16QAM	32	
Weight vector		$\mathcal{O}(16L^3) + 32KL^2 + 16L^2 + 4L$	(3.40)
LLRs		$8KL+16L+(M\log_2 M+4M+5)\log_2 M+6M+6$	(3.47)

3.2.4 SISO Interference Cancellation Using the MBER MUD

The MMSE algorithm does not guarantee the direct and explicit minimisation of the system's BER. However, the MBER beamforming design, in which the BER rather than the MSE was minimised at the MUD's output, is the true optimal solution and hence it generally outperforms the MMSE solution.

3.2.4.1 Bit Error Rate

In *M-ary* PSK systems supporting K users, the transmitted symbol combination may assume M^K possible combinations, here however we limit our discussions to BPSK (M=2) and QPSK (M=4). Let us now consider a QPSK system, where

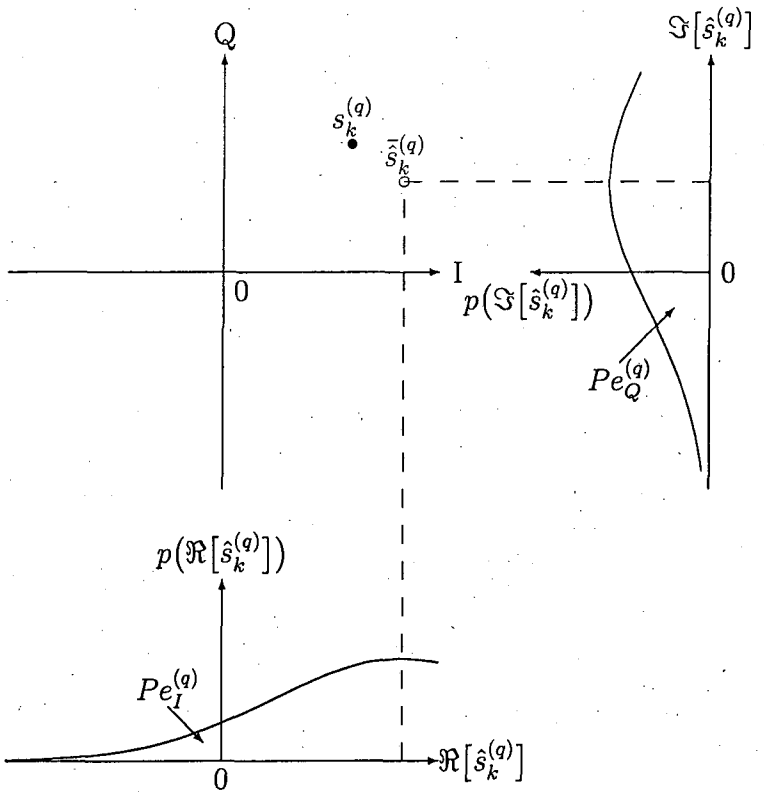

Figure 3.7: Symbol $s_k^{(q)}$ of a QPSK constellation with the interference-contaminated expectation $\bar{\hat{s}}_k^{(q)}$ of the estimated signal $\hat{s}_k^{(q)}$ and the PDFs of the in-phase and quadrature-phase component of the estimated signal.

the qth possible symbol combination $\mathbf{s}^{(q)}$ is transmitted, in which the desired user's symbol $s_k^{(q)}$ is $+\frac{\sqrt{2}}{2}+j\frac{\sqrt{2}}{2}$. Figure 3.7 shows the transmitted symbol $s_k^{(q)}$, the interference-contaminated expectation $\bar{\hat{s}}_k^{(q)}$ of the estimated signal $\hat{s}_k^{(q)}$ and the PDFs of the in-phase and quadrature-phase component of the estimated signal. As seen in Figure 3.7, the PDFs of the in-phase and quadrature-phase component of $\hat{s}_k^{(q)}$ are both one-dimensional Gaussian distributed. The error probabilities of the in-phase and quadrature-phase component are denoted by $Pe_I^{(q)}$ and $Pe_Q^{(q)}$, respectively. The error probability $Pe_I^{(q)}$ is given by the integral of the PDF $p(\Re[\hat{s}_k^{(q)}])$ the wrong side of the decision boundary of $\Re[\hat{s}_k^{(q)}] = 0$, and and $Pe_Q^{(q)}$ can be derived in a similar way.

By defining $x = \text{sgn}(\Re[s_k]) \cdot \Re[\hat{s}_k]$, the conditional PDF of x is a Gaussian

mixture given by [29]

$$p(x) = \sum_{q=1}^{M^K} \underline{P}_k\left(\mathbf{s}^{(q)}\right) \cdot \mathrm{sgn}\left(\Re\left[s_k^{(q)}\right]\right) \cdot p\left(\Re\left[\hat{s}_k^{(q)}\right]\right)$$
$$= \frac{1}{\sqrt{2\pi}\sigma_n\sqrt{\mathbf{w}_k^H\mathbf{w}_k}} \sum_{q=1}^{M^K} \underline{P}_k\left(\mathbf{s}^{(q)}\right) \cdot \exp\left(-\frac{\left(x - \mathrm{sgn}\left(\Re\left[s_k^{(q)}\right]\right) \cdot \Re\left[\bar{\hat{s}}_k^{(q)}\right]\right)^2}{2\sigma_n^2\mathbf{w}_k^H\mathbf{w}_k}\right), \tag{3.48}$$

where $\underline{P}_k\left(\mathbf{s}^{(q)}\right) = \frac{1}{M}\prod_{\forall k' \neq k} P\left(s_{k'}=s_{k'}^{(q)}\right)$ is the probability of transmitting the qth possible symbol combination $\mathbf{s}^{(q)}$ based on the *a priori* information of the other $(K-1)$ users except for user k, and $\bar{\hat{s}}_k^{(q)}$ is the kth user's estimated symbol, when ignoring the effects of noise, yielding

$$\bar{\hat{s}}_k^{(q)} = \mathbf{w}_k^H\left(\mathbf{H}\mathbf{s}^{(q)} - \mathbf{H}\underline{\bar{\mathbf{s}}}_k\right)$$
$$= \mathbf{w}_k^H\bar{\mathbf{r}}_k^{(q)}. \tag{3.49}$$

It can be readily shown that the error probability of the in-phase part is

$$Pe_I = P(x<0) = \int_{-\infty}^{0} p(x)dx$$
$$= \sum_{q=1}^{M^K} \underline{P}_k\left(\mathbf{s}^{(q)}\right) \cdot Pe_I^{(q)}$$
$$= \sum_{q=1}^{M^K} \underline{P}_k\left(\mathbf{s}^{(q)}\right) \cdot \mathrm{Q}\left(\frac{\mathrm{sgn}\left(\Re\left[s_k^{(q)}\right]\right) \cdot \Re\left[\bar{\hat{s}}_k^{(q)}\right]}{\sigma_n\sqrt{\mathbf{w}_k^H\mathbf{w}_k}}\right). \tag{3.50}$$

where $\mathrm{Q}(x) = \frac{1}{\sqrt{2\pi}}\int_{-\infty}^{-x} e^{-t^2/2}dt$. Similarly, the error probability of the quadrature-phase part is

$$Pe_Q = \sum_{q=1}^{M^K} \underline{P}_k\left(\mathbf{s}^{(q)}\right) \cdot \mathrm{Q}\left(\frac{\mathrm{sgn}\left(\Im\left[s_k^{(q)}\right]\right) \cdot \Im\left[\bar{\hat{s}}_k^{(q)}\right]}{\sigma_n\sqrt{\mathbf{w}_k^H\mathbf{w}_k}}\right). \tag{3.51}$$

Hence the BER of the beamformer is

$$Pe_b = \begin{cases} Pe_I & \text{(BPSK)} \\ \frac{1}{2}(Pe_I + Pe_Q) & \text{(QPSK)} \end{cases}. \tag{3.52}$$

3.2.4.2 Weights of the Soft MBER MUD

The MBER beamforming solution is then defined as [29]

$$\mathbf{w}_k = \arg\min_{\mathbf{w}_k} Pe_b. \tag{3.53}$$

This optimization problem can be solved using the SCG algorithm, which is detailed in Section 2.2.5. Basing on the derivation in Appendix A.1, the gradients of both the in-phase and quadrature-phase bit error probabilities are

$$\begin{aligned}\nabla Pe_I &= 2\frac{\partial Pe_I}{\partial \mathbf{w}_k^*} \\ &= \frac{1}{\sqrt{2\pi}\sigma_n\sqrt{\mathbf{w}_k^H\mathbf{w}_k}}\sum_{q=1}^{M^K} \underline{P}_k\left(\mathbf{s}^{(q)}\right)\cdot\exp\left(-\frac{\left(\Re\left[\tilde{s}_k^{(q)}\right]\right)^2}{2\sigma_n^2\mathbf{w}_k^H\mathbf{w}_k}\right)\cdot \\ &\quad \cdot\operatorname{sgn}\left(\Re\left[s_k^{(q)}\right]\right)\left(\frac{\Re\left[\tilde{s}_k^{(q)}\right]\mathbf{w}_k}{\mathbf{w}_k^H\mathbf{w}_k}-\bar{\mathbf{r}}_k^{(q)}\right)\end{aligned} \tag{3.54a}$$

and

$$\begin{aligned}\nabla Pe_Q &= 2\frac{\partial Pe_Q}{\partial \mathbf{w}_k^*} \\ &= \frac{1}{\sqrt{2\pi}\sigma_n\sqrt{\mathbf{w}_k^H\mathbf{w}_k}}\sum_{q=1}^{M^K} \underline{P}_k\left(\mathbf{s}^{(q)}\right)\cdot\exp\left(-\frac{\left(\Im\left[\tilde{s}_k^{(q)}\right]\right)^2}{2\sigma_n^2\mathbf{w}_k^H\mathbf{w}_k}\right)\cdot \\ &\quad \cdot\operatorname{sgn}\left(\Im\left[s_k^{(q)}\right]\right)\left(\frac{\Im\left[\tilde{s}_k^{(q)}\right]\mathbf{w}_k}{\mathbf{w}_k^H\mathbf{w}_k}+j\bar{\mathbf{r}}_k^{(q)}\right).\end{aligned} \tag{3.54b}$$

3.2.4.3 Weights of the Soft WL-MBER MUD

For QPSK systems, the WL-MBER solution can be applied, which is defined by

$$\mathbf{w}_{k,I} = \arg\min_{\mathbf{w}_k} Pe_I, \tag{3.55a}$$

$$\mathbf{w}_{k,Q} = \arg\min_{\mathbf{w}_k} Pe_Q. \tag{3.55b}$$

The gradient formulas of Equations (3.54) can be used to find the optimum weights for the WL-MBER solution. The WL-MBER weight calculation has the same complexity as that of the MBER MUD formulated in Equation (3.53).

3.2.4.4 Output LLRs of the Soft MBER MUD

Figure 3.8 shows the conditional PDFs of the MBER MUD's output signal supporting K=4 users at E_b/N_0=5dB both with and without *a priori* information. The arrival angles of the users' signal are 15°, 49°, −14° and −48°, respectively, as seen in Figure 3.4. We consider the first user as the desired user and assume that the transmitted symbol is $s_1 = +1$ for BPSK and $s_1 = +\frac{1}{\sqrt{2}}+j\frac{1}{\sqrt{2}}$ for QPSK. In the scenarios associated with *a priori* information, all the interfering users' *a priori* LLRs are listed in Table 3.1. For the BPSK system, despite the fact that the marginal conditional PDF of the imaginary part $p\big(\Im[\hat{s}_k]|s_k{=}s^{(p)}\big)$ seen in Figure 3.8a is clearly non-Gaussian distributed, the real part's $p\big(\Re[\hat{s}_k]|s_k{=}s^{(p)}\big)$, however, can be assumed to be Gaussian Gaussian distributed. For QPSK sys-

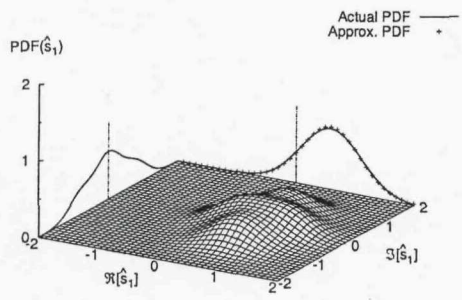

(a) BPSK without *a priori* information

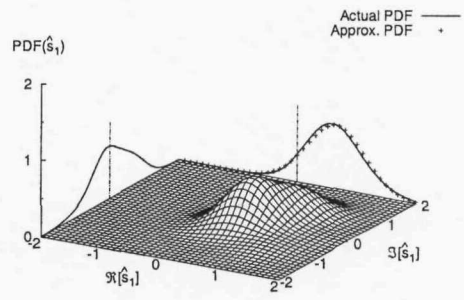

(b) BPSK with *a priori* information

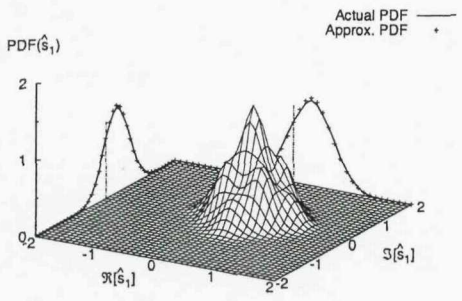

(c) QPSK without *a priori* information

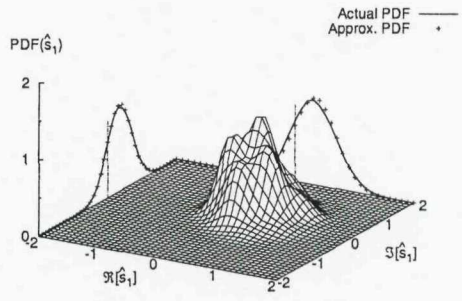

(d) QPSK with *a priori* information

Figure 3.8: Conditional PDF $p(\hat{s}_1)$ (surface), marginal conditional PDFs $p(\Re[\hat{s}_1])$ and $p(\Im[\hat{s}_1])$ (solid curves) of the MBER MUD's output signal, and approximate Gaussian marginal conditional PDFs (+).

tems, both the marginal conditional PDFs $p\big(\Re[\hat{s}_k]|s_k{=}s^{(p)}\big)$ and $p\big(\Im[\hat{s}_k]|s_k{=}s^{(p)}\big)$ are approximately Gaussian distributed as seen in Figure 3.8c. We should also observe that when the SNR is high, the Gaussian assumption mentioned above may no longer be accurate. Fortunately, the proposed SISO beamforming is employed in iterative systems, which typically operate in the low SNR region.

For our BPSK MBER design as suggested by Figure 3.8a, we assume that the conditional PDF $p\big(\Re[\hat{s}_k]|s_k{=}s^{(p)}\big)$ is Gaussian distributed. The conditional mean and variance of $\Re[\hat{s}_k]$ are given by

$$\begin{aligned}\mu_k^{(p)} &= \mathrm{E}\big[\Re[\hat{s}_k]|s_k{=}s^{(p)}\big] \\ &= s^{(p)}\Re\big[\mathbf{w}_k^H\mathbf{h}_k\big]\end{aligned} \tag{3.56}$$

and

$$\begin{aligned}\sigma_k^2 &= \mathrm{E}\big[\Re^2[\hat{s}_k]|s_k{=}s^{(p)}\big] - \big(\mu_k^{(p)}\big)^2 \\ &= \Re\big[\mathbf{w}_k^H\mathbf{H}\big]\underline{\mathbf{V}}_k\Re\big[\mathbf{H}^H\mathbf{w}_k\big] + \sigma_n^2\mathbf{w}_k^H\mathbf{w}_k.\end{aligned} \tag{3.57}$$

They are equivalent to the mean and variance expressions of the RMMSE solution seen in Equations (3.31) and (3.32), respectively. However, since the MBER design does not have a closed-form weight solution, the simplified Equation (3.33) cannot be applied for the MBER MUD's variance. Then the extrinsic output LLR can be expressed as

$$L_E\big(b_k(1)\big) = \frac{2\Re[\hat{s}_k]\Re\big[\mathbf{w}_k^H\mathbf{h}_k\big]}{\Re\big[\mathbf{w}_k^H\mathbf{H}\big]\underline{\mathbf{V}}_k\Re\big[\mathbf{H}^H\mathbf{w}_k\big] + \sigma_n^2\mathbf{w}_k^H\mathbf{w}_k}, \tag{3.58}$$

which is similar to Equation (3.35) for the RMMSE MUD, but no common factor $\Re\big[\mathbf{w}_k^H\mathbf{h}_k\big]$ exists in the numerator and the denominator in Equation (3.58).

For our QPSK MBER design based on Figure 3.8c, we assume that the marginal conditional PDFs $p\big(\Re[\hat{s}_k]|s_k{=}s^{(p)}\big)$ and $p\big(\Im[\hat{s}_k]|s_k{=}s^{(p)}\big)$ are both one-dimensional Gaussian distributed. Then, the means and variances of the in-phase and quadrature-phase components of $\hat{s}_k$ are given by

$$\begin{aligned}\mu_{k,I}^{(p)} &= \mathrm{E}\big[\Re[\hat{s}_k]|s_k{=}s^{(p)}\big] \\ &= \Re\big[s^{(p)}\mathbf{w}_k^H\mathbf{h}_k\big], \\ \mu_{k,Q}^{(p)} &= \mathrm{E}\big[\Im[\hat{s}_k]|s_k{=}s^{(p)}\big]\end{aligned} \tag{3.59a}$$

$$= \Im\left[s^{(p)}\mathbf{w}_k^H\mathbf{h}_k\right] \tag{3.59b}$$

and

$$\begin{aligned}\sigma_{k,I}^2 &= \mathrm{E}\left[\Re^2[\hat{s}_k]|s_k{=}s^{(p)}\right] - \left(\mu_{k,I}^{(p)}\right)^2 \\ &= \Re\left[\mathbf{w}_k^H\mathbf{H}\right]\underline{\mathbf{V}}_{k,I}\Re\left[\mathbf{H}^H\mathbf{w}_k\right] - \Im\left[\mathbf{w}_k^H\mathbf{H}\right]\underline{\mathbf{V}}_{k,Q}\Im\left[\mathbf{H}^H\mathbf{w}_k\right] + \sigma_n^2\mathbf{w}_k^H\mathbf{w}_k, \quad (3.60a) \\ \sigma_{k,Q}^2 &= \mathrm{E}\left[\Im^2[\hat{s}_k]|s_k{=}s^{(p)}\right] - \left(\mu_{k,Q}^{(p)}\right)^2 \\ &= \Re\left[\mathbf{w}_k^H\mathbf{H}\right]\underline{\mathbf{V}}_{k,Q}\Re\left[\mathbf{H}^H\mathbf{w}_k\right] - \Im\left[\mathbf{w}_k^H\mathbf{H}\right]\underline{\mathbf{V}}_{k,I}\Im\left[\mathbf{H}^H\mathbf{w}_k\right] + \sigma_n^2\mathbf{w}_k^H\mathbf{w}_k, \quad (3.60b)\end{aligned}$$

where $\underline{\mathbf{V}}_{k,I} = \mathrm{diag}[v_{1,I}\cdots v_{k-1,I}\ 0\ v_{k+1,I}\cdots v_{K,I}]$, $v_{k',I} = \frac{1}{2}E_s - \Re^2[\bar{s}_{k'}]$ and $\underline{\mathbf{V}}_{k,Q} = \mathrm{diag}[v_{1,Q}\cdots v_{k-1,Q}\ 0\ v_{k+1,Q}\cdots v_{K,Q}]$, $v_{k',Q} = \frac{1}{2}E_s - \Im^2[\bar{s}_{k'}]$. They are equivalent to Equations (3.44) and (3.45) for the WL-MMSE solution, but employ a single weight vector for the in-phase and quadrature-phase components. Then the extrinsic output LLRs can be expressed as

$$L_E\big(b_k(1)\big) = \ln\frac{\sum_{\forall s^{(p)}\ b^{(p)}(1)=+1}\exp\left(-\frac{\left(\Re[\hat{s}_k]-\mu_{k,I}^{(p)}\right)^2}{2\sigma_{k,I}^2}\right)P\big(b_k(2){=}b^{(p)}(2)\big)}{\sum_{\forall s^{(p)}\ b^{(p)}(1)=-1}\exp\left(-\frac{\left(\Re[\hat{s}_k]-\mu_{k,I}^{(p)}\right)^2}{2\sigma_{k,I}^2}\right)P\big(b_k(2){=}b^{(p)}(2)\big)}, \tag{3.61a}$$

$$L_E\big(b_k(2)\big) = \ln\frac{\sum_{\forall s^{(p)}\ b^{(p)}(2)=+1}\exp\left(-\frac{\left(\Im[\hat{s}_k]-\mu_{k,Q}^{(p)}\right)^2}{2\sigma_{k,Q}^2}\right)P\big(b_k(1){=}b^{(p)}(1)\big)}{\sum_{\forall s^{(p)}\ b^{(p)}(2)=-1}\exp\left(-\frac{\left(\Im[\hat{s}_k]-\mu_{k,Q}^{(p)}\right)^2}{2\sigma_{k,Q}^2}\right)P\big(b_k(1){=}b^{(p)}(1)\big)}, \tag{3.61b}$$

which are the same expressions as those of the WL-MMSE's output LLRs of Equations (3.47).

3.2.4.5 Output LLRs of the Soft WL-MBER MUD

Figure 3.9 shows the conditional PDFs of the WL-MBER MUD's output signal supporting K=4 QPSK users at E_b/N_0=5dB with the aid of *a priori* information. The arrival angles of the users' signal are 15°, 49°, −14° and −48°, respectively, as seen in Figure 3.4. We consider the first user as the desired user and assume that the transmitted symbol is $s_1 = +\frac{1}{\sqrt{2}}+j\frac{1}{\sqrt{2}}$. All the interfering users' *a priori* LLRs are listed in Table 3.1. We can assume that the marginal conditional PDFs $p\big(\Re[\hat{s}_k]|s_k{=}s^{(p)}, \mathbf{w}_{k,I}\big)$ and $p\big(\Im[\hat{s}_k]|s_k{=}s^{(p)}, \mathbf{w}_{k,Q}\big)$ of the detector's output are both one-dimensional Gaussian distributed, as suggested by the '+' points shown in

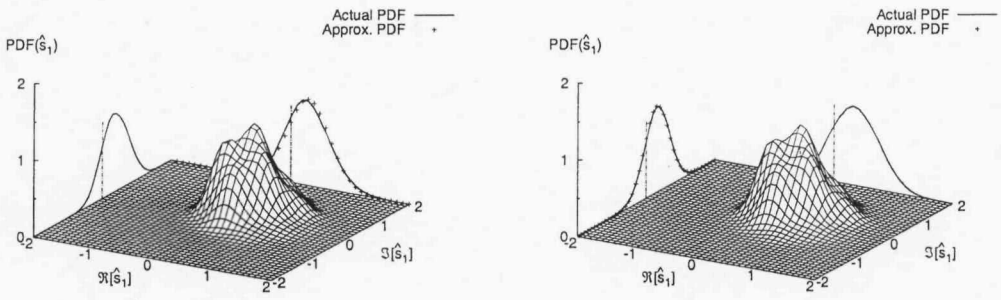

(a) Using weight $\mathbf{w}_{1,I}$ (b) Using weight $\mathbf{w}_{1,Q}$

Figure 3.9: Conditional PDF $p(\hat{s}_1)$ (surface), marginal conditional PDFs $p(\Re[\hat{s}_1])$ and $p(\Im[\hat{s}_1])$ (solid curves) of the WL-MBER MUD's output signal, and approximate Gaussian marginal conditional PDFs (+).

Figure 3.9.

The expressions of the extrinsic information delivered by the WL-MBER MUD for the in-phase and quadrature-phase components are the same as in Equations (3.61). However the means and variances of the in-phase and quadrature-phase components of $\hat{s}_k$ are changed to

$$\mu_{k,I}^{(p)} = \Re\left[s^{(p)}\mathbf{w}_{k,I}^H\mathbf{h}_k\right], \tag{3.62a}$$

$$\mu_{k,Q}^{(p)} = \Im\left[s^{(p)}\mathbf{w}_{k,Q}^H\mathbf{h}_k\right] \tag{3.62b}$$

and

$$\sigma_{k,I}^2 = \Re\left[\mathbf{w}_{k,I}^H\mathbf{H}\right]\underline{\mathbf{V}}_{k,I}\Re\left[\mathbf{H}^H\mathbf{w}_{k,I}\right] - \Im\left[\mathbf{w}_{k,I}^H\mathbf{H}\right]\underline{\mathbf{V}}_{k,Q}\Im\left[\mathbf{H}^H\mathbf{w}_{k,I}\right] + \sigma_n^2\mathbf{w}_{k,I}^H\mathbf{w}_{k,I}, \tag{3.63a}$$

$$\sigma_{k,Q}^2 = \Re\left[\mathbf{w}_{k,Q}^H\mathbf{H}\right]\underline{\mathbf{V}}_{k,Q}\Re\left[\mathbf{H}^H\mathbf{w}_{k,Q}\right] - \Im\left[\mathbf{w}_{k,Q}^H\mathbf{H}\right]\underline{\mathbf{V}}_{k,I}\Im\left[\mathbf{H}^H\mathbf{w}_{k,Q}\right] + \sigma_n^2\mathbf{w}_{k,Q}^H\mathbf{w}_{k,Q}, \tag{3.63b}$$

which may be contrasted to Equations (3.59) and (3.60).

3.2.4.6 Computational Complexity of the Soft MBER MUD

The soft MBER MUD's computational complexity per symbol per user is summarized in Table 3.5 in terms of the number of real-valued additions and multiplications evaluated. The related equations are also given in this table. It is shown

that the total computational complexity of the soft MBER mainly depends on the calculation of the weight vector, which is $\mathcal{O}\left(LN_{cg}M^K\right)$, where N_{cg} denotes the number of iterations required by the SCG method. The computational complexity of the soft MBER MUD increases exponentially with the number of users. This implies that the soft MBER MUD is significantly more complex than the soft MMSE MUD of Table 3.2 and the soft WL-MMSE MUD of Table 3.4. The soft WL-MBER MUD has the same complexity as the soft MBER MUD for QPSK systems, as seen by comparing Equations (3.55) with Equation (3.53).

Table 3.5: Computational complexity of the soft MBER MUD

		Computational complexity	Equation(s)
Mean & variance	BPSK	6	(3.10), (3.11)
	QPSK	12	
Weight vector		$\Big(\big((6L+6)\log_2 M + 8L - 2\big)N_{cg} + 8KL - 2L + 3K - 3\Big)M^K + (18L+2)N_{cg} + (M+8)\log_2 M - M$	(3.53), (3.54)
LLRs	BPSK	$12KL + 16L - 2$	(3.58)
	QPSK	$16KL + 38L + 10K + 57$	(3.61)

3.2.5 SISO Interference Cancellation Using the MSER MUD

The noise-free estimated symbol $\bar{\hat{s}}_k^{(q)}$ of Equation (3.49) can be rewritten as

$$\begin{aligned}\bar{\hat{s}}_k^{(q)} &= \mathbf{w}_k^H\Big(\mathbf{h}_k s_k^{(q)} + \sum_{k'\neq k}\mathbf{h}_{k'}s_{k'}^{(q)} - \mathbf{H}\bar{\underline{\mathbf{s}}}_k\Big)\\ &= \mathbf{w}_k^H\mathbf{h}_k s_k^{(q)} + \sum_{k'\neq k}\mathbf{w}_k^H\mathbf{h}_{k'}s_{k'}^{(q)} - \mathbf{w}_k^H\mathbf{H}\bar{\underline{\mathbf{s}}}_k,\end{aligned} \tag{3.64}$$

where $q \in \{1, 2, \cdots, M^K\}$. Let us now consider a specific transmitted symbol $s^{(p)}$ of user k in the constellation and investigate the properties of the symbol subset $\left\{\bar{\hat{s}}_k^{(q)} | s_k^{(q)}{=}s^{(p)}\right\}$. It is readily known from Equation (3.64) that this symbol subset has a center of $\left(\mathbf{w}_k^H\mathbf{h}_k s_k^{(q)} - \mathbf{w}_k^H\mathbf{H}\bar{\underline{\mathbf{s}}}_k\right)$. Furthermore, for any symbol $\bar{\hat{s}}_k^{(q)}$ in this subset, a symmetric symbol $\bar{\hat{s}}_k^{(\bar{q})}$ exists at the other side of the center with $s_{k'}^{(\bar{q})} = -s_{k'}^{(q)}$ for all $k' \neq k$.

In [33, 34], the MSER algorithm was investigated when the MUD has access

to no *a priori* information. This implies that the *a priori* probabilities of all symbol combinations $\{\mathbf{s}^{(q)}\}$ are the same, namely $\frac{1}{M^K}$. Moreover, in [34], the weight $\mathbf{w}_k$ was rotated to make $\mathbf{w}_k^H\mathbf{h}_k$ real and positive. Hence the symbol subset $\{\bar{\hat{s}}_k^{(q)}|s_k^{(q)}=s^{(p)}\}$ can be shifted parallel to the decision boundary, when user k transmits a neighboring symbol in the constellation. Under these constraints, the PDF subsets $\{P(\mathbf{s}^{(q)})\cdot p(\hat{s}_k^{(q)})\}$ satisfy the shifting properties and are symmetrically distributed [34], which may be used to simplify the weight vector calculation. However, when the MUD is provided with useful *a priori* information, these lemmas are invalid and the MSER method of [34] needs further modifications. Hence in this section we introduce the *a priori* information aided MSER MUD to resolve this problem.

3.2.5.1 Symbol Error Rate

Let us now consider an M-QAM system, and define the transmitted symbol as $s^{(m,n)} = \frac{\sqrt{3E_s}}{\sqrt{2(M-1)}}(2m-\sqrt{M}-1)+j\frac{\sqrt{3E_s}}{\sqrt{2(M-1)}}(2n-\sqrt{M}-1)$, where we have $m\in\{1,2,\cdots,\sqrt{M}\}$ and $n\in\{1,2,\cdots,\sqrt{M}\}$. Figure 3.10 shows an example of the estimated signal $\hat{s}_k^{(q)}$ and its marginal PDFs, when user k transmits symbol $s_k^{(q)}=s^{(m,n)}$. The PDF of $\hat{s}_k^{(q)}$ is a Gaussian distribution with a mean value of $\bar{\hat{s}}_k^{(q)}$, as seen in Figure 3.10. Then, when the kth user transmits symbol $s^{(m,n)}$, the conditional PDF of $\hat{s}_k$ is a Gaussian mixture defined by

$$\begin{aligned} p(\hat{s}_k|s_k=s^{(m,n)}) &= M\sum_{\substack{\forall \mathbf{s}^{(q)}\\ s_k^{(q)}=s^{(m,n)}}} \underline{P}_k(\mathbf{s}^{(q)})\cdot p(\hat{s}_k^{(q)}) \\ &= \frac{M}{2\pi\sigma_n^2\mathbf{w}_k^H\mathbf{w}_k}\sum_{\substack{\forall \mathbf{s}^{(q)}\\ s_k^{(q)}=s^{(m,n)}}} \underline{P}_k(\mathbf{s}^{(q)})\cdot\exp\left(-\frac{|\hat{s}_k-\bar{\hat{s}}_k^{(q)}|^2}{2\sigma_n^2\mathbf{w}_k^H\mathbf{w}_k}\right), \end{aligned} \quad (3.65)$$

where $\underline{P}_k(\mathbf{s}^{(q)}) = \frac{1}{M}\prod_{\forall k'\neq k}P(s_{k'}=s_{k'}^{(q)})$ is the probability of transmitting the qth possible symbol combination $\mathbf{s}^{(q)}$, given the *a priori* information of the other $(K-1)$ users, except for user k. By defining $b_i = \frac{\sqrt{3E_s}}{\sqrt{2(M-1)}}(2i-\sqrt{M})$, $i\in\{1,2,\cdots,\sqrt{M}-1\}$, the decision boundaries of $\hat{s}_k$ are determined by $b_i|\mathbf{w}_k^H\mathbf{h}_k|$ for the in-phase component and by $jb_i|\mathbf{w}_k^H\mathbf{h}_k|$ for the quadrature-phase component, as seen in Figure 3.10. Then the error rate is given by the integral of the PDF outside the corresponding decision boundaries. Figure 3.10 only shows the scenario of the inner constellation point, which is enclosed by boundaries. For

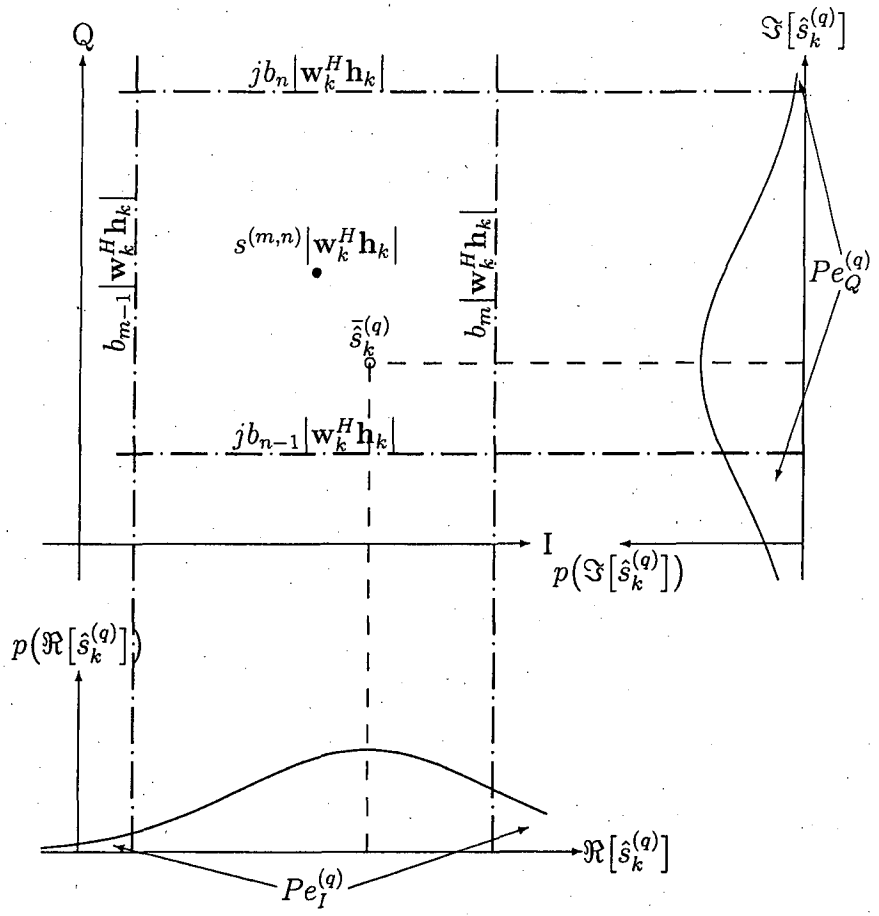

Figure 3.10: Decision boundaries, the interference-contaminated expectation $\bar{s}_k^{(q)}$ of the estimated signal $\hat{s}_k^{(q)}$, when we have $s_k^{(q)} = s^{(m,n)}$, and the PDFs of the in-phase and quadrature-phase component of the estimated signal.

the border constellation points, they may have open boundaries in one or two directions, which should be considered for the error rate calculation.

Let us now assume that the kth user transmits symbol $s^{(m,n)}$. Then the conditional in-phase component error probability of the hard detected symbol $\Re[\check{s}_k] \neq \Re[s^{(m,n)}]$ can be shown to be

$$Pe_I\left(s_k{=}s^{(m,n)}\right) = \sum_{\substack{\forall s^{(q)} \\ s_k^{(q)}=s^{(m,n)}}} Pe_I^{(q)}$$

$$
\begin{aligned}
&= \begin{cases}
\int_{b_1|\mathbf{w}_k^H\mathbf{h}_k|}^{+\infty} p\left(\hat{s}_k|s_k=s^{(m,n)}\right) d\Re[\hat{s}_k] & (m=1) \\
\int_{-\infty}^{b_{m-1}|\mathbf{w}_k^H\mathbf{h}_k|} p\left(\hat{s}_k|s_k=s^{(m,n)}\right) d\Re[\hat{s}_k] & \\
\quad + \int_{b_m|\mathbf{w}_k^H\mathbf{h}_k|}^{+\infty} p\left(\hat{s}_k|s_k=s^{(m,n)}\right) d\Re[\hat{s}_k] & (2\le m\le\sqrt{M}-1) \\
\int_{-\infty}^{b_{\sqrt{M}-1}|\mathbf{w}_k^H\mathbf{h}_k|} p\left(\hat{s}_k|s_k=s^{(m,n)}\right) d\Re[\hat{s}_k] & (m=\sqrt{M})
\end{cases} \\
&= \begin{cases}
M\sum\limits_{\substack{\forall \mathbf{s}^{(q)} \\ s_k^{(q)}=s^{(m,n)}}} \underline{P}_k\left(\mathbf{s}^{(q)}\right) \cdot \mathrm{Q}\left(\frac{b_1|\mathbf{w}_k^H\mathbf{h}_k| - \Re\left[\tilde{s}_k^{(q)}\right]}{\sigma_n\sqrt{\mathbf{w}_k^H\mathbf{w}_k}}\right) & (m=1) \\
M\sum\limits_{\substack{\forall \mathbf{s}^{(q)} \\ s_k^{(q)}=s^{(m,n)}}} \underline{P}_k\left(\mathbf{s}^{(q)}\right) \cdot \left(\mathrm{Q}\left(\frac{\Re\left[\tilde{s}_k^{(q)}\right] - b_{m-1}|\mathbf{w}_k^H\mathbf{h}_k|}{\sigma_n\sqrt{\mathbf{w}_k^H\mathbf{w}_k}}\right)\right. & \\
\quad \left. + \mathrm{Q}\left(\frac{b_m|\mathbf{w}_k^H\mathbf{h}_k| - \Re\left[\tilde{s}_k^{(q)}\right]}{\sigma_n\sqrt{\mathbf{w}_k^H\mathbf{w}_k}}\right)\right) & (2\le m\le\sqrt{M}-1) \\
M\sum\limits_{\substack{\forall \mathbf{s}^{(q)} \\ s_k^{(q)}=s^{(m,n)}}} \underline{P}_k\left(\mathbf{s}^{(q)}\right) \cdot \mathrm{Q}\left(\frac{\Re\left[\tilde{s}_k^{(q)}\right] - b_{\sqrt{M}-1}|\mathbf{w}_k^H\mathbf{h}_k|}{\sigma_n\sqrt{\mathbf{w}_k^H\mathbf{w}_k}}\right) & (m=\sqrt{M})
\end{cases}
\end{aligned}
\tag{3.66a}
$$

Similarly, the conditional quadrature-phase component error probability of the hard detected symbol $\Im[\check{s}_k] \neq \Im\left[s^{(m,n)}\right]$ can be shown to be

$$
\begin{aligned}
&Pe_Q\left(s_k=s^{(m,n)}\right) \\
&= \begin{cases}
M\sum\limits_{\substack{\forall \mathbf{s}^{(q)} \\ s_k^{(q)}=s^{(m,n)}}} \underline{P}_k\left(\mathbf{s}^{(q)}\right) \cdot \mathrm{Q}\left(\frac{b_1|\mathbf{w}_k^H\mathbf{h}_k| - \Im\left[\tilde{s}_k^{(q)}\right]}{\sigma_n\sqrt{\mathbf{w}_k^H\mathbf{w}_k}}\right) & (n=1) \\
M\sum\limits_{\substack{\forall \mathbf{s}^{(q)} \\ s_k^{(q)}=s^{(m,n)}}} \underline{P}_k\left(\mathbf{s}^{(q)}\right) \cdot \left(\mathrm{Q}\left(\frac{\Im\left[\tilde{s}_k^{(q)}\right] - b_{n-1}|\mathbf{w}_k^H\mathbf{h}_k|}{\sigma_n\sqrt{\mathbf{w}_k^H\mathbf{w}_k}}\right)\right. & \\
\quad \left. + \mathrm{Q}\left(\frac{b_n|\mathbf{w}_k^H\mathbf{h}_k| - \Im\left[\tilde{s}_k^{(q)}\right]}{\sigma_n\sqrt{\mathbf{w}_k^H\mathbf{w}_k}}\right)\right) & (2\le n\le\sqrt{M}-1) \\
M\sum\limits_{\substack{\forall \mathbf{s}^{(q)} \\ s_k^{(q)}=s^{(m,n)}}} \underline{P}_k\left(\mathbf{s}^{(q)}\right) \cdot \mathrm{Q}\left(\frac{\Im\left[\tilde{s}_k^{(q)}\right] - b_{\sqrt{M}-1}|\mathbf{w}_k^H\mathbf{h}_k|}{\sigma_n\sqrt{\mathbf{w}_k^H\mathbf{w}_k}}\right) & (n=\sqrt{M})
\end{cases}
\end{aligned}
\tag{3.66b}
$$

Then the average error probability of the in-phase and quadrature-phase component are given by

$$
Pe_I = \frac{1}{M}\sum_{m=1}^{\sqrt{M}}\sum_{n=1}^{\sqrt{M}} Pe_I\left(s_k=s^{(m,n)}\right) \tag{3.67a}
$$

and

$$Pe_Q = \frac{1}{M}\sum_{m=1}^{\sqrt{M}}\sum_{n=1}^{\sqrt{M}} Pe_Q\left(s_k=s^{(m,n)}\right), \tag{3.67b}$$

respectively. Since the resultant symbol error rate is equal to (one minus symbol-correct-rate), it can be expressed as

$$\begin{aligned} Pe_s &= 1-(1-Pe_I)(1-Pe_Q) \\ &= Pe_I + Pe_Q - Pe_I \cdot Pe_Q. \end{aligned} \tag{3.68}$$

3.2.5.2 Weights of the Soft MSER and WL-MSER MUDs

The resultant MSER solution is defined as the one that minimises the upper bound of the SER given by

$$\mathbf{w}_k = \arg\min_{\mathbf{w}_k}(Pe_I + Pe_Q). \tag{3.69}$$

The upper bound $(Pe_I + Pe_Q)$ is very close to the true SER Pe_s because our experiments not included here have shown that $Pe_I \cdot Pe_Q$ is typically negligible, which reduces the associated complexity. Similarly to the WL-MBER solution of Equations (3.55), the WL-MSER solution is defined as

$$\mathbf{w}_{k,I} = \arg\min_{\mathbf{w}_k} Pe_I, \tag{3.70a}$$

$$\mathbf{w}_{k,Q} = \arg\min_{\mathbf{w}_k} Pe_Q. \tag{3.70b}$$

In order to arrive at the optimum weights for the MSER and WL-MSER solutions, we need the gradients of Pe_I and Pe_Q, which can be derived from the gradients of the Q-functions in Equations (3.66) as stated in Appendix A.2, leading to

$$\begin{aligned} \nabla Q\left(\frac{\Re\left[\tilde{s}_k^{(q)}\right]-b_i\left|\mathbf{w}_k^H\mathbf{h}_k\right|}{\sigma_n\sqrt{\mathbf{w}_k^H\mathbf{w}_k}}\right) &= 2\frac{\partial}{\partial\mathbf{w}_k^*}Q\left(\frac{\Re\left[\tilde{s}_k^{(q)}\right]-b_i\left|\mathbf{w}_k^H\mathbf{h}_k\right|}{\sigma_n\sqrt{\mathbf{w}_k^H\mathbf{w}_k}}\right) \\ &= \frac{1}{\sqrt{2\pi}\sigma_n\sqrt{\mathbf{w}_k^H\mathbf{w}_k}}\cdot\exp\left(-\frac{\left(\Re\left[\tilde{s}_k^{(q)}\right]-b_i\left|\mathbf{w}_k^H\mathbf{h}_k\right|\right)^2}{2\sigma_n^2\mathbf{w}_k^H\mathbf{w}_k}\right) \\ &\quad\cdot\left(\frac{\left(\Re\left[\tilde{s}_k^{(q)}\right]-b_i\left|\mathbf{w}_k^H\mathbf{h}_k\right|\right)\mathbf{w}_k}{\mathbf{w}_k^H\mathbf{w}_k}-\bar{\mathbf{r}}_k^{(q)}+\frac{b_i\mathbf{h}_k\mathbf{h}_k^H\mathbf{w}_k}{\left|\mathbf{w}_k^H\mathbf{h}_k\right|}\right) \end{aligned} \tag{3.71a}$$

and

$$\nabla \mathrm{Q}\left(\frac{\Im\left[\tilde{\hat{s}}_k^{(q)}\right]-b_i\left|\mathbf{w}_k^H\mathbf{h}_k\right|}{\sigma_n\sqrt{\mathbf{w}_k^H\mathbf{w}_k}}\right)=2\frac{\partial}{\partial\mathbf{w}_k^*}\mathrm{Q}\left(\frac{\Im\left[\tilde{\hat{s}}_k^{(q)}\right]-b_i\left|\mathbf{w}_k^H\mathbf{h}_k\right|}{\sigma_n\sqrt{\mathbf{w}_k^H\mathbf{w}_k}}\right)$$
$$=\frac{1}{\sqrt{2\pi}\sigma_n\sqrt{\mathbf{w}_k^H\mathbf{w}_k}}\cdot\exp\left(-\frac{\left(\Im\left[\tilde{\hat{s}}_k^{(q)}\right]-b_i\left|\mathbf{w}_k^H\mathbf{h}_k\right|\right)^2}{2\sigma_n^2\mathbf{w}_k^H\mathbf{w}_k}\right)$$
$$\cdot\left(\frac{\left(\Im\left[\tilde{\hat{s}}_k^{(q)}\right]-b_i\left|\mathbf{w}_k^H\mathbf{h}_k\right|\right)\mathbf{w}_k}{\mathbf{w}_k^H\mathbf{w}_k}+j\bar{\mathbf{r}}_k^{(q)}+\frac{b_i\mathbf{h}_k\mathbf{h}_k^H\mathbf{w}_k}{\left|\mathbf{w}_k^H\mathbf{h}_k\right|}\right). \tag{3.71b}$$

3.2.5.3 Output LLRs of the Soft MSER MUD

Figure 3.11 shows the conditional PDFs of the MSER MUD's output signal supporting four 16QAM users at E_b/N_0=5dB both with and without *a priori* information. The arrival angles of the users' signal are 15°, 49°, −14° and −48°, respectively, as seen in Figure 3.4. We consider the first user as the desired user and assume the transmitted symbol is $s_1 = +\frac{3}{\sqrt{10}}+j\frac{3}{\sqrt{10}}$. In the scenario associated with *a priori* information, all the interfering users' *a priori* LLRs are listed in Table 3.1. It can be seen from the figure that the marginal conditional PDFs $p\left(\Re[\hat{s}_k]|s_k=s^{(m,n)}\right)$ and $p\left(\Im[\hat{s}_k]|s_k=s^{(m,n)}\right)$ can both be assumed as one-dimensional Gaussian distributed. Then the output extrinsic information delivered by the MSER MUD, similarly to those of the MBER MUD in Equa-

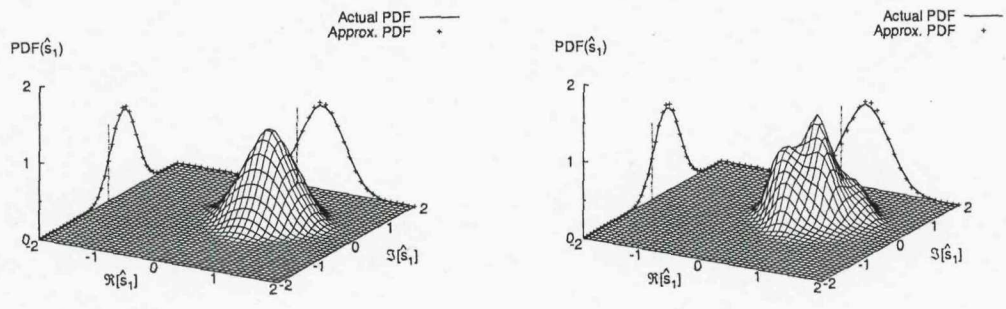

(a) Without *a priori* information

(b) With *a priori* information

Figure 3.11: Conditional PDF $p(\hat{s}_1)$ (surface), marginal conditional PDFs $p(\Re[\hat{s}_1])$ and $p(\Im[\hat{s}_1])$ (solid curves) of the MSER MUD's output signal, and approximate Gaussian marginal conditional PDFs (+).

tions (3.61), can be expressed as

$$L_E\big(b_k(i)\big) = \ln \frac{\sum_{\substack{\forall s^{(m,n)} \\ b^{(m,n)}(i)=+1}} \exp\left(-\frac{\left(\Re[\hat{s}_k]-\mu_{k,I}^{(m,n)}\right)^2}{2\sigma_{k,I}^2}\right) \prod_{\forall i' \neq i} P\big(b_k(i')=b^{(m,n)}(i')\big)}{\sum_{\substack{\forall s^{(m,n)} \\ b^{(m,n)}(i)=-1}} \exp\left(-\frac{\left(\Re[\hat{s}_k]-\mu_{k,I}^{(m,n)}\right)^2}{2\sigma_{k,I}^2}\right) \prod_{\forall i' \neq i} P\big(b_k(i')=b^{(m,n)}(i')\big)} \tag{3.72a}$$

when $b_k(i)$ is mapped to the real part of s_k, and

$$L_E\big(b_k(i)\big) = \ln \frac{\sum_{\substack{\forall s^{(m,n)} \\ b^{(m,n)}(i)=+1}} \exp\left(-\frac{\left(\Im[\hat{s}_k]-\mu_{k,Q}^{(m,n)}\right)^2}{2\sigma_{k,Q}^2}\right) \prod_{\forall i' \neq i} P\big(b_k(i')=b^{(m,n)}(i')\big)}{\sum_{\substack{\forall s^{(m,n)} \\ b^{(m,n)}(i)=-1}} \exp\left(-\frac{\left(\Im[\hat{s}_k]-\mu_{k,Q}^{(m,n)}\right)^2}{2\sigma_{k,Q}^2}\right) \prod_{\forall i' \neq i} P\big(b_k(i')=b^{(m,n)}(i')\big)} \tag{3.72b}$$

when $b_k(i)$ is mapped to the imaginary part of s_k. The calculation of the means $\mu_{k,I}^{(m,n)}$, $\mu_{k,Q}^{(m,n)}$ and the variances $\sigma_{k,I}^2$, $\sigma_{k,Q}^2$ are the same as those for the soft MBER solution in Equations (3.59) and (3.60).

3.2.5.4 Output LLRs of the Soft WL-MSER MUD

Figure 3.12 shows the conditional PDFs of the WL-MSER MUD's output signal supporting K=4 16QAM users at E_b/N_0=5dB with *a priori* information. All the

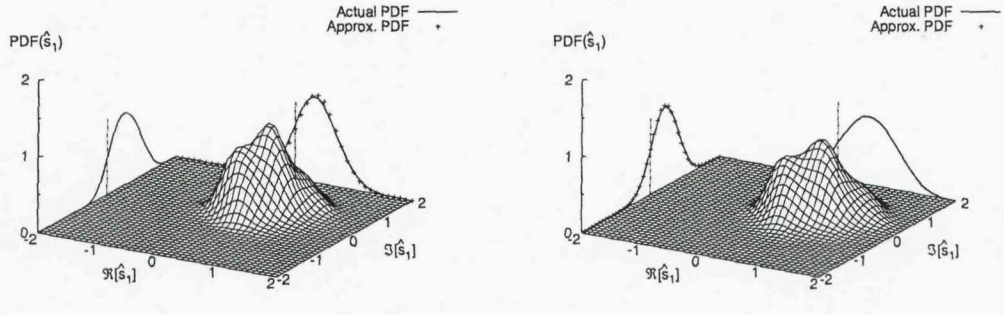

(a) Using weight $\mathbf{w}_{1,I}$ (b) Using weight $\mathbf{w}_{1,Q}$

Figure 3.12: Conditional PDF $p(\hat{s}_1)$ (surface), marginal conditional PDFs $p(\Re[\hat{s}_1])$ and $p(\Im[\hat{s}_1])$ (solid curves) of the WL-MSER MUD's output signal, and approximate Gaussian marginal conditional PDFs (+).

interfering users' *a priori* LLRs are listed in Table 3.1. Based on the Gaussian assumption again, as for the soft MSER solution, the WL-MSER MUD's output LLRs can be expressed as in Equations (3.72), where the calculation of the means and variances ensues in the same way as those of the WL-MBER MUD in Equations (3.62) and (3.63).

3.2.5.5 Computational Complexity of the Soft MSER MUD

The soft MSER MUD's computational complexity evaluated in the context of 16QAM systems per symbol per user in term of the number of real-valued additions and multiplications is summarized in Table 3.6. The related equations are also given in Table 3.6. Clearly, the complexity of the soft MSER MUD is $\mathcal{O}\left(LN_{cg}16^K\right)$. It is seen to be higher than the MMSE MUD's complexity shown in Table 3.2. Moreover, the soft WL-MSER MUD has the same complexity order as the soft MSER MUD as seen by comparing Equations (3.70) with Equation (3.69).

Table 3.6: Computational complexity of the soft MSER MUD

	Computational complexity	Equations
Mean & variance	25	(3.10), (3.11)
Weight vector	$\left((30L+18)N_{cg}+8KL-2L+3K-1\right)16^K+$ $(8L+7)N_{cg}+80$	(3.69), (3.71)
LLRs	$16KL+108L+10K+535$	(3.72)

3.3 EXIT Chart Analysis

3.3.1 EXIT Chart Introduction

For the sake of Extrinsic Information Transfer (EXIT) chart analysis, the receiver components (i.e., the MUD and the channel decoder) are modeled as components mapping a sequence of both received signal observations and the *a priori* information L_A to a new sequence constituting the extrinsic information L_E. The EXIT chart analysis computes the Mutual Information (MI) between the LLRs

L_A and the corresponding bits S, which is given by [36]

$$I(L_A;S) = \frac{1}{2}\sum_{s\in\{+1,-1\}}\int_{-\infty}^{\infty} p_{L_A}(x|s)\cdot\log_2\frac{2p_{L_A}(x|s)}{p_{L_A}(x|+1)+p_{L_A}(x|-1)}dx, \quad (3.73)$$

where we have $I(L_A;S)\in[0,1]$, and $p_{L_A}(x|s)$ represents the distribution of the *a priori* information conditioned on $s\in\{+1,-1\}$. After passing samples of L_A through the detector or the decoder, at the output the MI $I(L_E;S)$ between the extrinsic information L_E and S is obtained by applying Equation (3.73) using the distribution of L_E. This can be done by first approximating the PDF of L_E by the experimentally generated histogram of the output LLRs and then computing $I(L_E;S)$ numerically.

We denote the MI of the input and output LLRs, respectively by $I_A = I(L_A;S)$ and $I_E = I(L_E;S)$. When the Gaussian approximation is applied to the PDF of L_A, the MI I_A is a function of a single parameter, usually that of the variance σ_A^2 [36]

$$I_A(\sigma_A) = 1 - \int_{-\infty}^{\infty}\frac{e^{-\frac{(x-\sigma_A^2/2)^2}{2\sigma_A^2}}}{\sqrt{2\pi}\sigma_A}\cdot\log_2\left(1+e^{-x}\right)dx. \quad (3.74)$$

Let us define $J(\sigma_A) = I_A(\sigma_A)$ with the two extremal values of $\lim_{\sigma_A\to 0} J(\sigma_A) = 0$ and $\lim_{\sigma_A\to\infty} J(\sigma_A) = 1$, which correspond to having either none or perfect *a priori* information, respectively. The function J is monotonically increasing and thus it is invertible [36]

$$\sigma_A = J^{-1}(I_A). \quad (3.75)$$

It is infeasible to express J or its inverse in closed form. However, they can be closely approximated by [43]

$$J(\sigma) = \left(1-2^{-0.3073\times\sigma^{1.787}}\right)^{1.1064} \quad (3.76)$$

and

$$J^{-1}(I) = \left(-3.2541\times\log_2\left(1-I^{0.9038}\right)\right)^{0.5596}. \quad (3.77)$$

Note that for the MUD, the received signal has to be recorded for a given channel state and SNR, because the MUD's received signal is affected by the channel quality quantified here in terms of the noise power. The EXIT chart is either the nonlinear transfer function $I_{E,m} = f_m(I_{A,m}, SNR)$ of the MUD or the corresponding function $I_{E,d} = f_d(I_{A,d})$ of the channel decoder, which maps

the input variable I_A to the output variable I_E. The specific value of I_E in the range $[0, 1]$ characterizes the quality of the output LLRs of a receiver component. The essential idea of EXIT chart analysis is as follows. Firstly, with the introduction of the interleaver, we randomly reorder the input sequence of both the MUD and the channel decoder. This operation ensures that both the MUD and the channel decoder may be considered in isolation, where each of them is fed with sufficiently independent extrinsic information by the other constituent component. Secondly, we generate the EXIT curve $I_E = f(I_A)$ by assuming the *a priori* LLRs are Gaussian distributed. This simplifying assumption results in a discrepancy between the EXIT charts and the actually encountered real detection or decoding trajectories. This discrepancy is maybe sufficiently low so that we may ignore it [93]. When using the MI as our detection convergence metric, we do not require that the distribution of the output extrinsic information has to be Gaussian, since the MI is a function of the entire PDF, rather than that of the first and second moments of the extrinsic information, which is quite different from the philosophy of classic SNR analysis, especially when the distribution of the extrinsic information is non-Gaussian. Based on the latter feature, EXIT chart analysis can also be applied to multiuser communications over multipath fading channels, despite the fact that in this case the distribution of the output extrinsic information of the MUD cannot be approximated by a Gaussian PDF.

The numerical procedure invoked for obtaining the EXIT curve $I_E = f(I_A)$ can be described as follows:

1. We randomly generate the input bits $s \in \{+1, -1\}$ and the corresponding LLRs L_A according to the Gaussian distribution having a variance of σ_A^2 and a mean of $s \cdot \sigma_A^2/2$.
2. We then invoke an SISO detector (MUD or decoder) for detecting the sequence S.
3. From the obtained output LLRs L_E we calculate the resultant MI using Equation (3.73).
4. Repeating the above procedure for different values of σ_A^2 results in pairs of values $(I_{A,m}, I_{E,m})$, $(I_{A,d}, I_{E,d})$, which are used for approximating the functions $f_m(\cdot)$ and $f_d(\cdot)$.

The output of one of the constituent detectors is the input of the other, hence both transfer functions are shown in the same EXIT plane having coordinate axes

of $(I_{A,m}=I_{E,d})$, $(I_{E,m}=I_{A,d})$. The stair-case-shaped lines connecting the MI points evaluated during each iteration are referred to as the detecting trajectory. The substantial advantage of EXIT charts accrues from the fact that the detecting trajectory points recorded for both constituent components exchanging information fall on the continuous EXIT functions obtained independently, which is expressed as

$$I_{E,m}(n) = f_m\big(I_{E,d}(n-1)\big), \tag{3.78a}$$

$$I_{E,d}(n) = f_d\big(I_{E,m}(n)\big), \tag{3.78b}$$

where $I_{E,m}(n)$ and $I_{E,d}(n)$ represent the output MI produced during the n-th iteration.

An infinitesimally low BER may be attained, when there is a so-called open tunnel between the EXIT curves of the decoder and the MUD. This graphical representation gives us an immediate insight into the number of detection iterations required to attain the best possible BER performance. Finally, since the MI at the decoder's output may be directly mapped to the final BER [40], EXIT charts allow us to compare turbo receivers in terms of their overall BER performance.

3.3.2 EXIT Charts for Multiuser Beamforming

Unlike in single-user turbo coding or turbo equalization, in the multiuser detection scenario the MUD's EXIT curve recorded for the desired user depends on all the other $(K-1)$ users' channel decoder output MI, which implies that the MUD's EXIT surface should be K-dimensional. Unfortunately this K-dimensional EXIT hyperplane cannot be readily visualized. A feasible solution to resolve this problem is that of translating a single K-dimensional EXIT chart to K number of two-dimensional EXIT charts, where each two-dimensional EXIT chart corresponds to a single user. However, the MUD's EXIT curve in any of these two-dimensional EXIT charts changes upon each iteration, and it also depends on the other users' MI forwarded from the channel decoders to the MUD.

Nonetheless, we now slightly relaxed our simplifications and we assume that although all the users' angular locations are selected so that the relative time delay of all users with respect to the angularly closest neighbors is the same, one of the users has a higher power than the remaining equal-power users. In

CDMA or SDMA systems, if all the cross-correlation coefficients are equal, the Multiuser Interference (MUI) imposed by any of the users is equivalent. Hence we can use a pair of 2D EXIT charts for analysing the attainable convergence performance. More specifically, one of the EXIT charts is for the higher-power user, where the EXIT curves do not depend on the iteration index, while the other EXIT chart is for the average of the lower-power users, where the MUD's EXIT curve depends on the iteration index. However, in the context of beamforming systems operating under the above-mentioned conditions, the high-power user always imposes more interference on the angularly adjacent users than on the angularly better separated users. This implies that during the first iteration, the low-power users who are angularly close to the high-power user have a worse performance than the other low-power users. Furthermore, during later iterations, when a high-power user has a lower BER and can be essentially canceled, the angularly adjacent low-power users will have a better performance than the others. Hence the low-power users' signals cannot be readily combined into a single subset and hence their performance cannot be directly averaged. Therefore the 2D EXIT charts are unsuitable even for this simple beamforming scenario.

Based on the above reasons, in our simulations all users' SNRs were identical. Additionally, their angular locations were selected so that the relative time delay of all users with respect to the angularly closest neighbors was the same, as defined in Section 3.1.1. Hence the turbo MUD can average all the users' MI in order to generate the corresponding EXIT chart. When these constraints are not satisfied, the averaged EXIT trajectories will deviate from the EXIT transfer curves and consequently the EXIT chart analysis becomes less accurate.

3.4 Performance Analysis

In this section, simulation results are presented in order to illustrate the performance of the iterative beamforming receiver. EXIT charts are used to analyse the attainable performance. The system employs a two-element antenna array. All users have the same transmit power. Each user employs a different randomly generated interleaver. The interleaver length of each user is 2×10^4 bits.

3.4.1 BPSK Transmission Over AWGN Channels

Figure 3.13 shows the BER performance of the MMSE, RMMSE and MBER beamforming receivers of Section 3.2 communicating over AWGN channels supporting K=6 BPSK users and the corresponding single-user performance is also included as a reference. The system's schematic obeys the structure of Figure 3.2 and uses the parameters of Table 3.7. All users have the same channel coeffi-

Table 3.7: BPSK transmission parameters

Number of receive antennas	2
Number of users	6
DOAs of users' signal	68°, 36°, 15°, −4°, −24°, −48°
Modulation	BPSK
Interleaving length	2×10^4
Channel coding	NSC
Code rate	1/2
Constraint length	4
Polynomial generators	(15, 17)

cients of $h_k = 1.0+j0.0$, $k \in \{1, 2, \cdots, 6\}$, and employ the same rate 1/2 and

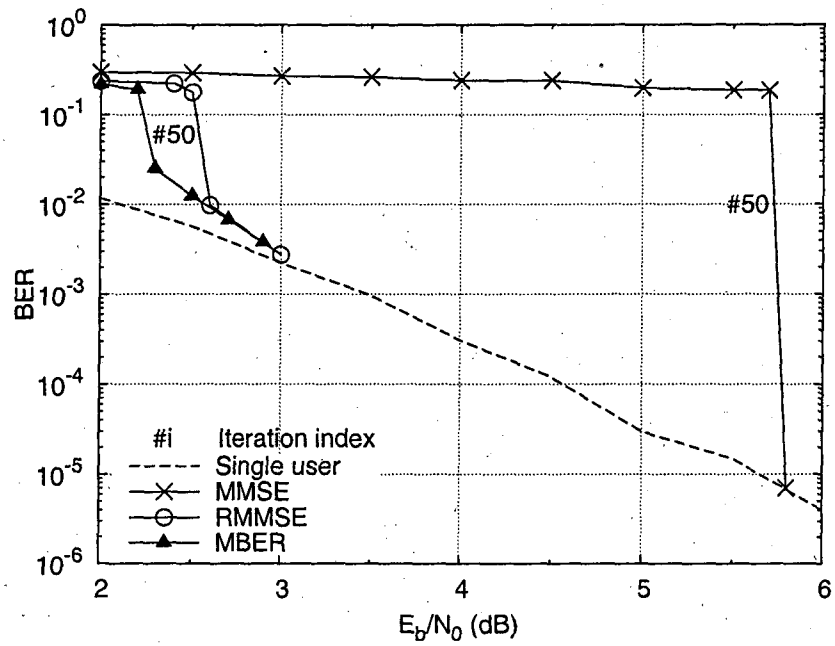

Figure 3.13: BER comparison of the MMSE, RMMSE and MBER iterative beamforming receivers of Section 3.2 for the BPSK system supporting K=6 users communicating over AWGN channels. The system's schematic obeys the structure of Figure 3.2 and uses the parameters of Table 3.7.

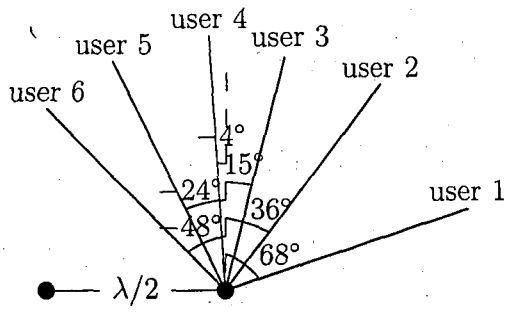

Figure 3.14: Two AEs, where the signal of users arrives from 68°, 36°, 15°, −4°, −24° and −48°.

constraint length 4 Non-Systematic Convolutional (NSC) code using the octally represented generators (15, 17). The arrival angles of users' signal are 68°, 36°, 15°, −4°, −24° and −48°, respectively, as seen in Figure 3.14. It can be seen that the performance of both the MBER and the RMMSE beamforming receivers has significantly improved after 50 iterations. Their performance approach the single-user bound when the SNR is higher than 2.3dB and 2.6dB respectively. However, the MMSE solution's BER approaches the single-user bound when the SNR is higher than 5.8dB. It is seen that in this 'overloaded' system supporting three times the number of users in comparison to the number of antennas, the MBER algorithm has 0.3dB and 3.5dB gain than the RMMSE and MMSE solution, respectively. On the other hand, at a high SNR condition, all the three algorithms have the same performance, i.e. the single-user BER.

3.4.1.1 EXIT-Chart Trajectories of the MBER MUD

According to the principles outlined in Section 3.3.1, in Figure 3.15 we plot both the EXIT charts and the simulated trajectories of the iterative MBER beamforming BPSK receiver supporting K=6 users at E_b/N_0=2dB and 3dB. All users employ the same rate 1/2 and constraint length 4 NSC code using the octally represented generators (15, 17).

The iterative detection process commences from the $I_{A,m}$=0 point, which implies the absence of *a priori* information for the MUD. Next, the output LLRs described by $I_{E,m}$=$I_{A,d}$ are fed into the decoder, yielding the LLRs described by $I_{E,d}$=$I_{A,m}$, which are then fed back to the MUD and so forth. The detection process is curtailed at the crossing of the EXIT curves of the MUD and the decoder

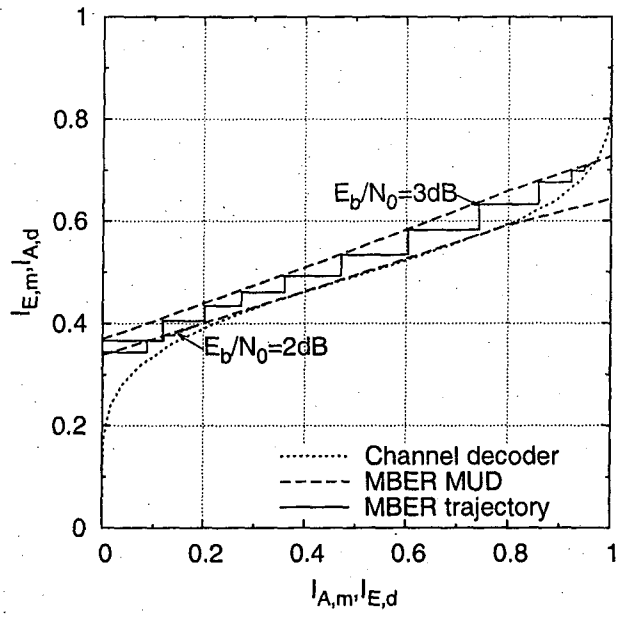

Figure 3.15: EXIT charts and simulated trajectories of the iterative MBER receiver of Section 3.2.4 supporting K=6 BPSK users communicating over AWGN channels at E_b/N_0=2dB and 3dB. The system's schematic obeys the structure of Figure 3.2 and uses the parameters of Table 3.7.

if the SNR is insufficiently high, as seen for E_b/N_0=2dB in Figure 3.15. The iterative detection process is represented by the staircase shaped trace between the transfer curves of the MUD (the doted line) and decoder (the dashed line) components.

Figure 3.15 also shows the detection trajectories (the solid lines) of the iterative process obtained by simulation. The detection trajectories closely follow the EXIT curves of the receiver components, which indicates that the EXIT chart analysis is valid for the MBER MUD. Again, as seen in Figure 3.15, at E_b/N_0=2dB the trajectory is curtailed after seven iterations, since the EXIT curves of the MUD and the decoder do intersect. By contrast, at E_b/N_0=3dB, the decoding trajectory passes through 'the bottleneck' and reaches the top-right corner, indicating an infinitesimally low BER, after fourteen iterations. We observe that after a few iterations, the trajectories slightly deviate from the EXIT curves, which is a consequence of the extrinsic information becoming correlated upon increasing the number of iterations, in particular, when the interleaving length is finite.

3.4.1.2 EXIT-Chart Based BER Estimation

EXIT charts can be used to obtain an estimate of the BER after an arbitrary number of iterations. For the channel decoder, the soft output of the coded bits generated after a given number of iterations can be written as the sum of the extrinsic information and the *a priori* information, which can be expressed as $L = L_{A,d} + L_{E,d}$. For the sake of deriving a simple formula for the channel coded bit error probability Pe_b, both the *a priori* information $L_{A,d}$ and the extrinsic information $L_{E,d}$ are assumed to be Gaussian distributed. Hence, the decoder's output L is also Gaussian with a variance of σ^2 and a mean of $\mu = \frac{\sigma^2}{2}$. Then the coded bit error probability can be written as [36]

$$Pe_b \approx \mathrm{Q}\left(\frac{\sigma}{2}\right). \tag{3.79}$$

Assuming perfect independence between the extrinsic information and the *a priori* information, we have $\sigma^2 = \sigma^2_{A,d} + \sigma^2_{E,d}$. Applying Equation (3.77), the variances $\sigma^2_{A,d}$ and $\sigma^2_{E,d}$ can be obtained from the corresponding MI $I_{A,d}$ and $I_{E,d}$.

Consider a six-user system communicating over an AWGN channel. We use a rate 1/2 NSC code having the octal generators of (15, 17). Table 3.8 compares the estimated coded BER results obtained from the EXIT chart to the simulation results characterizing the iterative MBER MUD at E_b/N_0=3dB. The table shows

Table 3.8: Comparison of BER estimation from EXIT chart and simulation results

Iteration index	$I_{L_{A,d}}, I_{L_{E,d}}$	$\sigma_{L_{A,d}}, \sigma_{L_{E,d}}$	Estimated BER	Simulated BER
1	0.367, 0.119	1.643, 0.845	$1.778e{-1}$	$2.467e{-1}$
2	0.405, 0.203	1.758, 1.142	$1.473e{-1}$	$1.981e{-1}$
3	0.434, 0.276	1.843, 1.37	$1.254e{-1}$	$1.634e{-1}$
4	0.461, 0.36	1.924, 1.623	$1.041e{-1}$	$1.314e{-1}$
5	0.492, 0.471	2.021, 1.956	$7.981e{-2}$	$9.702e{-2}$
6	0.534, 0.604	2.151, 2.382	$5.428e{-2}$	$6.667e{-2}$
7	0.582, 0.742	2.309, 2.916	$3.146e{-2}$	$3.683e{-2}$
8	0.633, 0.859	2.483, 3.55	$1.515e{-2}$	$1.61e{-2}$
9	0.676, 0.923	2.643, 4.111	$7.272e{-3}$	$7.267e{-3}$
10	0.698, 0.948	2.729, 4.433	$4.621e{-3}$	$4.9e{-3}$
11	0.706, 0.955	2.765, 4.551	$3.88e{-3}$	$4.233e{-3}$
12	0.709, 0.956	2.776, 4.581	$3.7e{-3}$	$3.85e{-3}$
13	0.71, 0.957	2.779, 4.6	$3.604e{-3}$	$3.617e{-3}$
14	0.71, 0.958	2.779, 4.608	$3.565e{-3}$	$3.5e{-3}$

that the EXIT chart in combination with the Gaussian approximation provides reasonable BER predictions.

3.4.1.3 Operating SNR Threshold Estimation

We can infer from the above results that the turbo detection scheme is capable of providing significant performance improvements, when the iterative process converges successfully. However, achieving successful convergence depends upon a number of factors, such as the user load, the type of detector, as well as the channel code and the SNR considered, all of which will be considered below.

From Figure 3.15, it is readily seen that if E_b/N_0 is a little bit higher than 2dB, there will be an open tunnel between the EXIT curve of the MUD and that of the decoder. The iterative process will hence successfully converge to an infinitesimally low BER. However, if E_b/N_0 is lower than 2dB, the EXIT tunnel will close and the iterative process fails to provide a significant BER performance improvement. Hence we estimate E_b/N_0=2.2dB as the operating SNR threshold of this system.

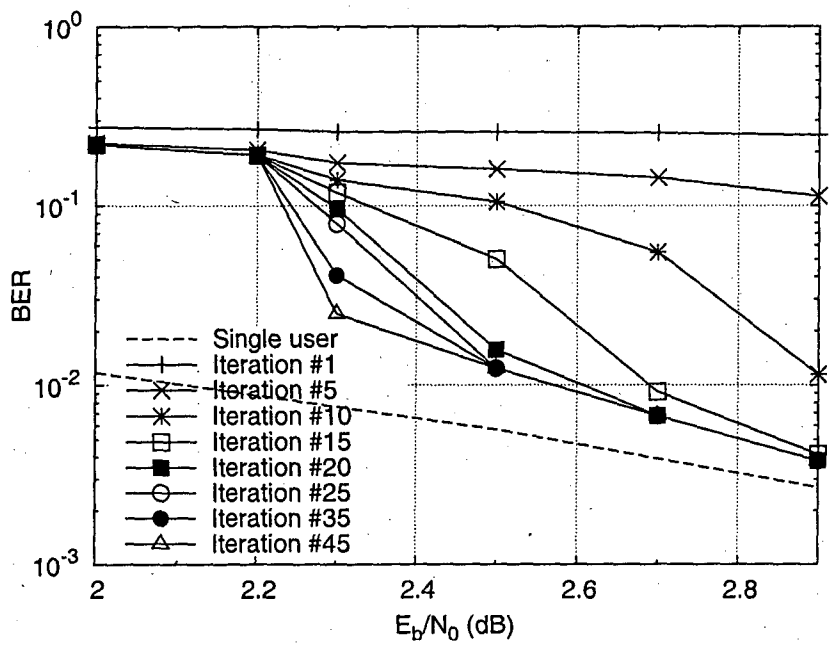

Figure 3.16: BER performance of the iterative MBER beamforming receiver of Section 3.2.4 supporting K=6 users communicating over AWGN channels, when increasing the number of iterations. The system's schematic obeys the structure of Figure 3.2 and uses the parameters of Table 3.7.

Figure 3.16 shows the BER performance of the system, when increasing the number of iterations. It can be seen that when the SNR is higher than 2.2dB, the achievable BER approaches that of the single-user bound, which confirms the predictions of the EXIT charts. Finally, it is worth noting that the narrower the EXIT tunnel, the higher the number of iterations required for achieving detection convergence.

3.4.1.4 The Number of Users Supported

In addition to the operating SNR threshold, there are other thresholds in turbo multiuser detection, which are of interest. For example, given a certain SNR, the EXIT curve of the detector moves downwards upon increasing the number of users K, potentially closing the convergence tunnel. This limits the maximum number of users that the system can support at this SNR.

Figure 3.17 shows the EXIT curves of the channel decoder and the MBER MUD, when supporting different number of BPSK users K at E_b/N_0=3dB. The DOAs of all users for different number of user are listed in Table 3.9. The channel code is a rate 1/2 NSC code having the octally represented generators of (15, 17).

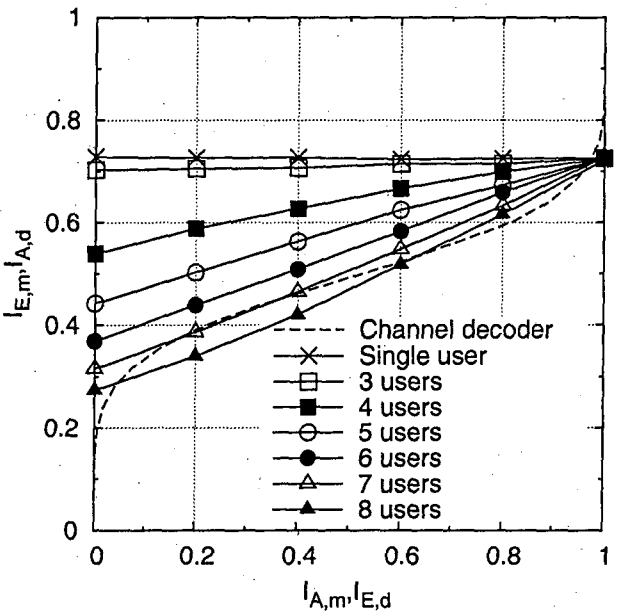

Figure 3.17: EXIT charts for the MBER MUD of Section 3.2.4 communicating over AWGN channels and NSC channel decoder for different number of BPSK users at E_b/N_0=3dB using the parameters of Tables 3.7 and 3.9.

Table 3.9: Arrival angles of users' signal

Single user	15°
2 users	15°, −4°
3 users	68°, 15°, −24°
4 users	49°, 15°, −14°, −48°
5 users	41°, 15°, −8°, −33°, −70°
6 users	68°, 36°, 15°, −4°, −24°, −48°
7 users	56°, 33°, 15°, −2°, −18°, −37°, −62°
8 users	49°, 31°, 15°, 1°, −14°, −29°, −48°, −82°

The EXIT chart shows that at E_b/N_0=3dB, the maximum number of users is K=6, where an open EXIT-tunnel is visible. It is clear that the maximum number of users supported is a function of the SNR, as well as of the specific detection and decoding schemes employed.

Figure 3.17 also shows that all the MUD EXIT curves converge to the ordinate value of $I_{E,m}\approx$0.73 at the abscissa of $I_{A,m}$=1. This is because regardless of the number of users, when the *a priori* information is perfect, all the other users' interference can be perfectly removed, resulting in a near-single-user performance. We also note that the point of perfect convergence at $[1, 1]$ is not reached, since the BER performance of the MUD depends on the SNR, when the MUI has been perfectly removed. When the SNR is infinitely high, the point of $[1, 1]$ can indeed be reached.

3.4.1.5 Comparison of Different Turbo-MUDs

Consider a six-user BPSK system employing two receive antennas. Figure 3.18 shows the EXIT characteristics of the iterative MUDs using the MBER, the MMSE and the RMMSE detection schemes operating at E_b/N_0=0dB, 3dB and 6dB. The MBER MUD has the potential of providing a marginally wider EXIT tunnel than the RMMSE scheme, followed by the MMSE MUD. Figure 3.18 also reveals that the three detectors yield the same value of $I_{E,m}<1$ with the advent of perfect *a priori* information corresponding to $I_{A,m}$=1. This is because for $|L_{A,m}|\rightarrow\infty$, the MAI can be completely removed from the received signal.

The main difference between the three detectors is the slope of the EXIT curves, which will then affect both the SNR convergence threshold and the convergence rate of the associated turbo receiver. Figure 3.13 shows the BER versus

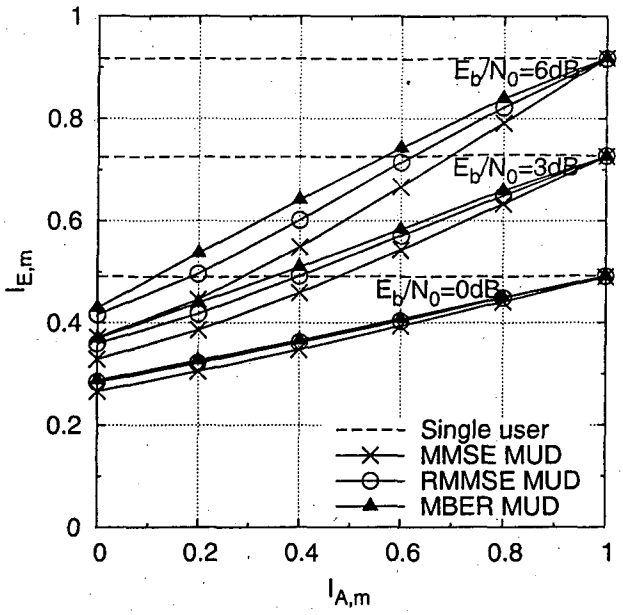

Figure 3.18: EXIT characteristics of the iterative MUDs using the MMSE, RMMSE and MBER detection schemes of Section 3.2 supporting K=6 BPSK users communicating over AWGN channels at E_b/N_0=0dB, 3dB and 6dB using the parameters of Table 3.7.

SNR performance of these three MUD algorithms, whose SNR thresholds are 2.3dB, 2.6dB and 5.8dB, respectively. It can be seen that the performance of all three beamforming receivers has significantly improved after i=50 iterations. In this rank-deficient system supporting three times the number of users in comparison to the number of antennas, the MBER algorithm has the lowest operating SNR requirement.

Figure 3.19 shows the lowest number of iterations required to achieve a near-single-user performance for the three MUDs, when the SNR experienced is higher than the SNR threshold. It is clear that the number of iterations required decreases upon increasing the SNR. At a given SNR, the MBER algorithm necessitates the least iterations to approach the single-user performance.

Figure 3.20 shows the number of users supported at different SNRs for the three MUDs. The MBER algorithm is likely to support more users than the other two algorithms.

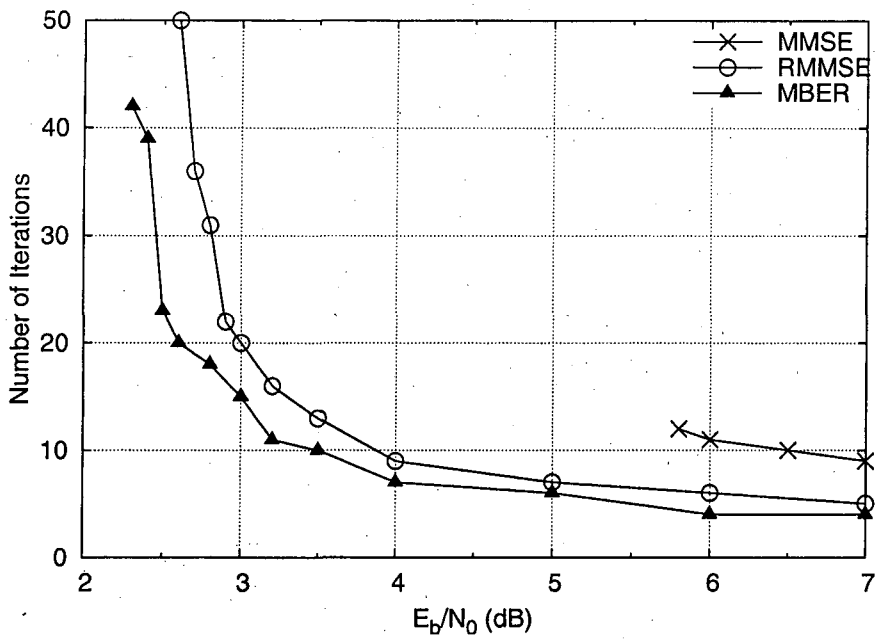

Figure 3.19: The number of iterations required to achieve a near-single-user performance by the MMSE, RMMSE and MBER SISO MUDs of Section 3.2 supporting K=6 users communicating over AWGN channels. The system's schematic obeys the structure of Figure 3.2 and uses the parameters of Table 3.7.

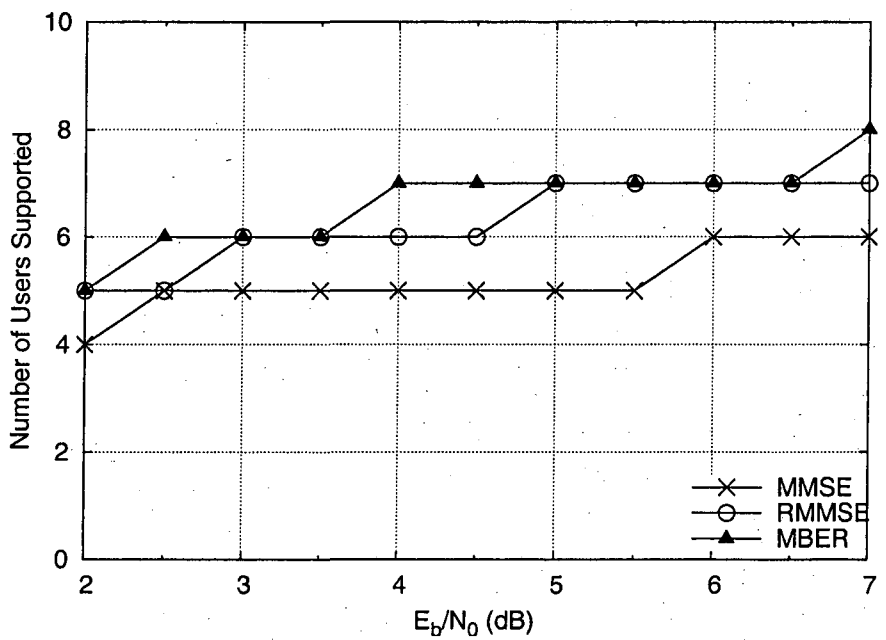

Figure 3.20: The number of users supported by the MMSE, RMMSE and MBER SISO MUDs of Section 3.2 communicating over AWGN channels. The system's schematic obeys the structure of Figure 3.2 and uses the parameters of Table 3.7.

3.4.1.6 Comparison of Different Channel Coding Schemes

Let us now compare the performance of the MBER turbo receivers using different channel codes, namely the previously used NSC code and a Recursive Systematic Convolutional (RSC) code. Both codes have the same code rate of 1/2 and constraint length 4. The generator polynomials are (15, 17) and (17/15) in octal representation, respectively. Figure 3.21 shows the EXIT curves of the NSC and RSC channel decoders. We can see that the EXIT curves of the NSC decoder and the RSC decoder are almost the same, which implies that the iterative receive systems employing either channel coding scheme have the same performance.

Now we consider two NSC channel codings using different parameters. Code-1 has constraint length 3 and octal generator polynomials (5, 7). By contrast, code-2 has constraint length 5 and octal generator polynomials (23, 35). Figure 3.22 shows the EXIT charts of these two NSC channel decoders along with the MBER MUD characteristics, when supporting K=6 BPSK users at E_b/N_0=2dB and 3dB. Observe in Figure 3.22 that when $I_{A,d}$ is lower than 0.5, code-1 has a higher output MI $I_{E,d}$ than code-2. However, as $I_{A,d}$ increases, code-2 starts to perform better. In Figure 3.22, the arrows indicate the intercept points of the channel decoders

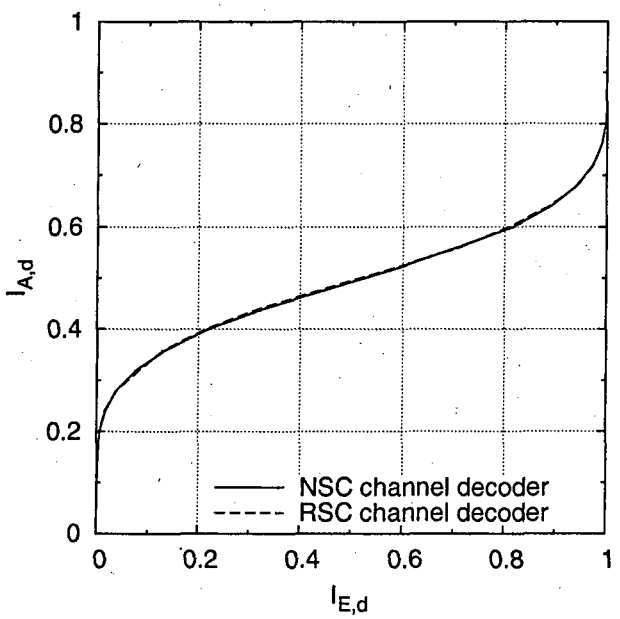

Figure 3.21: EXIT curves of the NSC and RSC channel decoders. Both codes have the same code rate of 1/2 and constraint length 4. The generator polynomials are (15, 17) and (17/15) in octal representation.

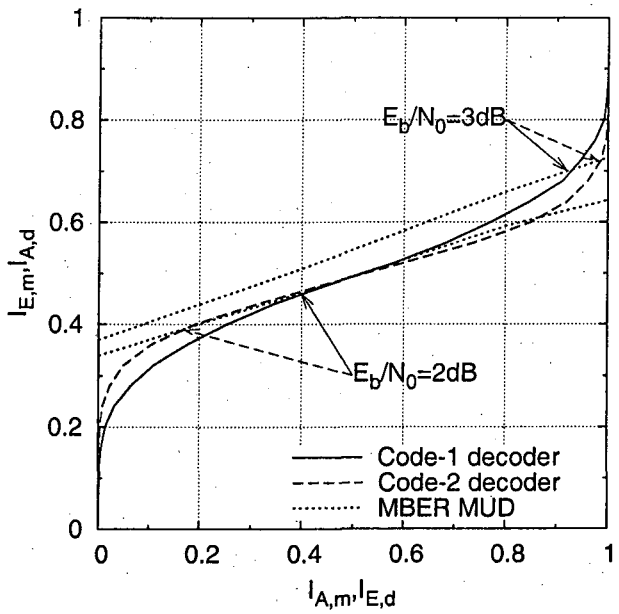

Figure 3.22: EXIT charts of two NSC channel decoders along with the MBER MUD's EXIT characteristics, when supporting K=6 BPSK users communicating over AWGN channels at E_b/N_0=2dB and 3dB. Code-1 has constraint length 3 and octal generator polynomials $(5, 7)$. Code-2 has constraint length 5 and octal generator polynomials $(23, 35)$.

and the MBER MUD at different SNRs. When the SNR is low, for example 2dB, the intercept points of both decoders are near the bottom-left corner, with that of code-2 being nearer. This implies that the receiver using shorter constraint length channel code has a better performance at low SNRs. When the SNR increases to 3dB, both codes provide open EXIT tunnel and the intercept point of the code-2 decoder is moved nearer to the top-right corner than that of code-1 scheme. Hence the receiver employing code-2 performs better. Figure 3.23 shows the simulated BER performance of these two NSC coded MBER receivers after i=50 iterations, which confirms the above EXIT-chart based conclusions.

Observe from Figure 3.23 that the code-2 receiver has a steep BER curve, while the code-1 receiver's BER curve is quite gently sloping. The reason for this difference can be explained by their EXIT charts. Comparing the EXIT characteristics of the code-2 decoder and the MBER MUD at 3dB in Figure 3.22, we also observe that the EXIT chart slope of the MUD is slightly steeper than that of the code-2 decoder. This implies that the bottleneck is at the left end of the tunnel. When the EXIT tunnel becomes just opened, the receiver becomes capable of achieving a significant BER versus SNR gain, which results in a steep

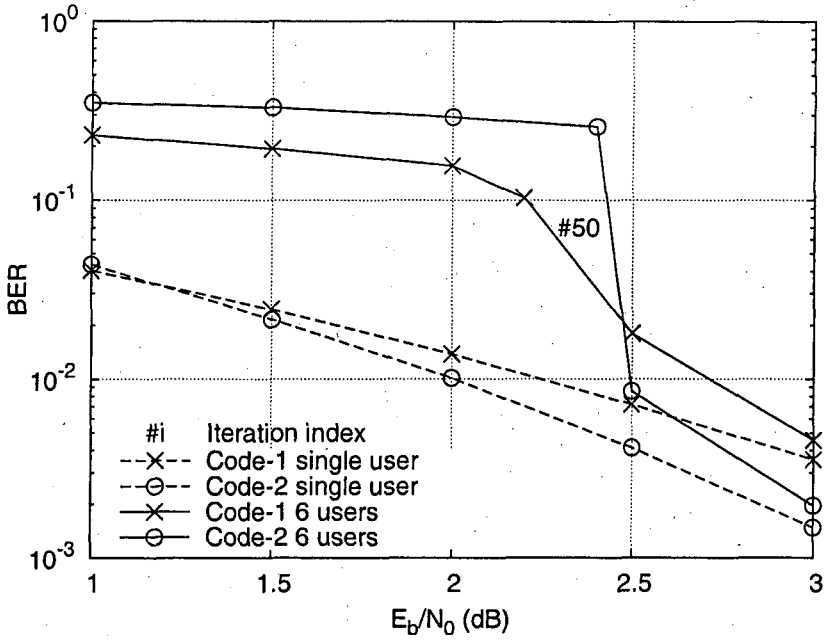

Figure 3.23: BER comparison of two NSC coded MBER turbo receivers of Section 3.2.4 supporting K=6 BPSK users communicating over AWGN channels. Code-1 has constraint length 3 and octal generator polynomials (5, 7). Code-2 has constraint length 5 and octal generator polynomials (23, 35). The system's schematic obeys the structure of Figure 3.2 and uses the parameters of Table 3.7.

BER curve. By contrast, for code-1 the slope of the decoder's EXIT curve is steeper than that of the MUD and hence the EXIT-chart intercept point moves more gradually upon increasing the SNR. Hence the BER curve of the code-1 receiver does not exhibit the same waterfall phenomenon.

Actually, at the threshold SNR value, the area between the two component curves is a measure of the performance loss relative to the channel capacity [94]. Therefore, both above-mentioned channel codes are somewhat deficient. To optimize the performance, we have to find a specific channel code, whose EXIT curve matches the MUD's curve in order to minimise the area between them. This will be investigated in next chapter.

3.4.2 BPSK Transmission Over Slow-Fading Channels

Consider a K=6 user BPSK system communicating over narrowband slow-fading channels obeying the schematic of Figure 3.2 and using the parameters of Ta-

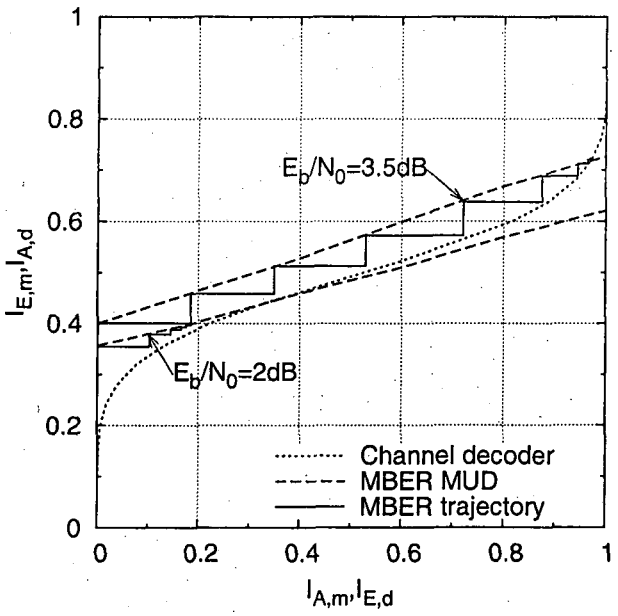

Figure 3.24: EXIT charts and simulated trajectories of the iterative MBER receiver of Section 3.2.4 supporting K=6 users communicating over flat-fading channels at E_b/N_0=2dB and 3.5dB. The system's schematic obeys the structure of Figure 3.2 and uses the parameters of Table 3.7.

ble 3.7. The normalized Doppler frequency is 10^{-2}, and the Ricean K-factor is 10. Figure 3.24 shows both the EXIT charts and the simulated trajectories of the iterative MBER beamforming receiver at E_b/N_0=2dB and 3.5dB. All users employ a 1/2-rate and constraint length 4 NSC code using the octal generators of $(15, 17)$. The arrival angles of users' signal are 68°, 36°, 15°, −4°, −24° and −48°, respectively, as seen in Figure 3.14. In Figure 3.24 we note that the trajectories of the iterative process obtained by Monte-Carlo simulations closely follow the EXIT curves of the receiver components and are curtailed at the crossing of the MUD's and the decoder's curves, which indicates that the EXIT chart analysis is quite accurate for the fading case.

Figure 3.25 shows the BER performance improvements of the system using the MMSE, RMMSE and MBER algorithms after i=30 iterations. Observe that for SNRs in excess of 3.5dB, the simulated BER of the MBER algorithm approaches the single-user BER, which confirms the predictions of the EXIT charts.

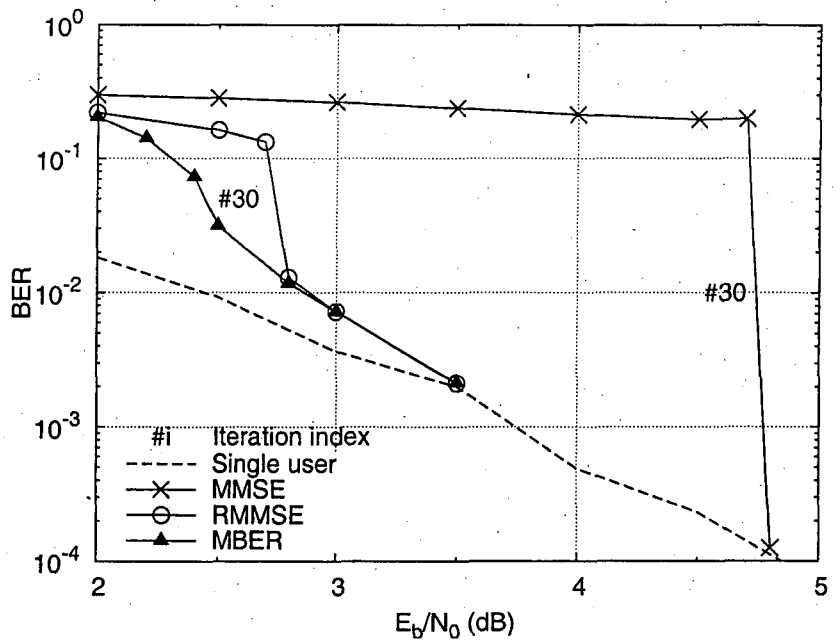

Figure 3.25: BER comparison of the iterative MMSE, RMMSE and MBER beamforming receivers of Section 3.2 supporting K=6 users communicating over flat-fading channels. The system's schematic obeys the structure of Figure 3.2 and uses the parameters of Table 3.7.

3.4.3 QPSK Transmission Over AWGN Channels

Figure 3.26 shows the BER versus SNR performance of the MMSE, WL-MMSE, MBER and WL-MBER beamforming receivers of Section 3.2 for transmission over AWGN channels supporting K=4 QPSK users in comparison to the corresponding single-user performance. The system's schematic was shown in Figure 3.2 and all parameters are summarized in Table 3.10. All users have the same chan-

Table 3.10: QPSK transmission parameters

Number of receive antennas	2
Number of users	4
DOAs of users' signal	49°, 15°, −14°, −48°
Modulation	QPSK
Interleaving length	2×10^4
Channel coding	NSC
Code rate	1/2
Constraint length	4
Polynomial generators	(15, 17)

nel coefficients of $h_k = 1.0+j0.0$, $k \in \{1, 2, 3, 4\}$, and employ a 1/2-rate and

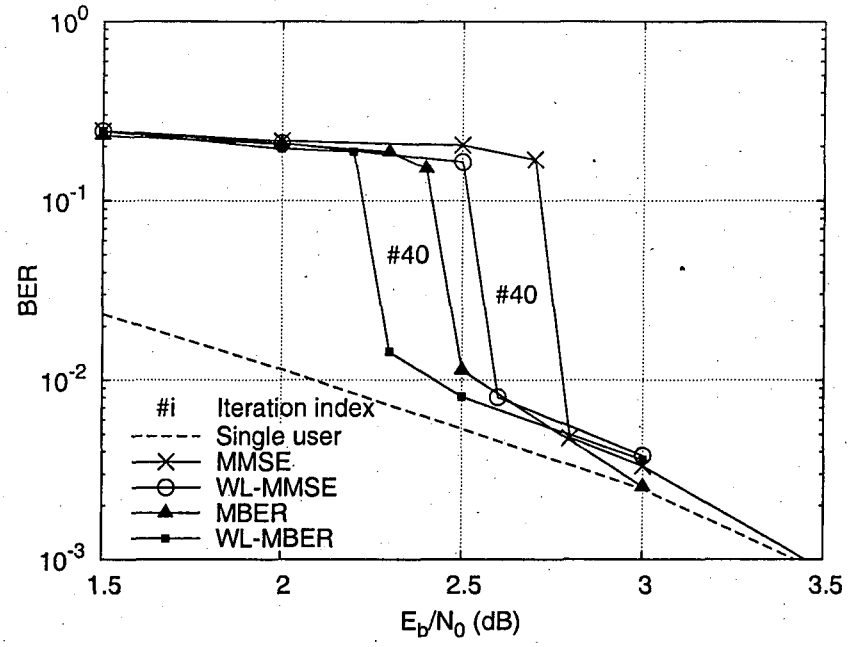

Figure 3.26: BER comparison of the MMSE, WL-MMSE, MBER and WL-MBER iterative beamforming receivers of Section 3.2 for the QPSK system supporting K=4 users communicating over AWGN channels. The system's schematic obeys the structure of Figure 3.2 and uses the parameters of Table 3.10.

constraint length 4 NSC code using the octal generators of (15, 17). The arrival angles of users' signal are 49°, 15°, −14° and −48°, respectively, as seen in Figure 3.4. Their performance approach the single-user bound, when the SNR is 2.8dB, 2.6dB, 2.5dB and 2.3dB for the MMSE, WL-MMSE, MBER and WL-MBER MUDs of Section 3.2, respectively. It can be seen that the performance of all beamforming receivers has significantly improved after i=40 iterations. In this rank-deficient system, namely when the channel-matrix becomes rank-deficient and non-invertible due to supporting twice the number of users in comparison to the number of antennas, the WL-MBER algorithm has the lower operating SNR requirement.

In Figure 3.27 we plot both the EXIT charts and the simulated trajectories of the iterative MMSE, WL-MMSE, MBER and WL-MBER beamforming QPSK receivers supporting K=4 users at E_b/N_0=2.5dB. When the *a priori* information is $I_{A,m}$=0, the MMSE MUD and the WL-MMSE MUD have the same output extrinsic information $I_{E,m}$, because in this scenario the two algorithms are equivalent. In this situation, the MBER MUD and the WL-MBER MUD of Section 3.2.4 also have the same $I_{E,m}$ value, which is marginally better than that of

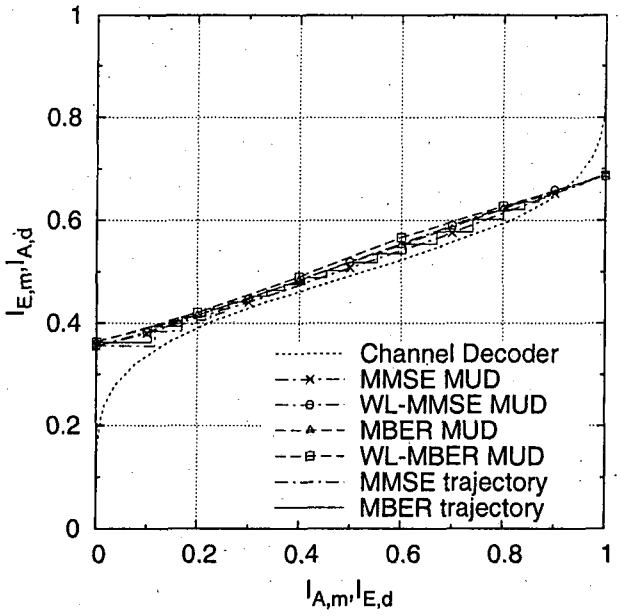

Figure 3.27: EXIT charts and simulated trajectories of the iterative MMSE, WL-MMSE, MBER and WL-MBER receivers of Section 3.2 supporting K=4 QPSK users communicating over AWGN channels at E_b/N_0=2.5dB. The system's schematic obeys the structure of Figure 3.2 and uses the parameters of Table 3.10.

the MMSE MUD and of the WL-MMSE MUD. All the four MUDs' EXIT curves have another point of intersection at $I_{A,m}$=1, where they achieve the single-user performance, although they all fail to reach the point of infinitesimally low BER typically associated with $(I_{A,m}, I_{E,m})$=(1, 1). When we have $I_{A,m} \in (0, 1)$, the WL-MMSE MUD outperforms the MMSE MUD, and the WL-MBER MUD outperforms the MBER MUD. The trajectories shown in Figure 3.27 indicate that the EXIT chart analysis is also accurate for the QPSK systems.

3.4.4 16QAM Transmission Over AWGN Channels

Consider a K=3 user 16QAM system obeying the schematic of Figure 3.2 and using the parameters of Table 3.11. All users have the same channel coefficients of $h_k = 1.0+j0.0$, $k \in \{1, 2, 3\}$, and employ the same rate 1/2 and constraint length 4 NSC code using the octally represented generators (15, 17). The arrival angles of users' signal are 68°, 15° and −24°, respectively, as seen in Figure 3.28.

Table 3.11: 16QAM transmission parameters

Number of receive antennas	2
Number of users	3
DOAs of users' signal	68°, 15°, −24°
Modulation	16QAM
Interleaving length	2×10^4
Channel coding	NSC
Code rate	1/2
Constraint length	4
Polynomial generators	(15, 17)

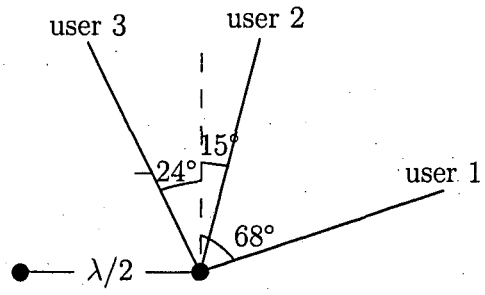

Figure 3.28: Two AEs, where the signal of users arrives from 68°, 15° and −24°.

Figure 3.29 shows the EXIT curves of the MMSE, WL-MMSE, MSER and WL-MSER MUDs of Section 3.2 and the simulated trajectories of the iterative MMSE and MSER 16QAM beamforming receivers supporting K=3 users at E_b/N_0=7.5dB. In this 16QAM system, the MMSE MUD, WL-MMSE MUD, MSER MUD and WL-MSER MUD have almost the same output $I_{E,m}$ value at both the axes at $I_{A,m}$=0 and $I_{A,m}$=1. Between these two points of intersection, the MMSE MUD has the lowest EXIT curve, and the WL-MSER's EXIT curve reaches the highest $I_{E,m}$ value.

Figure 3.30 shows the SER versus SNR performance of the MMSE, WL-MMSE, MSER and WL-MSER beamforming receivers for transmission over AWGN channels, when supporting K=3 16QAM users and the single-user performance. It can be seen that after i=20 iterations, all these iterative systems approach the single-user performance. The WL-MSER system has the lowest operating SNR threshold, which is 0.5dB, 0.2dB and 1.3dB lower than that of the MSER, WL-MMSE and MMSE systems, respectively.

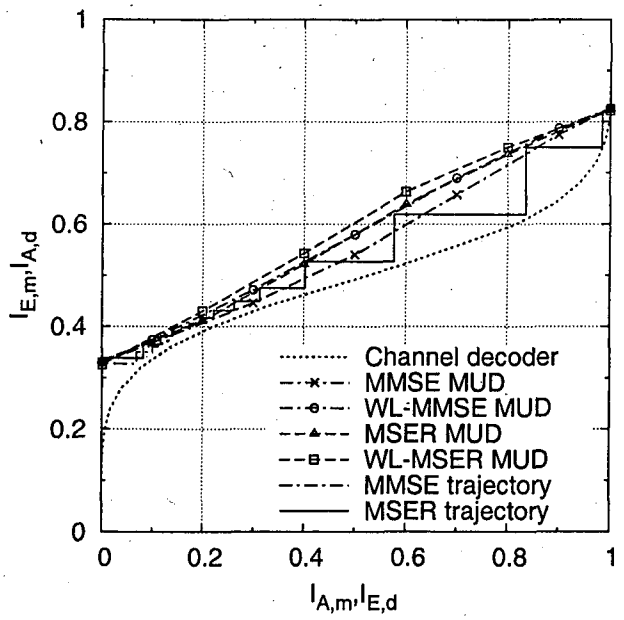

Figure 3.29: EXIT charts and simulated trajectories of the iterative MMSE, WL-MMSE, MSER and WL-MSER receivers of Section 3.2 supporting K=3 16QAM users communicating over AWGN channels at E_b/N_0=7.5dB. The system's schematic obeys the structure of Figure 3.2 and uses the parameters of Table 3.11.

3.5 Conclusions

In this chapter, we introduced the new iterative MBER SIC beamforming receiver of Section 3.2.4 for BPSK and QPSK systems, which directly minimises the BER instead of the MSE. This novel algorithm significantly outperforms the conventional MMSE SIC algorithm of Section 3.2.1 at the cost of a higher computational complexity. The RMMSE algorithm of Section 3.2.2 designed for BPSK was also considered, which minimises the MSE between the real-valued desired signal and the real part of the complex-valued beamformer output. The SISO WL-MMSE algorithm of Section 3.2.3 designed for higher-order QAM schemes was extended from the RMMSE solution. Similarly, the soft WL-MBER solution of Section 3.2.4 was also introduced, which has the same computational complexity as the MBER algorithm. Our simulations have shown that the MBER and WL-MBER solutions outperform both the conventional MMSE and the RMMSE or WL-MMSE iterative receivers. Furthermore, the SISO MSER and WL-MSER MUDs of Section 3.2.5 were also introduced and analysed in the context of 16QAM systems. They also outperform the MMSE or WL-MMSE systems at the cost of

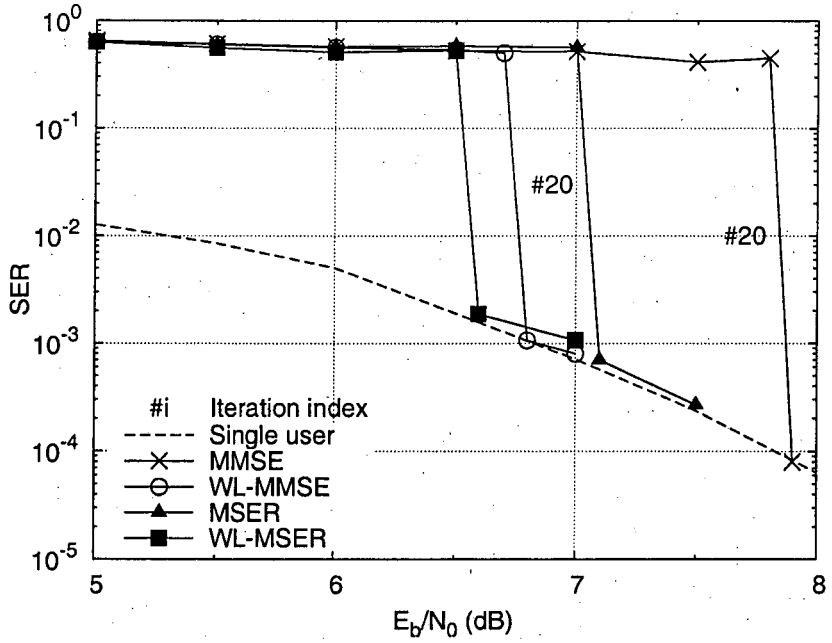

Figure 3.30: SER comparison of the MMSE, WL-MMSE, MSER and WL-MSER iterative beamforming receivers of Section 3.2 for the 16QAM system supporting K=3 users communicating over AWGN channels. The system's schematic obeys the structure of Figure 3.2 and uses the parameters of Table 3.11.

a high complexity.

The detailed performance and computational complexity of the methods mentioned above are summarized in Table 3.12. The system's schematic obeys the structure of Figure 3.2 and uses the parameters of Tables 3.7, 3.10 or 3.11, depending on the modulation scheme used. When quantitatively comparing the different SISO detectors' performance, we investigated the SNR threshold expressed in terms dBs, which indicates the lowest SNR where the iterative SIC MUD receiver is capable of achieving the BER performance of the single-user system for transmission over AWGN channels. As it becomes clear from Table 3.12, the MMSE SIC algorithm imposes lower complexity than both the MBER and the MSER methods. However, the MBER and the MSER MUD receivers have on approximately 3.5dB, 0.3dB and 0.8dB gain over the MMSE algorithm for BPSK, QPSK and 16QAM systems, respectively. It can also be seen in Table 3.12 that the WL algorithms outperform their corresponding non-WL methods at a similar complexity.

Despite the non-Gaussian distribution of the MI recorded in the MBER multi-

Table 3.12: Performance and complexity summary of iterative beamforming receivers

SISO MUD	Section	Complexity	Modulation	SNR threshold
MMSE	3.2.1	$\mathcal{O}(L^3)$	BPSK	5.8dB
			QPSK	2.8dB
			16QAM	7.9dB
RMMSE	3.2.2	$\mathcal{O}(L^3)$	BPSK	2.6dB
WL-MMSE	3.2.3	$\mathcal{O}(L^3)$	QPSK	2.6dB
			16QAM	6.8dB
MBER	3.2.4	$\mathcal{O}(LN_{cg}M^K)$	BPSK	2.3dB
			QPSK	2.5dB
WL-MBER	3.2.4	$\mathcal{O}(LN_{cg}M^K)$	QPSK	2.3dB
MSER	3.2.5	$\mathcal{O}(LN_{cg}M^K)$	16QAM	7.1dB
WL-MSER	3.2.5	$\mathcal{O}(LN_{cg}M^K)$	16QAM	6.6dB

user scenario, we succeeded in adopting the classic single-user EXIT-chart concept for our convergence analysis in Section 3.3.2. More explicitly, based on the EXIT charts of the SISO MUDs, the exchange of extrinsic information between the MUDs and the channel decoders was visualized, which facilitated their convergence analysis in the context of iterative detection. EXIT charts were also used for estimating the BER performance of the system at different user loads in Section 3.4.1.2, for estimating the operating SNR threshold in Section 3.4.1.3, for estimating the number of users supported in Section 3.4.1.4, and for comparing the convergence behaviour of various turbo receivers using different MUDs and channel codes in Sections 3.4.1.5 and 3.4.1.6.

Chapter 4

Three-stage Iterative Receiver Using Irregular Convolutional Codes

All the SISO MUDs discussed in Chapter 3 have a non-recursive nature, having a finite impulse response, which limits the achievable performance of the iterative system, because the extrinsic information exchange between the decoder components tends to be based on more correlated LLRs than in an IIR system. This disadvantage may be ameliorated with the aid of a simple unity-rate memory-1 recursive precoder incorporated at the transmitter. Hence the attainable iterative detection performance may be further improved [42]. Naturally, having a code rate for the precoder which is less than one restricts the achievable data throughput [38]. Furthermore, having a memory-1 structure slightly increases the system's complexity. Then the inner decoder component constituted by the MUD, the intermediate channel decoder and the outer channel decoder result in a three-stage serially concatenated scheme. In this chapter we design this three-stage concatenated multiuser receiver based on the MBER MUD for the sake of achieving a near-capacity performance [39]. By combining and projecting a series of three-dimensional EXIT functions onto a single two-dimensional EXIT chart [43], the convergence behaviour of the system is visualized. Specifically, IRCCs [38] are constructed, which are used as the outer code for the sake of solving the EXIT curve fitting problem of [44], i.e. that of minimising the area of the EXIT chart's open tunnel, implying that the system becomes capable of approaching the achievable data rate [44,38]. A near-capacity system can also be

designed by employing an irregular inner module [95], or two serially concatenated irregular modules [96,97].

4.1 System Description

The system supports K BPSK users and all users transmit signals on the same carrier frequency. The receiver is equipped with a linear antenna array consisting of L elements, which have a uniform element spacing of $\lambda/2$. Then the signal samples received at the symbol-rate can be expressed as $r_l(i) = \sum_{k=1}^{K} h_k(i)s_k(i)e^{j\omega t_l(\theta_k)} + n_l(i)$ for $l \in \{1, 2, \cdots, L\}$, where $s_k(i)$ is the ith symbol of the kth BPSK user, $h_k(i)$ is the complex-valued channel coefficient when transmitting the ith symbol of user k, $n_l(i)$ is the complex-valued Gaussian white noise having a power of $2\sigma_n^2$, and $t_l(\theta_k) = \frac{\pi}{\omega}(l-1)\sin(\theta_k)$ is the relative time delay at array element l for the source signal of user k, with θ_k being the LOS angle of arrival for source k. The system vector $\mathbf{h}_k = \left[h_k e^{j\omega t_1(\theta_k)} \;\; h_k e^{j\omega t_2(\theta_k)} \;\; \cdots \;\; h_k e^{j\omega t_L(\theta_k)}\right]^T$ constitutes the unique, user-specific signature of user k. We assume that the relative time delay of all users with respect to the angularly closest neighbours is the same. All the angular locations of the users were selected under this constraint.

Figure 4.1 depicts the system structure of the proposed three-stage serially concatenated multiuser communications system. In this figure, only one transmitter and the kth user's receiver were portrayed. At transmitter k, a block of information bits a_k is encoded by channel encoder I first. Then the outer encoded bits b_k are interleaved, yielding the permuted bits c_k, which are fed through the unity-rate memory-1 encoder II. The resultant 'double-encoded' bits d_k are interleaved by a second interleaver, yielding the interleaved bits e_k, which are fed to a bit-to-modulated-symbol mapper, as seen in Figure 4.1. After mapping, the modulated signal s_k is transmitted over a memoryless AWGN or fading channel. At the receiver of Figure 4.1, an iterative MUD/decoding structure is employed, where extrinsic information is exchanged between the three SISO modules, namely the SISO MUD, the *A Posteriori* Probability (APP)-based decoder II and the APP-based decoder I[1] in a number of consecutive iterations. To be specific, in Figure 4.1, $L_{A(\cdot)}$ denotes the *a priori* information represented in terms of LLRs [98], while $L_{E(\cdot)}$ denotes extrinsic information also expressed in terms of LLRs. Note that decoder II processes two *a priori* inputs arriving from both the

[1]Each user has a separate decoder I, decoder II, interleavers and deinterleavers.

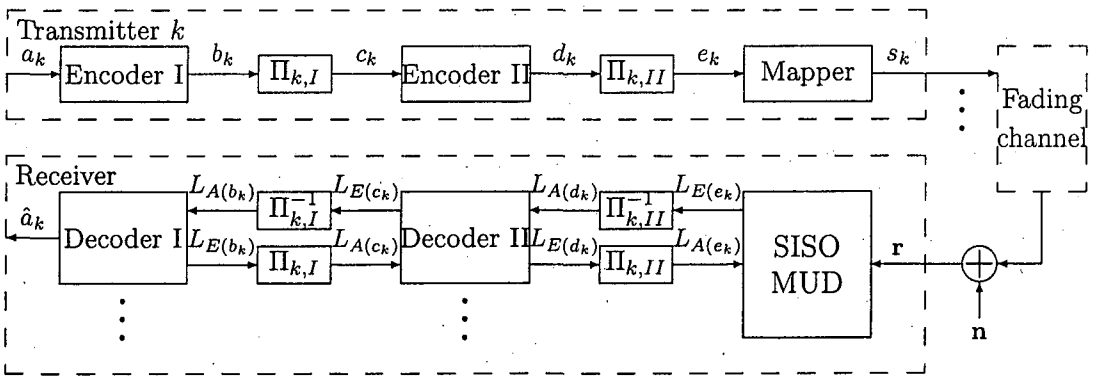

Figure 4.1: Three-stage iterative multiuser beamforming system structure, in which only the kth user's transmitter and receiver are portrayed.

MUD and decoder I in order to generate two extrinsic outputs. Following the last iteration, the estimates $\hat{a}_k$ of the original bits are generated by decoder I, as seen in Figure 4.1.

4.2 Convergence Analysis Using Projected EXIT Charts

The EXIT chart analysis computes the MI between the LLRs and the corresponding bits, as detailed in [37]. Let $I_{A(x)}$ denote the MI between the *a priori* values $L_{A(x)}$ and bit-sequence x. Furthermore, let $I_{E(x)}$ denote the MI between the extrinsic values $L_{E(x)}$ and the bit-sequence x. The EXIT function of decoder I is defined by[2]

$$I_{E(b)} = f_{d_I}\big(I_{A(b)}\big). \tag{4.1}$$

As seen from Figure 4.1, decoder II has two extrinsic MI outputs, namely $I_{E(c)}$ and $I_{E(d)}$, both of which are functions of the *a priori* MI inputs, namely $I_{A(c)}$ and $I_{A(d)}$. The two EXIT functions are defined by [43]

$$I_{E(c)} = f_{d_{II},o}\big(I_{A(c)}, I_{A(d)}\big), \tag{4.2}$$

[2]Each user employs the same channel coding I and channel coding II schemes, hence the subscript $_k$ can be omitted in the EXIT functions of decoder I and decoder II.

$$I_{E(d)} = f_{d_{II},i}\big(I_{A(c)}, I_{A(d)}\big). \tag{4.3}$$

Unlike in single-user turbo coding or turbo equalization, in the multiuser detection scenario the MUD's EXIT curve recorded for the desired user depends on all the other $(K-1)$ users' channel decoder output MI, which implies that the MUD's EXIT surface should be K-dimensional. Note that for the MUD, the received signal has to be recorded for a given channel state and SNR, because the MUD's received signal is affected by the channel quality quantified here in terms of the noise power. Then the EXIT function of the MUD for user k is defined by

$$I_{E(e_k)} = f_{m,k}\big(\forall I_{A(e_{k'})}, E_b/N_0\big), \tag{4.4}$$

where $k' \in \{1, \cdots, k-1, k+1, \cdots, K\}$. In our simulations all users' SNRs were identical. Additionally, their angular locations were selected so that the relative time delay of all users with respect to the angularly closest neighbors was the same, as defined in Section 4.1. Hence the turbo MUD can average all the users' MIs in order to simplify the EXIT chart function of (4.4) to

$$I_{E(e)} = f_m\big(I_{A(e)}, E_b/N_0\big). \tag{4.5}$$

Consider a half-rate NSC code using the octally represented generators (15, 17) as encoder I, and a simple rate-1 accumulator as encoder II, described by the octal generator polynomials of (1/3), where 3 represents the feedback polynomial. An SISO MBER MUD is employed as the inner component. All the EXIT functions can be plotted in two 3D EXIT charts. One for the EXIT functions of Equation (4.3) and Equation (4.5) as shown in Figure 4.2a, and another for the EXIT functions of Equation (4.1) and Equation (4.2), as shown in Figure 4.2b. The intersection of the surfaces seen in Figure 4.2a characterizes the best possible attainable performance, when exchanging information between the MUD and decoder II after an infinite number of iterations at different fixed values of $I_{A(c)}$, which is shown as a thick solid line. For each point $\big[I_{A(c)}, I_{A(d)}, I_{E(d)}\big]$ of this line in the 3D space of Figure 4.2a, there is a specific value of $I_{E(c)}$ determined by $I_{A(c)}$ and $I_{A(d)}$ according to the EXIT function of Equation (4.2). Therefore the solid line on the surface of the EXIT function of decoder II seen in Figure 4.2a is mapped to the solid line shown in Figure 4.2b. In order to avoid the cumbersome 3D representation, we now project the bold EXIT curve of Figure 4.2b onto the

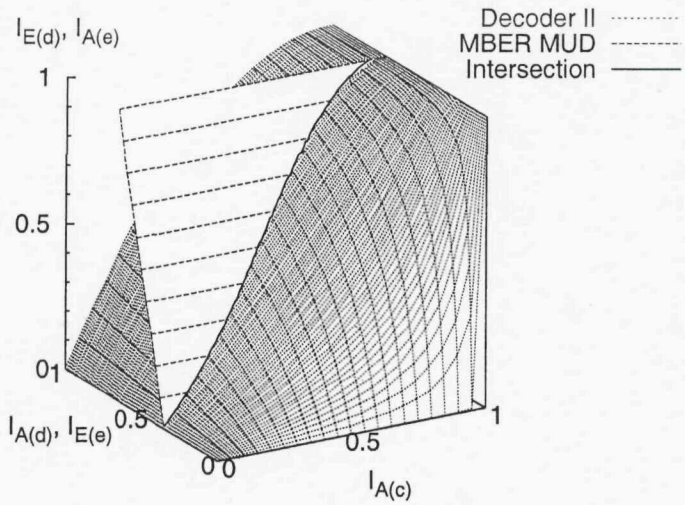

(a) Decoder II and the MBER MUD at E_b/N_0=2.1dB

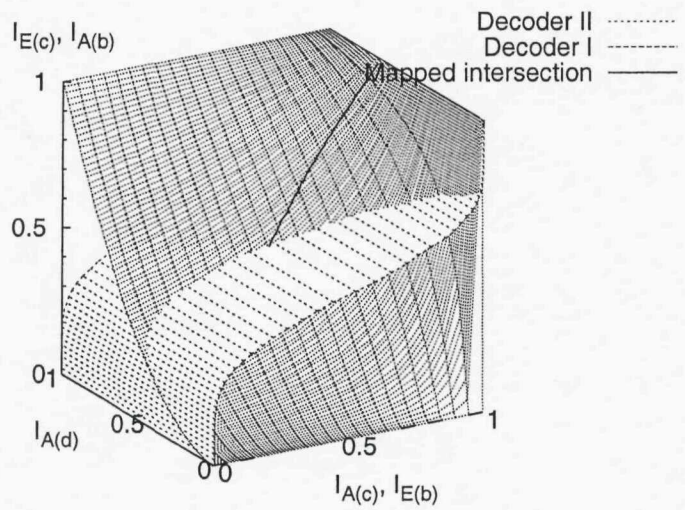

(b) Decoder I and decoder II

Figure 4.2: 3D EXIT charts of the 3-stage iterative MBER beamforming receiver supporting K=6 users with the aid of two antennas at E_b/N_0=2.1dB.

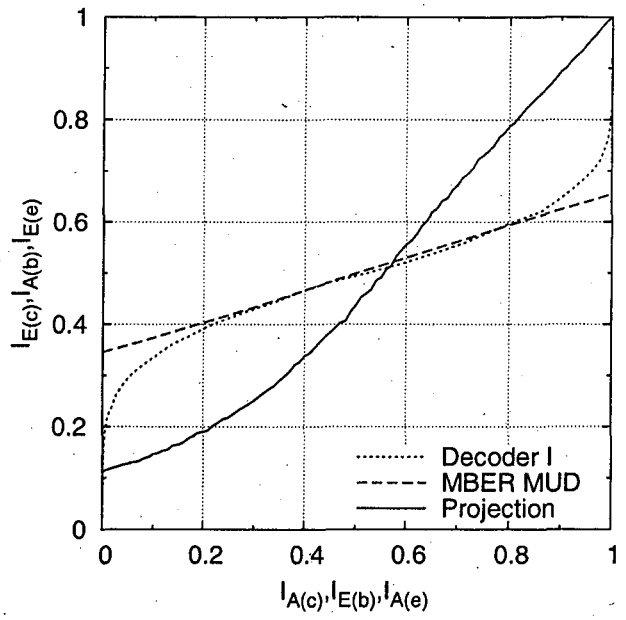

Figure 4.3: 2D projected EXIT charts of the 3-stage iterative MBER beamforming receiver supporting K=6 users with the aid of two antennas at E_b/N_0=2.1dB. The EXIT curves of the MBER MUD recorded at E_b/N_0=2.1dB and that of decoder I are also plotted.

2D plane at $I_{A(d)}$=0, yielding the solid line in Figure 4.3 [43]. The EXIT curves of the MBER MUD recorded at E_b/N_0=2.1dB and that of decoder I were also plotted in Figure 4.3. The projected EXIT curve can be described as

$$I_{E(c)} = f_p\big(I_{A(c)}, E_b/N_0\big), \tag{4.6}$$

which implies that the MUD and decoder II are combined into a single inner decoder component and hence the resultant 3-stage iterative scheme can be analysed as a traditional 2-stage iterative arrangement.

As for a traditional two-stage turbo scheme, the EXIT curve of the inner component and that of the outer component are used for analysing the associated convergence behaviour. As seen from Figure 4.3, the EXIT curve of the MBER MUD cannot reach the convergence point of $[1, 1]$ and intersects with the EXIT curve of the outer NSC code, which implies that residual errors persist, regardless of both the number of iterations used and the size of the interleaver. This explains the residual BER encountered by the traditional two-stage turbo scheme. On the other hand, if the inner MBER MUD and the intermediate decoder II are viewed as a single joint inner SISO module, then the projected EXIT

function of Equation (4.6) is the EXIT function of this module, which is capable of reaching the convergence point of $[1, 1]$. As long as there is an open tunnel between the EXIT curve of this joint inner module and that of the outer decoder, the three-stage concatenated system is capable of converging, hence achieving an infinitesimally low BER.

4.3 Design of Irregular Convolutional Coded Beamforming

According to the area properties [44, 38] of the EXIT charts, the area under the EXIT curve of the inner module is approximately equal to the achievable data rate when employing a specific multiuser detection scheme, when the channel's input is uniformly distributed. Furthermore, the area under the EXIT curve of the outer code is approximately equal to $1-R_I$, where R_I is the outer code rate. More explicitly, let A_{d_I} and $\bar{A}_{d_I}$ be the areas under $f_{d_I}(I)$ and its inverse $f_{d_I}^{-1}(I)$, $I \in [0, 1]$, respectively. Similarly, we define A_m for $f_m(I, E_b/N_0)$ and A_p for $f_p(I, E_b/N_0)$. Then we have $\bar{A}_{d_I} \approx R_I$, and for BPSK modulation $A_m \approx C$, where C is the achievable data rate of the communication channel when its input is uniformly distributed. Since the intermediate channel code II has a unity rate, the area A_p under the projected EXIT curve is also approximately equal to the above-mentioned uniform-input achievable data rate C. These area properties yield a design rule for our system: R_I should approach C as closely as possible under the constraint of

$$f_{d_I}^{-1}(I) < f_p(I, E_b/N_0) \qquad \forall I \in [0, 1), \tag{4.7}$$

implying that an outer code is sought, which ensures that the inverted EXIT curve $f_{d_I}^{-1}(I)$ fits to $f_p(I, E_b/N_0)$ as closely as possible, while maintaining an open EXIT tunnel, and hence minimising the area of the open EXIT tunnel.

However, as seen from Figure 4.3, even if the area under the projected EXIT curve plotted using the continuous line at E_b/N_0=2.1dB is $A_p \approx 0.51$, which is larger than the outer code rate of R_I=0.5, no open EXIT tunnel exists. In order to circumvent this problem, we introduce the novel concept of Irregular Convolutional Codes (IRCCs) [38], which allow us to shape the outer code's EXIT curve for the sake of matching that of the inner code. IRCCs were specifically

designed with the aid of EXIT charts for the sake of improving the convergence behaviour of iteratively decoded systems, and are constituted by a superposition of convolutional codes having different code rates. To be specific, an IRCC is constructed from a family of P subcodes. Each subcode has its own individual code rate $r_p (p \in \{1, \cdots, P\})$ and encodes a specific fraction of $\alpha_p r_p N$ of the original uncoded information bits, hence generating $\alpha_p N$ number of encoded bits, where N denotes the total number of encoded bits. Given the target overall average code rate of $R \in [0, 1]$, the weighting coefficient α_p has to satisfy $\sum_{p=1}^{P} \alpha_p = 1$, $\sum_{p=1}^{P} \alpha_p r_p = R$ and $\alpha_p \in [0, 1]$. Clearly, the individual code rates $\{r_p\}$ and the weighting coefficients $\{\alpha_p\}$ play crucial roles in shaping the EXIT function of the resultant IRCC. The EXIT function $f_{d_I}(I_A)$ of the target IRCC is the weighted superposition of its subcodes' EXIT functions $f_{d_I,p}(I_A)$ [38], yielding

$$f_{d_I}(I_A) = \sum_{p=1}^{P} \alpha_p f_{d_I,p}(I_A). \tag{4.8}$$

For example, a family of P=17 subcodes constructed from a recursive systematic, half rate, memory-4 mother code defined by the octal generator (27/31) was introduced in [38]. Higher rates are obtained by puncturing, while lower rates are obtained by adding more generators and by puncturing while maximizing the free distance. Table 4.1 shows the code rates, generator polynomials and puncturing patterns of all 17 subcodes. The EXIT curves of these subcodes are plotted in Figure 4.4. By using these 17 subcodes and the optimization criterion of

$$\min \int_0^1 \left(f_{d_I}^{-1}(I) - f_p(I, E_b/N_0) \right)^2 dI, \tag{4.9}$$

which minimises the squared error between the IRCC EXIT curve and the corresponding target curve, introduced in [38], we now optimize the weighting coefficients $\{\alpha_p\}$, so that the IRCC's EXIT curve matches the projected EXIT curve. Figure 4.5 shows the target projected MBER EXIT curve and the resultant EXIT curve of the optimized IRCC at E_b/N_0=2.1dB. The non-zero weights of the IRCC subcodes are listed in Table 4.2. The area under the projected EXIT curve at E_b/N_0=2.1dB is $A_p \approx 0.51$, which indicates that this E_b/N_0 value is close to the lowest possible convergence threshold for a system having an outer coding rate of R_I=0.5. Despite the fact that A_p and R_I are so close to each other, there is still an open tunnel between the two curves in Figure 4.5, which explicitly indicates the flexibility of the IRCCs. Figure 4.5 contrasts the projected MMSE EXIT curve

Table 4.1: An example of IRCC subcodes

Code rate	Generator polynomials	Puncturing pattern
0.1	(27,27,27,27,35,35,35,35,33)/31	1,1,1,1,1,1,1,1,1,1
0.15	(27,27,27,35,35,33)/31	7,7,7,7,7,7,3
0.2	(27,27,35,33)/31	1,1,1,1,1
0.25	(27,35,33)/31	1,1,1,1
0.3	(27,35,33)/31	7,7,7,1
0.35	(27,35)/31	177,177,077
0.4	(27,35)/31	3,3,1
0.45	(27,35)/31	777,777,021
0.5	27/31	1,1
0.55	27/31	3777,2737
0.6	27/31	7,3
0.65	27/31	17777,05253
0.7	27/31	177,025
0.75	27/31	7,1
0.8	27/31	17,1
0.85	27/31	377777,010101
0.9	27/31	777,1

Table 4.2: The non-zero weights of IRCC subcodes in percent for the optimized curve in Figure 4.5 using the family of 17 subcodes in Table 4.1

Subcode p	1	3	4	6	9	13	16	17
α_p in %	1.72	26.63	3.61	10.36	19.11	20.62	3.44	14.51

to that of the MBER MUD, where the area under the MMSE curve is about 0.48. This implies that the MMSE receiver needs a higher SNR for maintaining an open tunnel.

4.4 Performance Analysis

The system employs a two-element receive antenna array. All K=6 users employ BPSK modulation and have the same transmit power. The angular separation of users with respect to the antenna array are 68°, 36°, 15°, −4°, −24° and −48°. Each user employs two different randomly generated interleavers having a length of 2×10^4 bits. The code rate of encoder I is 0.5.

When communicating over AWGN channels, the iterative decoding trajectory recorded during our Monte Carlo simulations using the optimized IRCC at

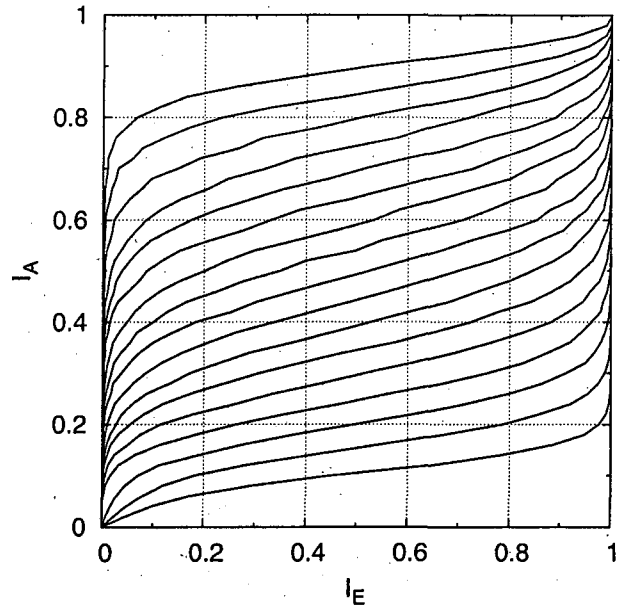

Figure 4.4: EXIT curves of a family of 17 IRCC subcodes, the code rates are from 0.1 to 0.9 bottom-up plotted with a step of 0.05.

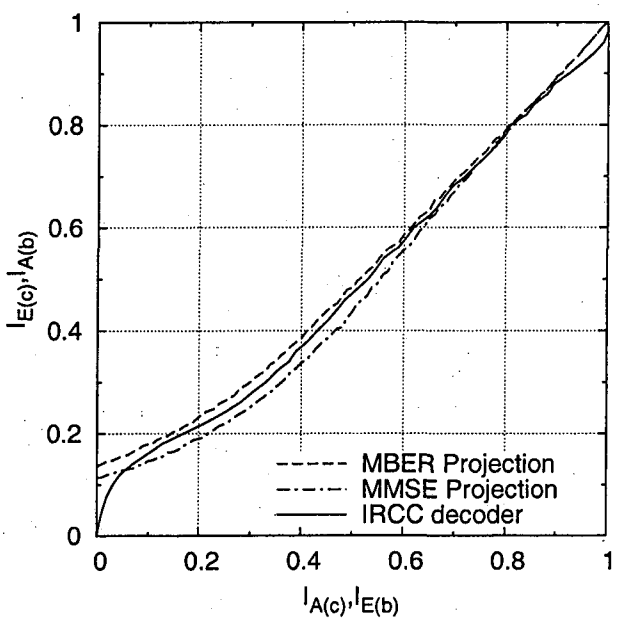

Figure 4.5: The projected EXIT curve and the optimized EXIT curve of the IRCC for the 3-stage iterative beamforming receiver supporting K=6 users with the aid of two antennas at E_b/N_0=2.1dB.

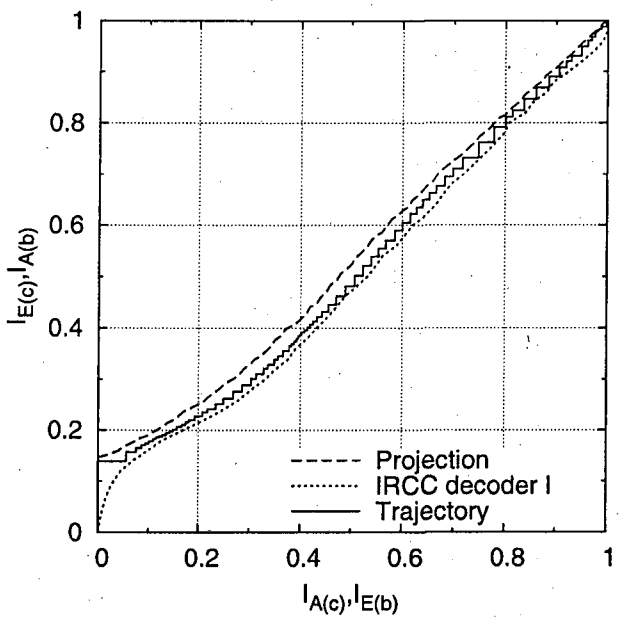

Figure 4.6: EXIT charts and recorded iterative trajectory for the 3-stage iterative MBER beamforming receiver using IRCCs for supporting K=6 users communicating over AWGN channels with the aid of two antennas at E_b/N_0=2.6dB. The system's schematic obeys the structure of Figure 4.1 and uses the parameters of Table 3.7.

E_b/N_0=2.6dB is depicted in Figure 4.6. It can be seen that the recorded trajectory converges to the $[I_{A(c)}, I_{E(c)}]$=[1, 1] point through the predicted EXIT chart tunnel. Furthermore, since the tunnel between the two EXIT curves is very narrow, a significant number of iterations are required for enabling the iterative receiver to converge to the point of [1, 1].

Figure 4.7 shows the BER performance of the three-stage iterative MBER beamforming scheme using IRCCs. The conventional two-stage system using a NSC code having a constraint length of 4 and octal generator polynomials of (15, 17) as the outer code is also plotted. It can be seen in Figure 4.7 that the 2-stage MBER receiver exhibits an error floor, which corresponds to the BER performance of the single-user case. By contrast, the 3-stage MBER and MMSE system becomes capable of achieving an infinitesimally low BER, when the E_b/N_0 encountered is higher than 2.5dB and 5.1dB, respectively. This BER figure confirms the performance difference of the two MUDs, which we have predicted from the EXIT curves of Figure 4.5.

We observe from Figure 4.5 that the 3-stage iterative system is capable of

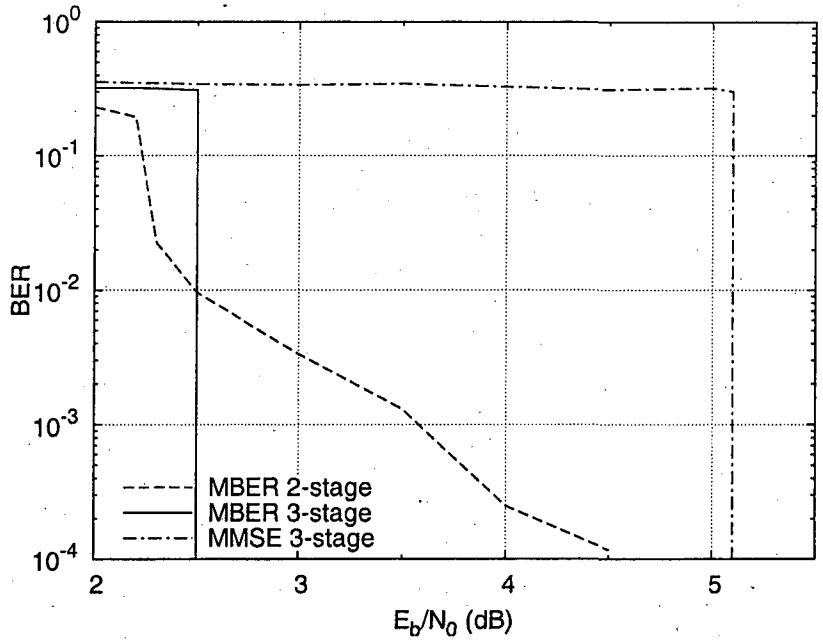

Figure 4.7: BER performance of the 3-stage and 2-stage iterative MBER beamforming receivers and the 3-stage iterative MMSE beamforming receiver supporting K=6 users communicating over AWGN channels with the aid of two antennas. The system's schematic obeys the structure of Figure 4.1 and uses the parameters of Table 3.7.

maintaining an open tunnel and hence of converging to the point of $[1, 1]$ in the EXIT-chart at E_b/N_0=2.1dB. However, the E_b/N_0 threshold of the 3-stage system characterized in Figure 4.7 is higher than 2.5dB. Figure 4.8 shows both the iterative decoding trajectory and the EXIT curves at E_b/N_0=2.5dB. In this figure, we can see the formation of an open tunnel. However, the actual decoding trajectory aborts at a point around [0.1,0.17] for the following reasons:

1. Our system is a multiuser system. Although we selected the arrival angles of the users' signals under the rule defined in Section 4.1, the achievable performance of the users is still not perfectly identical. In the EXIT charts, we used the average MUD EXIT curve and trajectory. When the average EXIT tunnel is quite narrow, a certain user's tunnel may in fact be closed. This poor performance of a single user may render the parallel IC mechanism unable to remove the MUI.

2. In our simulations, the activation order of the consecutive iterations is "MUD, decoder II, decoder I, decoder II, MUD ...". There is only one iteration between the MUD and decoder II before the extrinsic information

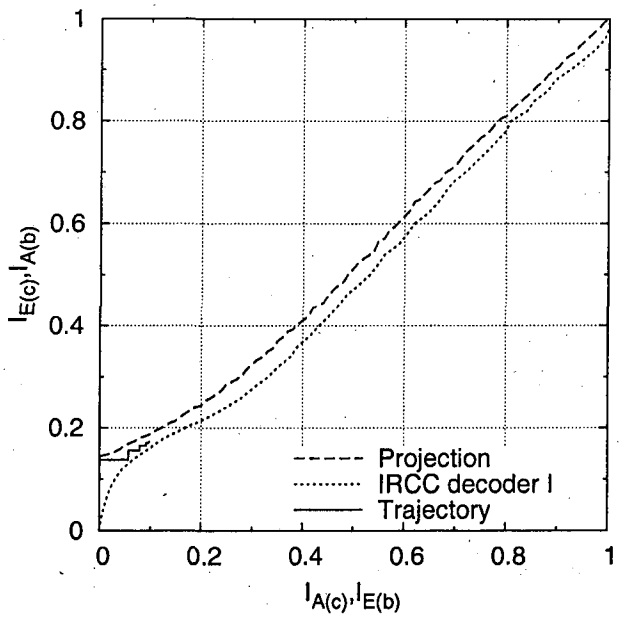

Figure 4.8: EXIT charts and recorded iterative decoding trajectory for the 3-stage iterative MBER beamforming receiver using IRCCs for supporting K=6 users communicating over AWGN channels with the aid of two antennas at E_b/N_0=2.5dB. The system's schematic obeys the structure of Figure 4.1 and uses the parameters of Table 3.7.

is transferred to decoder I. It implies that the accurate 2D projected curve recorded for this particular activation order of the decoders should be a little lower than the projected curve seen in Figure 4.8, and the actual tunnel may become narrower, or even closed.

3. The projected curve is the mapped intersection of the MUD's EXIT surface and the decoder II's EXIT surface. It represents the best possible output MI of the combined component. However, the practically achievable performance may be worse, potentially leading to a lower projected 2D-curve and higher SNR threshold.

Let us now consider the above-mentioned 3-stage system's convergence performance, when communicating over flat Ricean fading channels. The normalized Doppler frequency is 0.01, and the Ricean K-factor is 10. Our simulation results demonstrate that the E_b/N_0 threshold required for achieving an infinitesimally low BER is 2.9dB. At this SNR the recorded iterative decoding trajectory and the resultant EXIT curves are shown in Figure 4.9.

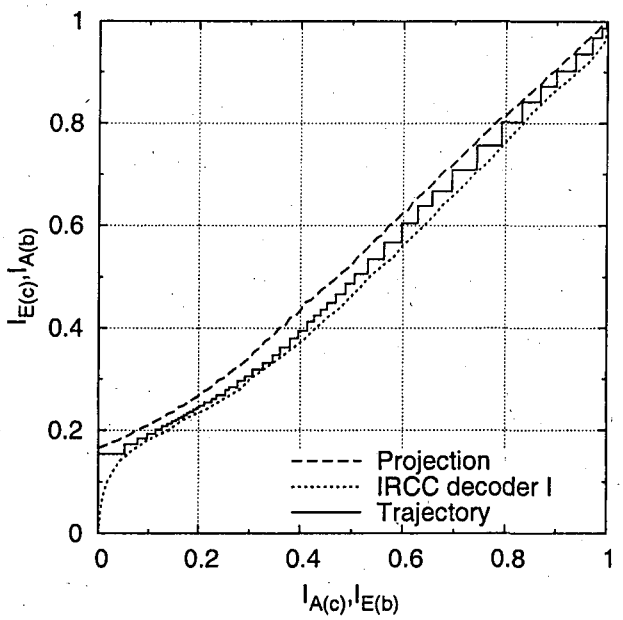

Figure 4.9: EXIT charts and recorded iterative trajectory for the 3-stage iterative MBER beamforming receiver using IRCCs for supporting K=6 users communicating over flat-fading channels with the aid of two antennas at E_b/N_0=2.9dB. The system's schematic obeys the structure of Figure 4.1 and uses the parameters of Table 3.7.

4.5 Conclusions

In this chapter, we proposed a three-stage serial concatenated multiuser system, where the inner SISO MBER MUD module cannot be rendered recursive. Hence the iterative receiver of Chapter 3 was extended to three SISO modules, namely the inner MBER MUD, the intermediate unity-rate channel decoder and the outer channel decoder. Furthermore, the convergence behaviour of our design example was analysed using 3D EXIT charts and their 2D projections in Section 4.2. It has been pointed out that although the EXIT function of the inner MBER MUD cannot reach the point of perfect convergence at $[1, 1]$, the joint EXIT function obtained for the amalgamated inner MBER MUD and the intermediate channel decoder with the aid of projection can. Therefore the three-stage system is capable of eliminating the residual BER encountered in the conventional two-stage system. With the advent of 2D projection, the IRCC of Section 4.3 was constructed for employment as the outer code, whose EXIT function was matched to the joint EXIT function of Section 4.2, and as a result, the channel capacity was closely approached.

Table 4.3 summarizes the performance of the 3-stage MUD and the 2-stage MUD receivers in terms of their SNR required for maintaining BER of 10^{-4} as well as for an infinitesimally low BER. The system's schematic obeys the structure of Figures 4.1 and 3.2. It can be seen that the proposed 3-stage MBER receiver significantly outperforms both the 2-stage MBER SIC receiver as well as the 3-stage MMSE receiver. Furthermore, the 3-stage iterative receivers are capable of achieving an infinitesimally low BER. However, the 2-stage receiver's performance has an error floor, which is identical to that of the single-user system.

Table 4.3: Performance summary of 3-stage iterative beamforming receivers

SISO MUD	SNR at a(n)	
	BER of 10^{-4}	infinitesimally low BER
3-stage MMSE	$>$ 5.1dB	$>$ 5.1dB
3-stage MBER	$>$ 2.5dB	$>$ 2.5dB
2-stage MBER	4.6dB	unachievable

Chapter 5

Beamforming Aided Multiuser Transmitter

Sophisticated multiuser detection techniques can be readily employed at the BS's uplink receiver, since the power consumption of the BS is less constrained than that of the MSs. By contrast, our goal is to design low-complexity, low-power MSs and hence it may be beneficial to design sophisticated transmitters in the interest of reducing the MS's receiver complexity.

Numerous techniques have been proposed for achieving this ambitious goal [99, 46, 47, 48, 51, 53], but their common feature is that they require the perfect knowledge of the CIRs to be encountered during the future instant of downlink transmissions to all the MSs. This unique, user-specific CIR or Angle of Arrival (AOA) may be used by the MUT to separate the users' downlink signals with the aid of appropriate transmit preprocessing techniques and hence to avoid or to mitigate the MUI imposed on each others' downlink signals. Naturally, the provision of accurate downlink CIR or AOA estimated for the BS's downlink MUT is a challenging task, because all MS receivers have to estimate their downlink channels and then have to report it back to the BS using the uplink control channels. This process is prone to both quantization errors as well as to signalling delays, which may be mitigated with the aid of using sophisticated Vector Quantization (VQ) techniques [100] and long-term channel prediction methods [101]. The simple philosophy of long-term channel prediction is that owing to the Doppler-frequency dependent correlation of the channel's envelope, it is possible to predict its future values based on its past values, which

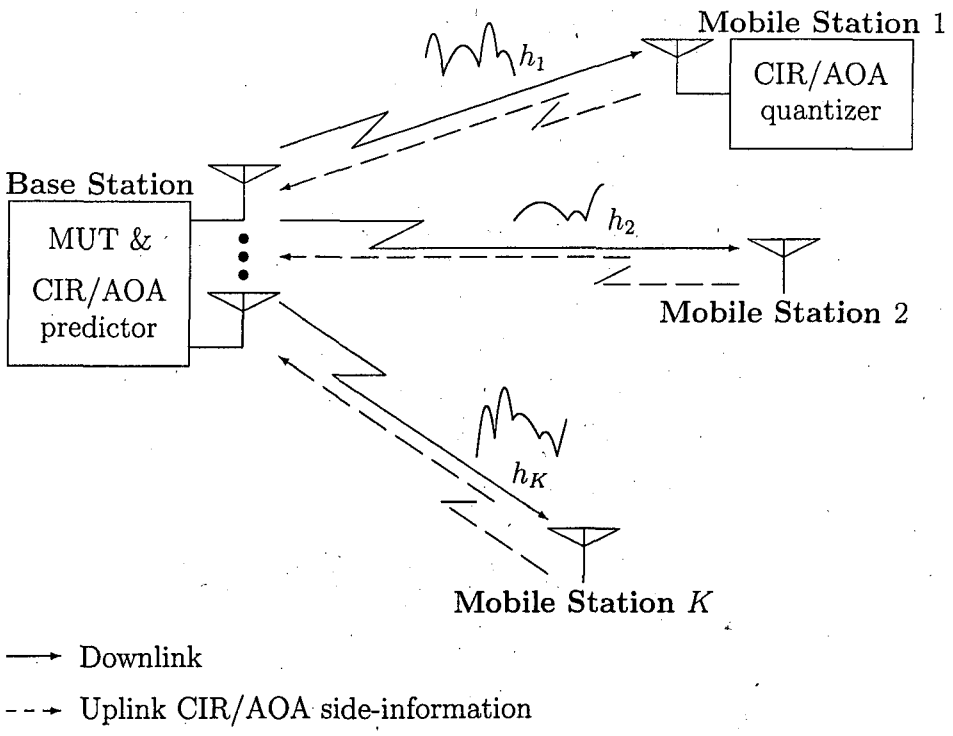

Figure 5.1: Downlink beamforming schematic supporting K users portraying the uplink CIR/AOA side-information signalling and long-term channel prediction at the BS.

have already been received and stored by the BS's uplink receiver. This allows the BS to avoid the above-mentioned signalling delay and to predict the channel envelope to be encountered between the BS's MUT and each MS during their next downlink transmission burst, as seen in Figure 5.1.

To elaborate a little further, the assumption that the downlink CIR is known at the BS may be deemed to be valid in TDD systems [45], because the uplink and the downlink share the same frequency band. Thus, all channel parameters may be considered to be similar for the uplink and downlink, provided that the coherence time of the channel is sufficiently high to ensure that the channel estimate is still valid, when it is used by the MUT algorithm. In Frequency Division Duplex (FDD) systems [45], the uplink and downlink reside in different frequency bands, hence the channel parameters have to be explicitly signalled, as discussed above.

Briefly returning to the family of downlink preprocessing techniques, it was argued in [102] that most MUD techniques have an MUT counterpart, such as the Transmit Zero Forcing (TZF), the Transmit Minimum Mean Squared Error

(TMMSE) [48, 100], the Transmit Wiener Filter (TWF) [51] etc. The network-layer benefits of both uplink and downlink beamforming were quantified in High-Speed Packet Access (HSPA) style third generation systems in [45]. Table 5.1 summarizes some state-of-the-art MUT papers and their novel contributions.

Table 5.1: Selection of MUT papers

Author(s)	Contribution
[99] Henry and Glance	Introduced the idea of exploiting the reciprocity of the uplink and downlink channels in TDD systems by applying a linear transmit filter in the downlink for flat fading channels and for multiple antenna elements at the BS.
[46] Esmailzadeh and Nakagawa	Proposed a pre-Rake combination method for multipath diversity signal combining designed for DS-CDMA communications, where multiple transmissions of each spreading code were activated and each transmission was independently delayed and amplified according to the channel's delay profile, i.e. according to the estimated CIR taps.
[47] Tang and Cheng	Proposed a pre-decorrelating strategy for single user detection in the downlink of a centrally controlled DS-CDMA systems. The basic idea is that instead of the direct superposition of each user's data, an appropriately weighted linear combination of the active users' data is transmitted.
[48] Vojčić and Jang	Proposed a transmitter preprocessing scheme, which represents a linear transformation of the transmitted signals, where the mean squared errors at the output of all receivers are minimised. It was shown that when either a conventional single-user receiver or a RAKE receiver is employed, both the multiple access and the intersymbol interference can be eliminated. The authors also discussed the possibility of including a specific transmit power constraint, which was referred to as the constrained MMSE transmit filter.
[49] Karimi *et al.*	Introduced the concept of the TWF method. The transmit MMSE filter was obtained by simply incorporating a weighted identity matrix in the TZF solution in an intuitive way.

Author(s)	Contribution
[103] Barreto and Fettweis	Two precoding schemes were proposed for the downlink of CDMA systems, which assist in reducing the multiuser interference by jointly preprocessing the transmitted signal based on the knowledge of the downlink channel. Also proposed an unequal transmit power constraint, and stated that the resultant optimization problem has no closed form solution.
[50] Joham *et al.*	Derived the transmit Wiener filter concept for DS-CDMA systems, which takes into account the noise power encountered at the receivers. Demonstrated that the transmit Wiener filter converges to the transmit matched filter and to the transmit zero-forcing filter for low and high SNRs, respectively.
[52] Irmer *et al.*	Proposed a novel approach to MUT design created for the CDMA downlink operating in frequency-selective channels. The key idea is to directly minimise the BER at the receivers with the aid of pre-distortion of the transmitted symbols.
[53] Irmer *et al.*	Suggested the extension of nonlinear minimum BER transmission to multiple transmit and receive antennas. Both linear and nonlinear multiple antenna aided MUT schemes were compared, when combined with the application of Pre-RAKE, RAKE and Singular Value Decomposition (SVD) aided eigen-mode preprocessing.
[54] Irmer *et al.*	The extension of nonlinear minimum BER transmission from the symbol-level to the more general chip-level was advocated using a phase-only nonlinear MUT scheme, which imposes a considerably reduced computational complexity.
[55] Hjørungnes and Diniz	Addressed the problem of designing an optimal prefilter transform for wireless Finite Impulse Response (FIR) MIMO communication systems. The BER was minimised under a given power constraint.
[51] Joham *et al.*	Examined and compared the different types of linear transmit processing schemes designed for MIMO systems. Demonstrated that the transmit filters are based on a similar optimization process as the respective receive filters, with an additional constraint imposed on the transmit power.

Author(s)	Contribution
[100] Yang *et al.*	Investigated the achievable performance of SDMA MIMO systems using transmitter preprocessing, when the channel knowledge required for preprocessing was acquired by the downlink receiver and then conveyed to the transmitter via realistic error-prone feedback channels that may also experience fading. The CIR magnitudes and phases were vector quantized and conveyed to the downlink transmitter separately.
[102] Yang	Introduced novel concepts for finding the relationship between MUDs and MUTs, so that the study of MUTs can benefit from the well-documented theory of MUDs. For any given linear MUD scheme, there exists a linear MUT counterpart, which can be readily designed from the original linear MUD.

5.1 System Description

Consider a downlink system communicating over non-dispersive channels. The transmitter has L_t downlink transmit antennas. The system supports K users and all the users have L_r receive antennas. The multiuser downlink system's structure is shown in Figure 5.2, where s_k is the source symbol transmitted to user k, and $\mathbf{p}_k$ is the preprocessing vector specifically derived for symbol s_k. Then the K-user transmit signal vector becomes $\mathbf{t} = \sum_{k=1}^{K} \mathbf{p}_k s_k = \mathbf{Ps}$, where $\mathbf{P} = [\mathbf{p}_1\ \mathbf{p}_2 \cdots \mathbf{p}_K] \in \mathbb{C}^{L_t \times K}$ and $\mathbf{s} = [s_1\ s_2 \cdots s_K]^T$. The estimated symbol of user k can be written as

$$\hat{s}_k = \mathbf{d}_k^H \mathbf{H}_k \mathbf{t} + \mathbf{d}_k^H \mathbf{n}_k, \tag{5.1}$$

where $\mathbf{H}_k$ is the $(L_r \times L_t)$-element non-dispersive downlink channel matrix of user k, $\mathbf{d}_k$ is the kth user's receive filter and $\mathbf{n}_k$ is the additional noise at the receiver of user k. When we represent the estimated symbols $\hat{s}_k$ of all the K users in the vectorial form $\hat{\mathbf{s}}$ similar to $\mathbf{s}$, the K users' downlink transmission can be expressed as

$$\hat{\mathbf{s}} = \mathbf{D}^H \mathbf{HPs} + \mathbf{D}^H \mathbf{n}, \tag{5.2}$$

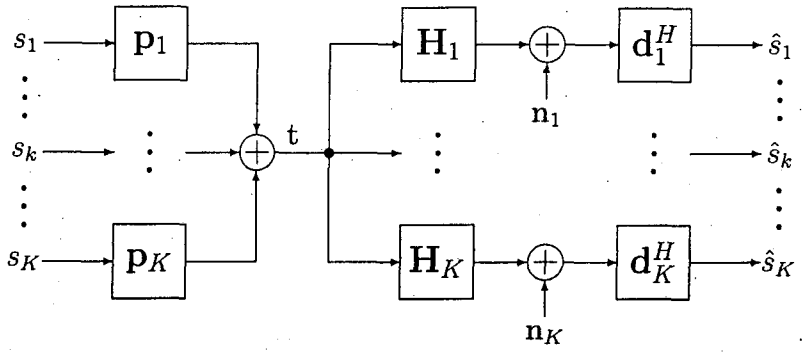

Figure 5.2: Multiuser downlink transmit preprocessing system structure supporting K users.

where we define the K users' channel matrix as $\mathbf{H} = \left[\mathbf{H}_1^T\ \mathbf{H}_2^T \cdots \mathbf{H}_K^T\right]^T \in \mathbb{C}^{KL_r \times L_t}$, $\mathbf{D} = \text{blockdiag}[\mathbf{d}_1\ \mathbf{d}_2 \cdots \mathbf{d}_K] \in \mathbb{C}^{KL_r \times K}$, and $\mathbf{n} = \left[\mathbf{n}_1^T\ \mathbf{n}_2^T \cdots \mathbf{n}_K^T\right]^T \in \mathbb{C}^{KL_r \times 1}$.

5.2 Multiuser Transmission Schemes

5.2.1 Transmit Matched Filter

The Transmit Matched Filter (TMF) concept was introduced by Esmailzadeh *et al.* [46] by moving the matched filter $\mathbf{H}^H$ conventionally match to the channel at the receiver to the transmitter. The TMF does not consider the effect of interference, but maximizes the desired signal's contribution to the estimate $\hat{\mathbf{s}}$ due to the transmitted signal $\mathbf{s}$ and hence beneficially uses the available transmit power E_t. Thus the TMF's transfer function is expressed as

$$\mathbf{P}_{MF} = \arg\max_{\mathbf{P}} \frac{\left|\mathrm{E}\left[\mathbf{s}^H\hat{\mathbf{s}}\right]\right|^2}{\mathrm{E}\left[\left\|\mathbf{D}^H\mathbf{n}\right\|^2\right]} \qquad \text{s.t.: } \mathrm{E}\left[\|\mathbf{Ps}\|^2\right] = E_t. \tag{5.3}$$

By introducing the transmitted signal's covariance matrix $\mathbf{R}_s = \mathrm{E}\left[\mathbf{ss}^H\right]$, the resultant TMF can be written as

$$\mathbf{P}_{MF} = \beta_{MF}\mathbf{H}^H\mathbf{D}, \tag{5.4}$$

where we have

$$\beta_{MF} = \sqrt{\frac{E_t}{\mathrm{tr}\left(\mathbf{H}^H\mathbf{D}\mathbf{R}_s\mathbf{D}^H\mathbf{H}\right)}} \tag{5.5}$$

and $\mathrm{tr}(\cdot)$ denotes the trace of a square-shaped matrix.

5.2.2 Transmit Zero Forcing

Since the transmitter has no influence on the noise encountered at the receivers, the most intuitive approach for transmit processing is using Transmit Zero Forcing (TZF), which removes all the interference at the receivers with the aid of appropriate transmit preprocessing. Tang *et al.* presented a pre-decorrelating technique for flat fading scenarios in [47], and Vojčić *et al.* proposed the more sophisticated transmitter precoding technique of [48]. The TZF coefficients are found by forcing the concatenated transmit filter $\mathbf{P}$, channel $\mathbf{H}$ and receive filter $\mathbf{D}^H$ to be an identity matrix according to $\mathbf{D}^H\mathbf{H}\mathbf{P} = \mathbf{I}$. Since the transmit power is constrained to E_t, the heuristic approach to meet this requirement is to scale the gain of the resultant filter. Then the cost function of the TZF can be expressed as

$$\{\mathbf{P}_{ZF}, \beta_{ZF}\} = \arg\min_{\mathbf{P},\beta} \beta^{-2} \quad \text{s.t.: } \mathbf{D}^H\mathbf{H}\mathbf{P} = \beta\mathbf{I}_K \text{ and } \mathrm{E}\left[\|\mathbf{P}\mathbf{s}\|^2\right] = E_t. \tag{5.6}$$

More explicitly, the optimization criterion is to maximize the received data symbol power, or to minimise the magnitude of the inverse power scaling factor β^{-2}. The first constraint is that of satisfying the zero-forcing condition i.e. to suppress the interference, while the second constraint defines the available transmit power E_t. Therefore, the TZF solution reads as follows

$$\mathbf{P}_{ZF} = \beta_{ZF}\left(\mathbf{H}^H\mathbf{D}\mathbf{D}^H\mathbf{H}\right)^{-1}\mathbf{H}^H\mathbf{D} \tag{5.7}$$

with

$$\beta_{ZF} = \sqrt{\frac{E_t}{\mathrm{tr}\left[\left(\mathbf{D}^H\mathbf{H}\mathbf{H}^H\mathbf{D}\right)^{-1}\mathbf{R}_s\right]}}. \tag{5.8}$$

5.2.3 Transmit Wiener Filter

In [48], Vojčić noted that in the absence of receiver noise the transmit filter minimising the MSE is the TZF. He also discussed the possibility of including a

transmit power constraint, which was referred to as a constrained MMSE transmit filter. Barreto *et al.* [103] proposed to replace the equality in the transmit power constraint $\mathrm{E}\left[\|\mathbf{Ps}\|^2\right] = E_t$ by an inequality, but stated that the resultant optimization had no closed-form solution. The Transmit Wiener Filter (TWF) concept was first mentioned by Karimi *et al.* in [49], who obtained the transmit MMSE filter by simply adding a weighted identity matrix in the solution of the TZF in an intuitive way. The optimization of the TWF was detailed by Joham *et al.* in [50] and [51].

The key to determining the TWF is to allow the transmit filter to generate a receive signal $\hat{\mathbf{s}}$, whose amplitude is different from that of the original desired signal $\mathbf{s}$. The amplitude β of the desired portion in the received signal has to be as high as possible in order to combat the effects of the noise, because the automatic gain control of the receiver is unable to separately scale the desired portion of the signal, it also scales the noise portion of the received signal according to β^{-1}. The TWF includes the weighting of the estimated signal $\hat{\mathbf{s}}$ with the factor β^{-1} in the definition of the MSE and uses the total available transmit power according to

$$\{\mathbf{P}_{WF}, \beta_{WF}\} = \arg\min_{\mathbf{P},\beta} \mathrm{E}\left[\left\|\mathbf{s} - \beta^{-1}\hat{\mathbf{s}}\right\|^2\right] \qquad \text{s.t.: } \mathrm{E}\left[\|\mathbf{Ps}\|^2\right] = E_t. \tag{5.9}$$

We can find the necessary conditions for the transmit filter $\mathbf{P}$ and for the real-valued amplitude weight β to satisfy Equations 5.9 by constructing the Lagrangian function and employing Equation (5.2). Then we have

$$\begin{aligned} L(\mathbf{P},\beta,\lambda) &= \mathrm{E}\left[\left\|\mathbf{s} - \beta^{-1}\hat{\mathbf{s}}\right\|^2\right] + \lambda\left(\mathrm{E}\left[\|\mathbf{Ps}\|^2\right] - E_t\right) \\ &= \mathrm{tr}\left(\mathbf{R}_s - \beta^{-1}\mathbf{R}_s\mathbf{P}^H\mathbf{H}^H\mathbf{D} - \beta^{-1}\mathbf{D}^H\mathbf{HPR}_s + \beta^{-2}\mathbf{D}^H\mathbf{HPR}_s\mathbf{P}^H\mathbf{H}^H\mathbf{D}\right. \\ &\quad \left. + \beta^{-2}\mathbf{D}^H\mathbf{R}_n\mathbf{D} + \lambda\mathbf{PR}_s\mathbf{P}^H\right) - \lambda E_t, \end{aligned} \tag{5.10}$$

where we define $\mathbf{R}_n = \mathrm{E}\left[\mathbf{nn}^H\right]$. By setting this Lagrangian function's gradient with respect to $\mathbf{P}$ to zero, we can derive

$$\begin{aligned} \nabla_{\mathbf{P}} L(\mathbf{P},\beta,\lambda) &= \frac{\partial L(\mathbf{P},\beta,\lambda)}{\partial \mathbf{P}} \\ &= -\beta^{-1}\mathbf{H}^T\mathbf{D}^*\mathbf{R}_s + \beta^{-2}\mathbf{H}^T\mathbf{D}^*\mathbf{D}^T\mathbf{H}^*\mathbf{P}^*\mathbf{R}_s + \lambda\mathbf{P}^*\mathbf{R}_s \\ &= \mathbf{0}_{L_t \times K}, \end{aligned} \tag{5.11}$$

where we used $\frac{\partial \mathrm{tr}(\mathbf{AXB})}{\partial \mathbf{X}} = \mathbf{A}^T\mathbf{B}^T$ and $\frac{\partial \mathrm{tr}(\mathbf{XC})}{\partial \mathbf{X}} = \mathbf{C}^T$. Then, the transmit filter

matrix can be expressed as

$$\mathbf{P} = \beta\left(\mathbf{H}^H\mathbf{D}\mathbf{D}^H\mathbf{H} + \lambda\beta^2\mathbf{I}_{L_t}\right)^{-1} \cdot \mathbf{H}^H\mathbf{D}. \tag{5.12}$$

Furthermore, based on Equation (5.12) and using $\mathrm{tr}(\mathbf{AB}) = \mathrm{tr}(\mathbf{BA})$, the gradient of Equation (5.10) with respect to β can be expressed as

$$\begin{aligned}\nabla_\beta L(\mathbf{P},\beta,\lambda) &= \frac{\partial L(\mathbf{P},\beta,\lambda)}{\partial\beta} \\ &= \mathrm{tr}\big(\beta^{-2}\mathbf{R}_s\mathbf{P}^H\mathbf{H}^H\mathbf{D} + \beta^{-2}\mathbf{D}^H\mathbf{H}\mathbf{P}\mathbf{R}_s \\ &\quad - 2\beta^{-3}\mathbf{D}^H\mathbf{H}\mathbf{P}\mathbf{R}_s\mathbf{P}^H\mathbf{H}^H\mathbf{D} - 2\beta^{-3}\mathbf{D}^H\mathbf{R}_n\mathbf{D}\big) \\ &= 2\beta^{-3}\mathrm{tr}\big(\beta\mathbf{H}^H\mathbf{D}\mathbf{R}_s\mathbf{P}^H - \mathbf{H}^H\mathbf{D}\mathbf{D}^H\mathbf{H}\mathbf{P}\mathbf{R}_s\mathbf{P}^H - \mathbf{D}^H\mathbf{R}_n\mathbf{D}\big) \\ &= 2\beta^{-3}\mathrm{tr}\big(\lambda\beta^2\mathbf{P}\mathbf{R}_s\mathbf{P}^H - \mathbf{D}^H\mathbf{R}_n\mathbf{D}\big). \end{aligned} \tag{5.13}$$

Setting this gradient to zero and using the power constraint $\mathrm{E}\left[\|\mathbf{P}\mathbf{s}\|^2\right] = \mathrm{tr}\left(\mathbf{P}\mathbf{R}_s\mathbf{P}^H\right) = E_t$, we have

$$\lambda\beta^2 = \frac{\mathrm{tr}\left(\mathbf{D}^H\mathbf{R}_n\mathbf{D}\right)}{E_t}. \tag{5.14}$$

Then, the closed form solution for the optimization problem formulated in Equation (5.12) is given by

$$\mathbf{P}_{WF} = \beta_{WF}\mathbf{F}^{-1}\mathbf{H}^H\mathbf{D}, \tag{5.15}$$

where we define

$$\mathbf{F} = \mathbf{H}^H\mathbf{D}\mathbf{D}^H\mathbf{H} + \frac{\mathrm{tr}\left(\mathbf{D}^H\mathbf{R}_n\mathbf{D}\right)}{E_t}\mathbf{I}_{L_t} \tag{5.16}$$

and

$$\beta_{WF} = \sqrt{\frac{E_t}{\mathrm{tr}\left(\mathbf{F}^{-2}\mathbf{H}^H\mathbf{D}\mathbf{R}_s\mathbf{D}^H\mathbf{H}\right)}}. \tag{5.17}$$

It may be readily shown that the TWF converges to the TMF at a low SNR, while to the TZF solution at a high SNR.

5.2.4 Nonlinear Minimum Bit Error Rate Transmission

minimising the downlink BER as transmit signal optimization criterion was proposed for Minimum Bit Error Rate Transmission (TMinBer) by Irmer *et al.* in [52, 53, 54], which exploited the knowledge of all users' transmitted symbols.

For uplink MUD, the perfect knowledge of the transmitted symbols is usually

not available since they arrive from geographically dispersed MSs, whereas in MUT the data symbols are known *a priori*. Using the nth actually transmitted symbol combination $\mathbf{s}(n)$, which may be preprocessed by a symbol- and user-specific coefficient, and assuming perfect channel knowledge, the symbols received by each MS can be calculated. Given the receiver noise variance, the average BER of all receivers may be calculated as

$$Pe(n) = \frac{1}{K}\sum_{k=1}^{K} \mathrm{Q}\left(\frac{\mathrm{sgn}(\Re[s_k(n)]) \cdot \Re\left[\mathbf{d}_k^H(n)\mathbf{H}_k(n)\mathbf{P}(n)\mathbf{s}(n)\right]}{\sigma_{nk}\sqrt{\mathbf{d}_k^H(n)\mathbf{d}_k(n)}}\right) \tag{5.18}$$

for BPSK modulation, where the noise variance of the kth receiver is $2\sigma_{nk}^2$. The BER of all MSs is then minimised by optimizing the BS's MUT preprocessing coefficients, where a constant total transmit power constraint has to be fulfilled. Then the TMinBer solution can be expressed as

$$\mathbf{P}_{TMinBer}(n) = \arg\min_{\mathbf{P}} Pe(n) \qquad \text{s.t.: } \mathrm{E}\left[\|\mathbf{Ps}(n)\|^2\right] = E_t. \tag{5.19}$$

Unfortunately, there is no closed-form analytical solution for the constrained non-linear TMinBer optimization problem. In fact, it is not even necessarily a convex optimization problem. Nonetheless, using state-of-the-art nonlinear optimization methods, such as Sequential Quadratic Programming (SQP) [104], satisfactory results can be achieved.

5.3 Linear Minimum Bit Error Rate Transmission

5.3.1 Bit Error Rate

When using a linear precessing matrix $\mathbf{P}$ in the transmitter, as shown in Figure 5.2 and Equation (5.2), the symbol estimated at the kth receiver is given by

$$\hat{s}_k = \mathbf{d}_k^H\mathbf{H}_k\mathbf{Ps} + \mathbf{d}_k^H\mathbf{n}_k. \tag{5.20}$$

Let us define $x = \mathrm{sgn}(\Re[s_k]) \cdot \Re[\hat{s}_k(\mathbf{P})]$ as a signed decision variable. The PDF of x is constituted by a mixture of the Gaussian distributions associated with each possible combination of the transmitted data symbols of all users. Similarly to the

MBER detector of Equation (2.26), under the assumption that all the noise-free signal states are equiprobable, the PDF of x is given by

$$p(x) = \frac{1}{M^K\sqrt{2\pi}\sigma_{nk}\sqrt{\mathbf{d}_k^H\mathbf{d}_k}} \sum_{q=1}^{M^K} \exp\left(-\frac{\left(x - \mathrm{sgn}\left(\Re\left[s_k^{(q)}\right]\right)\cdot\Re\left[\mathbf{d}_k^H\mathbf{H}_k\mathbf{P}\mathbf{s}^{(q)}\right]\right)^2}{2\sigma_{nk}^2\mathbf{d}_k^H\mathbf{d}_k}\right), \tag{5.21}$$

where M^K is the number of equiprobable combinations of the binary vectors of the K users for M-*ary* PSK systems. The erroneous decision events are associated with the area under the PDF curve in the interval $(-\infty, 0)$, hence similarly to the MBER MUD Equation (2.27), the average BER of the in-phase component at the receiver is quantified as

$$Pe_I = \frac{1}{KM^K}\sum_{q=1}^{M^K}\sum_{k=1}^{K} \mathrm{Q}\left(\frac{\mathrm{sgn}\left(\Re\left[s_k^{(q)}\right]\right)\cdot\Re\left[\mathbf{d}_k^H\mathbf{H}_k\mathbf{P}\mathbf{s}^{(q)}\right]}{\sigma_{nk}\sqrt{\mathbf{d}_k^H\mathbf{d}_k}}\right). \tag{5.22}$$

Comparing this expression to Equation (5.18), we can infer that the proposed Linear Minimum Bit Error Rate (LMBER) MUT considers all possible combinations of transmitted symbols to derive the BER, while the TMinBer solution of Section 5.2.4 only considers the specific transmitted symbols at the certain time. The LMBER MUT algorithm constitutes a linear method, which does not rely on the symbols transmitted from the BS. Similarly, the average BER of the quadrature-phase component is

$$Pe_Q = \frac{1}{KM^K}\sum_{q=1}^{M^K}\sum_{k=1}^{K} \mathrm{Q}\left(\frac{\mathrm{sgn}\left(\Im\left[s_k^{(q)}\right]\right)\cdot\Im\left[\mathbf{d}_k^H\mathbf{H}_k\mathbf{P}\mathbf{s}^{(q)}\right]}{\sigma_{nk}\sqrt{\mathbf{d}_k^H\mathbf{d}_k}}\right). \tag{5.23}$$

Hence the downlink BER of the MS's receiver is

$$Pe_b = \begin{cases} Pe_I & \text{(BPSK)} \\ \frac{1}{2}(Pe_I + Pe_Q) & \text{(QPSK)} \end{cases}. \tag{5.24}$$

5.3.2 Linear Minimum Bit Error Rate Solution

Similarly to the MBER detector of Equation (2.28), the LMBER transmission solution can be defined as

$$\mathbf{P}_{LMBER} = \arg\min_{\mathbf{P}} Pe_b \qquad \text{s.t.: } \mathrm{E}\left[\|\mathbf{P}\mathbf{s}\|^2\right] = E_t, \tag{5.25}$$

which is a constrained optimization problem. If λ is defined as the Lagrange multiplier used for imposing the constraint $\mathrm{E}\left[\|\mathbf{Ps}\|^2\right] = E_t$, then the Lagrangian expression $L(\mathbf{P}, \lambda)$ can be expressed as

$$\begin{aligned} L(\mathbf{P}, \lambda) &= Pe_b + \lambda\big(\mathrm{E}\left[\|\mathbf{Ps}\|^2\right] - E_t\big) \\ &= Pe_b + \lambda\Big(\mathrm{tr}\big(\mathbf{P}\mathbf{R}_s\mathbf{P}^H\big) - E_t\Big). \end{aligned} \tag{5.26}$$

Then the LMBER transmission solution becomes

$$\{\mathbf{P}_{LMBER}, \lambda_{LMBER}\} = \arg\min_{\mathbf{P},\lambda} L(\mathbf{P}, \lambda). \tag{5.27}$$

5.3.3 Constrained Optimization

Let us now define a real-valued vector $\mathbf{p} = \left[\Re^T[\mathbf{p}_1]\ \Re^T[\mathbf{p}_2] \cdots \Re^T[\mathbf{p}_K]\ \Im^T[\mathbf{p}_1] \cdots \Im^T[\mathbf{p}_K]\right]^T \in \mathbb{R}^{2KL_t}$, which is an alterative expression for the MUT preprocessing matrix $\mathbf{P}$ derived for simplifying the calculation of the first and second gradients of the BER formulae of Equations (5.22) and (5.23). Then, using the SQP algorithm [104] to solve the optimization problem of Equation (5.27), we arrive at

$$\begin{bmatrix} \nabla^2 Pe_b + \lambda\nabla^2\mathrm{tr}\big(\mathbf{P}\mathbf{R}_s\mathbf{P}^H\big) & \nabla\mathrm{tr}\big(\mathbf{P}\mathbf{R}_s\mathbf{P}^H\big) \\ \Big(\nabla\mathrm{tr}\big(\mathbf{P}\mathbf{R}_s\mathbf{P}^H\big)\Big)^T & 0 \end{bmatrix} \begin{bmatrix} \Delta\mathbf{p} \\ \Delta\lambda \end{bmatrix} = -\begin{bmatrix} \nabla Pe_b + \lambda\nabla\mathrm{tr}\big(\mathbf{P}\mathbf{R}_s\mathbf{P}^H\big) \\ \mathrm{tr}\big(\mathbf{P}\mathbf{R}_s\mathbf{P}^H\big) - E_t \end{bmatrix}, \tag{5.28}$$

where $\Delta\mathbf{p}$ is the correction of the transmit processing vector $\mathbf{p}$, and $\Delta\lambda$ is the Lagrange multiplier's correction. The first and second derivatives of the constraint $\mathrm{tr}\big(\mathbf{P}\mathbf{R}_s\mathbf{P}^H\big)$ in Equation (5.28) can be derived as

$$\begin{aligned} \nabla\mathrm{tr}\big(\mathbf{P}\mathbf{R}_s\mathbf{P}^H\big) &= \frac{\partial}{\partial\mathbf{p}}\mathrm{tr}\big(\mathbf{P}\mathbf{R}_s\mathbf{P}^H\big) \\ &= \Re_s\mathbf{p} \end{aligned} \tag{5.29}$$

and

$$\nabla^2\mathrm{tr}\big(\mathbf{P}\mathbf{R}_s\mathbf{P}^H\big) = \Re_s, \tag{5.30}$$

where $\Re_s = \mathrm{blockdiag}\left[E_{s1}\mathbf{I}_{L_t}\ E_{s2}\mathbf{I}_{L_t} \cdots E_{sK}\mathbf{I}_{L_t}\ E_{s1}\mathbf{I}_{L_t} \cdots E_{sK}\mathbf{I}_{L_t}\right] \in \mathbb{R}^{2KL_t \times 2KL_t}$, E_{sk} is the average symbol energy of user k. The first-order and second-order gradients of Pe_b in Equation (5.28) can be derived from the gradients of Pe_I and Pe_Q. Based on the derivations in Appendix B, the gradients of both the in-phase

and quadrature-phase bit error probabilities are given by

$$\nabla Pe_I = \frac{\partial Pe_I}{\partial \mathbf{p}} = \frac{-1}{\sqrt{2\pi}KM^K}\sum_{q=1}^{M^K}\sum_{k=1}^{K}\exp\left(-\frac{\left(\Re\left[\mathbf{d}_k^H\mathbf{H}_k\mathbf{P}\mathbf{s}^{(q)}\right]\right)^2}{2\sigma_{nk}^2\mathbf{d}_k^H\mathbf{d}_k}\right)\cdot\frac{\operatorname{sgn}\left(\Re\left[s_k^{(q)}\right]\right)}{\sigma_{nk}\sqrt{\mathbf{d}_k^H\mathbf{d}_k}}\mathbf{v}_{k,I}^{(q)}, \tag{5.31a}$$

$$\nabla Pe_Q = \frac{\partial Pe_Q}{\partial \mathbf{p}} = \frac{-1}{\sqrt{2\pi}KM^K}\sum_{q=1}^{M^K}\sum_{k=1}^{K}\exp\left(-\frac{\left(\Im\left[\mathbf{d}_k^H\mathbf{H}_k\mathbf{P}\mathbf{s}^{(q)}\right]\right)^2}{2\sigma_{nk}^2\mathbf{d}_k^H\mathbf{d}_k}\right)\cdot\frac{\operatorname{sgn}\left(\Im\left[s_k^{(q)}\right]\right)}{\sigma_{nk}\sqrt{\mathbf{d}_k^H\mathbf{d}_k}}\mathbf{v}_{k,Q}^{(q)} \tag{5.31b}$$

and

$$\nabla^2 Pe_I = \frac{1}{\sqrt{2\pi}KM^K}\sum_{q=1}^{M^K}\sum_{k=1}^{K}\exp\left(-\frac{\left(\Re\left[\mathbf{d}_k^H\mathbf{H}_k\mathbf{P}\mathbf{s}^{(q)}\right]\right)^2}{2\sigma_{nk}^2\mathbf{d}_k^H\mathbf{d}_k}\right)\cdot\frac{\operatorname{sgn}\left(\Re\left[s_k^{(q)}\right]\right)\cdot\Re\left[\mathbf{d}_k^H\mathbf{H}_k\mathbf{P}\mathbf{s}^{(q)}\right]}{\sigma_{nk}^3\left(\mathbf{d}_k^H\mathbf{d}_k\right)^{\frac{3}{2}}}\mathbf{v}_{k,I}^{(q)}\left(\mathbf{v}_{k,I}^{(q)}\right)^T, \tag{5.32a}$$

$$\nabla^2 Pe_Q = \frac{1}{\sqrt{2\pi}KM^K}\sum_{q=1}^{M^K}\sum_{k=1}^{K}\exp\left(-\frac{\left(\Im\left[\mathbf{d}_k^H\mathbf{H}_k\mathbf{P}\mathbf{s}^{(q)}\right]\right)^2}{2\sigma_{nk}^2\mathbf{d}_k^H\mathbf{d}_k}\right)\cdot\frac{\operatorname{sgn}\left(\Im\left[s_k^{(q)}\right]\right)\cdot\Im\left[\mathbf{d}_k^H\mathbf{H}_k\mathbf{P}\mathbf{s}^{(q)}\right]}{\sigma_{nk}^3\left(\mathbf{d}_k^H\mathbf{d}_k\right)^{\frac{3}{2}}}\mathbf{v}_{k,Q}^{(q)}\left(\mathbf{v}_{k,Q}^{(q)}\right)^T, \tag{5.32b}$$

where $\mathbf{v}_{k,I}^{(q)} = \left[\Re\left[s_1^{(q)}\mathbf{d}_k^H\mathbf{H}_k\right]\ \Re\left[s_2^{(q)}\mathbf{d}_k^H\mathbf{H}_k\right]\ \cdots\ \Re\left[s_K^{(q)}\mathbf{d}_k^H\mathbf{H}_k\right]\ -\Im\left[s_1^{(q)}\mathbf{d}_k^H\mathbf{H}_k\right]\ \cdots\ -\Im\left[s_K^{(q)}\mathbf{d}_k^H\mathbf{H}_k\right]\right]^T \in \mathbb{R}^{2KL_t}$ and $\mathbf{v}_{k,Q}^{(q)} = \left[\Im\left[s_1^{(q)}\mathbf{d}_k^H\mathbf{H}_k\right]\ \Im\left[s_2^{(q)}\mathbf{d}_k^H\mathbf{H}_k\right]\ \cdots\ \Im\left[s_K^{(q)}\mathbf{d}_k^H\mathbf{H}_k\right]\ \Re\left[s_1^{(q)}\mathbf{d}_k^H\mathbf{H}_k\right]\ \cdots\ \Re\left[s_K^{(q)}\mathbf{d}_k^H\mathbf{H}_k\right]\right]^T \in \mathbb{R}^{2KL_t}$.

The SQP algorithm operates as follows [104]:

Initialization: Set the iteration index i=1. Choose a step size of δ>0 and a termination scalar of β>0. Given $\lambda(1)$, $\mathbf{P}(1)$ and $\mathbf{p}(1) = \left[\Re^T[\mathbf{p}_1(1)]\ \Re^T[\mathbf{p}_2(1)]\ \cdots\ \Re^T[\mathbf{p}_K(1)]\ \Im^T[\mathbf{p}_1(1)]\ \cdots\ \Im^T[\mathbf{p}_K(1)]\right]^T$, carry out:

Loop:

$$c(i) = \mathrm{tr}\big(\mathbf{P}(i)\mathbf{R}_s\mathbf{P}(i)^H\big) - E_t, \tag{5.33}$$

$$\mathbf{g}(i) = \begin{bmatrix} \nabla Pe_b\big(\mathbf{P}(i)\big) + \lambda(i)\nabla c(i) \\ c(i) \end{bmatrix}, \tag{5.34}$$

$$\mathbf{D}(i) = \begin{bmatrix} \nabla^2 Pe_b\big(\mathbf{P}(i)\big) + \lambda(i)\nabla^2 c(i) & \nabla c(i) \\ \big(\nabla c(i)\big)^T & 0 \end{bmatrix}, \tag{5.35}$$

$$\begin{bmatrix} \Delta\mathbf{p}(i) \\ \Delta\lambda(i) \end{bmatrix} = -\mathbf{D}(i)^{-1}\mathbf{g}(i), \tag{5.36}$$

$$\mathbf{p}(i{+}1) = \mathbf{p}(i) + \delta\Delta\mathbf{p}(i), \tag{5.37}$$

$$\lambda(i{+}1) = \lambda(i) + \delta\Delta\lambda(i), \tag{5.38}$$

transform the real-valued vector $\mathbf{p}(i{+}1)$ back to a complex-valued matrix $\mathbf{P}(i{+}1)$, and $i = i + 1$. If $\|\Delta\mathbf{p}(i)\| < \beta$, goto **End**. Else, goto **Loop**.

End: Weight matrix $\mathbf{P}(i)$ is the chosen solution.

5.4 Computational Complexity Comparison

The comparison of the different MUT schemes' computational complexity imposed by computing the preprocessing matrix $\mathbf{P}$ is summarized in Table 5.2. The number of real-valued operations is used as the unit of complexity, while the complexities imposed by a real-valued multiplication and a real-valued addition might be considered equivalent. It can be seen in Table 5.2 that the TMF MUT has the lowest complexity of $\mathcal{O}\big(KL_t^2\big)$. The TZF and TWF transmitters have similar computational complexities, which are $\mathcal{O}\big(K^3 + L_t^3 + K^2L_t + KL_t^2\big)$ and $\mathcal{O}\big(L_t^3 + KL_t^2\big)$, respectively. The TMinBer MUT has a higher complexity of $\mathcal{O}\big(K^3L_t^3N_{sqp}\big)$, where N_{sqp} denotes the number of iterations in the SQP algorithm. The LMBER method has the highest complexity of $\mathcal{O}\big(K^3L_t^2M^KN_{sqp}\big)$ in Table 5.2, which is about $\frac{M^K}{L_t}$ times higher than that of the TMinBer MUT.

These MUT schemes' computational complexity can be considered for different channel conditions. The first channel condition is the fast-fading uncorrelated channel, in which the channel experienced by the transmitted signal is varying rapidly. Then the preprocessing matrix $\mathbf{P}$ has to be re-calculated for each trans-

Table 5.2: Computational complexity comparison of different MUT schemes

MUT	Computational complexity	Equation(s)
TMF	$8KL_t^2 + 8KL_tL_r + 2KL_t - 2L_t^2 + L_t + 1$	(5.4), (5.5)
TZF	$\mathcal{O}(8K^3) + \mathcal{O}(8L_t^3) + 8K^2L_t + 16KL_t^2 + 8KL_tL_r - 2L_t^2 - 2KL_t + K + 1$	(5.7), (5.8)
TWF	$\mathcal{O}(8L_t^3) + 24KL_t^2 + 8KL_tL_r + 6KL_r - 4L_t^2 + 2L_t + 1$	(5.15), (5.16), (5.17)
TMinBer	$\Big(\mathcal{O}(8K^3L_t^3) + 8K^3L_t^2 + 8K^2L_t^2 + 14K^2L_t + 8KL_t^2 + 8KL_tL_r + 6K^2 + 18KL_t + 8KL_r - 2L_t^2 + 2K + L_t + 11\Big)N_{sqp}$	(5.19)
LMBER	$\Big(\big(8K^3L_t^2 + 6K^2L_t + 8K^2 + 6KL_t + 4K\big)M^K + \mathcal{O}(8K^3L_t^3) + 8K^2L_t^2 + 8K^2L_t + 8KL_t^2 + 8KL_tL_r + 12KL_t + 8KL_r - 2K^2 - 2L_t^2 + L_t - 2K + 11\Big)N_{sqp}$	(5.28), (5.31), (5.32)

mitted signal, regardless of which MUT algorithm is employed. The other channel model considered is the block-fading, i.e. slow-fading channel. Under the corresponding slow-fading conditions, we assume that the fading envelop remains constant for N_b symbols, i.e. the channel can be considered as time-invariant. Then it is faded independently at the end of this period. Hence the computational complexity of all linear schemes, namely of the TMF, TZF, TWF and LMBER MUTs, can be reduced by a factor of N_b with respect to the corresponding value seen in Table 5.2. However, the non-linear TMinBer algorithm still has a similar complexity under the block-fading conditions to that recorded for the fast-fading conditions.

5.5 Performance Analysis

5.5.1 Performance with Perfect Channel Information

Let us now consider a downlink transmit beamforming system employing a three-element antenna array and benefitting from perfect channel information. All users have the same transmit power as well as non-dispersive CIR coefficients of $h_k = 1.0+j0.0$ ($k \in \{1, \cdots, K\}$). Figure 5.3 shows the BER versus E_b/N_0 performance of the Wiener, TMinBer and LMBER MUTs supporting K=5 BPSK users. This corresponds to a challenging rank-deficient scenario, where the channel matrix

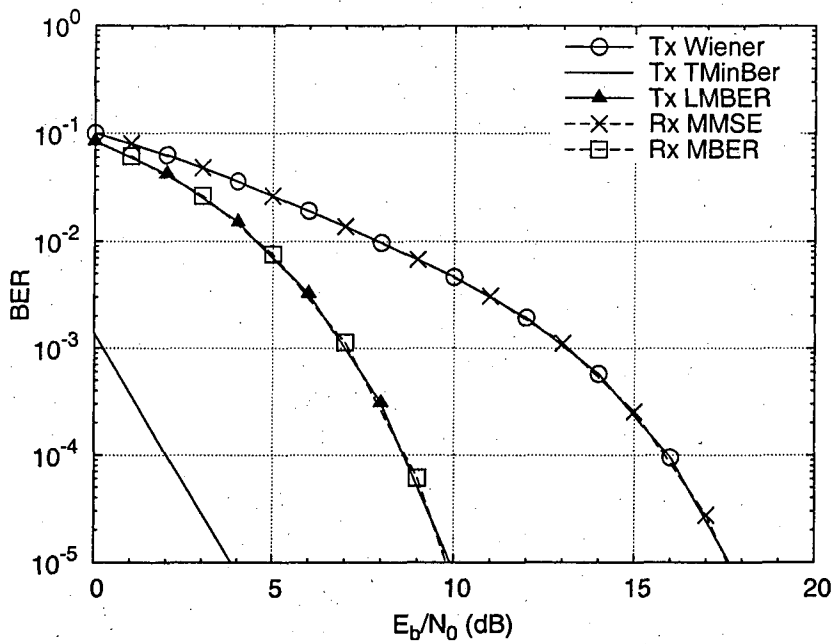

Figure 5.3: BER versus E_b/N_0 performance of the Wiener, TMinBer and LMBER MUTs employing L_t=3 transmit AEs for supporting K=5 BPSK users communicating over AWGN channels. The transmit angles of the users' signal are seen in Figure 5.4.

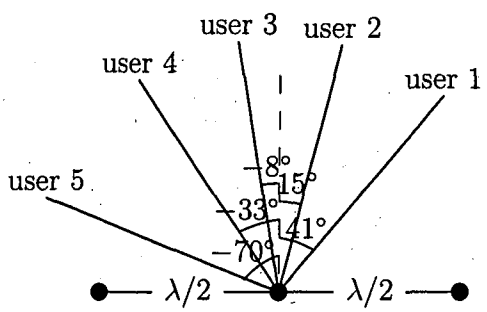

Figure 5.4: Three AEs, where the signal of the individual users are transmitted at angles of 41°, 15°, −8°, −33° and −70°.

becomes non-invertible. The transmit angles of the users' signal were 41°, 15°, −8°, −33° and −70°, respectively, as seen in Figure 5.4. It can be observed that the LMBER transmitter substantially outperforms the Wiener MUT, namely by about 7.8dB at the BER of 10^{-5}. However, the optimum linear LMBER MUT has a decreased performance compared to non-linear TMinBer transmission. In Figure 5.3, the BER performance of the MMSE MUD and of the MBER MUD uplink systems employing three-element uplink receiver antenna arrays and

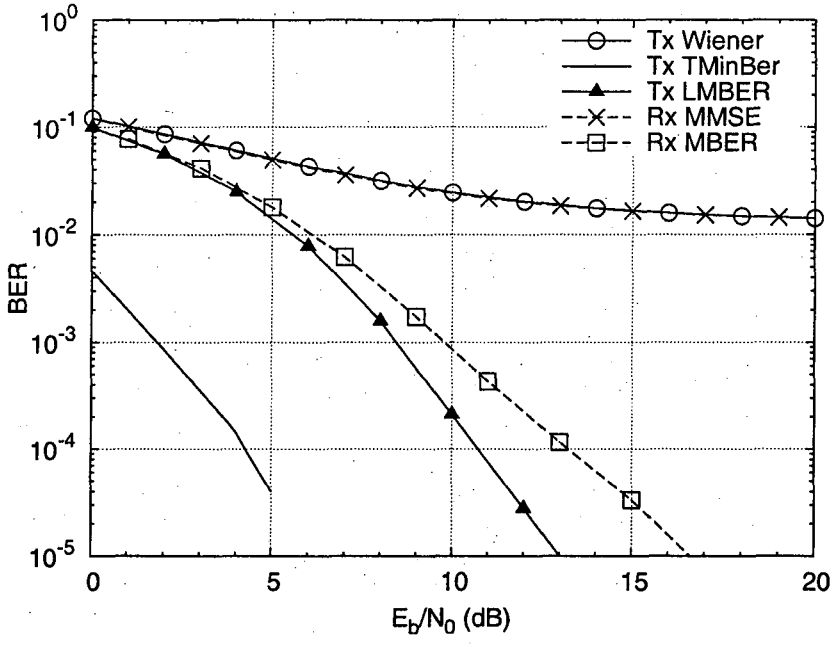

Figure 5.5: BER versus E_b/N_0 performance of the Wiener, TMinBer and LMBER MUTs employing L_t=3 transmit AEs for supporting K=5 BPSK users communicating over flat-fading channels when the Doppler frequency is 10^{-2}. The transmit angles of the users' signal are seen in Figure 5.4.

supporting five users are also plotted. It is shown that the LMBER transmit processing and MBER receive processing have the same performance.

Consider a K=5 user BPSK downlink system communicating over narrow-band slow-fading channels. The normalized Doppler frequency is 10^{-2}, and the Ricean K-factor is 10. Figure 5.5 shows the BER performance of the Wiener, TMinBer and LMBER MUTs, as well as those of the MMSE and MBER MUDs. Observe that the LMBER MUT significantly outperforms the Wiener MUT. The Wiener MUT has an error floor higher than 10^{-2}, while the LMBER MUT is capable of achieving an infinitesimally low BER at high SNRs. Under these fading conditions, the non-linear TMinBer MUT outperforms the proposed LMBER scheme, which is a linear preprocessing method. Figure 5.5 also shows that the LMBER MUT has an approximately 3.5dB gain over the MBER MUD at the BER of 10^{-5}. The reason of this performance difference is that the multiuser transmit preprocessing is capable of potentially providing a better power allocation solution. By contrast, the MUD remains unable of optimizing the users' transmit power without power control feedback information.

5.5.2 Performance Subject to Channel Estimation Errors

All simulations assumed so-far perfectly known channel information at the transmitter. However, in realistic scenarios the achievable performance will be degraded owing to channel estimation errors imposed by the quantization error and the outdated fading feedback channels. To evaluate the achievable performance in the presence of channel estimation errors without assuming a specific channel estimation algorithm or a channel information feedback algorithm, a simple channel estimation error model is used. Explicitly, the channel estimation error is modeled as an additive complex Gaussian variable with a variance of σ_{ce}^2 at the transmitter. Of interest is its ratio to the mean variance of all channel taps. The additive channel estimation error is assumed to have the same variance, regardless of the current channel coefficient, which is subject to fading.

Figure 5.6 plots the BER performance of the Wiener and LMBER MUTs, when the CIR taps are contaminated by an additive complex Gaussian estimation error. Again, the transmitter has a three-element transmit antenna array supporting K=5 BPSK users communicating over narrowband slow-fading chan-

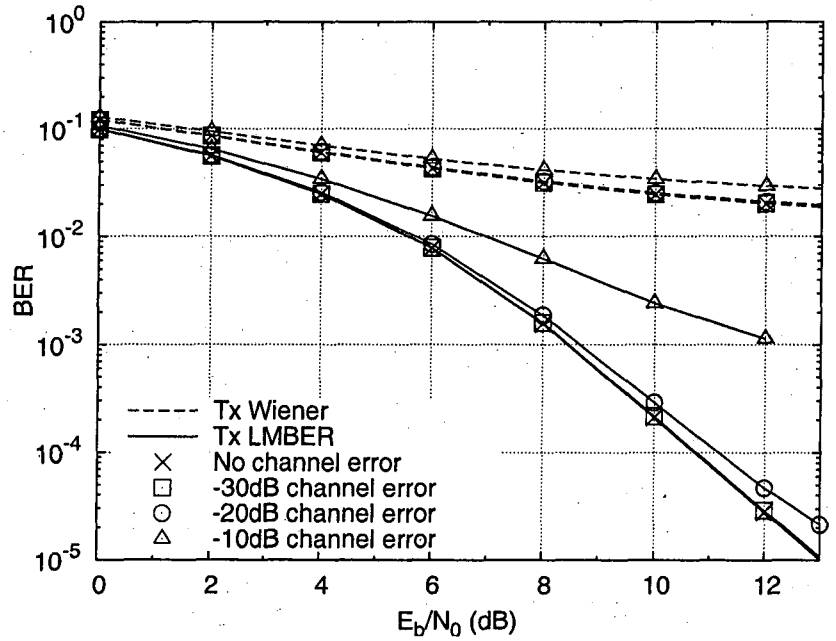

Figure 5.6: BER versus E_b/N_0 performance of the Wiener and LMBER MUTs employing L_t=3 transmit AEs supporting K=5 BPSK users communicating over flat-fading channels with additive channel estimation errors. The transmit angles of the users' signal are seen in Figure 5.4.

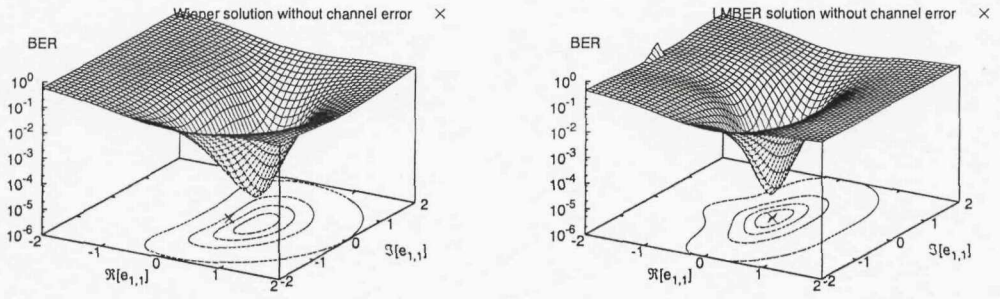

(a) Tx Wiener (b) Tx LMBER

Figure 5.7: The first user's BER surface of the Wiener and LMBER MUT employing L_t=3 transmit AEs supporting K=5 BPSK users communicating over flat-fading channels with additive channel estimated errors at E_b/N_0=10dB. The transmitter has perfect knowledge of all users' channels, except for the CIR spanning from the first of the L_t=3 transmit antennas to the single antenna of the first user.

nels. The normalized Doppler frequency is 10^{-2}, and the Ricean K-factor is 10. It can be seen that when the CIR tap estimation error related Noise-to-Signal Ratio (NSR) is -30dB, the system has almost the same performance as that having perfect channel information. However, as the channel error's variance increases, the MUT aided system has a gradually degrading BER performance. We can also see in Figure 5.6 that for the channel estimation NSR of -10dB, the LMBER MUT's BER performance degrades faster than that of the Wiener MUT. This means that the LMBER MUT is more sensitive to the channel estimation errors than the Wiener MUT. This may be anticipated, since the more sophisticated LMBER MUT achieves its better performance by making use of the accurate channel information. When the channel information is contaminated, it becomes more challenging to separate the users at the MUT with the aid of their unique CIRs.

Let us now assume that the transmitter has perfect knowledge of all users' channels, except for the CIR spanning from the first of the L_t=3 transmit antennas to the single antenna of the first user. Figure 5.7 plots the first user's BER surface of the Wiener MUT and the LMBER MUT at E_b/N_0=10dB. The horizontal axes labeled as $\Re[e_{1,1}]$ and $\Im[e_{1,1}]$ represent the real and the imaginary part of the channel estimation error from the first of the multiple transmit antennas to the single receive antenna of the first user, respectively. The contours

of the BER surface and the point corresponding to zero channel estimation error are both plotted on the base plate of the figure. We can observe in Figure 5.7b that as expected, the BER performance of the LMBER MUT degrades, when the channel estimation error is increased in any direction from the error-free point. However, for the Wiener MUT characterized in Figure 5.7a, it is possible that the performance may improve, when the Wiener filter based transmitter has imperfect channel information, as observed for example when the channel estimation error becomes $e_{1,1} = 0.5$. This is one of the reasons why the LMBER MUT is more sensitive to the channel estimation errors than the Wiener MUT.

5.5.3 Performance with Outdated Channel Information

In practical applications the downlink channel knowledge used for transmit preprocessing might not be updated for each transmitted symbol. When the channel information is fed back from the MSs to the BS, the transmitter has to rely on outdated channel knowledge. In this section, we will investigate the influence of the outdated channel information on the MUT-aided system's performance.

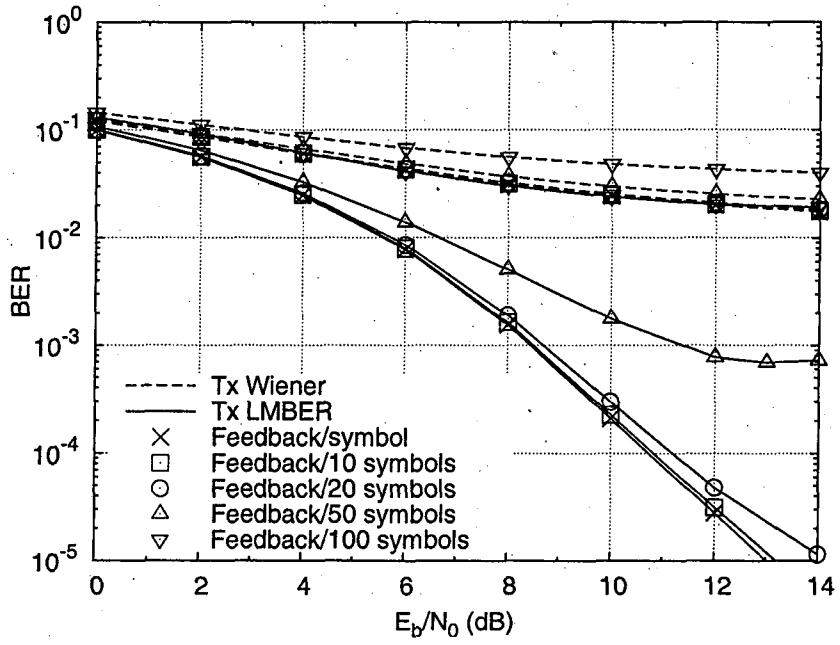

Figure 5.8: BER versus E_b/N_0 performance of the Wiener and LMBER MUTs employing L_t=3 transmit AEs supporting K=5 BPSK users communicating over flat-fading channels at differently delayed channel information updates. The transmit angles of the users' signal are seen in Figure 5.4.

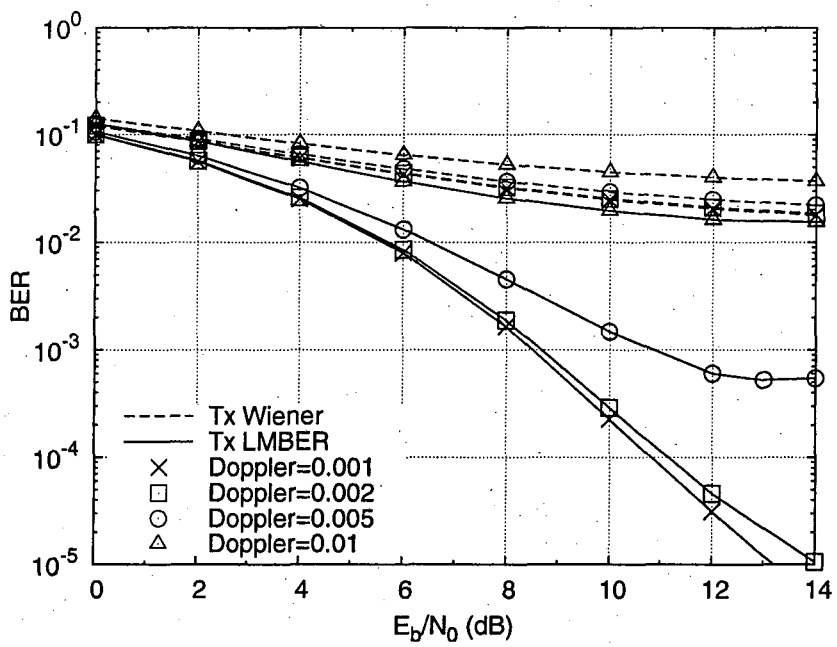

Figure 5.9: BER versus E_b/N_0 performance of the Wiener and LMBER MUTs employing L_t=3 transmit AEs for supporting K=5 BPSK users communicating over flat-fading channels using outdated channel information at different Doppler frequencies. The transmit angles of the users' signal are seen in Figure 5.4.

Let us consider a system employing a three-element transmit antenna array for supporting K=5 BPSK users communicating over narrowband slow-fading channels. The normalized Doppler frequency is 10^{-3}, and the Ricean K-factor is 10. We assume that the BS receives perfect channel information from the MSs every N transmitted symbols. This means that $(N-1)$ out of the N downlink symbols have to rely on outdated channel knowledge. When N=1, the transmitter employs perfect channel information for all transmitted symbols. Figure 5.8 shows the Wiener and the LMBER MUTs' performance for N = 1, 10, 20, 50 and 100. The LMBER MUT system outperforms the Wiener MUT system, and naturally, the BER performance of both systems degrades, when the parameter N increases.

Figure 5.9 also plots the BER performance of various MUT systems employing outdated channel knowledge, when we consider the influence of different normalized Doppler frequencies. In this scenario, we assume that the channel information is fed back to the MUT every 10 symbols, where the Doppler frequencies considered are 10^{-3}, 2×10^{-3}, 5×10^{-3} and 10^{-2}, respectively. As the Doppler frequency increases, which implies encountering more rapidly fading channels, both the Wiener filter and the LMBER aided systems' performance degrades. We can

also see in Figure 5.9 that the LMBER MUT is more sensitive to the outdated channel information than the Wiener filter based MUT.

5.6 Conclusions

In this chapter a linear MUT that minimises the BER subject to a power constraint was proposed. It was shown by simulations that better BER results can be achieved by the proposed LMBER transmission scheme of Section 5.3, when compared to the Wiener filter based MUT of Section 5.2.3. The optimum LMBER MUT solution can be found by exploiting a power-constrained optimization problem, which was investigated in Section 5.3.3. Furthermore, other preprocessing schemes, such as the TMF MUT of Section 5.2.1, the TZF MUT of Section 5.2.2 and the non-linear TMinBer MUT of Section 5.2.4 were also introduced.

The computational complexity and the achievable BER performance when communicating over Ricean fading channels recorded for the methods mentioned above are summarized in Table 5.3. The system's schematic obeys the structure of Figure 5.2. Although the proposed LMBER preprocessing aided transmission algorithm has a better performance than the other linear MUTs, it is more sensitive against channel estimation errors, and the computational complexity imposed by finding the proposed MUT solution is higher. Once the solution is found, it has a similar implementational complexity to those of the other linear transmission algorithms. Under block-fading conditions, the complexity of the LMBER MUT can be significantly reduced, although it fails to achieve a performance similar to that of the non-linear TMinBer algorithm.

Table 5.3: Performance and complexity summary of beamforming aided MUTs

MUD	Section	Complexity	SNR at a BER of 10^{-4}
TMF	5.2.1	$\mathcal{O}\left(KL_t^2\right)$	unachievable
TZF	5.2.2	$\mathcal{O}\left(K^3 + L_t^3 + K^2L_t + KL_t^2\right)$	unachievable
TWF	5.2.3	$\mathcal{O}\left(L_t^3 + KL_t^2\right)$	unachievable
TMinBer	5.2.4	$\mathcal{O}\left(K^3L_t^3N_{sqp}\right)$	4.2dB
LMBER	5.3	$\mathcal{O}\left(K^3L_t^2M^KN_{sqp}\right)$	10.9dB

Chapter 6

Conclusions and Future Research

6.1 Conclusions

The conclusions provided in this chapter constitute an amalgam of our previously drawn conclusions provided at the end of Chapter 2–5 and establishes their logical connection.

In **Chapter 2** we presented various categories of multiple antenna aided communication systems, which perform spatio-temporal information processing with the aid of multiple antennas. Different smart antenna assisted architectures provide different benefits, such as achieving array gain, diversity gain, multiplexing gain, interference reduction and/or coding gain. The concepts of multi-functional MIMOs and distributed MIMOs have recently gained considerable interest. The former structure combines the benefits of different smart antenna aided techniques for the sake of combining their advantages, highlighted in Table 2.2. By contrast, in the latter concept, multiple MSs may cooperate and share their single antennas in order to achieve the improved performance of MIMO systems.

Various MIMO assisted multiuser detection algorithms were also introduced in Chapter 2. The 'System 1' column in Table 6.1 quantifies the achievable performance versus computational complexity of different MUDs when employing no Forward Error Correction (FEC). As assumed in Section 2.2.9, all users' signals are transmitted over AWGN channels and the receiver employs a three-element antenna array. The number of users and their DOAs were plotted in Figures 2.12, 2.14 and 2.16 for BPSK, QPSK and 16QAM schemes, respectively.

As seen in Table 6.1, the Bayesian detector constitutes the optimum nonlinear receiver, which significantly outperforms all linear MUDs at the cost of a higher complexity. The conventional MMSE beamformer combines the signals received with the aid of each AE for the sake of minimising the MSE between the complex-valued locally stored and received reference signal. For BPSK systems, however, the beamformer's desired output is real-valued. By minimising the MSE between the beamformer's desired output and the real part of the beamformer output, the system's achievable BER performance can be significantly enhanced, and this was referred to as the RMMSE design. However, the MMSE and RMMSE algorithms do not guarantee the direct and explicit minimisation of the system's BER. This motivated the design of MBER beamforming, where the BER rather than the MSE was minimised at the MUD's output. The MBER beamformer design is the optimal linear solution and hence it generally outperforms the MMSE and the RMMSE solutions, as seen in Table 6.1. The MBER detectors are challenging to derive for higher-order QAM, hence a novel MSER beamforming assisted receiver was designed for high-throughput QAM schemes, which also outperforms the MMSE solution by minimising the SER at the MUD's output. It can be seen in Table 6.1 that the proposed MBER and MSER MUDs have a higher complexity than the Bayesian MUD, although they cannot achieve a similarly high performance to that of the Bayesian MUD. However, they may impose a lower computational complexity, when communicating over block-fading channels. Furthermore, all linear MUDs have their corresponding equivalent WL methods, where the latter employ two separate weight vectors for separately detecting the in-phase and quadrature-phase component of the transmitted symbol. As discussed in Section 3.2.3, under the zero *a priori* information conditions these WL algorithms have two identical weight vectors and therefore have the same performance as their corresponding non-WL solutions.

In **Chapter 3**, multiuser detection and channel decoding were combined in order to improve the achievable multiuser beamforming receiver's performance following the 'turbo detection principle'. The resultant iterative multiuser receiver is designed based on the soft parallel IC algorithm. In the iterative receivers, the MUD and the channel decoder exchange extrinsic information in a number of consecutive iterations. During each iteration, the extrinsic information is alternately extracted either from the MUD or the channel decoder and then used as the *a priori* input by the other detection stage in the next iteration. Based on the EXIT chart technique, we also analysed both the achievable performance and

the convergence behaviour of different joint detection schemes, both of which are highly dependent upon the different system parameters and channel conditions.

The attainable performance versus computational complexity of different iterative MUD aided receivers was summarized in the 'System 2' column of Table 6.1. The system's schematic obeys the structure of Figure 3.2 and uses the parameters of Tables 3.7, 3.10 or 3.11, depending on the modulation scheme employed. We defined the SNR threshold expressed in terms dBs as the lowest SNR, where the iterative SIC MUD receiver is capable of approaching the BER performance of the single-user system for transmission over AWGN channels. In Chapter 3, we introduced the new iterative MBER SIC beamforming receiver designed for BPSK and QPSK systems, which directly minimises the BER instead of the MSE. This novel algorithm significantly outperforms the conventional MMSE SIC algorithm at the cost of a higher computational complexity. The RMMSE algorithm designed for BPSK was also considered, which minimises the MSE between the real-valued desired signal and the real part of the complex-valued beamformer output. The SISO WL-MMSE algorithm designed for higher-order QAM schemes was derived from the RMMSE solution. Similarly, the soft WL-MBER solution was also introduced, which has the same computational complexity as the MBER algorithm. Table 6.1 has shown that the MBER and WL-MBER solutions outperform both the conventional MMSE and the RMMSE or WL-MMSE iterative receivers. Furthermore, the SISO MSER and WL-MSER MUDs were also introduced and analysed in the context of 16QAM systems. They also outperform the MMSE or WL-MMSE systems at the cost of a high complexity. In contrast to the performance of the MUD receivers dispensing with FEC and characterized in the 'System 1' column of Table 6.1, the WL MUD aided iterative receivers are capable of achieving a better performance than their corresponding non-WL iterative counterparts as a benefit of having non-zero *a priori* information for the MUDs. We can also observe that the SNRs required for achieving a BER of 10^4 by all MUD receivers are similar, except for the MMSE receiver of the BPSK system. The reason for this observation is that they may achieve the single-user performance at an SNR lower than that required for maintaining a BER of 10^4.

All the SISO MUDs discussed in Chapter 3 have a non-recursive nature characterized by a finite, rather than IIR which limits the achievable performance of the iterative system, because the extrinsic information exchange between the decoder components tends to be based on more correlated LLRs than in an IIR system. This disadvantage may be ameliorated with the aid of a simple unity-

rate memory-1 recursive precoder incorporated at the transmitter. Hence the attainable iterative detection performance may be further improved. Then the inner decoder component constituted by the MUD, the intermediate channel decoder and the outer channel decoder constitute a three-stage serially concatenated scheme. In **Chapter 4** we designed this three-stage concatenated multiuser receiver based on the MBER MUD for the sake of achieving a near-capacity performance. By projecting a series of three-dimensional EXIT functions onto a single two-dimensional EXIT chart as seen in Figures 4.2 and 4.3, the convergence behaviour of the system was visualized. Specifically, IRCCs were constructed, which were used as the outer code for the sake of solving the EXIT curve fitting problem, i.e. that of minimising the area of the EXIT chart's open tunnel, implying that the system becomes capable of approaching the achievable capacity.

The 'System 3' column of Table 6.1 summarized the performance of the 3-stage iterative MUD receivers in terms of their SNR required for maintaining a BER of 10^{-4} as well as for an infinitesimally low BER. The system's schematic obeys the structure of Figures 4.1 and uses the parameters of Tables 3.7. It can be seen that the proposed 3-stage MBER iterative receiver significantly outperforms both the 2-stage MBER SIC receiver as well as the 3-stage MMSE receiver. Furthermore, the 3-stage iterative receivers are capable of achieving an infinitesimally low BER. However, the 2-stage receivers' performance has an error floor, which is identical to that of the single-user system.

Sophisticated multiuser detection techniques can be readily employed at the BS's uplink receiver, since the power consumption of the BS is less constrained than that of the MSs. By contrast, for downlink transmission, it may be beneficial to design sophisticated transmitters in the interest of reducing the MS's receiver complexity. The BS is capable of acquiring the required MIMO channel coefficients with the aid of the side-information feedback channel transmitted from the MS or by estimating the uplink channel and assuming that the downlink channel is similar. In **Chapter 5** a linear MUT that minimises the BER subject to a power constraint was proposed. It was shown in Table 5.3 that better BER results can be achieved by the proposed LMBER transmission scheme, when compared to the TMF, TZF and Wiener filter based MUTs. The optimum LMBER MUT solution can be found by exploiting a power-constrained optimization problem, which was investigated in Section 5.3.3. Furthermore, the effects of channel estimation error and outdated channel information imposed on both the Wiener filter and on the LMBER MUTs were investigated. Compared to the

Table 6.1: Summary of the achievable performance versus computational complexity of different MUD beamforming receivers extracted from Tables 2.5, 3.12 and 4.3. The SNR threshold expressed in terms dBs is defined as the lowest SNR, where the iterative SIC MUD receiver is capable of approaching the BER performance of the single-user system for transmission over AWGN channels.

MUD algorithm	Modulation	System 1: MUDs, no FEC		System 2: 2-stage iterative MUDs			System 3: 3-stage iterative MUDs	
		SNR at a BER of 10^{-3}	Complexity	SNR threshold	SNR at a BER of 10^{-4}	Complexity	SNR at a BER of 10^{-4}	SNR at a BER of 0
Bayesian	BPSK	25.5dB	$\mathcal{O}\left(LM^K\right)$	not evaluated			not evaluated	
	QPSK	18dB						
	16QAM	18.5dB						
MMSE	BPSK	unachievable	$\mathcal{O}\left(\frac{L^3}{K}\right)$	5.8dB	5.8dB	$\mathcal{O}\left(L^3\right)$	> 5.1dB	> 5.1dB
	QPSK	unachievable		2.8dB	4.5dB		not evaluated	
	16QAM	unachievable		7.9dB	7.9dB			
RMMSE	BPSK	40dB	$\mathcal{O}\left(\frac{L^3}{K}\right)$	2.6dB	4.6dB	$\mathcal{O}\left(L^3\right)$	not evaluated	
WL-MMSE	QPSK	unachievable	$\mathcal{O}\left(\frac{L^3}{K}\right)$	2.6dB	4.5dB	$\mathcal{O}\left(L^3\right)$	not evaluated	
	16QAM	unachievable		6.8dB	7.9dB			
MBER	BPSK	29dB	$\mathcal{O}\left(LN_{cg}M^K\right)$	2.3dB	4.6dB	$\mathcal{O}\left(LN_{cg}M^K\right)$	> 2.5dB	> 2.5dB
	QPSK	29dB		2.5dB	4.5dB		not evaluated	
WL-MBER	QPSK	29dB	$\mathcal{O}\left(LN_{cg}M^K\right)$	2.3dB	4.5dB	$\mathcal{O}\left(LN_{cg}M^K\right)$	not evaluated	
MSER	16QAM	27.5dB	$\mathcal{O}\left(LN_{cg}M^K\right)$	7.1dB	7.9dB	$\mathcal{O}\left(LN_{cg}M^K\right)$	not evaluated	
WL-MSER	16QAM	27.5dB	$\mathcal{O}\left(LN_{cg}M^K\right)$	6.6dB	7.9dB	$\mathcal{O}\left(LN_{cg}M^K\right)$	not evaluated	

Wiener filter based MUT, the LMBER MUT is more sensitive against channel estimation errors, and the computational complexity imposed by finding the proposed MUT solution is higher. Once the MUT solution is found, it has a similar implementational complexity to those of the other linear transmit preprocessing algorithms. Under slow-fading conditions, the complexity of the LMBER MUT can be significantly reduced, although it fails to achieve a performance similar to that of the non-linear TMinBer algorithm.

Finally, some open issues to be solved for the practical implementation of our systems are addressed. In Chapter 2–4, we assumed that the receivers have perfect channel knowledge, which hardly exists in reality. Naturally, when employing imperfect channel information, the systems' performance degrades. In our iterative beamforming systems, we also assumed that the relative time delay of all users with respect to the angularly closest neighbours is the same. This constraint guarantees that the parallel interference cancellation aided systems are capable of achieving good performance and the systems' convergence behaviour can be analysed by using EXIT charts. However, the realistic arrival angles of the users' signals could be arbitrary, which decreases the achievable performance. The complexity of the MBER/MSER MUD aided system has to be further reduced, before their practical implementation becomes a reality.

6.2 Future Research

6.2.1 Linear Minimum Symbol Error Rate Transmission

The LMBER MUT solution cannot be directly applied in high-order QAM systems. Hence, similar to the MSER multiuser detection algorithm of Section 2.2.6, the Linear Minimum Symbol Error Rate (LMSER) transmission method is motivated, which minimises the average SER at all users' receivers under a certain maximum transmit power constraint.

Let us consider the system model of Section 5.1 for an M-QAM system, and define the constellation symbol as $s^{(m,n)} = \frac{\sqrt{3E_s}}{\sqrt{2(M-1)}}\left(2m - \sqrt{M} - 1\right) + j\frac{\sqrt{3E_s}}{\sqrt{2(M-1)}}\left(2n - \sqrt{M} - 1\right)$, where we have $m \in \{1, 2, \cdots, \sqrt{M}\}$ and $n \in \{1, 2, \cdots, \sqrt{M}\}$. Assuming that the downlink transmitter has to transmit the qth legitimate symbol combination $\mathbf{s}^{(q)}$, $q \in \{1, 2, \cdots, M^K\}$, the kth user's estimated signal can

be expressed as

$$\hat{s}_k^{(q)} = \mathbf{d}_k^H \mathbf{H}_k \mathbf{P} \mathbf{s}^{(q)} + \mathbf{d}_k^H \mathbf{n}_k. \tag{6.1}$$

Then the PDF of $\hat{s}_k^{(q)}$ is given by

$$p\big(\hat{s}_k^{(q)}\big) = \frac{1}{2\pi\sigma_{nk}^2 \mathbf{d}_k^H \mathbf{d}_k} \exp\left(- \frac{\big|\hat{s}_k^{(q)} - \mathbf{d}_k^H \mathbf{H}_k \mathbf{P} \mathbf{s}^{(q)}\big|^2}{2\sigma_{nk}^2 \mathbf{d}_k^H \mathbf{d}_k} \right). \tag{6.2}$$

By defining $b_i = \frac{\sqrt{3E_s}}{\sqrt{2(M-1)}}\big(2i - \sqrt{M}\big)$, $i \in \{1, 2, \cdots, \sqrt{M}-1\}$, the decision boundaries of $\hat{s}_k$ are determined by $b_i \big|\mathbf{d}_k^H \mathbf{H}_k \mathbf{P}\big|$ for the in-phase component and by $jb_i \big|\mathbf{d}_k^H \mathbf{H}_k \mathbf{P}\big|$ for the quadrature-phase component. Assuming that the symbol transmitted to user k is $s_k^{(q)} = s^{(m,n)}$, the conditional in-phase component and quadrature-phase component error probabilities of the hard detected symbol $\check{s}_k^{(q)} \neq s^{(m,n)}$ can be shown to be

$$Pe_{I,k}^{(q)} = \begin{cases} \int_{b_1 |\mathbf{d}_k^H \mathbf{H}_k \mathbf{P}|}^{+\infty} p\big(\hat{s}_k^{(q)}\big) d\Re\big[\hat{s}_k^{(q)}\big] & (m = 1) \\ \int_{-\infty}^{b_{m-1} |\mathbf{d}_k^H \mathbf{H}_k \mathbf{P}|} p\big(\hat{s}_k^{(q)}\big) d\Re\big[\hat{s}_k^{(q)}\big] & \\ \quad + \int_{b_m |\mathbf{d}_k^H \mathbf{H}_k \mathbf{P}|}^{+\infty} p\big(\hat{s}_k^{(q)}\big) d\Re\big[\hat{s}_k^{(q)}\big] & (1 < m < \sqrt{M}) \\ \int_{-\infty}^{b_{\sqrt{M}-1} |\mathbf{d}_k^H \mathbf{H}_k \mathbf{P}|} p\big(\hat{s}_k^{(q)}\big) d\Re\big[\hat{s}_k^{(q)}\big] & (m = \sqrt{M}) \end{cases} \tag{6.3a}$$

and

$$Pe_{Q,k}^{(q)} = \begin{cases} \int_{b_1 |\mathbf{d}_k^H \mathbf{H}_k \mathbf{P}|}^{+\infty} p\big(\hat{s}_k^{(q)}\big) d\Im\big[\hat{s}_k^{(q)}\big] & (n = 1) \\ \int_{-\infty}^{b_{n-1} |\mathbf{d}_k^H \mathbf{H}_k \mathbf{P}|} p\big(\hat{s}_k^{(q)}\big) d\Im\big[\hat{s}_k^{(q)}\big] & \\ \quad + \int_{b_n |\mathbf{d}_k^H \mathbf{H}_k \mathbf{P}|}^{+\infty} p\big(\hat{s}_k^{(q)}\big) d\Im\big[\hat{s}_k^{(q)}\big] & (1 < n < \sqrt{M}) \\ \int_{-\infty}^{b_{\sqrt{M}-1} |\mathbf{d}_k^H \mathbf{H}_k \mathbf{P}|} p\big(\hat{s}_k^{(q)}\big) d\Im\big[\hat{s}_k^{(q)}\big] & (n = \sqrt{M}) \end{cases} \tag{6.3b}$$

Then the resultant symbol error rate is given by

$$Pe_s = \frac{1}{KM^K} \sum_{q=1}^{M^K} \sum_{k=1}^{K} \big(Pe_{I,k}^{(q)} + Pe_{Q,k}^{(q)} - Pe_{I,k}^{(q)} \cdot Pe_{Q,k}^{(q)}\big). \tag{6.4}$$

The LMSER transmission solution can be defined as

$$\mathbf{P}_{LMSER} = \arg\min_{\mathbf{P}} Pe_s \qquad \text{s.t.: } \mathrm{E}\big[\|\mathbf{P}\mathbf{s}\|^2\big] = E_t. \tag{6.5}$$

This optimization problem can be solved by constructing the Lagrangian function

and employing the SQP algorithm, as seen in Section 5.3.

6.2.2 Joint Multiuser Transmission and Iterative Multiuser Detection

In this treatise, both multiuser transmission and iterative multiuser detection were investigated for downlink and uplink communication systems, respectively. However, for a point-to-point MIMO system, it is possible to construct a joint MUT and iterative MUD structure.

For an iterative MUD system dispensing with transmit preprocessing, the receiver's performance and convergence behaviour can be analysed by exploiting the EXIT chart technique. When increasing the number of transmitted data streams, which imposed an increased higher MAI on the receiver, the EXIT curve of the MUD may be shifted to a lower position, which renders the open tunnel between the EXIT curves of the MUD and the channel decoder narrower. However, if transmit preprocessing is employed, the MAI at the receiver may be decreased, and hence this joint MUT and MUD system becomes capable of achieving an increased system capacity.

6.2.3 Cooperative Minimum Error Rate Transmission

The joint MUT and iterative MUD structure of Section 6.2.2 can be extended to a multiuser uplink scenario by introducing a cooperation aided transmission scheme. This attractive idea is capable of exploiting the advantages of MIMOs by exploiting the transmit cooperation of distributed antennas belonging to many different users, which has gained considerable interest [75, 77, 78]. Hence a topic of our future research is the investigation of MBER and MSER aided cooperative transmission systems.

6.2.4 Minimum Error Rate at the Output of Channel Decoders

All proposed minimum error rate multiuser detection algorithms proposed in this treatise were designed for minimising the error rate at the output of the MUDs.

However, for the sake of resisting interference and channel noise, various practical wireless communication systems employ channel coding schemes, where the error rate minimising at the output of the MUDs cannot guarantee the minimisation of the receiver's error rate. Hence, the effect of channel coefficients and noise power on the error rate of the channel decoders' output becomes an interesting topic. If we formulate the BER/SER expression at the channel decoders' output, a more novel minimum error rate detection algorithm can be exploited.

Appendix A

Gradients of Bit/Symbol Error Rate for Multiuser Detection

A.1 Bit Error Rate Gradient

The bit error probabilities of the in-phase part and the quadrature-phase part in Equations (3.50) and (3.51) can be written as

$$Pe = \sum_{q=1}^{M^K} \underline{P}_k\left(\mathbf{s}^{(q)}\right) \cdot \mathrm{Q}\left(x^{(q)}\right), \tag{A.1}$$

where the variable $x^{(q)}$ is defined as

$$x^{(q)} = \begin{cases} x_I^{(q)} = \dfrac{\mathrm{sgn}\left(\Re\left[s_k^{(q)}\right]\right) \cdot \Re\left[\bar{s}_k^{(q)}\right]}{\sigma_n \sqrt{\mathbf{w}_k^H \mathbf{w}_k}} & (\text{for } Pe_I) \\ x_Q^{(q)} = \dfrac{\mathrm{sgn}\left(\Im\left[s_k^{(q)}\right]\right) \cdot \Im\left[\bar{s}_k^{(q)}\right]}{\sigma_n \sqrt{\mathbf{w}_k^H \mathbf{w}_k}} & (\text{for } Pe_Q) \end{cases}. \tag{A.2}$$

Then the gradient of Equation (A.1) can be expressed as

$$\nabla Pe = \sum_{q=1}^{M^K} \underline{P}_k\left(\mathbf{s}^{(q)}\right) \cdot \frac{-1}{\sqrt{2\pi}} \exp\left(-\frac{\left(x^{(q)}\right)^2}{2}\right) \nabla x^{(q)}, \tag{A.3}$$

where

$$\nabla = 2\frac{\partial}{\partial \mathbf{w}_k^*}. \tag{A.4}$$

Using Equation (3.49), we can derive the following equations

$$\begin{aligned}\nabla x_I^{(q)} &= \frac{\operatorname{sgn}\left(\Re\left[s_k^{(q)}\right]\right)}{\sigma_n} \cdot \nabla \frac{\Re\left[\mathbf{w}_k^H \bar{\mathbf{r}}_k^{(q)}\right]}{\sqrt{\mathbf{w}_k^H \mathbf{w}_k}} \\ &= \frac{\operatorname{sgn}\left(\Re\left[s_k^{(q)}\right]\right)}{\sigma_n} \left(\frac{\nabla \Re\left[\mathbf{w}_k^H \bar{\mathbf{r}}_k^{(q)}\right]}{\sqrt{\mathbf{w}_k^H \mathbf{w}_k}} + \Re\left[\mathbf{w}_k^H \bar{\mathbf{r}}_k^{(q)}\right] \cdot \nabla \frac{1}{\sqrt{\mathbf{w}_k^H \mathbf{w}_k}} \right) \\ &= \frac{\operatorname{sgn}\left(\Re\left[s_k^{(q)}\right]\right)}{\sigma_n} \left(\frac{\bar{\mathbf{r}}_k^{(q)}}{\sqrt{\mathbf{w}_k^H \mathbf{w}_k}} - \frac{\Re\left[\mathbf{w}_k^H \bar{\mathbf{r}}_k^{(q)}\right] \mathbf{w}_k}{\left(\mathbf{w}_k^H \mathbf{w}_k\right)^{\frac{3}{2}}} \right) \\ &= \frac{\operatorname{sgn}\left(\Re\left[s_k^{(q)}\right]\right)}{\sigma_n \sqrt{\mathbf{w}_k^H \mathbf{w}_k}} \left(\bar{\mathbf{r}}_k^{(q)} - \frac{\Re\left[\bar{\hat{s}}_k^{(q)}\right] \mathbf{w}_k}{\mathbf{w}_k^H \mathbf{w}_k} \right) \end{aligned} \tag{A.5a}$$

and

$$\begin{aligned}\nabla x_Q^{(q)} &= \frac{\operatorname{sgn}\left(\Im\left[s_k^{(q)}\right]\right)}{\sigma_n} \cdot \nabla \frac{\Im\left[\mathbf{w}_k^H \bar{\mathbf{r}}_k^{(q)}\right]}{\sqrt{\mathbf{w}_k^H \mathbf{w}_k}} \\ &= \frac{\operatorname{sgn}\left(\Im\left[s_k^{(q)}\right]\right)}{\sigma_n} \left(\frac{\nabla \Im\left[\mathbf{w}_k^H \bar{\mathbf{r}}_k^{(q)}\right]}{\sqrt{\mathbf{w}_k^H \mathbf{w}_k}} + \Im\left[\mathbf{w}_k^H \bar{\mathbf{r}}_k^{(q)}\right] \cdot \nabla \frac{1}{\sqrt{\mathbf{w}_k^H \mathbf{w}_k}} \right) \\ &= \frac{\operatorname{sgn}\left(\Im\left[s_k^{(q)}\right]\right)}{\sigma_n} \left(- \frac{j\bar{\mathbf{r}}_k^{(q)}}{\sqrt{\mathbf{w}_k^H \mathbf{w}_k}} - \frac{\Im\left[\mathbf{w}_k^H \bar{\mathbf{r}}_k^{(q)}\right] \mathbf{w}_k}{\left(\mathbf{w}_k^H \mathbf{w}_k\right)^{\frac{3}{2}}} \right) \\ &= \frac{\operatorname{sgn}\left(\Im\left[s_k^{(q)}\right]\right)}{\sigma_n \sqrt{\mathbf{w}_k^H \mathbf{w}_k}} \left(- j\bar{\mathbf{r}}_k^{(q)} - \frac{\Im\left[\bar{\hat{s}}_k^{(q)}\right] \mathbf{w}_k}{\mathbf{w}_k^H \mathbf{w}_k} \right). \end{aligned} \tag{A.5b}$$

Substituting $\nabla x^{(q)}$ in Equation (A.3), we can express the gradients of both the in-phase and quadrature-phase component as

$$\begin{aligned}\nabla Pe_I = \frac{1}{\sqrt{2\pi}\sigma_n \sqrt{\mathbf{w}_k^H \mathbf{w}_k}} \sum_{q=1}^{M^K} \underline{P}_k\left(\mathbf{s}^{(q)}\right) \cdot \exp\left(- \frac{\left(\Re\left[\bar{\hat{s}}_k^{(q)}\right]\right)^2}{2\sigma_n^2 \mathbf{w}_k^H \mathbf{w}_k} \right) \\ \cdot \operatorname{sgn}\left(\Re\left[s_k^{(q)}\right]\right) \left(\frac{\Re\left[\bar{\hat{s}}_k^{(q)}\right] \mathbf{w}_k}{\mathbf{w}_k^H \mathbf{w}_k} - \bar{\mathbf{r}}_k^{(q)} \right) \end{aligned} \tag{A.6a}$$

and

$$\begin{aligned}\nabla Pe_Q = \frac{1}{\sqrt{2\pi}\sigma_n \sqrt{\mathbf{w}_k^H \mathbf{w}_k}} \sum_{q=1}^{M^K} \underline{P}_k\left(\mathbf{s}^{(q)}\right) \cdot \exp\left(- \frac{\left(\Im\left[\bar{\hat{s}}_k^{(q)}\right]\right)^2}{2\sigma_n^2 \mathbf{w}_k^H \mathbf{w}_k} \right) \\ \cdot \operatorname{sgn}\left(\Im\left[s_k^{(q)}\right]\right) \left(\frac{\Im\left[\bar{\hat{s}}_k^{(q)}\right] \mathbf{w}_k}{\mathbf{w}_k^H \mathbf{w}_k} + j\bar{\mathbf{r}}_k^{(q)} \right). \end{aligned} \tag{A.6b}$$

A.2 Symbol Error Rate Gradient

All the Q-functions in Equation (3.66a) can be classified into two types, which are $\mathrm{Q}\left(\frac{\Re\left[\tilde{\bar{s}}_k^{(q)}\right]-b_i\left|\mathbf{w}_k^H\mathbf{h}_k\right|}{\sigma_n\sqrt{\mathbf{w}_k^H\mathbf{w}_k}}\right)$ and $\mathrm{Q}\left(\frac{b_i\left|\mathbf{w}_k^H\mathbf{h}_k\right|-\Re\left[\tilde{\bar{s}}_k^{(q)}\right]}{\sigma_n\sqrt{\mathbf{w}_k^H\mathbf{w}_k}}\right)$, $i \in \{1,2,\cdots,\sqrt{M}-1\}$. The latter one can also be written as

$$\mathrm{Q}\left(\frac{b_i\left|\mathbf{w}_k^H\mathbf{h}_k\right|-\Re\left[\tilde{\bar{s}}_k^{(q)}\right]}{\sigma_n\sqrt{\mathbf{w}_k^H\mathbf{w}_k}}\right)=1-\mathrm{Q}\left(\frac{\Re\left[\tilde{\bar{s}}_k^{(q)}\right]-b_i\left|\mathbf{w}_k^H\mathbf{h}_k\right|}{\sigma_n\sqrt{\mathbf{w}_k^H\mathbf{w}_k}}\right), \tag{A.7}$$

whose gradient can be expressed as

$$\nabla\mathrm{Q}\left(\frac{b_i\left|\mathbf{w}_k^H\mathbf{h}_k\right|-\Re\left[\tilde{\bar{s}}_k^{(q)}\right]}{\sigma_n\sqrt{\mathbf{w}_k^H\mathbf{w}_k}}\right)=-\nabla\mathrm{Q}\left(\frac{\Re\left[\tilde{\bar{s}}_k^{(q)}\right]-b_i\left|\mathbf{w}_k^H\mathbf{h}_k\right|}{\sigma_n\sqrt{\mathbf{w}_k^H\mathbf{w}_k}}\right). \tag{A.8}$$

Therefore, the problem of calculating the gradient of Equation (3.66a) becomes that of calculating the gradient $\nabla\mathrm{Q}\left(\frac{\Re\left[\tilde{\bar{s}}_k^{(q)}\right]-b_i\left|\mathbf{w}_k^H\mathbf{h}_k\right|}{\sigma_n\sqrt{\mathbf{w}_k^H\mathbf{w}_k}}\right)$. Similarly, we have to calculate $\nabla\mathrm{Q}\left(\frac{\Im\left[\tilde{\bar{s}}_k^{(q)}\right]-b_i\left|\mathbf{w}_k^H\mathbf{h}_k\right|}{\sigma_n\sqrt{\mathbf{w}_k^H\mathbf{w}_k}}\right)$ to derive the gradient of Equation (3.66b).

The gradient of the Q-function $\mathrm{Q}\left(\frac{\Re\left[\tilde{\bar{s}}_k^{(q)}\right]-b_i\left|\mathbf{w}_k^H\mathbf{h}_k\right|}{\sigma_n\sqrt{\mathbf{w}_k^H\mathbf{w}_k}}\right)$ is

$$\begin{aligned}\nabla\mathrm{Q}\left(\frac{\Re\left[\tilde{\bar{s}}_k^{(q)}\right]-b_i\left|\mathbf{w}_k^H\mathbf{h}_k\right|}{\sigma_n\sqrt{\mathbf{w}_k^H\mathbf{w}_k}}\right)=&-\frac{1}{\sqrt{2\pi}\sigma_n}\exp\left(-\frac{\left(\Re\left[\tilde{\bar{s}}_k^{(q)}\right]-b_i\left|\mathbf{w}_k^H\mathbf{h}_k\right|\right)^2}{2\sigma_n^2\mathbf{w}_k^H\mathbf{w}_k}\right)\\&\cdot\nabla\frac{\Re\left[\mathbf{w}_k^H\bar{\mathbf{r}}_k^{(q)}\right]-b_i\left|\mathbf{w}_k^H\mathbf{h}_k\right|}{\sqrt{\mathbf{w}_k^H\mathbf{w}_k}},\end{aligned} \tag{A.9}$$

where

$$\begin{aligned}\nabla\frac{\Re\left[\mathbf{w}_k^H\bar{\mathbf{r}}_k^{(q)}\right]-b_i\left|\mathbf{w}_k^H\mathbf{h}_k\right|}{\sqrt{\mathbf{w}_k^H\mathbf{w}_k}}=&\frac{\nabla\Re\left[\mathbf{w}_k^H\bar{\mathbf{r}}_k^{(q)}\right]-b_i\nabla\left|\mathbf{w}_k^H\mathbf{h}_k\right|}{\sqrt{\mathbf{w}_k^H\mathbf{w}_k}}\\&+\left(\Re\left[\mathbf{w}_k^H\bar{\mathbf{r}}_k^{(q)}\right]-b_i\left|\mathbf{w}_k^H\mathbf{h}_k\right|\right)\cdot\nabla\frac{1}{\sqrt{\mathbf{w}_k^H\mathbf{w}_k}}\\=&\frac{\bar{\mathbf{r}}_k^{(q)}}{\sqrt{\mathbf{w}_k^H\mathbf{w}_k}}-\frac{b_i\mathbf{h}_k\mathbf{h}_k^H\mathbf{w}_k}{\sqrt{\mathbf{w}_k^H\mathbf{w}_k}\left|\mathbf{w}_k^H\mathbf{h}_k\right|}\\&-\frac{\left(\Re\left[\mathbf{w}_k^H\bar{\mathbf{r}}_k^{(q)}\right]-b_i\left|\mathbf{w}_k^H\mathbf{h}_k\right|\right)\mathbf{w}_k}{\left(\mathbf{w}_k^H\mathbf{w}_k\right)^{\frac{3}{2}}}\end{aligned}$$

$$= \frac{1}{\sqrt{\mathbf{w}_k^H \mathbf{w}_k}} \left(\bar{\mathbf{r}}_k^{(q)} - \frac{b_i \mathbf{h}_k \mathbf{h}_k^H \mathbf{w}_k}{|\mathbf{w}_k^H \mathbf{h}_k|} - \frac{\left(\Re\left[\tilde{s}_k^{(q)}\right] - b_i |\mathbf{w}_k^H \mathbf{h}_k| \right) \mathbf{w}_k}{\mathbf{w}_k^H \mathbf{w}_k} \right). \tag{A.10}$$

Similarly, the gradient of the Q-function $\mathrm{Q}\left(\frac{\Im\left[\tilde{s}_k^{(q)}\right] - b_i |\mathbf{w}_k^H \mathbf{h}_k|}{\sigma_n \sqrt{\mathbf{w}_k^H \mathbf{w}_k}} \right)$ is

$$\nabla \mathrm{Q}\left(\frac{\Im\left[\tilde{s}_k^{(q)}\right] - b_i |\mathbf{w}_k^H \mathbf{h}_k|}{\sigma_n \sqrt{\mathbf{w}_k^H \mathbf{w}_k}} \right) = -\frac{1}{\sqrt{2\pi}\sigma_n} \exp\left(-\frac{\left(\Im\left[\tilde{s}_k^{(q)}\right] - b_i |\mathbf{w}_k^H \mathbf{h}_k| \right)^2}{2\sigma_n^2 \mathbf{w}_k^H \mathbf{w}_k} \right) \cdot \nabla \frac{\Im\left[\mathbf{w}_k^H \bar{\mathbf{r}}_k^{(q)}\right] - b_i |\mathbf{w}_k^H \mathbf{h}_k|}{\sqrt{\mathbf{w}_k^H \mathbf{w}_k}}, \tag{A.11}$$

where

$$\begin{aligned} \nabla \frac{\Im\left[\mathbf{w}_k^H \bar{\mathbf{r}}_k^{(q)}\right] - b_i |\mathbf{w}_k^H \mathbf{h}_k|}{\sqrt{\mathbf{w}_k^H \mathbf{w}_k}} &= \frac{\nabla \Im\left[\mathbf{w}_k^H \bar{\mathbf{r}}_k^{(q)}\right] - b_i \nabla |\mathbf{w}_k^H \mathbf{h}_k|}{\sqrt{\mathbf{w}_k^H \mathbf{w}_k}} \\ &\quad + \left(\Im\left[\mathbf{w}_k^H \bar{\mathbf{r}}_k^{(q)}\right] - b_i |\mathbf{w}_k^H \mathbf{h}_k| \right) \cdot \nabla \frac{1}{\sqrt{\mathbf{w}_k^H \mathbf{w}_k}} \\ &= -\frac{j \bar{\mathbf{r}}_k^{(q)}}{\sqrt{\mathbf{w}_k^H \mathbf{w}_k}} - \frac{b_i \mathbf{h}_k \mathbf{h}_k^H \mathbf{w}_k}{\sqrt{\mathbf{w}_k^H \mathbf{w}_k} |\mathbf{w}_k^H \mathbf{h}_k|} \\ &\quad - \frac{\left(\Im\left[\mathbf{w}_k^H \bar{\mathbf{r}}_k^{(q)}\right] - b_i |\mathbf{w}_k^H \mathbf{h}_k| \right) \mathbf{w}_k}{\left(\mathbf{w}_k^H \mathbf{w}_k \right)^{\frac{3}{2}}} \\ &= -\frac{1}{\sqrt{\mathbf{w}_k^H \mathbf{w}_k}} \left(j \bar{\mathbf{r}}_k^{(q)} + \frac{b_i \mathbf{h}_k \mathbf{h}_k^H \mathbf{w}_k}{|\mathbf{w}_k^H \mathbf{h}_k|} \right. \\ &\quad \left. + \frac{\left(\Im\left[\tilde{s}_k^{(q)}\right] - b_i |\mathbf{w}_k^H \mathbf{h}_k| \right) \mathbf{w}_k}{\mathbf{w}_k^H \mathbf{w}_k} \right). \end{aligned} \tag{A.12}$$

Then we have

$$\nabla \mathrm{Q}\left(\frac{\Re\left[\tilde{s}_k^{(q)}\right] - b_i |\mathbf{w}_k^H \mathbf{h}_k|}{\sigma_n \sqrt{\mathbf{w}_k^H \mathbf{w}_k}} \right) = \frac{1}{\sqrt{2\pi}\sigma_n \sqrt{\mathbf{w}_k^H \mathbf{w}_k}} \exp\left(-\frac{\left(\Re\left[\tilde{s}_k^{(q)}\right] - b_i |\mathbf{w}_k^H \mathbf{h}_k| \right)^2}{2\sigma_n^2 \mathbf{w}_k^H \mathbf{w}_k} \right) \cdot \left(\frac{\left(\Re\left[\tilde{s}_k^{(q)}\right] - b_i |\mathbf{w}_k^H \mathbf{h}_k| \right) \mathbf{w}_k}{\mathbf{w}_k^H \mathbf{w}_k} - \bar{\mathbf{r}}_k^{(q)} + \frac{b_i \mathbf{h}_k \mathbf{h}_k^H \mathbf{w}_k}{|\mathbf{w}_k^H \mathbf{h}_k|} \right) \tag{A.13a}$$

and

$$\nabla Q\left(\frac{\Im\left[\tilde{\hat{s}}_k^{(q)}\right]-b_i\left|\mathbf{w}_k^H\mathbf{h}_k\right|}{\sigma_n\sqrt{\mathbf{w}_k^H\mathbf{w}_k}}\right)=\frac{1}{\sqrt{2\pi}\sigma_n\sqrt{\mathbf{w}_k^H\mathbf{w}_k}}\exp\left(-\frac{\left(\Im\left[\tilde{\hat{s}}_k^{(q)}\right]-b_i\left|\mathbf{w}_k^H\mathbf{h}_k\right|\right)^2}{2\sigma_n^2\mathbf{w}_k^H\mathbf{w}_k}\right)$$
$$\cdot\left(\frac{\left(\Im\left[\tilde{\hat{s}}_k^{(q)}\right]-b_i\left|\mathbf{w}_k^H\mathbf{h}_k\right|\right)\mathbf{w}_k}{\mathbf{w}_k^H\mathbf{w}_k}+j\bar{\mathbf{r}}_k^{(q)}+\frac{b_i\mathbf{h}_k\mathbf{h}_k^H\mathbf{w}_k}{\left|\mathbf{w}_k^H\mathbf{h}_k\right|}\right). \tag{A.13b}$$

Appendix B

First and Second Gradients of Bit Error Rate for Multiuser Transmission

Similarly to the derivation of the Q-function's gradient in Equation (A.3), the first-order gradients of the bit error probabilities of the in-phase and the quadrature-phase signals formulated in Equations (5.22) and (5.23) can be expressed as

$$\nabla Pe_I = \frac{1}{KM^K} \sum_{q=1}^{M^K} \sum_{k=1}^{K} \frac{-1}{\sqrt{2\pi}} \exp\left(- \frac{\left(\Re\left[\mathbf{d}_k^H \mathbf{H}_k \mathbf{P} \mathbf{s}^{(q)}\right]\right)^2}{2\sigma_{nk}^2 \mathbf{d}_k^H \mathbf{d}_k} \right) \cdot \frac{\operatorname{sgn}\left(\Re\left[s_k^{(q)}\right]\right)}{\sigma_{nk}\sqrt{\mathbf{d}_k^H \mathbf{d}_k}} \cdot \nabla\left(\Re\left[\mathbf{d}_k^H \mathbf{H}_k \mathbf{P} \mathbf{s}^{(q)}\right]\right) \tag{B.1a}$$

and

$$\nabla Pe_Q = \frac{1}{KM^K} \sum_{q=1}^{M^K} \sum_{k=1}^{K} \frac{-1}{\sqrt{2\pi}} \exp\left(- \frac{\left(\Im\left[\mathbf{d}_k^H \mathbf{H}_k \mathbf{P} \mathbf{s}^{(q)}\right]\right)^2}{2\sigma_{nk}^2 \mathbf{d}_k^H \mathbf{d}_k} \right) \cdot \frac{\operatorname{sgn}\left(\Im\left[s_k^{(q)}\right]\right)}{\sigma_{nk}\sqrt{\mathbf{d}_k^H \mathbf{d}_k}} \cdot \nabla\left(\Im\left[\mathbf{d}_k^H \mathbf{H}_k \mathbf{P} \mathbf{s}^{(q)}\right]\right), \tag{B.1b}$$

where

$$\nabla = \frac{\partial}{\partial \mathbf{p}}. \tag{B.2}$$

Then, the only unresolved problem is that of deriving the gradients $\nabla\Big(\Re\big[\mathbf{d}_k^H\mathbf{H}_k\mathbf{P}\mathbf{s}^{(q)}\big]\Big)$ and $\nabla\Big(\Im\big[\mathbf{d}_k^H\mathbf{H}_k\mathbf{P}\mathbf{s}^{(q)}\big]\Big)$.

Let us define $\mathbf{d}_k^H\mathbf{H}_k = \mathbf{a}^T \in \mathbb{C}^{1\times L_t}$ and $\mathbf{s}^{(q)} = \mathbf{b} \in \mathbb{C}^{K\times 1}$. Then $\mathbf{d}_k^H\mathbf{H}_k\mathbf{P}\mathbf{s}^{(q)}$ can be written as

$$\begin{aligned}\mathbf{d}_k^H\mathbf{H}_k\mathbf{P}\mathbf{s}^{(q)} &= \mathbf{a}^T\mathbf{P}\mathbf{b}\\ &= \sum_{l=1}^{L_t}\sum_{k=1}^{K} a_l p_{lk} b_k,\end{aligned} \tag{B.3}$$

where a_l is the lth element of vector $\mathbf{a}$, b_k is the kth element of vector $\mathbf{b}$, and p_{lk} is the element that lies in the lth row and the kth column of matrix $\mathbf{P}$. Furthermore, we have

$$\Re\big[\mathbf{d}_k^H\mathbf{H}_k\mathbf{P}\mathbf{s}^{(q)}\big] = \sum_{l=1}^{L_t}\sum_{k=1}^{K}\big(\Re[a_l b_k]\Re[p_{lk}] - \Im[a_l b_k]\Im[p_{lk}]\big) \tag{B.4a}$$

and

$$\Im\big[\mathbf{d}_k^H\mathbf{H}_k\mathbf{P}\mathbf{s}^{(q)}\big] = \sum_{l=1}^{L_t}\sum_{k=1}^{K}\big(\Im[a_l b_k]\Re[p_{lk}] + \Re[a_l b_k]\Im[p_{lk}]\big). \tag{B.4b}$$

Since the real-valued vector $\mathbf{p}$ was defined as

$$\begin{aligned}\mathbf{p} &= \big[\Re^T[\mathbf{p}_1]\ \ \Re^T[\mathbf{p}_2]\ \cdots\ \Re^T[\mathbf{p}_K]\ \ \Im^T[\mathbf{p}_1]\ \cdots\ \Im^T[\mathbf{p}_K]\big]^T\\ &= \big[\Re[p_{11}]\ \ \Re[p_{21}]\ \cdots\ \Re[p_{L_t1}]\\ &\quad\ \Re[p_{12}]\ \ \Re[p_{22}]\ \cdots\ \Re[p_{L_t2}]\\ &\quad\ \cdots\\ &\quad\ \Re[p_{1K}]\ \ \Re[p_{2K}]\ \cdots\ \Re[p_{L_tK}]\\ &\quad\ \Im[p_{11}]\ \ \Im[p_{21}]\ \cdots\ \Im[p_{L_t1}]\\ &\quad\ \cdots\\ &\quad\ \Im[p_{1K}]\ \ \Im[p_{2K}]\ \cdots\ \Im[p_{L_tK}]\big]^T,\end{aligned} \tag{B.5}$$

we can readily derive that the gradients of $\Re\big[\mathbf{d}_k^H\mathbf{H}_k\mathbf{P}\mathbf{s}^{(q)}\big]$ and $\Im\big[\mathbf{d}_k^H\mathbf{H}_k\mathbf{P}\mathbf{s}^{(q)}\big]$, yielding

$$\nabla\Re\big[\mathbf{d}_k^H\mathbf{H}_k\mathbf{P}\mathbf{s}^{(q)}\big] = \big[\Re[a_1b_1]\ \ \Re[a_2b_1]\ \cdots\ \Re[a_{L_t}b_1]$$

$$
\begin{aligned}
&\Re[a_1 b_2] \;\; \Re[a_2 b_2] \;\cdots\; \Re[a_{L_t} b_2] \\
&\cdots \\
&\Re[a_1 b_K] \;\; \Re[a_2 b_K] \;\cdots\; \Re[a_{L_t} b_K] \\
&-\Im[a_1 b_1] \;\; -\Im[a_2 b_1] \;\cdots\; -\Im[a_{L_t} b_1] \\
&\cdots \\
&-\Im[a_1 b_K] \;\; -\Im[a_2 b_K] \;\cdots\; -\Im[a_{L_t} b_K]\Big]^T \\
&= \Big[\Re\big[\mathbf{a}^T b_1\big] \;\; \Re\big[\mathbf{a}^T b_2\big] \;\cdots\; \Re\big[\mathbf{a}^T b_K\big] \;\; -\Im\big[\mathbf{a}^T b_1\big] \;\cdots\; -\Im\big[\mathbf{a}^T b_K\big]\Big]^T \\
&= \Big[\Re\big[\mathbf{d}_k^H \mathbf{H}_k s_1^{(q)}\big] \;\; \Re\big[\mathbf{d}_k^H \mathbf{H}_k s_2^{(q)}\big] \;\cdots\; \Re\big[\mathbf{d}_k^H \mathbf{H}_k s_K^{(q)}\big] \\
&\quad -\Im\big[\mathbf{d}_k^H \mathbf{H}_k s_1^{(q)}\big] \;\cdots\; -\Im\big[\mathbf{d}_k^H \mathbf{H}_k s_K^{(q)}\big]\Big]^T \\
&= \mathbf{v}_{k,I}^{(q)}
\end{aligned}
\tag{B.6a}
$$

and

$$
\begin{aligned}
\nabla\Im\big[\mathbf{d}_k^H \mathbf{H}_k \mathbf{P}\mathbf{s}^{(q)}\big] = &\big[\Im[a_1 b_1] \;\; \Im[a_2 b_1] \;\cdots\; \Im[a_{L_t} b_1] \\
&\Im[a_1 b_2] \;\; \Im[a_2 b_2] \;\cdots\; \Im[a_{L_t} b_2] \\
&\cdots \\
&\Im[a_1 b_K] \;\; \Im[a_2 b_K] \;\cdots\; \Im[a_{L_t} b_K] \\
&\Re[a_1 b_1] \;\; \Re[a_2 b_1] \;\cdots\; \Re[a_{L_t} b_1] \\
&\cdots \\
&\Re[a_1 b_K] \;\; \Re[a_2 b_K] \;\cdots\; \Re[a_{L_t} b_K]\big]^T \\
= &\Big[\Im\big[\mathbf{a}^T b_1\big] \;\; \Im\big[\mathbf{a}^T b_2\big] \;\cdots\; \Im\big[\mathbf{a}^T b_K\big] \;\; \Re\big[\mathbf{a}^T b_1\big] \;\cdots\; \Re\big[\mathbf{a}^T b_K\big]\Big]^T \\
= &\Big[\Im\big[\mathbf{d}_k^H \mathbf{H}_k s_1^{(q)}\big] \;\; \Im\big[\mathbf{d}_k^H \mathbf{H}_k s_2^{(q)}\big] \;\cdots\; \Im\big[\mathbf{d}_k^H \mathbf{H}_k s_K^{(q)}\big] \\
&\quad \Re\big[\mathbf{d}_k^H \mathbf{H}_k s_1^{(q)}\big] \;\cdots\; \Re\big[\mathbf{d}_k^H \mathbf{H}_k s_K^{(q)}\big]\Big]^T \\
= &\, \mathbf{v}_{k,Q}^{(q)}.
\end{aligned}
\tag{B.6b}
$$

Then the first-order gradients in Equations (B.1) are expressed as

$$
\nabla Pe_I = \frac{-1}{\sqrt{2\pi} K M^K} \sum_{q=1}^{M^K} \sum_{k=1}^{K} \exp\left(- \frac{\big(\Re\big[\mathbf{d}_k^H \mathbf{H}_k \mathbf{P}\mathbf{s}^{(q)}\big]\big)^2}{2\sigma_{nk}^2 \mathbf{d}_k^H \mathbf{d}_k} \right) \cdot \frac{\operatorname{sgn}\big(\Re\big[s_k^{(q)}\big]\big)}{\sigma_{nk}\sqrt{\mathbf{d}_k^H \mathbf{d}_k}} \mathbf{v}_{k,I}^{(q)}
\tag{B.7a}
$$

and

$$\nabla Pe_Q = \frac{-1}{\sqrt{2\pi}KM^K}\sum_{q=1}^{M^K}\sum_{k=1}^{K}\exp\left(-\frac{\left(\Im\left[\mathbf{d}_k^H\mathbf{H}_k\mathbf{P}\mathbf{s}^{(q)}\right]\right)^2}{2\sigma_{nk}^2\mathbf{d}_k^H\mathbf{d}_k}\right)\cdot\frac{\operatorname{sgn}\left(\Im\left[s_k^{(q)}\right]\right)}{\sigma_{nk}\sqrt{\mathbf{d}_k^H\mathbf{d}_k}}\mathbf{v}_{k,Q}^{(q)}. \tag{B.7b}$$

The second-order gradients of Equations (5.22) and (5.23) can be derived as

$$\begin{aligned}
\nabla^2 Pe_I &= \frac{-1}{\sqrt{2\pi}KM^K}\sum_{q=1}^{M^K}\sum_{k=1}^{K}\nabla\exp\left(-\frac{\left(\Re\left[\mathbf{d}_k^H\mathbf{H}_k\mathbf{P}\mathbf{s}^{(q)}\right]\right)^2}{2\sigma_{nk}^2\mathbf{d}_k^H\mathbf{d}_k}\right)\cdot\frac{\operatorname{sgn}\left(\Re\left[s_k^{(q)}\right]\right)}{\sigma_{nk}\sqrt{\mathbf{d}_k^H\mathbf{d}_k}}\left(\mathbf{v}_{k,I}^{(q)}\right)^T \\
&= \frac{-1}{\sqrt{2\pi}KM^K}\sum_{q=1}^{M^K}\sum_{k=1}^{K}\exp\left(-\frac{\left(\Re\left[\mathbf{d}_k^H\mathbf{H}_k\mathbf{P}\mathbf{s}^{(q)}\right]\right)^2}{2\sigma_{nk}^2\mathbf{d}_k^H\mathbf{d}_k}\right)\cdot\left(-\frac{\Re\left[\mathbf{d}_k^H\mathbf{H}_k\mathbf{P}\mathbf{s}^{(q)}\right]}{\sigma_{nk}^2\mathbf{d}_k^H\mathbf{d}_k}\right) \\
&\quad\cdot\nabla\left(\Re\left[\mathbf{d}_k^H\mathbf{H}_k\mathbf{P}\mathbf{s}^{(q)}\right]\right)\cdot\frac{\operatorname{sgn}\left(\Re\left[s_k^{(q)}\right]\right)}{\sigma_{nk}\sqrt{\mathbf{d}_k^H\mathbf{d}_k}}\left(\mathbf{v}_{k,I}^{(q)}\right)^T \\
&= \frac{1}{\sqrt{2\pi}KM^K}\sum_{q=1}^{M^K}\sum_{k=1}^{K}\exp\left(-\frac{\left(\Re\left[\mathbf{d}_k^H\mathbf{H}_k\mathbf{P}\mathbf{s}^{(q)}\right]\right)^2}{2\sigma_{nk}^2\mathbf{d}_k^H\mathbf{d}_k}\right) \\
&\quad\cdot\frac{\operatorname{sgn}\left(\Re\left[s_k^{(q)}\right]\right)\cdot\Re\left[\mathbf{d}_k^H\mathbf{H}_k\mathbf{P}\mathbf{s}^{(q)}\right]}{\sigma_{nk}^3\left(\mathbf{d}_k^H\mathbf{d}_k\right)^{\frac{3}{2}}}\mathbf{v}_{k,I}^{(q)}\left(\mathbf{v}_{k,I}^{(q)}\right)^T
\end{aligned} \tag{B.8a}$$

and

$$\begin{aligned}
\nabla^2 Pe_Q &= \frac{-1}{\sqrt{2\pi}KM^K}\sum_{q=1}^{M^K}\sum_{k=1}^{K}\nabla\exp\left(-\frac{\left(\Im\left[\mathbf{d}_k^H\mathbf{H}_k\mathbf{P}\mathbf{s}^{(q)}\right]\right)^2}{2\sigma_{nk}^2\mathbf{d}_k^H\mathbf{d}_k}\right)\cdot\frac{\operatorname{sgn}\left(\Im\left[s_k^{(q)}\right]\right)}{\sigma_{nk}\sqrt{\mathbf{d}_k^H\mathbf{d}_k}}\left(\mathbf{v}_{k,Q}^{(q)}\right)^T \\
&= \frac{-1}{\sqrt{2\pi}KM^K}\sum_{q=1}^{M^K}\sum_{k=1}^{K}\exp\left(-\frac{\left(\Im\left[\mathbf{d}_k^H\mathbf{H}_k\mathbf{P}\mathbf{s}^{(q)}\right]\right)^2}{2\sigma_{nk}^2\mathbf{d}_k^H\mathbf{d}_k}\right)\cdot\left(-\frac{\Im\left[\mathbf{d}_k^H\mathbf{H}_k\mathbf{P}\mathbf{s}^{(q)}\right]}{\sigma_{nk}^2\mathbf{d}_k^H\mathbf{d}_k}\right) \\
&\quad\cdot\nabla\left(\Im\left[\mathbf{d}_k^H\mathbf{H}_k\mathbf{P}\mathbf{s}^{(q)}\right]\right)\cdot\frac{\operatorname{sgn}\left(\Im\left[s_k^{(q)}\right]\right)}{\sigma_{nk}\sqrt{\mathbf{d}_k^H\mathbf{d}_k}}\left(\mathbf{v}_{k,Q}^{(q)}\right)^T \\
&= \frac{1}{\sqrt{2\pi}KM^K}\sum_{q=1}^{M^K}\sum_{k=1}^{K}\exp\left(-\frac{\left(\Im\left[\mathbf{d}_k^H\mathbf{H}_k\mathbf{P}\mathbf{s}^{(q)}\right]\right)^2}{2\sigma_{nk}^2\mathbf{d}_k^H\mathbf{d}_k}\right) \\
&\quad\cdot\frac{\operatorname{sgn}\left(\Im\left[s_k^{(q)}\right]\right)\cdot\Im\left[\mathbf{d}_k^H\mathbf{H}_k\mathbf{P}\mathbf{s}^{(q)}\right]}{\sigma_{nk}^3\left(\mathbf{d}_k^H\mathbf{d}_k\right)^{\frac{3}{2}}}\mathbf{v}_{k,Q}^{(q)}\left(\mathbf{v}_{k,Q}^{(q)}\right)^T.
\end{aligned} \tag{B.8b}$$

Bibliography

[1] G. J. Foschini and M. J. Gans, "On limits of wireless communication in a fading environment when using multiple antennas," *Wireless Personal Communications*, vol. 6, pp. 311–335, March 1998.

[2] C. E. Shannon, "A mathematical theory of communication," *Bell System Technical Journal*, vol. 27, pp. 379–423 and 623–656, July and October 1948.

[3] A. Goldsmith, S. A. Jafar, N. Jindal, and S. Vishwanath, "Capacity limits of MIMO channels," *IEEE Journal on Selected Areas in Communications*, vol. 21, pp. 684–702, June 2003.

[4] S. Shamai and T. L. Marzetta, "Multiuser capacity in block fading with no channel state information," *IEEE Transactions on Information Theory*, vol. 48, pp. 938–942, April 2002.

[5] E. Biglieri, J. Proakis, and S. Shamai, "Fading channels: Information-theoretic and communications aspects," *IEEE Transactions on Information Theory*, vol. 44, pp. 2619–2692, October 1998.

[6] L. Hanzo, M. Münster, B.-J. Choi, and T. Keller, *OFDM and MC-CDMA for Broadband Multi-user Communications, WLANs and Broadcasting.* John Wiley and IEEE Press, 2003.

[7] 3rd Generation Partnership Project, *Technical Specification Group Radio Access Network; Evolved Universal Terrestrial Radio Access (E-UTRA); Physical Channels and Modulation (Release 8)*, March 2008. 3GPP TS 36.211 V8.2.0.

[8] IEEE Computer Society, *Supplement to IEEE Standard for Information technology – Telecommunications and information exchange between systems – Local and metropolitan area networks – Specific Requirements –*

Part 11: Wireless LAN Medium Access Control (MAC) and Physical Layer (PHY) specifications: Highspeed Physical Layer in the 5 GHz Band, June 2003. IEEE Std 802.11a-1999(R2003).

[9] IEEE Computer Society and the IEEE Microwave Theory and Techniques Society, *IEEE Standard for Local and metropolitan area networks - Part 16: Air Interface for Fixed Broadband Wireless Access Ayatems*, October 2004. IEEE Std 802.16-2004.

[10] H. Ekström, A. Furuskär, J. Karlsson, M. Meyer, S. Parkvall, J. Torsner, and M. Wahlqvist, "Technical solutions for the 3G long-term evolution," *IEEE Communications Magazine*, vol. 44, pp. 38–45, March 2006.

[11] J. S. Blogh and L. Hanzo, *Third generation systems and intelligent wireless networking - smart anttenas and adaptive modulation.* John Wiley and IEEE Press, 2002.

[12] C. Berrou, A. Glavieux, and P. Thitimajshima, "Near Shannon limit error correcting coding and decoding: Turbo codes," in *Proceeding on IEEE International Conference on Communications*, vol. 2, pp. 1064–1070, May 1993.

[13] L. Hanzo, T. H. Liew, and B. L. Yeap, *Turbo Coding, Turbo Equalisation and Space-Time Coding for Transmission over Fading Channels.* John Wiley and IEEE Press, 2002.

[14] L. Hanzo, C. H. Wong, and M. S. Yee, *Adaptive Wireless Transceivers: Turbo-Coded, Turbo-Equalised and Space-Time Coded TDMA, CDMA and OFDM Systems.* John Wiley and IEEE Press, 2002.

[15] M. Tüchler, A. C. Singer, and R. Koetter, "Minimum mean squared error equalization using *a priori* information," *IEEE Transactions on Signal Processing*, vol. 50, pp. 673–682, March 2002.

[16] M. Tüchler, R. Koetter, and A. C. Singer, "Turbo equalization: Principles and new results," *IEEE Transactions on Communications*, vol. 50, pp. 754–767, May 2002.

[17] L. Hanzo, L. L. Yang, E. L. Kuan, and K. Yen, *Single- and Multi-Carrier DS-CDMA: Multi-User Detection, Space-Time Spreading, Synchronisation, Standards and Networking.* John Wiley and IEEE Press, 2003.

[18] X. Wang and H. V. Poor, "Iterative (Turbo) soft interference cancellation and decoding for coded CDMA," *IEEE Transactions on Communications*, vol. 47, pp. 1046–1060, July 1999.

[19] A. Tarable, G. Montorsi, and S. Benedetto, "A linear front end for iterative soft interference cancellation and decoding in coded CDMA," *IEEE Transactions on Wireless Communications*, vol. 4, pp. 507–518, March 2005.

[20] X. Li and J. A. Ritcey, "Trellis-coded modulation with bit interleaving and iterative decoding," *IEEE Journal on Selected Areas in Communications*, vol. 17, pp. 715–724, April 1999.

[21] I. N. Psaromiligkos, S. N. Batalama, and D. A. Pados, "On adaptive minimum probability of error linear filter receivers for DS-CDMA channels," *IEEE Transactions on Communications*, vol. 47, pp. 1092–1102, July 1999.

[22] C.-C. Yeh and J. R. Barry, "Adaptive minimum bit-error rate equalization for binary signaling," *IEEE Transactions on Communications*, vol. 48, pp. 1226–1235, July 2000.

[23] S. Chen, A. K. Samingan, B. Mulgrew, and L. Hanzo, "Adaptive minimum-BER linear multiuser detection for DS-CDMA signals in multipath channels," *IEEE Transactions on Signal Processing*, vol. 49, pp. 1240–1247, June 2001.

[24] B. Mulgrew and S. Chen, "Adaptive minimum-BER decision feedback equalisers for binary signalling," *Signal Processing*, vol. 81, pp. 1479–1489, July 2001.

[25] A. K. Samingan, *Minimum bit error rate multiuser detection techniques for DS-CDMA*. PhD thesis, School of Electronics and Computer Sciences, University of Southampton, UK, December 2003.

[26] S. Chen, L. Hanzo, and B. Mulgrew, "Adaptive minimum symbol-error-rate decision feedback equalization for multi-level pulse-amplitude modulation," *IEEE Transactions on Signal Processing*, vol. 52, pp. 2092–2101, July 2004.

[27] M. Y. Alias, *Minimum bit error rate multiuser detection for multiple antenna aided uplink OFDM*. PhD thesis, School of Electronics and Computer Sciences, University of Southampton, UK, October 2004.

[28] N. N. Ahmad, *Minimum bit error rate beamforming.* PhD thesis, School of Electronics and Computer Sciences, University of Southampton, UK, May 2005.

[29] S. Chen, N. N. Ahmad, and L. Hanzo, "Adaptive minimum bit error rate beamforming," *IEEE Transactions on Wireless Communications*, vol. 4, pp. 341–348, March 2005.

[30] M. Y. Alias, S. Chen, and L. Hanzo, "Multiple-antenna-aided OFDM employing genetic-algorithm-assisted minimum bit error rate multiuser detection," *IEEE Transactions on Vehicular Technology*, vol. 54, pp. 1713–1721, September 2005.

[31] S. Chen, A. Livingstone, and L. Hanzo, "Minimum bite-error rate design for space-time equalization-based multiuser detection," *IEEE Transactions on Communications*, vol. 54, pp. 824–832, May 2006.

[32] S. Chen, L. Hanzo, and A. Livingstone, "Mber space-time decision feedback equalization assisted multiuser detection for multiple antenna aided sdma systems," *IEEE Transactions on Signal Processing*, vol. 54, pp. 3090–3098, August 2006.

[33] C.-C. Yeh and J. R. Barry, "Adaptive minimum symbol-error rate equalization for quadrature amplitude modulation," *IEEE Transactions on Signal Processing*, vol. 51, pp. 3263–3269, December 2003.

[34] S. Chen, H.-Q. Du, and L. Hanzo, "Adaptive minimum symbol error rate beamforming assisted receiver for quadrature amplitude modulation systems," in *Proceeding on IEEE Vehicular Technology Conference*, vol. 5, pp. 2236–2240, May 2006.

[35] B. Picinbono and P. Chevalier, "Widely linear estimation with complex data," *IEEE Transactions on Signal Processing*, vol. 43, pp. 2030–2033, August 1995.

[36] S. ten Brink, "Convergence of iterative decoding," *Electronics Letter*, vol. 35, pp. 1117–1118, June 1999.

[37] S. ten Brink, "Convergence behavior of iteratively decoded parallel concatenated codes," *IEEE Transactions on Communications*, vol. 49, pp. 1727–1737, October 2001.

[38] M. Tüchler, "Design of serially concatenated systems depending on the block length," *IEEE Transactions on Communications*, vol. 52, pp. 209–218, February 2004.

[39] J. Wang, S. X. Ng, A. Wolfgang, L. L. Yang, S. Chen, and L. Hanzo, "Near-capacity three-stage MMSE turbo equalization using irregular convolutional codes," in *Proceedings of the International Symposium on Turbo Codes*, April 2006. Electronic Publication.

[40] K. Li and X. Wang, "EXIT chart analysis of Turbo multiuser detection," *IEEE Transactions on Wireless Communications*, vol. 4, pp. 300–311, January 2005.

[41] S. Benedetto, D. Divsalar, G. Montorsi, and F. Pollara, "Serial concatenation of interleaved codes: Performance analysis, design, and iterative decoding," *IEEE Transactions on Information Theory*, vol. 44, pp. 909–926, May 1998.

[42] I. Lee, "The effect of a precoder on serially concatenated coding systems with an ISI channel," *IEEE Transactions on Communications*, vol. 49, pp. 1168–1175, July 2001.

[43] F. Brännström, L. K. Rasmussen, and A. J. Grant, "Convergence analysis and optimal scheduling for multiple concatenated codes," *IEEE Transactions on Information Theory*, vol. 51, pp. 3354–3364, September 2005.

[44] A. Ashikhmin, G. Kramer, and S. ten Brink, "Extrinsic information transfer functions: Model and erasure channel properties," *IEEE Transactions on Information Theory*, vol. 50, pp. 2657–2673, November 2004.

[45] L. Hanzo, J. Blogh, and S. Ni, *3G, HSPA and FDD Versus TDD Networking: Smart Antennas and Adaptive Modulation.* John Wiley and IEEE Press, 2008.

[46] R. Esmailzadeh and M. Nakagawa, "Pre-RAKE diversity combination for direct sequence spread spectrum mobile communications systems," *IEICE Transactions on Communications*, vol. E76-B, pp. 1008–1015, August 1993.

[47] Z. Tang and S. Cheng, "Interference cancellation for DS-CDMA systems over flat fading channels through pre-decorrelating," in *Proceeding on IEEE*

International Symposium on Personal, Indoor and Mobile Radio Communications, vol. 2, pp. 435–438, September 1994.

[48] B. R. Vojčić and W. M. Jang, "Transmitter precoding in synchronous multiuser communications," *IEEE Transactions on Communications*, vol. 46, pp. 1346–1355, October 1998.

[49] H. R. Karimi, M. Sandell, and J. Salz, "Comparison between transmitter and receiver array processing to achieve interference nulling and diversity," in *Proceeding on International Symposium on Personal, Indoor and Mobile Radio Communications*, vol. 3, pp. 997–1001, September 1999.

[50] M. Joham, K. Kusume, M. H. Gzara, W. Utschick, and J. A. Nossek, "Transmit Wiener filter for the downlink of TDD DS-CDMA systems," in *Proceeding on IEEE International Symposium on Spread Spectrum Techniques and Applications*, vol. 1, pp. 9–13, September 2002.

[51] M. Joham, W. Utschick, and J. A. Nossek, "Linear transmit processing in MIMO communications systems," *IEEE Transactions on Signal Processing*, vol. 53, pp. 2700–2712, August 2005.

[52] R. Irmer, W. Rave, and G. Fettweis, "Minimum BER transmission for TDD-CDMA in frequency-selective channels," in *Proceeding on IEEE Personal, Indoor and Mobile Radio Communications*, vol. 2, pp. 1260–1264, September 2003.

[53] R. Irmer, R. Habendorf, W. Rave, and G. Fettweis, "Nonlinear multiuser transmission using multiple antennas for TDD-CDMA," in *Proceeding on IEEE Wireless, Personal and Mobile Communications*, vol. 3, pp. 251–255, October 2003.

[54] R. Irmer, R. Habendorf, W. Rave, and G. Fettweis, "Nonlinear chip-level multiuser transmission for TDD-CDMA in frequency-selective MIMO channels," in *Proceeding on International ITG Conference on Source and Channel Coding*, pp. 363–370, January 2004.

[55] A. Hjørungnes and P. S. R. Diniz, "Minimum BER prefilter transform for communications systems with binary signaling and known FIR MIMO channel," *IEEE Signal Processing Letters*, vol. 12, pp. 234–237, March 2005.

[56] S. Tan, L. Xu, S. Chen, and L. Hanzo, "Iterative soft interference cancellation aided minimum bit error rate uplink receiver beamforming," in *Proceeding on IEEE Vehicular Technology Conference*, vol. 1, pp. 17–21, May 2006.

[57] L. Xu, S. Tan, S. Chen, and L. Hanzo, "Iterative minimum bit error rate multiuser detection in multiple antenna aided OFDM," in *Proceeding of IEEE Wireless Communications & Networking Conference*, vol. 3, pp. 1603–1607, April 2006.

[58] S. Tan, S. Chen, and L. Hanzo, "MBER turbo multiuser beamforming aided QPSK receiver design using EXIT chart analysis," in *Proceeding on IEEE Vehicular Technology Conference*, vol. 1, pp. 561–565, October 2007.

[59] S. Tan, S. Chen, and L. Hanzo, "On multi-user EXIT chart analysis aided turbo-detected MBER beamforming designs," *IEEE Transactions on Wireless Communications*, vol. 7, pp. 314–323, January 2008.

[60] S. Tan, S. Chen, and L. Hanzo, "Iterative multiuser minimum symbol error rate beamforming aided QAM receiver," *IEEE Signal Processing Letters*, vol. 15, pp. 301–304, February 2008.

[61] S. Tan, S. Chen, and L. Hanzo, "Minimum symbol error rate turbo multiuser beamforming aided QAM receiver," in *Proceeding on IEEE Wireless Communications & Networking Conference*, pp. 912–916, April 2008.

[62] S. Tan, J. Wang, S. X. Ng, S. Chen, and L. Hanzo, "Three-stage turbo MBER multiuser beamforming receiver using irregular convolutional codes," *IEEE Transactions on Vehicular Technology*, vol. 57, pp. 1657–1663, May 2008.

[63] A. Paulraj, R. Nabar, and D. Gore, *Introduction to Space-Time Wireless Communications*. Cambridge University Press, 2003.

[64] G. J. Foschini, "Layered space-time architecture for wireless communication in a fading environment when using multi-element antennas," *Bell Laboratories Technical Journal*, vol. 1, pp. 41–59, October 1996.

[65] V. Tarokh, N. Seshadri, and A. R. Calderbank, "Space-time codes for high data rate wireless communication: Performance criterion and code construction," *IEEE Transactions on Information Theory*, vol. 44, pp. 744–765, March 1998.

[66] P. W. Wolniansky, G. J. Foschini, G. D. Golden, and R. A. Valenzuela, "V-BLAST: An architecture for realizing very high data rates over the rich-scattering wireless channel," in *Proceeding on International Symposium on Signals, Systems, and Electronics*, pp. 295–300, September 1998.

[67] S. M. Alamouti, "A simple transmit diversity technique for wireless communications," *IEEE Journal on Select Areas in Communications*, vol. 16, pp. 1451–1458, October 1998.

[68] V. Tarokh, H. Jafarkhani, and A. R. Calderbank, "Space-time block coding for wireless communications: Performance results," *IEEE Journal on Select Areas in Communications*, vol. 17, pp. 451–460, March 1999.

[69] V. Tarokh, A. Naguib, N. Seshadri, and A. R. Calderbank, "Combined array processing and space-time coding," *IEEE Transactions on Information Theory*, vol. 45, pp. 1121–1128, May 1999.

[70] V. Tarokh, H. Jafarkhani, and A. R. Calderbank, "Space-time block codes from orthogonal designs," *IEEE Transactions on Information Theory*, vol. 45, pp. 1456–1467, July 1999.

[71] G. J. Foschini, G. D. Golden, R. A. Valenzuela, and P. W. Wolniansky, "Simplified processing for high spectral efficiency wireless communication employing multi-element arrays," *IEEE Journal on Selected Areas in Communications*, vol. 17, pp. 1841–1852, November 1999.

[72] H. Jafarkhani, "A quasi-orthogonal space-time block code," *IEEE Transactions on Communications*, vol. 49, pp. 1–4, January 2001.

[73] M. Sellathurai and S. Haykin, "Turbo-BLAST for wireless communications: Theory and experiments," *IEEE Transactions on Signal Processing*, vol. 50, pp. 2538–2546, October 2002.

[74] G. J. Foschini, D. Chizhik, M. J. Gans, C. Papadias, and R. A. Valenzuela, "Analysis and performance of some basic space-time architectures," *IEEE Journal on Selected Areas in Communications*, vol. 21, pp. 303–320, April 2003.

[75] S. N. Diggavi, N. Al-Dhahir, A. Stamoulis, and A. R. Calderbank, "Great expectations: The value of spatial diversity in wireless networks," *Proceeding of the IEEE*, vol. 92, pp. 219–270, February 2004.

[76] M. Tao and R. S. Cheng, "Generalized layer space-time codes for high data rate wireless communications," *IEEE Transactions on Wireless Communications*, vol. 3, pp. 1067–1075, July 2004.

[77] R. Pabst, B. H. Walke, D. C. Schultz, P. Herhold, H. Yanikomeroglu, S. Mukherjee, H. Viswanathan, M. Lott, W. Zirwas, M. Dohler, H. Aghvami, D. D. Falconer, and G. P. Fettweis, "Relay-based deployment concepts for wireless and mobile broadband radio," *IEEE Communications Magazine*, vol. 42, pp. 80–89, September 2004.

[78] A. Nosratinia, T. E. Hunter, and A. Hedayat, "Cooperative communication in wireless networks," *IEEE Communications Magazine*, vol. 42, pp. 74–80, October 2004.

[79] S. Verdú, "Minimum probability of error for asynchronous Gaussian multiple-access channels," *IEEE Transactions on Information Theory*, vol. IT-32, pp. 85–96, January 1986.

[80] S. Verdú, *Multiuser Detection.* Cambridge University Press, 1998.

[81] A. J. Viterbi, "Error bounds for convolutional codes and an asymptotically optimum decoding algorithm," *IEEE Transactions on Information Theory*, vol. IT-13, pp. 260–269, April 1967.

[82] J. G. Proakis, *Digital Communications.* McGraw-Hill, 1995.

[83] D. Gesbert, "Robust linear MIMO receivers: A minimum error-rate approach," *IEEE Transactions on Signal Processing*, vol. 51, pp. 2863–2871, November 2003.

[84] S. Chen, S. Tan, L. Xu, and L. Hanzo, "Adaptive minimum error-rate filtering design: A review," *Signal Processing*, vol. 88, pp. 1671–1697, July 2008.

[85] S. M. Kay, *Fundamentals of Statistical Signal Processing, Estimation Theory.* New Jersey: Prentice Hall, 1993.

[86] P. Patel and J. Holtzman, "Analysis of a simple successive interference cancellation scheme in a DS/CDMA system," *IEEE Journal on Selected Areas in Communications*, vol. 12, pp. 798–807, June 1994.

[87] M. K. Varanasi and B. Aazhang, "Multistage detection in asynchronous code division multiple access communications," *IEEE Transactions on Communications*, vol. 38, pp. 509–519, April 1990.

[88] M. C. Reed, C. B. Schlegel, P. D. Alexander, and J. A. Asenstorfer, "Iterative multiuser detection for CDMA with FEC: Near single user performance," *IEEE Transactions on Communications*, vol. 46, pp. 1693–1699, December 1998.

[89] R. Schober, W. H. Gerstacker, and L. Lampe, "On suboptimum receivers for DS-CDMA with BPSK modulation," *Signal Processing*, vol. 85, pp. 1149–1163, June 2005.

[90] M. S. Bazaraa, H. D. Sherali, and C. M. Shetty, *Nonlinear Programming: Theory and Algorithms.* New York: John Wiley, 1993.

[91] S. Benedetto, D. Divsalar, G. Montorsi, and F. Pollara, "Analysis, design, and iterative decoding of double serially concatenated codes with interleavers," *IEEE Journal on Selected Areas in Communications*, vol. 16, pp. 231–244, February 1998.

[92] C. Douillard, M. Jézéquel, C. Berrou, A. Picart, P. Didier, and A. Glavieux, "Iterative correction of intersymbol interference: Turbo-equalization," *European Transactions on Communications*, vol. 6, pp. 507–511, September-October 1995.

[93] J. Hou, P. H. Siegel, and L. B. Milstein, "Design of multi-input multi-output systems based on low-density parity-check codes," *IEEE Transactions on Communications*, vol. 53, pp. 601–611, April 2005.

[94] S. ten Brink, "Designing iterative decoding schemes with the extrinsic information transfer chart," *AEÜ - International Journal of Electronics and Communications*, vol. 54, pp. 389–398, November 2000.

[95] N. Wu and L. Hanzo, "Near-capacity irregular precoded linear dispersion codes," in *Proceeding of IEEE International Conference on Communications*, pp. 4501–4505, May 2008.

[96] R. Y. S. Tee, R. G. Maunder, J. Wang, and L. Hanzo, "Near-capacity irregular bit-interleaved coded modulation," in *Proceeding of IEEE Vehicular Technology Conference*, pp. 549–553, May 2008.

[97] R. G. Maunder and L. Hanzo, "Near-capacity irregular variable length coding and irregular unity rate coding," *IEEE Transactions on Wireless Communications*. Submitted.

[98] J. Hagenauer, E. Offer, and L. Papke, "Iterative decoding of binary block and convolutional codes," *IEEE Transactions on Information Theory*, vol. 42, pp. 429–445, March 1996.

[99] P. S. Henry and B. S. Glance, "A new approach to high-capacity digital mobile radio," *Bell System Technical Journal*, vol. 60, pp. 1891–1904, October 1981.

[100] D. Yang, L.-L. Yang, and L. Hanzo, "Performance of MIMO systems using transmitter preprocessing based on limited noisy feedback of vector-quantized channel impulse responses," in *Proceeding of IEEE Vehicular Technology Conference*, vol. 1, pp. 22–25, April 2007.

[101] A. Duel-Hallen, S. Hu, and H. Hallen, "Long-range prediction of fading signals," *IEEE Signal Processing Magazine*, vol. 17, pp. 62–75, May 2000.

[102] L.-L. Yang, "Design linear multiuser transmitters from linear multiuser receivers," in *Proceeding of IEEE International Conference on Communications*, pp. 24–28, June 2007.

[103] A. N. Barreto and G. Fettweis, "Capacity increase in the downlink of spread spectrum systems through joint signal precoding," in *Proceeding on IEEE International Conference on Communications*, vol. 4, pp. 1142–1146, June 2001.

[104] J. Nocedal and S. J. Wright, *Numerical Optimization*. New York: Springer, 1999.

Index

Author Index